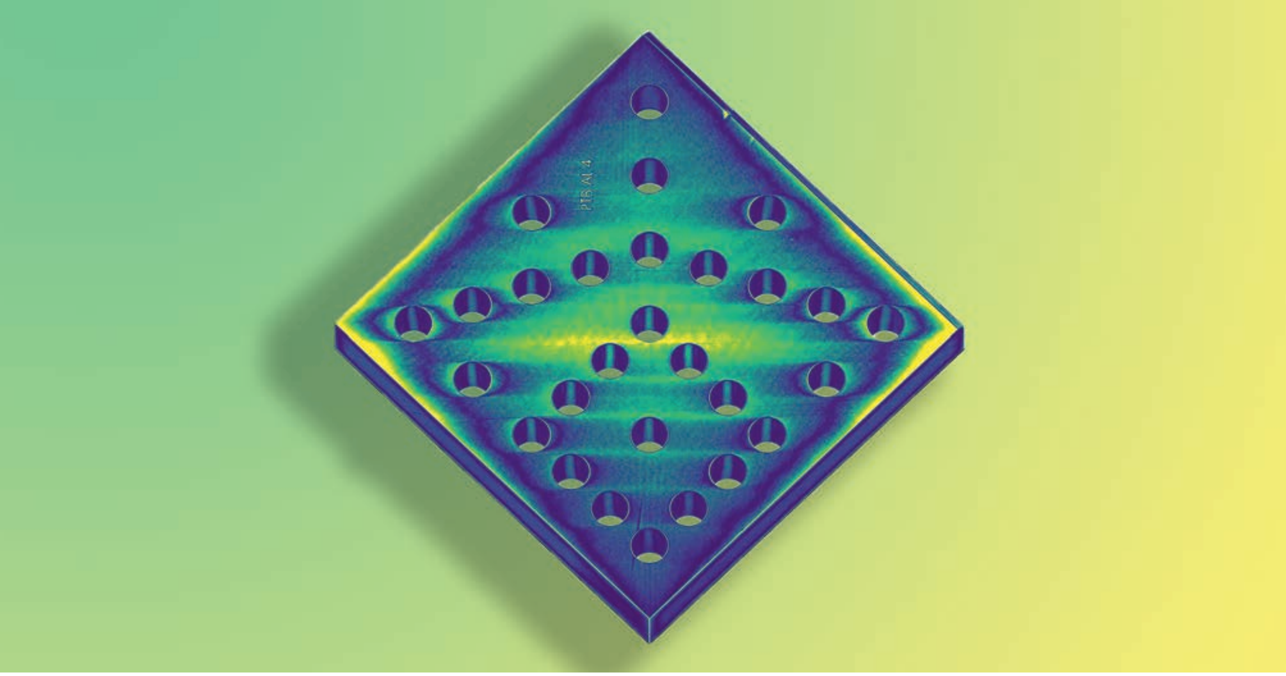

FAU Studien aus dem Maschinenbau 454

Andreas Michael Müller

Definition and applications of the spatially discrete metrological descriptor framework for triangle mesh geometry data in 3D coordinate metrology

FAU University Press

Andreas Michael Müller

Definition and applications of the spatially discrete metrological descriptor framework for triangle mesh geometry data in 3D coordinate metrology

FAU Studien aus dem Maschinenbau

Band 454

Herausgeber/-innen:

Prof. Dr.-Ing. Jörg Franke
Prof. Dr.-Ing. Nico Hanenkamp
Prof. Dr.-Ing. habil. Tino Hausotte
Prof. Dr.-Ing. habil. Marion Merklein
Prof. Dr.-Ing. Sebastian Müller
Prof. Dr.-Ing. Michael Schmidt
Prof. Dr.-Ing. Sandro Wartzack

Andreas Michael Müller

Definition and applications of the spatially discrete metrological descriptor framework for triangle mesh geometry data in 3D coordinate metrology

Dissertation aus dem Lehrstuhl für Lehrstuhl für Fertigungsmesstechnik (FMT) Prof. Dr.-Ing. habil. Tino Hausotte

Erlangen
FAU University Press
2024

Bibliografische Information der Deutschen Nationalbibliothek:
Die Deutsche Nationalbibliothek verzeichnet diese Publikation in der Deutschen Nationalbibliografie; detaillierte bibliografische Daten sind im Internet über http://dnb.d-nb.de abrufbar.

Kontakt: Andreas Michael Müller, Friedrich-Alexander-Universität
Erlangen-Nürnberg, (https://ror.org/00f7hpc57)

Bitte zitieren als
Müller, Andreas Michael. 2024. *Definition and applications of the spatially discrete metrological descriptor framework for triangle mesh geometry data in 3D coordinate metrology*. FAU Studien aus dem Maschinenbau Band 454. Erlangen: FAU University Press. DOI: 10.25593/978-3-96147-783-8

Verlag und Auslieferung:
FAU University Press, Universitätsstraße 4, 91054 Erlangen

Druck: docupoint GmbH

ISBN: 978-3-96147-782-1 (Druckausgabe)
eISBN: 978-3-96147-783-8 (Online-Ausgabe)
ISSN: 2625-9974
DOI: 10.25593/978-3-96147-783-8

Definition and applications of the spatially discrete metrological descriptor framework for triangle mesh geometry data in 3D coordinate metrology

Definition und Anwendungen eines Rahmens für räumlich diskrete metrologische Deskriptoren für Geometrien auf Basis von Dreiecksnetzen in der 3D-Koordinatenmesstechnik

Der Technischen Fakultät
der Friedrich-Alexander-Universität
Erlangen-Nürnberg

zur

Erlangung des Doktorgrades Dr.-Ing.

vorgelegt von

Andreas Michael Müller

aus Ansbach

Als Dissertation genehmigt
von der Technischen Fakultät
der Friedrich-Alexander-Universität Erlangen-Nürnberg

Tag der mündlichen Prüfung:	08.04.2024
Gutachter:	Prof. Dr.-Ing. habil. Tino Hausotte Prof. Dr.-Ing. habil. Andreas Maier

Contents

List of Symbols and Abbreviations

Elements are listed in order of appearance. The table lists elements with global scope across multiple chapters / sections, which are reused at least once.

Symbol	***Description***
(ISO) GPS	Geometrical Product Specification (series of standards)
TCMS	tactile coordinate measurement system
CMS	coordinate measurement system
CAD	computer-aided design
VCMM	virtual coordinate measuring machine
SLS	structured-light 3D scanner
CT	metrological X-ray computed tomography system
STEP	standard for the exchange of product model data
CSG	constructive solid geometry
BREP	boundary representation
$\boldsymbol{c}$	centre point of STEP curve and surface entity
N_v	number of vertices in a mesh
N_e	number of edges in a mesh
N_f	number of facets in a mesh
$\overrightarrow{PQ}$	line segment defined by points P and Q
$\triangle_{ABC}$	triangle consisting of edge points A, B and C
STL	stereolithography / standard triangle language / standard tessellation language
(C)DT	(constrained) Delaunay triangulation
VIM	international vocabulary of metrology
GUM	Guide to the Expression of Uncertainty in Measurement
$\mathcal{O}$	measurement object
$\mathcal{A}$	examined measurement system
$\mathcal{M}^\dagger$	data of a single measurement
$\mathcal{M}$	data of a series of measurements of size n_MS

Symbol	***Description***
n_{MS}	size of measurement series (number of single measurements)
$\mathcal{R}$	reference measurement data
$\mathcal{B}$	reference measurement system
$\mathcal{N}$	nominal geometry data of $\mathcal{O}$
PDF	probability density function
$\{\boldsymbol{n}_{\mathrm{f},i}\}_{i=1}^{N_{\mathrm{f}}}$	set of N_{f} face normal vectors of a mesh
$\nabla_{\mathrm{norm}}\boldsymbol{x}$	normalised gradient of a point $\boldsymbol{x}$
$\{\boldsymbol{n}_{\mathrm{v},i}\}_{i=1}^{N_{\mathrm{v}}}$	set of N_{v} vertex normal vectors of a mesh
$v_{\boldsymbol{a}}$	valence of mesh vertex $\boldsymbol{a}$
$\mathrm{BB}_{\mathrm{tf}}$	tight fitting bounding box of an object
$\triangle_A$	triangle designated A
$w(\boldsymbol{p})$	winding number of $\boldsymbol{p} \in \mathbb{R}^2 \vee \boldsymbol{p} \in \mathbb{R}^3$
$\mathcal{S}$	sampling start geometry
$\mathcal{T}$	sampling target geometry
$\boldsymbol{s}_i$	sampling start coordinate: (single) point on $\mathcal{S}$
$\boldsymbol{h}_i$	hit location on $\mathcal{T}$ as a result from sampling starting at $\boldsymbol{s}_i$
$\boldsymbol{d}_i = \boldsymbol{h}_i - \boldsymbol{s}_i$	connection vector between $\boldsymbol{s}_i$ and $\boldsymbol{h}_i$
$N_{\mathcal{S},v}$	number of triangle vertices in $\mathcal{S}$
$N_{\mathcal{T},v}$	number of triangle vertices in $\mathcal{T}$
$N_{\mathcal{T},f}$	number of faces vertices in $\mathcal{T}$
$\mathcal{M}^{\mathrm{tri}}$	triangle mesh
$\boldsymbol{C}_{\mathrm{approx}}$	result of a registration routine which approximates the true coordinate transform $\boldsymbol{C}$ between two geometries
$\mathcal{M}^{\mathrm{tri}}_{\mathrm{data}}$	triangle mesh, for which a registration result is determined with respect to $\mathcal{M}^{\mathrm{tri}}_{\mathrm{template}}$
$\mathcal{M}^{\mathrm{tri}}_{\mathrm{template}}$	triangle mesh, against which $\mathcal{M}^{\mathrm{tri}}_{\mathrm{data}}$ is registered
ICP	Iterative Closest Point (algorithm for registration)
$\mathcal{S}_{\mathrm{reg}}$	sampling start geometry in the context of registration
$\mathcal{T}_{\mathrm{reg}}$	sampling target geometry in the context of registration
$\boldsymbol{s}_{\mathrm{reg},i}$	sampling start coordinate in the context of registration: point on $\mathcal{S}_{\mathrm{reg}}$

Symbol	***Description***
$\boldsymbol{h}_{\mathrm{reg},i}$	hit location on $\mathcal{T}_{\mathrm{reg}}$ as a result from sampling starting at $\boldsymbol{s}_{\mathrm{reg},i}$ in the context of registration
CEP	distance metric ”closest edge point”
SD	distance metric ”shortest distance”
SDSP	distance metric ”shortest distance from start plane”
SDHP	distance metric ”shortest distance to hit plane”
VNV	distance metric ”vertex normal vector”
$\mathrm{TMA}_{\mathcal{A},\mathcal{B}}$	triangle mesh affinity between two triangle meshes $\mathcal{A}$ and $\mathcal{B}$
$\mathrm{REG}_{1\rightarrow 1}$	registration where two geometries are registered against each other
$\mathrm{REG}_{1\rightarrow n}$	registration where one geometry is simultaneously registered against n geometries
E_{sys}	spatially discrete metrological descriptor: estimation of the systematic measurement error at $\boldsymbol{s}_i$
E_{rand}	spatially discrete metrological descriptor: estimation of the random measurement error at $\boldsymbol{s}_i$
Δ_{cmp}	spatially discrete metrological descriptor: estimation of the local geometric deviations of the examined component at $\boldsymbol{s}_i$
$\Delta_{\mathrm{cmp}}^{E_{\mathrm{sys}}}$	spatially discrete metrological descriptor: estimation of the superimposition of the local systematic measurement error and the geometric deviations of the examined component at $\boldsymbol{s}_i$
UC	use case of the the spatially discrete metrological descriptor framework
SS	sampling start surface with respect to a specific UC
PST	primary sampling target surface with respect to a specific UC
SST	secondary sampling target surface with respect to a specific UC
U_{exp}	spatially discrete metrological descriptor: estimation of the expanded measurement uncertainty at $\boldsymbol{s}_i$
α_i	spatially discrete metrological descriptor: angle between $\boldsymbol{d}_i$ and $\boldsymbol{n}_{\mathcal{S},\mathrm{v},i}$
α_{sys}, α_{rand}	statistics regarding $\{\alpha_{i,j}\}_{j=1}^{n_{\mathrm{MS}}}$ for each $\boldsymbol{s}_i$

Symbol	***Description***
β_i	spatially discrete metrological descriptor: angle between $\boldsymbol{d}_i$ and $\nabla_{\text{norm}}\boldsymbol{h}_i$
β_{sys}, β_{rand}	statistics regarding $\{\beta_{i,j}\}_{j=1}^{n_{\text{MS}}}$ for each $\boldsymbol{s}_i$
$\lambda_{\text{ratio},i}$	spatially discrete metrological descriptor based on the eigenvalues of the covariance matrix of $\{\boldsymbol{d}_{i,j}\}_{j=1}^{n_{\text{MS}}}$ for each $\boldsymbol{s}_i$
γ_i	spatially discrete metrological descriptor based on the eigenvectors of the covariance matrix of $\{\boldsymbol{d}_{i,j}\}_{j=1}^{n_{\text{MS}}}$ for each $\boldsymbol{s}_i$
Drift	spatially discrete metrological descriptor with respect to potential measurement drifts

1 Introduction

The importance of metrology, the science of measurement, is well known in areas linked to engineering, construction and manufacturing but its effects also generate societal impacts through trade and economy [1]. The main activities of metrology are the definition of units of measurement, the realisation of units of measurement by scientific methods and the establishment of traceability chains by determining and documenting the accuracy of the measurement value [2].

1.1 The context: Measurement uncertainty in industrial (geometrical) metrology

The system of the Geometrical Product Specification (GPS, also ISO GPS) describes a set of rules for the technical communication of geometrical requirements of products in the field of mechanical engineering [3]. Comprehensive overviews over the ISO GPS system can be found in [4, 5]. It is also depicted as the ”engineer’s language” [5]. The series of standards represents a framework to specify the requirements of a measurement object regarding its geometrical features, such that the function of the part is guaranteed. Geometrical features are defined as a point, a line, a surface, a volume or a set of those elements [6, 7]. A measurement object can in turn be fully specified regarding its geometry by indication of dimensions (e.g. length, diameter, distance), the properties and relations of geometry elements (form, position and orientation) and surface properties (waviness and roughness) [8]. The goal of the definition of geometry element features as well as the relationship between geometry elements, respectively, is to define a rule-based specification methodology [5]. Production-related deviations from the nominal geometrical specifications are unavoidable. Thus, permissible limits must be set using tolerances. It is accepted by agreement that the function of a measurement object is guaranteed if no specified feature exceeds its associated tolerance limit [9].

The ISO GPS system is based on several fundamental principles, one of which is the duality principle. Its operator concept states that the specifications for measurement object features are formulated as specification operators with the verification operator being the physical implementation of the aforementioned. Furthermore, the specification operator is defined independently of any measurement procedure or measurement equipment. The acceptability of a verification operator is based on the evaluation of the measurement uncertainty and possible ambiguities in the specification. [9]

ISO GPS defines seven different types of operations which are used to obtain ideal and non-ideal geometry elements [6]. Specification and verification operators are defined by the ordered application of selected operations, respectively [9]. Thus, these operators are also defined independently of the measurement procedure or measurement equipment. Operators are defined as a special tool to determine the elements or values as well as the nominal value and boundaries of a feature [5, 6].

Coordinate metrology is used to technically implement the ISO GPS verification operator and thus determines if the geometrical properties comply with the specification within its given tolerances. However, the ISO GPS system of standards does not specify any particular measurement or test procedure for the verification of the conformity of geometric tolerances [8]. Coordinate metrology is an universal measurement technique based on point by point sampling of the physical boundary of a measurement object. Nonetheless, every measurement itself is affected by uncertainty, the true (quantity) value [10] of a measurand is basically fictional [11, 12]. The reason for that is that a measurement is always an inaccurate operation due to physical conditions [13]. In order to evaluate the trustworthiness of a measurement and to facilitate its comparability the indication of the measurement uncertainty is required [11]. The measurement uncertainty is a non-negative quantity and originates from the facts that the verification operator is not identical to the specification operator (method uncertainty) and because the verification operator is not physically perfect (implementation uncertainty) [4]. Thus, a complete measurement result consists of the measured value with the unit of measurement, a statement about the measurement uncertainty as well as all relevant information describing the acquisition of the measurement result [8]. The measurement uncertainty is of great economic importance and is a requirement for the comparability and acceptance of measurement results [8] as well as for applying decision rules for proving conformance or non-conformance with specifications [14].

1.2 The motivation

The measurement result of any measurement system in the context of coordinate metrology consists at least of a limited number of coordinates in three-dimensional space. Each of these measurement points is the result of an unique interaction between the measurement object and the measurement device, including all data processing. Consequently, it is in general not correct to expect a common value for the measurement uncertainty for a set of points representing a specific geometric feature (e.g. a cylindrical bore hole). However, data processing instructions within ISO GPS (e.g. operations partition and association) and other measurement data processing steps (e.g. registration[1]) usually do not consider[2] point-wise uncertainty information. However considering point-wise uncertainty information in different data processing steps could theoretically reduce the overall measurement uncertainty of a measurement task, because points with a lower effective measurement uncertainty could contribute more towards the target quantity compared to worse measurement points.

Due to the advancing digitalisation, new algorithms and new data processing methods (e.g. based on ”big data” and ”artificial intelligence”) are introduced into the field of dimensional metrology. Because of that, new tools for measurement system analysis are required which can directly evaluate the impact of certain mathematical operations within the measurement chain onto the resulting measurement points. For example, a mathematical method is applied in order to correct measurement artefacts which have an impact on the surface of a geometric feature. The established procedure is to compare the measurement results of different measurands against their respective calibration values. However, for many use cases it is especially interesting how accurately the complete surface is captured compared to a reference surface, without the need for definition and evaluation of many individual geometrical inspection features. Typical inspection features represent the combination of many individual surface points into a small number of geometrical parameters, e.g. the information contained in all measurement coordinates representing a bore hold is combined into mathematical parameters describing a cylinder. Therefore, it is possible that influences which only affect a subset of these measurement points are poorly reflected by the resulting cylinder parameters alone. This possibly makes this geometry element based method insensitive towards the effects of the aforementioned mathematical correction method, which complicates the development feedback loop [16].

This work was additionally motivated by the concept of deduction of quality parameters for single measurement points by evaluation of intermediate measurement data for specific measurement methods (e.g. voxel data for industrial X-ray computed tomography). Depending on the underlying physical interactions the algorithmic determination of measurement coordinates

---

[1] Registration is the estimation of a mapping $\boldsymbol{T}$ between the coordinate systems of two different modalities $\boldsymbol{A}$ and $\boldsymbol{B}$ such that $\boldsymbol{x_A} = \boldsymbol{T x_B}$ with x_A and x_B being the same coordinates observed by the different coordinate systems of $\boldsymbol{A}$ and $\boldsymbol{B}$ [15].

[2] The ISO GPS standards do not specify a methodology of how to include uncertainty information into the underlying mathematical tools. However, it cannot be excluded that suppliers of metrological software products are using uncertainty information within their algorithms in order to improve the measurement results, e.g. by the application of a VCMM (see sec. 2.1.1).

is more or less affected by measurement artefacts, which can be observed by an alternative evaluation of the underlying data. Here, the resulting point-wise abstract quality parameters can give important conclusions about the chosen measurement setup and are also suitable to be used as mathematical weighting factors in subsequent data processing operations. Thus, finding a correlation between abstract quality parameters and traceable measurement error/uncertainty for the same surface location was identified as a research goal.

1.3 The aim

In the context of this thesis, which specifically deals with coordinate metrology, the measurement uncertainty at a specific location on the surface of a measurement object is called "spatially discrete (measurement) uncertainty". It is based on experimental determination using a sufficient number of measurement repetitions and a single reference measurement. The measurement uncertainty is one of many provided metrological descriptors which characterise the geometrical dispersion of coordinate data in the context of 3D coordinate metrology. In this context, "measurement data" describes the complete set of measured coordinates which completely[3] describe the geometry of the measurement object. Thus, the determined values for the spatially discrete uncertainty describe the local measurement uncertainty of a distinct measurement task (consisting of measurement object, measurement device and user-defined measurement parameters) with respect to the used reference measurement procedure (consisting of the same measurement object, a reference measurement system and user-defined measurement parameters). The overarching goal is to obtain a description of the local measurement uncertainty with respect to the complete surface of an object. Here, metrological descriptors (including e.g. systematic and random measurement error, respectively) are observed by comparison of surface coordinates against their nominal/reference position by means of statistical methods. This goal can be reached without the requirement of the definition and evaluation of typical user-defined inspection features, which leads to great universality and flexibility with regards to the application of the complete framework. All data processing pipelines are designed such that the areal representation of the different types of geometry data is preserved at all times in form of a triangle mesh (instead of a point cloud description), which distinguishes this work from similar research efforts (see sec. 4). The main goals of this work are:

---

[3] Completely means that all geometrical features described by the nominal geometry are probed with a sufficient number of measurement points.

- Develop the complete data processing pipeline required in order to robustly determine the spatially discrete metrological descriptors from repeated measurements for different tactile, optical and tomographic coordinate measurement sensor technologies. That pipeline should be able to process geometry data representing real physical objects, which requires the enforcement of a complete geometry representation. This also includes methods for handling corrupted geometry data and also estimating unknown coordinate transformations between different geometries.
- Develop a complete framework capable of performing comprehensive measurement system analyses in order to quantise the local influence of different influences onto the measurement chain on the acquired measurement surface. This makes it possible to effectively implement measurement strategy optimisations even for complex measurement tasks as well as the assessment of the accuracy of digital twins.
- Realise high lateral surface sampling rates[4] corresponding to at least half of the estimated structural resolution of the used measurement method while maintaining competitive computation durations. This requires suitable methods, capable of processing large geometry models.
- Investigate the potential for improving the accuracy of exemplary ISO GPS operations by considering point-wise metrological descriptor information within the required optimisation algorithms.
- Contribute to research efforts dealing with improved process-oriented tolerance management based on virtual computer-aided engineering tools by providing methods to consider the measurement uncertainty already during the design phase. This approach makes it possible to adjust the required feature tolerances during the design phase based on the observed local measurement uncertainty.

Ideally, the spatially discrete metrological descriptor framework presents a capable method to estimate the metrological characteristics for arbitrary surface points of the examined geometry without the need for any additional information. As such, very subtle changes in local measurement accuracy and precision, respectively, could be observed with high sensitivity, thus improving the decision making in 3D coordinate metrology in many different applications and contexts.

1.4 The outline

In order to realise the motivated work, this thesis is structured as follows: Firstly, a technical introduction to 3D coordinate metrology is given in chap. 2. This includes prominent representatives of typical measurement systems,

---

[4] i.e. number of samples per unit length / area

important fundamentals of geometry data representation and the concept behind measurement uncertainty determination. The problem statement and the objective of this work are given in chap. 3, followed by the identification of related work in chap. 4. A technical description of the data processing pipeline is presented in chap. 5, which includes required triangle mesh processing, definition of distance metrics between two triangles after their geometric alignment, as well as the derivation of conventional and unconventional metrological descriptors. After the presentation of selected applications in chap. 6, an introduction to the applied heterogeneous computing concept for managing the associated computational demands is given in chap. 7. The work is finalised by a discussion (chap. 8), followed by a summary and outlook (chap. 9).

1.5 Contribution to own publications and students' theses

This section was added based on regulatory requirements of the examination office. In Table 1, the own contributor roles are given for each of the own publications referenced in this thesis. The contributor roles are used according to CRediT [17]. Additionally, [P1, P2] are the author's own student theses with content relevance. The author contributions for [P3–P16] are explicitly given in each article.

Within the context of this work, a number of students' theses were supervised [S1–S10].

Table 1: Statement about contributions to own publications following the CASRAI CRediT contributor roles taxonomy [17].

Publication(s)	Own contributor roles taken
[P17–P19]	Software, Investigation, Visualisation
[P20]	Methodology, Software
[P21]	Formal Analysis, Software, Writing – original draft, Writing – review & editing
[P22, P23]	Investigation, Software, Visualisation, Writing – original draft
[P24]	Investigation, Visualisation, Writing – original draft
[P25–P34]	Conceptualisation, Data curation, Formal analysis, Investigation, Methodology, Software, Validation, Visualisation, Writing – original draft, Writing – review & editing

1.6 Mathematical notation

This section gives a short overview of the used mathematical notation within this work, which is aimed at increasing the readability of the document.

Scalars are denoted by italic letters, e.g. a, A.

A vector $\boldsymbol{p}$ embedded in three-dimensional Euclidean space $\mathbb{R}^3$ with unit vectors $\boldsymbol{e}_x$, $\boldsymbol{e}_y$ and $\boldsymbol{e}_z$ is denoted using lowercase bold italic letters as (1).

$$\boldsymbol{p} = p_x \boldsymbol{e}_x + p_y \boldsymbol{e}_y + p_z \boldsymbol{e}_z = \left[p_x \; p_y \; p_z\right]^{\mathrm{T}} \tag{1}$$

The scalar product c between two vectors $\boldsymbol{a}$ and $\boldsymbol{b}$ of length n is designated by (2).

$$c = \boldsymbol{a} \cdot \boldsymbol{b} = \sum_{i=1}^{n} a_i b_i \tag{2}$$

The vector product $\boldsymbol{c}$ between two vectors $\boldsymbol{a}$ and $\boldsymbol{b}$ is indicated by (3).

$$\boldsymbol{c} = \boldsymbol{a} \times \boldsymbol{b} \tag{3}$$

The Euclidean norm[5] [18] l of $\boldsymbol{p}$ is given as (4).

$$l = \|\boldsymbol{p}\| = \sqrt{\boldsymbol{p} \cdot \boldsymbol{p}} \tag{4}$$

A vector $\boldsymbol{p}$ is called a ”normal vector” or ”normalised” if $l = 1$ is satisfied.

An array is a data structure, where $k = m \cdot n$ values are arranged in a rectangular dense pattern of size $m \times n$, e.g. $\mathtt{c} = [\mathtt{c}]^{m \times n}$. Singleton dimensions can be omitted and array variables are written in typewriter font style. The difference between a matrix and an array is their mathematical and data-structural context, respectively.

A set of n scalars is denoted as $\{x_i\}_{i=1}^{n}$. Similarly, a set of vectors is described as $\{\boldsymbol{x}_i\}_{i=1}^{n}$. This notation can be extended to higher dimensions as follows: $\{\{x_{ij}\}_{i=1}^{n}\}_{j=1}^{m}$.

Newly defined mathematical instructions are formulated and used as functions, $c = a + b = \mathtt{plus}(a, b)$, their names are written in typewriter font style.

A matrix is denoted using uppercase bold italic letters, e.g. $\boldsymbol{A}$.

Much of the benefit of the presented work can be found in its information-dense false-colour plots. Because of strong criticism towards ”rainbow”

---

[5] Also known as length or amount of a vector.

colour-maps [19–22], which typically show a colour transition from blue over yellow to red (e.g. MATLAB's jet [23]), this thesis uses the widely accepted Viridis colour map [24], which is publicly available at [25, 26]. Presented results from earlier publications were adjusted accordingly.

2 3D coordinate metrology

The origins of coordinate metrology date back to the 17th century, when the idea of using a coordinate system for the description of the relation between an object and its reference was formulated [13]. However, only the development of computer technology made it possible to apply the required mathematical tools in order to construct the first[6] ”numerically controlled coordinate machine” UMM 550 by (the company) Zeiss in 1973 [13], thus starting modern coordinate metrology and its industrial application [13]. Today, the coordinate measuring technology plays a critical role in the applications of production engineering. However, coordinate metrology is constantly developing through new calibration technologies and methods of assessment of measurement accuracy. [13, 27, 29]

Coordinate metrology is a measurement method used for a wide range of tasks and is thus characterised by its universality. It is based on the principle of point-wise probing and scanning of the surface of the examined measurement object while mathematically linking all sampling points with each other in a common three dimensional coordinate system. Subsequently, sets of measurement points representing a specific geometric feature (e.g. bore hole) are assigned to their ideal geometric associated element (e.g. cylinder surface) by the application of mathematical optimisation tools [8, 29]. These associated elements are then used as a reference for the determination of specific measures and the calculation of deviations in form, position and orientation of the examined measurement object [8]. This procedure yields a lot of flexibility with regards to the definition of measurands and inspection features but for that it requires further specifications and conventions [29]. Binding conventions are established in the system of standards ”GPS - Geometrical Product Specifications and Verification” (ISO GPS) [29]. The entire GPS system of standards forms the basis for the internationally uniform interpretative understanding of geometric product specifications and their testing [29].

---

[6] A different source is reporting the launch of the first ”universal coordinate measuring machine with a three dimensional measuring probe head” by Carl Zeiss in 1973 [27]. Zeiss states on the company homepage that ”In 1973, the first high-precision three-dimensional coordinate measuring machine built by Carl Zeiss was published under the name Universal Measuring Machine (UMM 500) with a measuring probe, integrated table, computer and its own measuring software called UMESS. This still largely unknown and sophisticated technology made it possible for the first time to measure components in three dimensions.” [28].

This chapter gives an overview over important measurement sensors and geometry data representations used in their context. Furthermore, the concept of metrological traceability and the measurement uncertainty are introduced, which includes a presentation of important standards in the context of 3D coordinate metrology.

2.1 Prominent representatives of measurement systems

The following section gives an overview over three different types of measurement systems used in 3D coordinate metrology. They represent exemplary tactile, optical areal and tomographic volumetric methods and therefore cover a large part of available technologies and design types (comprehensive overviews can be found in [8, 29–31]).

2.1.1 Tactile coordinate measurement systems

Tactile coordinate measurement systems (tactile CMS / TCMS, also called coordinate measuring machines, CMM) are based on the mechanical interaction between a probing system and the surface of the measurement object. The probe element is touching the surface of the measurement object and is itself characterised by low form deviations, high stiffness and high hardness. They are mostly implemented as synthetic ruby spheres with different diameters, depending on the specific use case. The achieved measurement uncertainty of a measurement task is influenced by the probing strategy which consists of the selection of a probing system (e.g. design, size) and its operating parameters (e.g. probing force, travel speed), the measurement mode and the number and distribution of measurement points. The measurement mode ”single point probing” is characterised by a low number of measurement points with high accuracy compared to the mode ”scanning” where more measurement points are recorded with reduced measurement accuracy. Another influencing factor is the probing itself, which causes deformations of the probing system and the measurement object. Different procedures to determine the probing error associated with measurements using single point probing and scanning are defined in DIN EN ISO 10360-2:2010-06 [32]. [29]

Usually, automated TCMS measurements require the provision of the nominal geometry of the measurement object (e.g. as a CAD object, see sec. 2.2.2) and an exact definition of the measurands to be measured (e.g. from a technical drawing according to ISO GPS). Such a measurement is characterised by the following aspects:

- All measurement points are represented in the intrinsic coordinate system of the TCMS. The measurement tasks are either defined in the coordinate system of the nominal geometry of the examined measurement object or by the explicit definition of datum systems using an ISO GPS specification. In either case, the relationship between the different coordinate systems usually needs to be determined based on manual assignment of corresponding features.
- TCMS usually cannot measure objects of unknown geometry, because the location of the expected surface needs to be known in advance within a relatively small tolerance in order to perform sampling with the correct probing vectors. One exception are so called free-form scans, but those only work locally (e.g. scans on a plane or a cylinder surface), which means that additional pre-knowledge is required nonetheless.
- Although many different technical implementations of probing systems and machine design types exist, including the possibility to change probing elements during a measurement, the manageable complexity of measurement objects is usually limited by the accessibility of the probing surface.
- The necessary clamping of the measurement object directly implies that it is not possible to measure the complete surface within a single object placement. The combination of the measurement data of different placements into one common coordinate system is technically possible. This however comes with a significant increase in measurement uncertainty of the parameters describing affected geometry elements due to the determination of the coordinate systems with the same features but different physical probing locations.
- One key characteristic of TCMS is the recording of few measurement points which leads to a strong undersampling and sometimes low pass filtering of the surface of the measurement object. Even though each of these measurement points is captured with high accuracy it is not possible to assess surface regions not covered by measurement points. Therefore, the recorded coordinates often represent only a small sample of the complete geometry element. Because of that, the interpretation of the measurement results typically assumes a high correlation of the properties of probed and un-probed surface regions, respectively; and therefore small deviations in form. This effect can be reduced in the direction of movement of the probing system by using the ”scanning” measurement mode with more sampling points.
- The duration of the measurement is strongly correlated with the number of geometrical features captured. That means that the measurement is usually strictly limited to the features defined in the corresponding technical drawing. Thus, the measurement of the complete geometry of a measurement object is in many cases impractical. The general goal of measurement dura-

  tion reduction without a significant reduction in measurement accuracy is still difficult to achieve for TCMS [33, 34].
- The measurement results are given as a point cloud (see 2.2.1) per measured feature together with probing vectors which represent the surface normal vector based on the mechanical interaction with the probing system. An areal representation of the measured geometry is typically not provided.

The task specific measurement uncertainty for measurements performed with TCMS can be determined by means of a simulation tool, known as Virtual Coordinate Measuring Machine (VCMM) [35–37]. The VCMM is based on Monte Carlo methods [38, 39] and is capable of considering complex influencing factors on a coordinate measurement, such as guidance deviations, thermic influences on machine and measurement object, deviations caused by drifts and by the mechanical probing as well as the surface roughness of the measurement object [35, 36]. In 2017, further developments were reported, which include the support of tactile scanning measurements and the consideration of uncertainty contributions arising from undersampling of features [40, 41]. Two other procedures (uncertainty budgets: VDI/VDE 2617 Part 11 [42] and the substitution method: DIN EN ISO 15530-3:2018-09 [43]) are both applicable for TCMS and also the subsequently described systems.

2.1.2 Structured-light 3D scanner

A structured-light 3D scanner (SLS) represents an optical areal measurement method and describes the technical combination of the measurement methods structured-light projection and photogrammetry. The former is based on the principle of active triangulation. The measurement setup consists of two cameras, which form the triangulation base by calibration of their location and orientation with respect to each other. Simpler design types with only one camera exist, but are less capable and more reliant on the quality of the required structured-light generator. This generator, which is usually positioned between the two cameras, projects an optical pattern onto the surface of the measurement object. That pattern is subject to a rapid phase shift, which is synchronised with the shutter speed of the cameras. The form and orientation of the measurement object surface may distort the projected pattern. Each camera records the resulting fringe line image and the application of the principles of triangulation allows the determination of the 3D coordinates of the measured surface for each camera pixel from both camera images. Therefore, structured-light projection is generating a camera-bound point cloud [8, 44, 45].

The basis of passive photogrammetry is the ability to determine three dimensional coordinates from two images recorded from different camera positions by means of stereo vision. The correspondence problem between two images is solved by the application of optical markers onto the surface of the measurement object. The more markers are visible in different images the higher is the redundancy and thus the lower is the resulting measurement uncertainty of that data fusion operation. Photogrammetry is then able to determine three dimensional coordinates at the location of each marker, given that sufficient images were recorded. [8, 46, 47]

Structured-light projection alone is only capable of measuring geometry from single sensor positions with respect to the measurement object. However, the imaging of its complete form requires the geometrical linking of different sensor positions. Thus, a full 3D measurement of an object can be realised by the combination of structured-light projection and photogrammetry by the additional placement of optical reference markers onto the surface of the measurement object. Additionally, the integration of a manipulator system (e.g. rotary axis) is required. Such measurement systems are widely used in the field of industrial metrology and are characterised by the following aspects and limitations [8, 29, 48–50]:

- Optical measurements require cooperative surface properties, here in form of diffuse reflection characteristics and sufficient optical accessibility represented by a maximum angle between the surface normal vector and the optical axis. Therefore, geometric features with large aspect ratios as well as undercuts are not measurable with structured-light 3D scanners, the same applies for reflective surfaces. The latter, however, can be compensated by special surface spray coatings which can in return negatively influence the geometric properties of the examined measurement object. Another possibility is high dynamic range (HDR) imaging, where multiple images with different exposures are merged such that the resulting image contains a wider dynamic range than a single image [51].
- Usually, the complete surface of the measurement object is not accessible even with a high number of sensor positions due to the required clamping. It is however possible to reposition the measurement object in the clamping system and perform further scan series. The photogrammetric properties of the measurement system make it possible to combine arbitrary sensor-object combinations into one measurement result. The clamping system is usually also captured by the measurement system and a separation with respect to the measurement object of the resulting measurement result has to be done manually in a data post-processing step.
- The required markers usually have to be applied manually in form of stickers. Furthermore, the underlying surface under the sticker is then covered and must be approximated from the surrounding measurement data.

- A 3D scan consisting of several work piece clamping positions and with several dozen sensor positions each can require a significant amount of measurement data processing, depending also on the camera resolution, in order to calculate the measurement result in form of the 3D geometry (see sec. 2.2).
- The duration of a measurement is correlated with the size and optical accessibility of the measurement object.
- The measurement result is usually a triangle mesh (see sec. 2.2.3) representing the measured surface. The conformance tests for specific geometric features are subsequently possible with additional processing of the measured surface.

2.1.3 Industrial X-ray computed tomography

Metrological X-ray computed tomography systems (CTs) are used in the context of dimensional metrology since 2005 and are regarded as an alternative to tactile or optical 3D coordinate measurement systems [52, 53]. CTs measure the attenuation of ionising radiation caused by its physical interactions with the matter inside the measurement volume, including the measurement object. Historically, the term X-ray describes the photon energy range between ultraviolet and gamma radiation [54]. Today however, X-ray and gamma radiation are only distinguished by their way of origin and thus defined as a common class of radiation with energies between 4 eV and $2 \cdot 10^{10}$ eV [54]. The maximum energy of the radiation used during a measurement is defined by the operating voltage of the X-ray tube (typical configurations reaching up to 450 kV [52, 53]) used to accelerate electrons onto a target which causes the emission of fundamentally polychromatic electromagnetic radiation. Metrological CTs mostly apply a cone beam geometry and therefore consist of the aforementioned X-ray tube, a rotary stage, a flat panel detector in combination with specialised computer hardware. The measurement object is placed onto the rotary stage and must be completely enclosed[7] by the given measurement volume. Increasing geometrical magnification enabled by the variable positioning of the rotary axis between source and detector shrinks the effective measurement volume but can increase the measurement resolution. The measurement object is exposed to polychromatic radiation resulting in a

---

[7] In case of region-of-interest (ROI) tomography, this condition can potentially be relaxed using available pre-knowledge about the complete geometry of the object. [55]

measurement of the attenuation line integral by each detector pixel (5) [54, 56].

$$
\begin{aligned}
I_{\text{pix}}(L) &= \int_0^{E_{\max}} I_0(E) e^{-\int_0^L \mu(E,l) dl} dE \\
\mu &= \tau + \sigma_{\text{c}} + \sigma_{\text{r}} + \kappa
\end{aligned}
\tag{5}
$$

The measured intensity $I_{\text{pix}}(L)$ is dependent on the radiation (X-rays) with energy E and starting intensity $I_0(E)$, the material specific macroscopic linear attenuation coefficient $\mu(E,l)$ and the penetration length L. The coefficient μ represents the combination of the possible physical interaction processes photoelectric effect τ, Compton (incoherent) scattering σ_{c}, Rayleigh/Thomson (coherent) scattering σ_{r} and pair production[8] κ. The mathematical model of measuring attenuation line integrals is only correct for the photoelectric effect τ, because the scattering mechanisms typically cause a change in direction of the concerned photon and therefore possibly result in contribution of radiation intensity to different detector pixels off the corresponding "line". A single X-ray attenuation image from a fixed angular position with respect to the rotary axis is also called a projection. A CT scan consists of a set of a few hundred up to a few thousand projections including a description of the system geometry and measurement parameters. This scan information is then handed to the reconstruction program which calculates a volume data model from the measured projection data in form of voxel data. For cone beam CTs the FDK[9] algorithm [57] is a popular implementation of analytical reconstruction based on the principles of filtered back-projection. Each voxel carries the calculated information about the local radiation attenuation, which is larger for dense volume regions (occupied by the measurement object) than the surrounding atmosphere. Using suitable edge detection methods, the surface of the measurement object (interface between volume regions with different voxel values) can be determined and metrological evaluations can be performed subsequently on that surface. [52, 53, 56, 58]
Furthermore, CTs are characterised by the following properties:

- Because of energy density (thermal) limitations, the electron focal spot of the X-ray tube onto the target must have a finite size. Consequently, the resulting X-ray source cannot be point-shaped, which causes tube power dependent blurring in the projections.

---

[8] Pair production processes play no role in current industrial applications as they require photon energies of at least two times (interaction with Coulomb field of the nucleus) and four times (interaction with Coulomb field of a shell electron) the electron rest mass equivalent $m_{\text{e}}c^2 \approx 511$ keV, respectively [54].

[9] The algorithm is named after its inventors Feldkamp, Davis and Kress.

- The resulting circular trajectory of a 360° rotation does not satisfy the Tuy sufficiency condition [59], which causes the appearance of cone beam artefacts [60], thus locally increasing the measurement uncertainty.
- For many applications, rigid mechanical clamping of the measurement object is not required. Instead, special foams made out of polyurethane with close to no elastic deformation[10] and little X-ray attenuation properties are used for the fixing of the measurement object. Consequently, the complete surface of the measurement object can be measured without any voids.
- The generation of monochromatic X-rays of sufficient energy and intensity can be realised by the use of a synchrotron, which is a complex and expensive method [61]. Therefore, X-ray tubes producing a polychromatic energy spectrum from the interaction with high-energy electrons with a target material (bremsstrahlung) are used instead [62, 63]. Due to the facts that the detector is measuring radiation intensity and that the interaction processes are dependent of the energy of the radiation, beam hardening artefacts occur [64]. These artefacts can be reduced but not completely avoided by a pre-hardening of the applied radiation by the application of pre-filters (usually made out of copper) which partly suppresses the part of the spectrum with lower energy.
- The quality of a CT measurement strongly depends on the material composition of the measurement object. Both dense materials as well as different (heterogeneous) materials within a measurement object can cause challenges for the determination of the geometry because of boundary ambiguities at the presence of measurement artefacts.
- CT measurements are generally affected by noise from different sources (e.g. quantisation of X-ray photons, electronic noise, X-ray scattering) which limits the achievable accuracy of certain dimensional measurement task to about a tenth of the voxel size[11] [52, 65, 66].
- The duration of a CT measurement does not correlate with the number of geometrical features of the measurement object. This property distinguishes CT from TCMS and SLS, where this does not apply.
- Strictly speaking, a CT measurement only consists of the measured projections. However, different classifications exist and with respect to this thesis the measurement result is represented by the surface representation of the measurement object (after volume reconstruction and surface determination) in form of a triangle mesh (see sec. 2.2.3). Compared to SLS, the same dimensional evaluations can then take place by further processing of the obtained surface geometry.

---

[10] This property is important because it limits object drifts caused by relaxation of the used foam. For the same reason styrofoam should be avoided.

[11] The voxel size is determined by the pixel size of the detector and the configured geometrical magnification.

2.1.4 Comparison of the presented measurement systems

Because of their different functionality and physical interaction principles with the measurement object, the presented types of measurement systems also exhibit different properties with respect to measuring the geometry of a measurement object. Table 2 shows a comparison for different properties with respect to the used systems for measurements in this thesis.

Table 2: Comparison of 3D coordinate measurement systems with respect to the used machines (see Appendix).
Rating values are defined as follows (from negative to positive): −−, −, 0, +, ++
TCMS: Tactile coordinate measurement system
SLS: Structured-light 3D scanner
CT: Industrial X-ray computed tomography

Property	TCMS	SLS	CT
Size of measurement object	++	+	+
Limitations caused by physical properties of the measurement object	++	0	0
Typical measurement duration (complete surface)	−−	+	0
Geometrical complexity of the measurement object	−	−−	++
Measurement point density	−−	+	++
Typically achieved measurement uncertainty	++	−	0
Time to set up the measurement	−−	+	++
Measurement of objects with unknown geometry	−−	+	++
Measurement of inner features non-destructively	−−	−−	+
Total cost of ownership	−	+	−

2.2 Measurement and geometry data representation

This thesis deals with the processing of geometry data in the context of 3D coordinate metrology. The following explanations assume that all geometry data are embedded within an Euclidean vector space [18]. The used measurement systems describe the produced geometry data in different formats and representations which need to be unified in order to make comprehensive algorithmic processing possible. Additionally, the data representation of the nominal geometry of the measurement object which originates from computer-aided design (CAD) tools needs to be handled along with the measurement data.

2.2.1 Point cloud

Tactile coordinate measurement systems (TCMS)[12] output a point-based geometry representation which represents a sampling of the continuous physical boundary of the measurement object. The set of measurement data points is called a point cloud, which can be regarded as a piecewise constant surface approximant [67]. The structure may have additional attributes besides the raw coordinates and is regarded as unorganised but spatially coherent, however with an unsharp boundary [68]. With respect to TCMS, each data point consists of three components:

1. A coordinate triple $\boldsymbol{p} = \left[p_x \; p_y \; p_z\right]^{\mathrm{T}} \in \mathbb{R}^3$ in Cartesian coordinates describing the measured location of a measurement point.
2. The measured normal vector[13] $\boldsymbol{n} = \left[n_x \; n_y \; n_z\right]^{\mathrm{T}} \in \mathbb{R}^3$ of the surface determined from the physical contact with the measurement object at $\boldsymbol{p}$. These normal vectors are not necessarily equivalent to those resulting from local surface gradient calculations based on neighbouring measurement points.
3. The distance $t \in \mathbb{R}$ from the measured surface point $\boldsymbol{p}$ to the corresponding point on the surface of the nominal geometry $\boldsymbol{p}_{\mathrm{n}} \in \mathbb{R}^3$ in the direction of the corresponding nominal surface normal vector $\boldsymbol{n}_{\mathrm{n}}$, such that (6) is satisfied. Here, the nominal geometry (CAD) is required to define the measurement strategy. Otherwise, this property is not reported.

$$\boldsymbol{p}_{\mathrm{n}} = \boldsymbol{p} + \boldsymbol{n}_{\mathrm{n}} t \tag{6}$$

Point clouds do not explicitly carry information about the connectivity of the points with each other. However, in the case of TCMS, this information is implicitly given because of the relationship to the underlying nominal geometry, e.g. the measurement of a conical surface feature results in a set of measurement points, which can therefore be locally parametrised with respect to a cone. Nonetheless, the resulting point clouds need additional data processing in order to obtain a complete areal 3D geometry representation.

2.2.2 The description of geometry based on STEP CAD

STEP (standard for the exchange of product model data) is defined in the standard ISO 10303 (Industrial automation systems and integration - Product data representation and exchange) and describes a computer-interpretable representation of product manufacturing information throughout the product life cycle [69]. Thus, this standard can represent 3D objects for computer-aided

---

[12] Descriptions with respect to the used measurement system as reported in Appendix.

[13] By convention, normal vectors point outwards from the surface for closed manifolds.

design (CAD) including relevant additional information, e.g. ISO GPS[14] specifications and material properties. A STEP file is human-readable due to its ASCII (American Standard Code for Information Interchange) structure, its encoding format is defined in ISO 10303-21. The data model for the design and characteristics of a product is specified in the EXPRESS[15] data modelling language specified in ISO 10303-11 [72]. Within EXPRESS, objects (in the sense of programming) are called entities [69]. They support describing the data structure of such an entity without the mechanisms of executable functions or methods [69]. The primary application of ISO 10303-42:2019 is to represent the form or geometry of a product model [73]. Due to its normative foundation, the STEP format is supported widely by many CAD software vendors, however, numerous other formats exist, including proprietary ones. Within the scope of this thesis STEP is used to represent the nominal geometry of measurement objects and all further references to its name are meant explicitly in the context of ISO 10303-42:2019.

STEP deals with solid[16] modelling, which is defined as a body of theory, techniques and systems focused on the representation of solids that permit any well-defined geometrical property or any represented solid to be calculated automatically [75]. In principle, two major representation schemata exist in solid modelling: constructive solid geometry (CSG) and boundary representation (BREP) [76]. The first method uses the combination of primitive solid objects and Boolean operations to create a complex geometry where both the surface and interior of the object are implicitly defined [76]. A BREP on the other hand describes the oriented surface of a solid as a data structure consisting of vertices, edges and faces[17] [76]. A solid is therefore described as a collection of connected surface elements [77]. In order to combine the advantages of both methods, many modelers (including STEP [77]) are designed as dual-representation modelers [76]. STEP is capable of representing geometry using both CSG and BREP [73], however in the scope of this thesis only the BREP representation is used to represent geometry data.

---

[14] STEP provides different application protocols for different engineering scopes which are all based on the same set of integrate resources [70]. For example, ISO 10303-242:2020 (Managed model-based 3D engineering) contains a model of geometric tolerances and dimension (also known as GD&T) information [71].

[15] A graphical form of EXPRESS exists, it is called EXPRESS-G [69].

[16] Solid geometry deals with geometry of three-dimensional, Euclidean spaces. The 2D counterpart is plane geometry. [74]

[17] Here, a face refers to any non-self-intersecting 3D surface of arbitrary curvature. Otherwise, this term is used in this thesis to describe planar triangular facets.

The following example demonstrates how geometry is represented using the STEP format. The explanations[18] reference the technical documentation [73, 80] available on the website of STEP Tools, Inc., a company that provides software products and services associated with STEP and related standards. Each STEP object is constructed by the combination of different entities. Each entity has an unique numerical identifier which is used for cross referencing within the data structure. Entities are organised as a tree structure and can point to multiple other entities, e.g. a `closed_shell`[19] (a bound for a region in $\mathbb{R}^3$ [80]) can consist of multiple `advanced_face` (a surface that is bound by edges and vertices [80]). Figure 1 shows the geometry of a simple hole plate[20] with rounded edges and symmetrical properties in the vertical direction. Its tight-fitting bounding box has the dimensions 35 mm × 30 mm × 10 mm. The shape of this hole plate can be described by the combination of different surface sections. Figure 2 shows the hierarchical structure[21] of the STEP object with the number of occurrences in brackets.

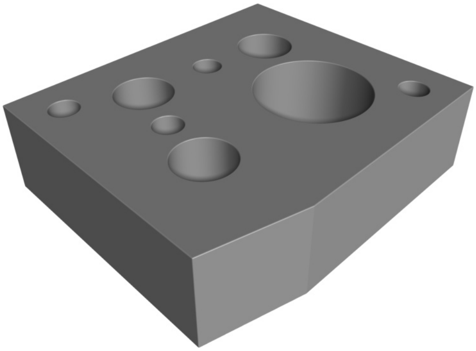

Figure 1: Hole plate with round edges consisting of different geometric surface elements: cylindrical, spherical and toroidal surfaces, respectively, as well as planes.

---

[18] Additionally, the NIST STEP File Analyser and Viewer [78] was used to parse the STEP file in order to generate an easier to process entity categorisation. However, this is not absolutely necessary and can be substituted by a different string parser (e.g. based on regular expressions [79]).

[19] This text uses the entity identifiers as defined in [73, 80] written in typewriter font and explicitly without plural.

[20] The object was designed within the context of [P5].

[21] With minor simplifications to improve visual quality.

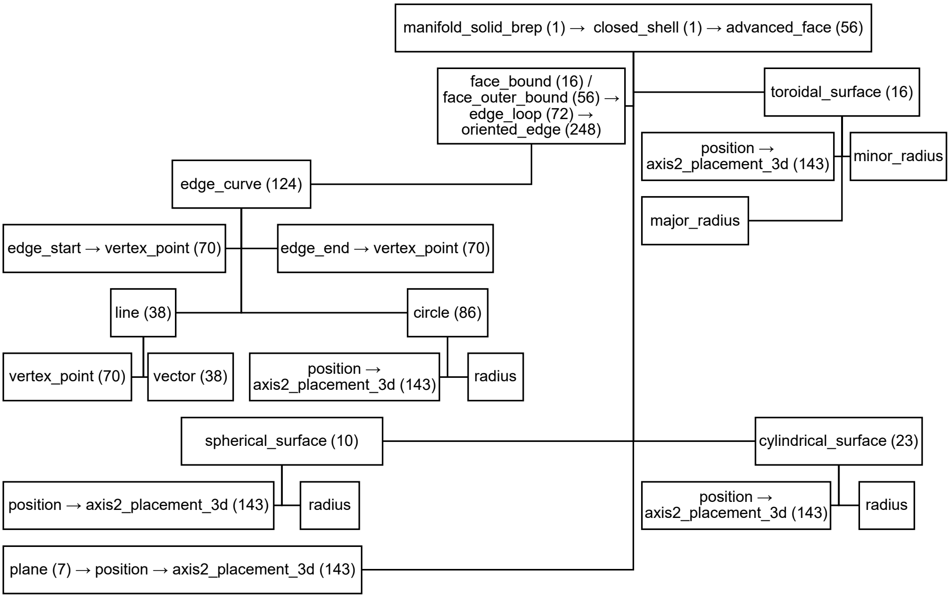

Figure 2: Visualisation of the hierarchical structure between the main entities of the object shown in Figure 1. The entity identifiers are equivalent to those used in the STEP file. The hierarchy only exists vertically which is also denoted by the symbol "→". The number of elements in this model are given in round brackets.

> "A `manifold_solid_brep` is a type of `solid_model`[22] which is a finite, arcwise connected volume bounded by one or ore surfaces, each of which is a connected, oriented, finite, closed 2-manifold." [73]

With respect to the example, it consists of one `closed_shell`, which consists of 56 `advanced_face` which again consist of different `elementary_surface` (16 `toroidal_surface`, 10 `spherical_surface`, 23 `cylindrical_surface` and 7 `plane`). In this example, each `advanced_face` is bound by a `face_outer_bound` entity, which consist of `edge_curve` of type `line` or `circle`. The holes in the top and bottom `plane` are described by `face_bound` entities (here `circle`).

The placement of each entity is given by individual coordinate systems as `axis2_placement_3d` with respect to a global coordinate frame $\{\boldsymbol{e}_x, \boldsymbol{e}_y, \boldsymbol{e}_z\} \subseteq \mathbb{R}^3$ (also called world coordinate system, WCS). The local coordinate system is described by a centre point $\boldsymbol{c} \in \mathbb{R}^3$ (origin) and two

---

[22] "A `solid_model` is a type of `geometric_representation_item` which is a complete representation of the nominal shape of a product such that all points in the interior are connected. Any point can be classified as being inside, outside or on the boundary of a solid." [73]

distinct (ideally orthogonal) axes $\boldsymbol{z} \in \mathbb{R}^3$ (placement z-axis direction) and $\boldsymbol{a} \in \mathbb{R}^3$ (approximate placement x-axis direction). The local base of an entity $\{\boldsymbol{x}, \boldsymbol{y}, \boldsymbol{z}\} \in \mathbb{R}^{3\times 3}$ is then defined by $\boldsymbol{x} \in \mathbb{R}^3$, $\boldsymbol{y} \in \mathbb{R}^3$ and $\boldsymbol{z}$ according to (7)[23][73].

$$\begin{aligned} \boldsymbol{x} &= \frac{\boldsymbol{a} - (\boldsymbol{a} \cdot \boldsymbol{z})\boldsymbol{z}}{\|\boldsymbol{a} - (\boldsymbol{a} \cdot \boldsymbol{z})\boldsymbol{z}\|} \\ \boldsymbol{y} &= \frac{\boldsymbol{z} \times \boldsymbol{x}}{\|\boldsymbol{z} \times \boldsymbol{x}\|} \end{aligned} \tag{7}$$

The parametrisation of commonly used curve and surface entities, respectively, is provided in the following. These descriptions are required within the data processing pipeline (see chapter 5) and they follow the technical STEP documentation available at [73].

Most geometric objects consist of many different surface elements. Their boundaries are described by curves in the sense of the path of a point moving in its coordinate space. Applicable to all curves is the result of the parametrisation $\boldsymbol{\lambda}(u) \in \mathbb{R}^3$ in the WCS with respect to a scalar dimensionless parameter $u \in \mathbb{R}$.

Line: A line is an unbounded curve with constant tangent direction. It is defined by a point $\boldsymbol{p} \in \mathbb{R}^3$ and a direction vector $\boldsymbol{v} \in \mathbb{R}^3$ (8) [73].

$$\boldsymbol{\lambda}_{\text{line}}(u) = \boldsymbol{p} + u\boldsymbol{v} \tag{8}$$

Circle: A circle lies in its $\boldsymbol{xy}$-plane with radius $r \in \mathbb{R}^+$ and centre point $\boldsymbol{c}$ (9) [73].

$$\boldsymbol{\lambda}_{\text{circle}}(u) = \boldsymbol{c} + r(\cos(u)\boldsymbol{x} + \sin(u)\boldsymbol{y}) \tag{9}$$

Ellipse: The ellipse lies in its $\boldsymbol{xy}$-plane with two additional parameters $a, b \in \mathbb{R}$, representing the semi-major and semi-minor diameters, respectively (10) [73].

$$\boldsymbol{\lambda}_{\text{ellipse}}(u) = \boldsymbol{c} + a\cos(u)\boldsymbol{x} + b\sin(u)\boldsymbol{y} \tag{10}$$

B-spline curve: A B-spline curve is a piecewise parametric polynomial curve described by a set of control points and basis functions, with $k+1$ defining

---

[23] For certain edge cases this approach is numerically more stable than using another vector product to obtain $\boldsymbol{x}$.

the number of control points and $\mathfrak{N}_i^d(u)$ representing the B-spline basis functions of degree d [81] (11) [73].

$$\boldsymbol{\lambda}_{\text{Bspline curve}}(u) = \sum_{i=0}^{k} \boldsymbol{p}_i \mathfrak{N}_i^d(u) \tag{11}$$

Other important curves include hyperbola, parabola and the polyline. The curves circle, ellipse, hyperbola and parabola form the group of conics, which are planar curves produced by intersecting a plane with a cone [73].

STEP defines a surface as a set of connected points in 3D which is always locally 2D [73]. The parametrisation of the five elementary surfaces is described as $\boldsymbol{\sigma}(u, v) \in \mathbb{R}^3$ with respect to two independent and dimensionless scalar parameters $u, v \in \mathbb{R}$. The unit normal vector $\boldsymbol{n}(u, v) \in \mathbb{R}^3$ at any point on the surface is given by the cross product of both partial derivatives (12) [73].

$$\boldsymbol{n}(u, v) = \frac{\partial \boldsymbol{\sigma}(u, v)}{\partial u} \times \frac{\partial \boldsymbol{\sigma}(u, v)}{\partial v} \tag{12}$$

Depending on the orientation of the surface (this information is provided by the STEP file), a normal vector flip is required, because e.g. a cylindrical surface can both represent a bore hole or a pin with the same geometric description. The following equations assume $\boldsymbol{q} = \{q_x, q_y, q_z\}$ to be a Cartesian coordinate on a particular entity E in its local coordinate system $\{\boldsymbol{x}, \boldsymbol{y}, \boldsymbol{z}\}$. The values $\overline{u}$ and $\overline{v}$ are the result of the transformation from $\boldsymbol{q}$ to the parameter space $\{u, v\}$. In the following the function atan2(Y, X) is the 2-argument arctangent of a point in $\mathbb{R}^2$.

Plane: Additional parameters: none, parametrisation according to (13) [73].

$$\begin{aligned} \boldsymbol{\sigma}_{\text{plane}}(u, v) &= \boldsymbol{c} + u\boldsymbol{x} + v\boldsymbol{y} \\ \boldsymbol{n}_{\text{plane}} &= \boldsymbol{z} \\ \overline{u} &= q_x \\ \overline{v} &= q_y \end{aligned} \tag{13}$$

Cylindrical surface: Additional parameters: radius r, parametrisation according to (14) [73]. The axis of the cylinder is represented by $\boldsymbol{z}$.

$$\begin{aligned} \boldsymbol{\sigma}_{\text{cylinder}}(u,v) &= \boldsymbol{c} + r(\cos(u)\boldsymbol{x} + \sin(u)\boldsymbol{y}) + v\boldsymbol{z} \\ \boldsymbol{n}_{\text{cylinder}}(u,v) &= \cos(u)\boldsymbol{x} + \sin(u)\boldsymbol{y} \\ \overline{u} &= \operatorname{atan2}(q_y, q_x) \\ \overline{v} &= Q_z \end{aligned} \tag{14}$$

Conical surface: Additional parameters: radius r, angle α, parametrisation according to (15) [73]. The axis of the cone is represented by $\boldsymbol{z}$. Conical surfaces are present for example at angled edges of a bore hole.

$$\begin{aligned} \boldsymbol{\sigma}_{\text{cone}}(u,v) &= \boldsymbol{c} + (r + v\tan(\alpha))(\cos(u)\boldsymbol{x} + \sin(u)\boldsymbol{y}) + v\boldsymbol{z} \\ \boldsymbol{n}_{\text{cone}}(u,v) &= \operatorname{sign}(r + v\tan(\alpha))\frac{\cos(u)\boldsymbol{x} + \sin(u)\boldsymbol{y} - \tan(\alpha)\boldsymbol{z}}{\sqrt{1 + \tan(\alpha)^2}} \\ \overline{u} &= \operatorname{atan2}(q_y, q_x) \\ \overline{v} &= q_z \end{aligned} \tag{15}$$

Spherical surface: Additional parameters: radius r, parametrisation according to (16) [73].

$$\begin{aligned} \boldsymbol{\sigma}_{\text{sphere}}(u,v) &= \boldsymbol{c} + r\cos(v)(\cos(u)\boldsymbol{x} + \sin(u)\boldsymbol{y}) + r\sin(v)\boldsymbol{z} \\ \boldsymbol{n}_{\text{sphere}}(u,v) &= \cos(v)(\cos(u)\boldsymbol{x} + \sin(u)\boldsymbol{y}) + \sin(v)\boldsymbol{z} \\ \overline{u} &= \operatorname{atan2}(q_y, q_x) \\ \overline{v} &= \arcsin\left(\frac{q_z}{\|\boldsymbol{q}\|}\right) \end{aligned} \tag{16}$$

Toroidal surface: Additional parameters: major radius R, minor radius r, parametrisation according to (17) [73]. $R > r$ must be satisfied, otherwise the resulting surface will be self-intersecting. The axis of the torus is represented by $\boldsymbol{z}$. It turns out, that such surfaces are quite common, e.g. as rounded edges of a bore hole.

$$\begin{aligned} \boldsymbol{\sigma}_{\text{torus}}(u,v) &= \boldsymbol{c} + (R + r\cos(v))(\cos(u)\boldsymbol{x} + \sin(u)\boldsymbol{y}) + r\sin(v)\boldsymbol{z} \\ \boldsymbol{n}_{\text{torus}}(u,v) &= \cos(v)(\cos(u)\boldsymbol{x} + \sin(u)\boldsymbol{y}) + \sin(v)\boldsymbol{z} \\ \overline{u} &= \operatorname{atan2}(q_y, q_x) \\ \overline{v} &= \operatorname{sign}(q_z)\arccos\left(\frac{\|\boldsymbol{q}\|^2 - R^2}{\sqrt{(\|\boldsymbol{q}\|^2 - R^2)^2 + 4R^2q_z^2}}\right) \end{aligned} \tag{17}$$

Additionally, the following aspects are important in the context of this work:

- In principle, surfaces can also be expressed as rational or polynomial parametric surfaces using the mathematical model of non-uniform rational basis splines (NURBS) [81], such as `b_spline_surface`. Thus, for example, `elementary_surface` such as these used in Figure 2 can also have an alternative representation. Different CAD software products might choose different mathematical representations.
- STEP geometry definition can also be affected by uncertainty which is defined by the entity `global_uncertainty_assigned_context`. Within a STEP file, this parameter is described as ”maximum model space distance between geometric entities at asserted connectivities”. With respect to the hole plate example, the associated `distance_accuracy_value` is given as 10 µm, which can be regarded as substantial. However, based on the given specifications with `elementary_surface`, this limit is typically not reached. Nonetheless, small inaccuracies might occur when rational or polynomial parametric surfaces are used. Within STEP files, numbers are represented with up to 15 digits, which suggests the internal use of double precision 64 bit numbers. This at the same time represents the lower limit for the uncertainty of specifications using STEP.
- For many applications in 3D coordinate metrology (e.g. nominal-actual comparisons, geometry input for CT simulation) the STEP model must be converted into a tessellated surface in form of a triangle mesh. For curved geometric forms, the result is an approximation of the original form (see also sec. 2.2.3), which must be taken into account when evaluating the accuracy of observations.

2.2.3 Triangle mesh

A polygonal mesh is defined as a finite collection of vertices (single points in 3D), edges (line segments whose end points are vertices) and faces (convex polygons in 3D), such that neither isolated vertices nor edges as well as interpenetration of faces are allowed [82]. Thus geometrically, a mesh is a piecewise planar surface. The main representation for 3D geometry data within the context of this thesis is the triangle mesh (also called trimesh [82]), which is a polygonal mesh consisting exclusively of triangles. Triangle meshes are widely used in many different areas of computer graphics and geometry processing [83] which is reflected by the fact that most current computer hardware uses triangles as the fundamental rendering primitive [84]. Triangle meshes are characterised by their algorithmic simplicity, numerical robustness and efficient display [85]. Two important properties of triangles are that they are the only n-sided polygon always guaranteed to be convex [84] and that all vertices defining a face are always contained within their common plane. It can be shown, that the average valence (number of incident edges per vertex) in a closed manifold triangle mesh is 6 [86]. A polygonal mesh describing a finite collection of vertices, edges and faces must satisfy the following constraints [82]:

1. Each vertex must be shared by at least one edge (no isolated vertices are allowed) and each edge must be shared by at least one face (no isolated edges or polylines are allowed).
2. A mesh is connected, if each face has at least one adjacent face. Otherwise, the mesh consists of multiple connected sub-meshes, each called a connected component.
3. A mesh is a manifold if each edge is shared by at most two faces.
4. A manifold mesh is orientable if additionally the vertex orderings for the faces are defined such that adjacent faces have consistent orderings (result in consistent inside/outside classification). This is a requirement for many graphics applications.
5. A mesh is closed if it is manifold with each edge shared by exactly two faces with no self intersections. This definition includes that a closed mesh is also orientable. This describes the desired property of a (triangle) mesh in the context of this thesis.

In case each of these constraints is fulfilled and the mesh consists of a single connected component, the mesh is called a polyhedron[24] [82]. For polyhedrons, the Euler formula (18) states the relation between the number of vertices N_v, the number of faces N_f, the number of edges N_e and the genus[25] of the surface g [87, 88].

$$N_\mathrm{v} - N_\mathrm{e} + N_\mathrm{f} = 2(1 - g) \tag{18}$$

In [87] the definition of a triangle mesh is given as: ”A triangle mesh is 2-manifold (two-dimensional manifold) if it contains neither non-manifold edges (edges with more than two incident triangles) nor non-manifold vertices (a vertex is incident to more than one fan of triangles) nor self-intersections.” Closed meshes are also described as watertight meshes [89]. A practical way to estimate these properties is to import the mesh into a program that visualises the front and back side of triangles, according the triangle face normal vector (see sec. 5.1), with different colours. The observer should always only see one colour at a time (depending on the location of the

---

[24] Not to be confused with a polytope which is a polyhedron enclosing a convex region [82].

[25] The genus intuitively counts the number of handles of an object such that a sphere has $g = 0$, a torus $g = 1$ and double-torus $g = 2$ [87].

camera), otherwise the mesh is not a watertight 2-manifold. If this condition is fulfilled, $N_\mathrm{f} \approx 2N_\mathrm{v}$ and $N_\mathrm{e} \approx 3N_\mathrm{v}$ can be derived from (18) [87].

Because of the fact that a triangle mesh is a piecewise planar surface, curved surfaces can only be approximated with this type of geometry representation. While the mesh can be constructed in such a way that the position of the vertices is exact with respect to the described curved surface (but not necessarily its vertex normal vector), the face itself deviates from the geometry to be approximated depending on its local curvature and the size of the triangle faces. In principle the accuracy of the approximation can be improved by either raising the degree of the polynomial (p-refinement) or by reduction of the size of individual elements (h-refinement) [87]. The first-mentioned variant is not considered here, because it would mean to substitute triangles by higher-degree primitives. The n-refinement approximation error can be estimated in 2D by evaluating the properties of a linear approximation of a circle with line segments (Figure 3): A circle with radius $r \in \mathbb{R}^+$ and centre point M is approximated by $n \in \{2, 3, 4, \ldots\}$ equal length line segments $\overrightarrow{PQ}$ such that (19).

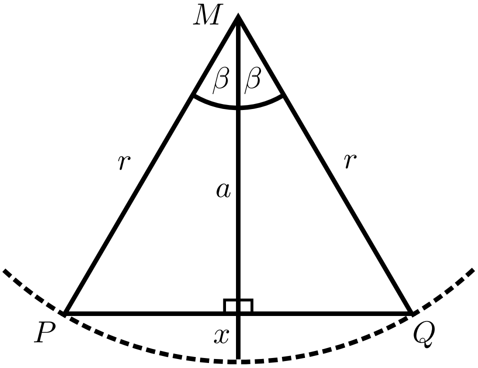

Figure 3: Observation of error x when approximating a circle with n line segments $\overrightarrow{PQ}$.

$$2\beta = \frac{2\pi}{n} \tag{19}$$

The maximum distance between $\overrightarrow{PQ}$ and circle M is given by the sagitta $x = r - a$. Thus, for a unit circle with $r = 1$, the error of approximation x with respect to its curvature r^{-1} and n can be calculated as (20).

$$x = 1 - \cos\left(\frac{\pi}{n}\right) \tag{20}$$

For the case that $n = 2$, $x = r$ and $M \in \overrightarrow{PQ}$ holds, which results in a degenerate triangle $\triangle_{PQM}$ with zero area [87] (see sec. 5.2.1). Figure 4 shows

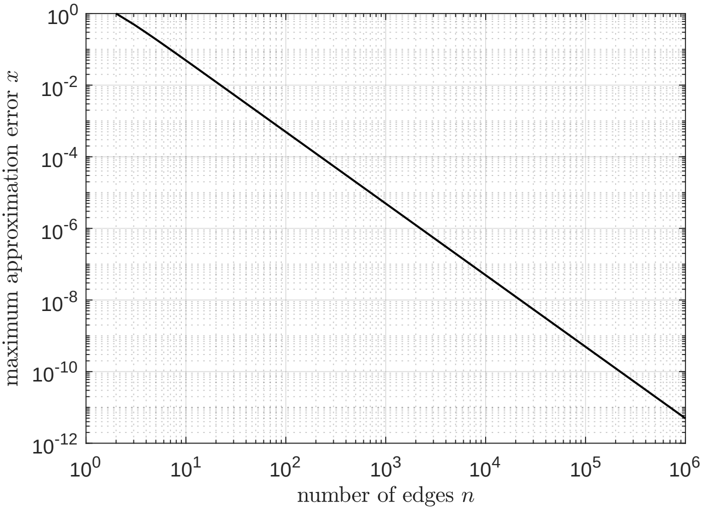

Figure 4: Approximation error x with respect to the number of edges n for the geometrical problem pictured in Figure 3 with $r = 1$.

the exponential relationship between n and x from (20) in a log-log plot. Here, for the slope s of the curve $\lim_{n \to \infty} s = -2$ holds[26], which means that a doubling of n causes a reduction of x by the factor of (roughly) four[27]. This halving of the edge $\overrightarrow{PQ}$ (and projecting the new vertex at location $\frac{P+Q}{2}$ back onto the circle) splits each triangle $\triangle_{PQM}$ into 2 sub-triangles, therefore the approximation error of a triangle mesh is inversely proportional to its number of faces [87]. This favourable behaviour means that the value of x can be controlled with reasonable effort. Consequently, although triangle meshes are not capable of a completely error free approximation of curved surfaces, x is zero at both P and Q and an upper limit for x can be given for any curvature, which are desired properties of triangle meshes in the context of this work.

The STL (stereolithography[28]) file is a neutral file format representing triangle meshes. It was designed such that any CAD system can process geometrical data resulting a spread into other applications, e.g. machining [90]. STL

---

[26] This can be derived from the Taylor series $\sum_{n=0}^{f^n(a)}(x-a)^n$ of the cosine function about $a = 0$: $\cos x = \sum_{n=0}^{\infty} \frac{(-1)^n}{(2n)!} x^{2n} = 1 - \frac{x^2}{2} + \frac{x^4}{24} - ....$

[27] The normal vector is constant on $\overrightarrow{PQ}$. The associated approximation error of that surface normal vector reaches its maximum value at both P and Q (Figure 3) and is only reduced by a factor of two when doubling n. Furthermore, the error of position x is largest when the error of the normal vector is smallest and vice versa.

[28] Other definitions of the acronym STL exist (e.g. standard triangle language, standard tessellation language), however the inventor reported that it stands for stereolithography. [90]

was developed by 3D Systems, Inc. and has become a de facto standard [91] because of its two major strengths, namely, simplicity and independence from specific modelling methods [92, 93]. However, because of its simplicity, the represented geometry can contain topological errors, such as gaps due to missing facets, non-manifold facets, overlapping facets, incorrect normal vectors and self-intersections [92–94]. Another disadvantage is that the format exclusively communicates geometry without any meta data, such as author, date and the unit of reference[29]. The case-insensitive STL file extension is ".stl". A binary as well as an ASCII file format exist, but the latter is rarely used because of significantly increased storage requirements and less efficient data parsing. The binary STL file uses the IEEE 754 integer and floating point numerical representation and is defined as follows [95, 96]:

1. 80 B[30] header with no data significance, which is generally ignored.
2. 4 B `uint32`[31] representing the number of triangle faces N_f in the file.
3. Each face is described by 50 B of data as described in Table 3. Therefore, the theoretical binary STL file size limit is $80 + 4 + 2^{32} \cdot 50\,\mathrm{B} \approx 200\,\mathrm{GiB}$.

Table 3: Binary STL file specification for each triangle face

bytes (B)	data type	description
$3 \cdot 4$	`real32`[32]	face normal vector $\{n_x, n_y, n_z\}$
$3 \cdot 4$	`real32`	triangle vertex $\{P_x, P_y, P_z\}$
$3 \cdot 4$	`real32`	triangle vertex $\{Q_x, Q_y, Q_z\}$
$3 \cdot 4$	`real32`	triangle vertex $\{R_x, R_y, R_z\}$
2	`uint8`[33]	attribute, usually unused

Inspecting the STL file structure (Table 3), the connectivity between different triangles is only given implicitly by repeated vertex coordinates. The STL file format is constructed based on the following special rules for tessellation and for storing information [95, 96]:

---

[29] Many software implicitly assume the unit of reference to be millimetre.

[30] A byte (B) is a group of usually eight adjacent binary digits (bits) operated on as a unit. Prefixes for binary multiplies shall be used to indicate multiplication by 2^{10n} with $n = \{1, 2, \ldots, 6\}$. [97, 98]

[31] 32 bit unsigned integer

[32] 32 bit floating point number

[33] 8 bit unsigned integer

1. The Vertex-To-Vertex rule: Each triangle must share two vertices with its neighbouring triangles. Thus, a vertex of one triangle cannot lie on the edge[34] of another triangle.
2. The Orientation Rule: The direction of surface normal vectors should point outwards and the vertices are listed in counter-clockwise order when looking at the object from the outside (right-hand-rule).
3. The All Positive Octant Rule: 3D objects must be placed in the all-positive octant of the 3D Cartesian coordinate system. This rule can result in reduced storage requirements when using the ASCII file format, but plays no role for the binary file format, because unsigned floating point numbers do not exist according to IEEE 775. This rule can be ignored, if the data is represented in the binary file format.
4. The Triangle Sorting Rule: Triangles should appear in ascending z-value order. This rule could help to slice 3D models faster but it is not strictly enforced and is therefore ignored.

After the STL file is read, the vertices of all N_f triangles are stored in an array[35] $\mathtt{v}_\mathrm{import} = [v_{ix}\ v_{iy}\ v_{iz}]^{3N_\mathrm{f}}$. Because of data consistency reasons, the face normals are not imported but instead computed from $\mathtt{v}_\mathrm{import}$ at a later time (see sec. 5.1), thus satisfying the stated Orientation Rule. It should be noted, that the triangle coordinates are only stored with an accuracy of 32 bit, which limits the minimum distance between two triangle vertices to approx. seven (decimal) orders of magnitude (base 10) relative to their most significant digit, based on an evaluation of the machine epsilon [99, 100].

2.2.4 Constrained Delaunay triangulations

The data processing pipeline (sec. 5) uses triangulations in order to improve the properties of the represented geometry data. Therefore, a short introduction to (constrained) Delaunay triangulations is given here. [101] defines a triangulation as a partition of a geometric domain, such as a point set, polygon or polyhedron into simplices that meet only at shared faces[36]. For a point set, the triangulation covers its convex hull [101]. If the geometric domain is a point set, which is the targeted use in the context of this thesis, the following definition of a triangulation is given [102]: ”A triangle in $\mathbb{R}^d$ is a d-dimensional simplex, which is defined by its $(d+1)$ vertices, and a triangulation of a set of points in $\mathbb{R}^d$ is a simplicial decomposition of the convex hull of the point set where the vertices of the triangles are contained in the point set.” Consequently, in 2D the simplex is a triangle and in 3D a

---

[34] Here, the edge means the line without its start and end points.

[35] Arrays (data structure) are denoted in typewriter font (sec. 1.6).

[36] This means ”edges” for 2D.

tetrahedron. 3D triangulations are therefore called tetrahedralisations [101]. A Delaunay triangulation is characterised by the property that the circumscribing hypersphere of each simplex encloses no input points [101, 102]. The dual of the Delaunay triangulation is the Voronoi diagram [103]. Both have been applied in many areas of mathematics and the natural sciences and they are of central importance in computational geometry with hundreds of papers discussing algorithms and extensions [101]. Efficient algorithms to compute the Delaunay triangulation of point sets in $\mathbb{R}^d$ exist: Two examples are the Bowyer-Watson algorithm[37] [104, 105] and the incremental flip algorithm [106]. Both algorithms have the worst-case complexity $O(n^2)$ with an expected complexity of $O(n \log n)$, with n denoting the number of points in the underlying set of points.

A constrained Delaunay triangulation (CDT) is a variation of Delaunay triangulation that is constrained with respect to pre-defined edges (2D) and faces (3D). The Delaunay criterion (empty hypersphere) is relaxed such that the pre-defined edges (2D) and faces (3D) restrict the visibility of points inside that hypersphere. Consequently, in 3D, a hypersphere with 4 points can now also contain additional points if they are on different sides of a constraining face with respect to the first four points. CDTs were introduced in 2D by [107] and generalised to higher dimensions by [108, 109]. In other words, using

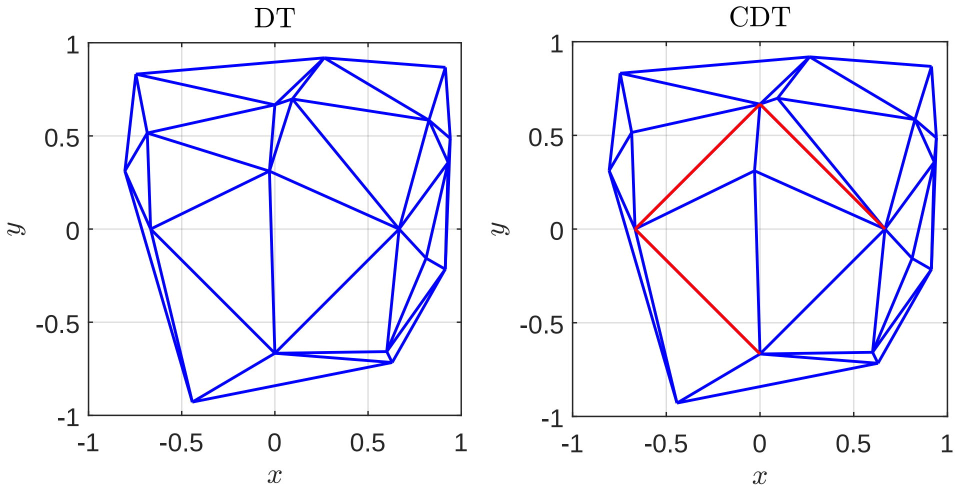

Figure 5: Example of a Delaunay triangulation (DT) and a constrained Delaunay triangulation (CDT). The added constraints for the CDT are marked red. The three red edges are not part of the original DT and are therefore forced into the triangulation by additional constraints.

---

[37] Both cited authors devised the same algorithm independently of each other and published it in the same issue of ”The Computer Journal”.

constraints forces the triangulation to implement certain edges, as shown in Figure 5. In 2D, the constraints are given as edges between two points must be part of the point set. The constraints must not intersect with each other. Equivalently, constraints in a 3D triangulation are given as triangles, the shape of the tetrahedron facets.

2.3 Metrological traceability and measurement uncertainty

The international vocabulary of metrology (VIM) defines metrological traceability as a "property of a measurement result whereby the result can be related to a reference through a documented unbroken chain of calibrations, each contributing to the measurement uncertainty" [10]. That means that measurement results have to be traceable to the SI units through chains of calibrations. In the context of dimensional metrology, the metre as the SI base unit of length is of central importance[38]. Traceability is required by different standards, including ISO 9001 [113], ISO 17025 [114] and ISO 14253-1 [14]. In order to be able to guarantee the comparability of measurement results, uniform procedures for determining them are necessary [8]. Decisions that are based on measurement results cannot be carried out reliably without knowledge of the measurement uncertainty. Historically, it was formulated in the Golden Rule of metrology (also known as gauge maker's rule [115]) that the measurement uncertainty should not exceed 10 % to 20 % of the tolerance to be verified by the measurement [116, 117]. A similar statement can also be derived from the standard ISO 14253-1 meaning that the estimated uncertainty of a measurement should be taken into account when determining conformity or non-conformity with respect to a specification [14].
The internationally accepted standard Guide to the Expression of Uncertainty in Measurement (GUM, also called ISO/IEC Guide 98)[39] describes

---

[38] Since 1983, the metre is defined with respect to the speed of light in vacuum c and the caesium frequency $\Delta\nu_{\mathrm{Cs}}$ as $1\,\mathrm{m} = (\frac{c}{299792458})\,\mathrm{s} = (\frac{9192631770 \cdot c}{299792458 \cdot \Delta\nu_{\mathrm{Cs}}})$, with $c = 299792458\,\mathrm{m\,s^{-1}}$ and $\Delta\nu_{\mathrm{Cs}} = 9192631770\,\mathrm{Hz}$. [110–112].

[39] The ISO/IEC Guide 98 currently consists of the following seven documents:
Part 1: Introduction to the expression of uncertainty in measurement [118]
Part 3: Guide to the expression of uncertainty in measurement (GUM:1995) [12]
Part 3 - Supplement 1: Propagation of distributions using a Monte Carlo method [38]
Part 3 - Supplement 1 - Technical corrigendum 1 [39]
Part 3 - Supplement 2: Extension to any number of output quantities [119]
Part 4: Role of measurement uncertainty in conformity assessment [120]
Part 6: Developing and using measurement models [121]
The GUM documents are identical in terms of content with respect to ISO/IEC Guide 98 and also available on the website of its advisory board, the "JCGM - Joint Committee for Guides in Metrology" [122].

in a comprehensive form the procedures for determining the measurement uncertainty and defines that the specification of an uncertainty together with the estimated value for the measurand is an elementary part of a measurement result [8]. The methods described in GUM focus on the mathematical treatment of the measurement uncertainty while using an explicit model of evaluation. That model can consist of mathematical equations (analytical determination) or a calculation rule (algorithm, numerical determination, see ISO/IEC GUIDE 98-3:2008, sec. 4.1.2 [12]) and describes the measurement method as well as the method of evaluation [11]. The measurand is the output variable of that model of evaluation and is connected to this model via one or more input variables. [12, 118]

However, within the context of this thesis, no explicit model of evaluation based on physical input quantities, which influence the measurement result, exists for any of the used measurement systems. Instead, the measurement uncertainty is determined from n measurements of measurand $\mathcal{X}$ repeated under constant environmental conditions, resulting in the exemplary set of uncorrelated measurements $\boldsymbol{x} = \{x_i\}_{i=1}^{n} = w + b + e_i$, with the true quantity value w and systematic and random measurement errors b and e_i, respectively [11]. In general[40], the random measurement error e_i can be described sufficiently well by a Gaussian distribution[41] [11]. The best available estimate $\hat{x}$ of the true value w of the measurand with measurements $\boldsymbol{x}$ is its arithmetic mean $\bar{x}$ minus the known estimate of the systematic measurement error b[42] (21) [11, 12].

$$\begin{aligned} \bar{x} &= \frac{1}{n}\sum_{i=1}^{n} x_i \\ \hat{x} &= \bar{x} - b \end{aligned} \tag{21}$$

This also means, that $\bar{x}$ is the best estimate for w if the systematic measurement error is unknown, such that $b = 0$. In practise, the value b can be determined by means of a measurement of a calibrated standard. The estimated variance $s^2(x_i)$ and the (positive) experimental standard deviation

---

[40] This does not apply for asymmetry sizes [123, 124].

[41] This can also be justified by the Central Limit Theorem which states that a resulting convolved distribution $Y = \sum_{i=1}^{n} c_i X_i$ converges to a normal distribution for $n \to \infty$ even if the distributions of the X_i are not normally distributed themselves [12]. Consequently, a random quantity can be regarded as normally distributed if it originated from superposition of many influences of equal importance [11].

[42] The estimate of a systematic measurement error is also called (measurement) bias. [10]

$s(x_i)$ characterise the dispersion of the individual values x_i about their mean $\bar{x}$ (22) [11, 12]. This quantity can also describe the measurement precision [10].

$$s^2(x_i) = \frac{1}{n-1}\sum_{i=1}^{n}(x_i - \bar{x})^2 \tag{22}$$

The uncertainty of these individual values follows $u(x_i) = s(x_i)$ [11]. The best estimate of the variance of the mean value $\bar{x}$ is given by (23) [11, 12, 18].

$$s^2(\bar{x}) = \frac{s^2(x_i)}{n} \tag{23}$$

The uncertainty of the mean measurement value $\bar{x}$ is given as $u(\bar{x}) = \sqrt{s^2(\bar{x})}$ [11]. The standard uncertainty $u(\bar{x})$ is also called "Type A standard uncertainty". It is a measure of the uncertainty of the mean due to random effects. [11, 12]

Now let $\boldsymbol{x}$ be affected by known (uncorrected) systematic errors. The GUM recommends correcting $\boldsymbol{x}$ for known systematic errors b before determining the measurement uncertainty, such that $\hat{x} = \bar{x} - b$ [12]. In this case, the combined uncertainty $u_\mathrm{c}(\hat{x})_{\mathrm{corr\,b}}$ is calculated as (24) [125].

$$u_\mathrm{c}(\hat{x})_{\mathrm{corr\,b}} = \sqrt{u(\bar{x})^2 + u(b)^2} \tag{24}$$

The parameter $u(b)$ denotes the standard uncertainty of the estimate b, which describes the uncertainty of the calibration. On the other hand, if a correction with b is not possible, and instead the uncorrected estimate $\hat{x} = \bar{x}$ is used, the combined uncertainty $u_\mathrm{c}(\hat{x})_{\mathrm{uncorr\,b}}$ can be given as (25) [125–127].

$$u_\mathrm{c}(\hat{x})_{\mathrm{uncorr\,b}} = \sqrt{u(\bar{x})^2 + u(b)^2 + b^2} \tag{25}$$

Importantly, the resulting $u_\mathrm{c}(\hat{x})_{\mathrm{uncorr\,b}}$ is not a standard uncertainty and shall not be used for uncertainty propagation [128]. The calculation of the expanded measurement uncertainty U is therefore not advisable using measurements without applied corrections of known systematic measurement errors. The expanded measurement uncertainty U describes an interval that may be expected to encompass a large fraction of the distribution of $\hat{x}$, according to the chosen coverage probability p. This is realised by the introduction of an expansion factor k, such that (26) holds.

$$U = k \cdot u_\mathrm{c}(\hat{x}) \tag{26}$$

The relationship between p and k is dependent on the distribution of the measurement results $x_i - b$, which can only be estimated if b is unknown. Typically used values for k range between 2 and 3. The quantity value of the measurand $\mathcal{X}$ can then be presented as $\hat{x} \pm U$. [11]

Importantly, two competing mathematical perspectives [129, 130] exist with respect to the method of reporting measurement uncertainty: In Bayesian statistics, probability expresses a degree of belief in an event, which may be based on prior knowledge about the event. Contrary to that, frequentism views probability as the limit of the relative frequency of an event after many trials. In this context, the GUM is a work of compromise, such that criticism from both sides remains [131, 132].

3 Problem statement and objective

The measurement results in 3D coordinate metrology represent a subset of the infinite set of coordinates representing the physical boundary of the measurement object. Thus, the description of that continuous surface of the measurement object based on discrete measurement points requires some form of interpolation[43] between measurement points. If no additional information is available, linear interpolation is the simplest choice, which is implicitly given for a triangle mesh (see sec. 2.2.3). The description of a surface, based on a set of coordinates, is only complete if the connectivity information between these coordinates is clearly defined and maintained at all times through all required data processing steps. Additionally, the measurement data must represent the surface of a physical object, which makes the enforcement of certain consistency requirements necessary.

Given these requirements, the vision of this thesis can be described as the *"development and application of a strictly (measurement) data driven framework which is capable of determining the measurement uncertainty of arbitrary points on the surface of the examined object"*.

A more technical description of the problem statement emphasises the connection to well-known nominal-actual comparisons (e.g. definition in VDI/VDE 2630 Part 1.1 [133]) and can be described as follows: The geometry of a measurement object $\mathcal{O}$ is completely[44] captured with measurement system $\mathcal{A}$ resulting in a single measurement $\mathcal{M}^{\dagger}$[45], which is equivalent to the "primary extracted surface" described in ISO 14406:2011-04 [134]. That measurement is repeated $n_{\text{MS}} - 1$ times with $\mathcal{A}$ under conditions satisfying the repeatability condition of measurement given in VIM [10], resulting in a measurement series with n_{MS} measurements, which is described by the set $\mathcal{M} = \{M_i\}_{i=1}^{n_{\text{MS}}}$. Additionally, an equivalent measurement $\mathcal{R}$ of the geometry of $\mathcal{O}$ is performed with a reference measurement system $\mathcal{B}$, satisfying the corresponding definition in VIM [10]. After transforming $\mathcal{M}$ and $\mathcal{R}$ into a common coordinate system such that both geometries are "as closely aligned with each other as possible"[46], local distances between each $\mathcal{M} = \{M_i\}_{i=1}^{n_{\text{MS}}}$ and $\mathcal{R}$ can be computed for arbitrary points $\mathcal{P} \in \mathcal{R}$. Consequently, the local measurement

---

[43] Strictly speaking, also extrapolation of unmeasured features can be required which is unfortunately impossible.

[44] Meaning the defining geometric features are probed with a "sufficient" number of measurement points.

[45] In other words, the collection of geometric features describing $\mathcal{O}$ represents the single measurand of this measurement task.

[46] More rigorous descriptions of that criterion are discussed in sec. 5.6.

uncertainty as a special metrological descriptor could be determined based on statistical evaluation of these n_{MS} distances associated with each $\mathcal{P} \in \mathcal{R}$, which form the basis to calculate both the random measurement error and the systematic measurement error of $\mathcal{A}$, respectively, with respect to $\mathcal{B}$. Put differently, in this case, this procedure (and one objective of this thesis) can be illustrated as a "nominal-actual comparison with uncertainty".

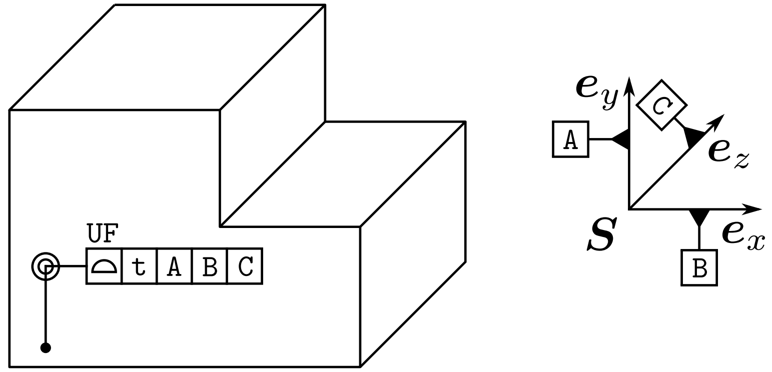

Figure 6: The specification of a surface profile tolerance `t` of the complete surface as closed all-around united feature. Here, the evaluation must explicitly respect an external coordinate system (affine transformation matrix) $\boldsymbol{S}(\mathtt{A,B,C})$ which locks three translational and three rotational degrees of freedom, respectively.

From another point of view, this task can be partly compared to the evaluation of a profile tolerance of the complete object surface, as defined in ISO 1101 [135, 136] (Figure 6). The goal of the given specification is to validate whether the complete geometry of the object conforms to the given surface profile tolerance `t` with respect to a given external coordinate system (affine transformation matrix) $\boldsymbol{S}(\mathtt{A}, \mathtt{B}, \mathtt{C})$[47], which locks three translational and three rotational degrees of freedom, respectively. The specification is defined on the nominal geometry $\mathcal{N}$ of $\mathcal{O}$, which is in practice mostly represented by a CAD model. The dependence on an external coordinate system is caused by the fact that the geometry data of a single measurement $\mathcal{M}^\dagger$ and $\mathcal{N}$ are represented in different coordinate systems and their subsequent evaluation requires the transformation into one common coordinate frame. In case of real physical measurements, this transformation rule cannot be determined exactly and must be approximated using mathematical tools. In order to comply with the given specification (Figure 6), each point of $\mathcal{M}^\dagger$ has to lie

---

[47] This notation means that $\boldsymbol{S}(\mathtt{A,B,C})$ represents a Cartesian base with vectors `A`, `B`, `C` (Figure 6, right) describing the transformation rule between the measurement data and a global coordinate system.

within the given tolerance `t`. Misalignment errors caused by a poor determination of the required transformation rule between $\mathcal{M}^\dagger$ and $\mathcal{N}$ directly affect the evaluation of t, which is why the dependence on an external coordinate system is explicitly given. This exemplary conformance testing task is performed by associating each measurement coordinate with its ”corresponding coordinate” on the nominal geometry $\mathcal{N}$. This concept of ”corresponding coordinates” deviates from the duality principle defined in ISO GPS, which states that the specifications for measurement object features are formulated as specification operators with the verification operator being the physical implementation of the aforementioned [9]. Consequently, the fundamental idea of work is the direct comparison between multiple geometries with the goal of determining spatially discrete metrological descriptors, e.g. measurement uncertainty. The difficulties associated with the determination of ”corresponding coordinates” are discussed next.

In the following it is assumed that the subsequently listed three different representations of the geometry of $\mathcal{O}$ are available:

- n_{MS} measurements $\mathcal{M}$ captured with $\mathcal{A}$,
- a reference measurement $\mathcal{R}$ captured with $\mathcal{B}$ and
- the nominal geometry $\mathcal{N}$.

Then it is possible to extend that principle of a profile tolerance validation visualised in Figure 6, which is based on the comparison of only two geometries, and instead statistically evaluate the comparisons of all the different representations of $\mathcal{O}$ listed above with each other. The general approach is visualised for a clipping of the examined geometry after the alignment into a common coordinate frame, such that $\mathcal{M}$, $\mathcal{R}$ and $\mathcal{N}$ superimpose each other (Figure 7). In order to simplify the following explanations it is assumed that the mean geometry $\overline{\mathcal{M}}$ was computed[48] from $\mathcal{M} = \{M_i\}_{i=1}^{n_{\mathrm{MS}}}$. The measurement series $\mathcal{M}$ is then visualised as the combination of $\overline{\mathcal{M}}$ and an interval $\overline{\mathcal{M}} \pm e_{\mathrm{rand}}(x_{\overline{\mathcal{M}}})$, wherein all measurement points of $\mathcal{M}$ are located. The measurement data $\mathcal{M}$ is described in local coordinates $x_{\overline{\mathcal{M}}}$ such that $\overline{\mathcal{M}} = \overline{\mathcal{M}}(x_{\overline{\mathcal{M}}})$ and the same principle is applied to $\mathcal{R} = \mathcal{R}(x_{\mathcal{R}})$ and $\mathcal{N} = \mathcal{N}(x_{\mathcal{N}})$. In Figure 7, double arrows indicate (signed) distances, which are functions of x. For the coordinate x holds $x \in \left\{x_{\overline{\mathcal{M}}}, x_{\mathcal{R}}, x_{\mathcal{N}}\right\}$, which means that the targeted quantities are obtained from (signed) distance measurements with respect to $\overline{\mathcal{M}}$, $\mathcal{R}$ or $\mathcal{N}$. In other words, these target quantities can be determined from different observers $\overline{\mathcal{M}}$, $\mathcal{R}$ or $\mathcal{N}$. This property is important in order to link the target quantities with the data structure of different geometries in order to assist powerful visualisation of the obtained results. Additionally, the coordinates

---

[48] A possible approach was previously published in [P11].

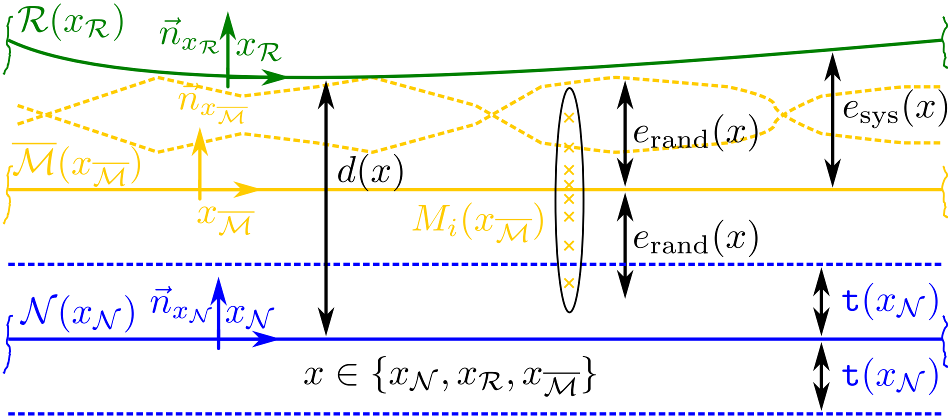

Figure 7: Visualisation of the metrological interaction of different geometries $\overline{\mathcal{M}}$, $\mathcal{N}$ and $\mathcal{R}$ within a common coordinate frame x by examination of different parameters of $d(x)$, $e_{\mathrm{rand}}(x)$ and $e_{\mathrm{sys}}(x)$ which was inspired by the validation of surface profile tolerances. Each of the different parameters is obtained by (signed) distance measurements (indicated by double arrows) between the geometries with respect to one of the observers $\overline{\mathcal{M}}$, $\mathcal{N}$ and $\mathcal{R}$ (indicated by x). In order to improve the visual clarity it is assumed that $\mathcal{R}$ is unaffected by measurement uncertainty and that $\mathtt{t}(x_{\mathcal{N}}) = \mathtt{const}$.

$\{x_{\overline{\mathcal{M}}}, x_{\mathcal{R}}, x_{\mathcal{N}}\}$ cannot be perfectly linked with each other, even if the perfect transformation between the geometries could be obtained, because $\mathcal{M}$, $\mathcal{R}$ and $\mathcal{N}$ differ locally with respect to each other due to measurement error and manufacturing deviations of the physical object. The profile tolerance $\mathtt{t}$ (Figure 6) is defined in the coordinate frame of $\mathcal{N}$ as $\mathtt{t} = \mathtt{t}(x_{\mathcal{N}})$, which is constant in this example. These target quantities are subsequently called "spatially discrete metrological descriptors" and are namely in this example:

- the random measurement error $e_{\mathrm{rand}}(x)$,
- the systematic[49] measurement error[50] $e_{\mathrm{sys}}(x)$ and
- the geometric deviations of the workpiece compared to $\mathcal{N}$, $d(x)$.

The underlying "correct" distance measurements between these geometries can be a challenging task, which is dealt with in sec. 5.3.

A strict tolerance validation of the specification shown in Figure 6 with tolerance $\mathtt{t}(x_{\mathcal{N}})$ based on a single measurement $M_i(x_{\overline{\mathcal{M}}})$ would result in the evaluation of a random surface (from the set of all possible measurement sur-

---

[49] The signs of $e_{\mathrm{sys}}(x)$ and $d(x)$ are dependent on the orientation of the observer geometries (not shown).

[50] In the GUM [12], known systematic errors $e_{\mathrm{sys}}(x)$ are denoted by the measurement bias b, which is avoided in this work because in the context of this thesis the differentiation between "known" and "unknown" measurement errors is not useful.

faces $\mathcal{M}$) within the scatter band $\overline{\mathcal{M}} \pm e_{\text{rand}}(x)$, because a single measurement is expected to scatter around its expected value[51]. Consequently, in certain edge cases of $M_i(x_{\overline{\mathcal{M}}})$, it is based on randomness if $\mathtt{t}$ is satisfied, because it can lie either inside or outside the tolerance $\mathtt{t}$. This is visualised in Figure 7 by several exemplary measurement coordinates within the black ellipse for $M_i(x_{\overline{\mathcal{M}}})$. Therefore this approach would not consider locally different measurement uncertainty, because conformance (defined in ISO 9000 [137]) testing according to [14] only intends the construction of acceptance intervals based on constant measurement uncertainty for a measurement (here the profile of the object). In this example, the measurement result is (27), which would have to lie within the acceptance interval [120] / conformance zone [14] of $\mathtt{t}$ in order to pass tolerance conformance testing.

$$\text{conforms to specification}\begin{cases}\text{yes} & \text{if}\, \mathtt{max}(|\{\forall x, \forall i | M_i(x) - \mathcal{N}(x)\}|) \leq \mathtt{t}(x)\\ \text{no} & \text{otherwise}\end{cases} \tag{27}$$

In this case, (27) also does not consider the measurement uncertainty. Therefore, the objective of this thesis, which was also inspired by areal profile tolerance conformity testing, is to provide a full description of the local metrological interaction of different geometries representing the same object, which are all connected by a common but typically unknown coordinate system, which makes it possible under certain conditions[52] to specifically target measurement uncertainty parameters at arbitrary surface locations x (28).

$$u(x) = \sqrt{e_{\text{rand}}(x)^2 + e_{\text{sys}}(x)^2} \tag{28}$$

Although the shown example in Figure 7 assumes that $\mathcal{R}$ is unaffected by uncertainty in order to clarify the visualisation, the concept is nonetheless capable of considering additional measurement systems and series when evaluating the uncertainty of a certain measurement task.

This objective associated with the problem statement can be further specified by first stating important requirements, boundary conditions and sub-goals of the targeted solution:

1. A description of the nominal (theoretically perfect) geometry $\mathcal{N}$ of $\mathcal{O}$ is available in (or transformable into) the STEP CAD format.
2. The data structure of the observer geometry defines discrete sampling points, at which the spatially discrete metrological descriptors are determined. The realised lateral sampling density must be high enough to

---

[51] Assuming no drifts within sequentially recorded measurements $M_i(x)$.

[52] See sec. 5.7.

capture all features within the range of the structural resolution of $\mathcal{A}$ (the examined measurement system).

3. The used algorithms must explicitly be suited for the application in metrology meaning that their supposedly introduced deviations and required additional information must be specified exactly. Algorithms should strictly be designed for general validity.
4. Data processing should take place with the least possible amount of manual user interaction in order to lay the foundation for large scale examinations.
5. Data processing durations should not exceed the combined time required for taking all measurements.
6. Suitable methods for visualisation and statistical treatment should be provided in order to compare the results between different measurement series and objects, respectively.
7. The underlying problem is related to geometrical nominal-actual comparisons used in the context of 3D coordinate metrology. However, there is no complete mathematical definition given for how to perform such an analysis, possibly resulting in lack of clarity about that metrological tool. Complementary to the explanations given in different parts of the guideline VDI/VDE 2630 [133, 138, 139], a technical definition of a nominal-actual comparison should be worked out.
8. Additional metrological descriptors besides the ones named above should be defined in order to provide additional information about the examined measurement task.

The main result of the data processing pipeline is the possibility to associate arbitrary coordinates describing the geometry of an object originating from different data sources ($\mathcal{M}$, $\mathcal{R}$, $\mathcal{N}$) with each other. From this association, the components of the local measurement error of arbitrary points on the object geometry can then be calculated among others, using specialised descriptors. The overall approach is therefore referred to as the spatially discrete metrological descriptor framework, because different metrological properties of a measurement task (ultimately describing the measurement uncertainty under certain conditions) can be determined at discrete points.

The second part deals with the usability of the spatially discrete metrological descriptor framework in order to create added value for metrological dimensional examinations. The fact that metrological descriptors of arbitrary points of the observer geometry can contain information about the local measurement error makes the implementation of specifically adapted algorithms possible. These opportunities include without being limited to the following:

1. Provide suitable tools to visualise the distribution of different metrological descriptors (e.g. different measurement error components or the measurement uncertainty for certain use cases) over the complete surface of a measurement object. This can yield valuable information about the local quality of a measurement. Thus, new algorithm prototypes designed to reduce measurement artefacts can be validated both quantitatively and visually.
2. Perform comprehensive measurement system analysis with respect to the locally determined metrological descriptors. Ideally, the sensitivity is high enough that even small changes in the measurement chain are detectable and therefore assessable with respect to their impact on the measurement result.
3. The configuration of simulation tools such that they can exactly match the metrological behaviour of the targeted real measurement system is a complex task. The comparison of real and simulated measurements with respect to a reference measurement can identify further steps for improvement of the simulation tool.
4. Evaluate the validity of local abstract quality parameters obtained from alternative measurement data evaluation [P7] in the context of industrial X-ray computed tomography.
5. Improve the accuracy of geometry element regression used to determine the parametrisation of a collection of measurement points representing a common geometric feature (e.g. points representing a bore hole).

This work presents the spatially discrete metrological descriptor framework for the comparison and evaluation of different kinds of geometries derived from a measurement object (measurement series, reference measurement(s), nominal geometry) with the goal of determining insights about the metrological characteristics resulting from the interaction of the used measuring systems and objects. Ultimately, by rigorously controlling the complete data processing pipeline with respect to metrological design guidelines, the spatially discrete metrological descriptor framework constitutes an important complement to traditional methods for a better understanding of measurement systems and their outputs.

4 Related work

The guideline VDI/VDE 2630 Part 1.1 loosely defines a nominal-actual (value) comparison as a comparison between two data sets (nominal and actual) regarding their geometric properties [133]. Part 1.2 of VDI/VDE 2630 mentions the colour-coded representation of the obtained deviations between the two data sets, the indication of selected deviations at defined points and the statistical evaluation of the observed deviations [138]. In the context of the measurement of free-form surfaces, VDI/VDE 2630 Part 2.1 recommends the following procedure [139]: "Starting from the reference point, the distance of the surface obtained by the (...) measurement shall be analysed in the direction of the surface normal assigned to the reference point." While this procedure is valid for continuous surface regions this type of sampling can lead to problems when evaluating surface regions with local discontinuities (sharp edges).

In the context of product design and development, skin models describe geometric deviations that are expected, predicted or already observed in the real manufacturing processes [140]. They are based on the theoretical foundations of Geometrical Product Specification (GPS) [6] and the two axioms of manufacturing imprecision and measurement uncertainty [140], formulated by [141]. The concept of skin models was developed to enrich the nominal geometry considering physical shapes. One application is the visualisation of expected deviations from a CAD model using false-colour imaging, similar to the above mentioned nominal-actual comparisons [140, 142]. They are mostly created by simulation of geometric deviations followed by a statistical shape analysis for geometrical variability considerations [140, 142, 143].

In 2021, Kaufmann et al. demonstrated how to analyse measurement uncertainty propagation for virtual assembly based on repeated CT measurements [144].

In many fields, scientific data sets are not considered complete without additional information about uncertainty, accuracy or levels of confidence. This includes the creation and visualisation of nominal-actual comparisons, as mentioned above. Therefore, data uncertainty visualisation techniques play a large role in many scientific disciplines. They are continuously evolving with further advances in computing technology. Exemplary overviews over different methods for visualising uncertainty are [145–148], followed by a selection of special applications [149–157].

In 2021, Senin, Catalucci et al. reported an approach to investigate measurement uncertainty in coordinate metrology based on fitting Gaussian random fields to high-density point clouds produced by measurement results [158]. Catalucci describes algorithmic solutions to compute indicators of measurement performance directly from the measured point clouds in a fully automated way [159–162]. These publications partially show distinct similarities to the work presented in this thesis and were developed around the same time horizon independently of each other. Some of the main distinctions are:

- The focus on point cloud data as opposed to complete surface representations,
- the emphasis on optical 3D coordinate measurements and the explicit treatment of missing measurement data (e.g. due to shadowing),
- the usage of statistical tools to develop local as well as global measurement quality parameters,
- and lastly without a particular focus on high-performance applications of the developed algorithms.

Mathematically rigorous descriptions of weighted geometry element regression analysis, where uncertainty information for each measurement point is given, were published in [163] and reported for the specific example of fitting a straight line in [164]. In [165, 166] methods to consider uncertainty matrices associated with coordinate data in surface fitting problems were reported.

5 The data processing pipeline for calculation of spatially discrete metrological descriptors

This chapter introduces all data processing routines required in order to determine the spatially discrete metrological descriptors for a metrological task. Figure 8 gives an overview over the interdependence of operations. Within the context of this thesis, three different types of geometry exist for a measurement object: its nominal geometry (CAD), measurement data recorded with a primary[53] measurement system and reference measurement data captured with a secondary system, which acts as a metrological reference with respect to the first system in the sense of a ”reference measurement procedure” described in VIM [10]. However, depending on the usage scenario not all of these geometry types need to be provided (see sec. 5.7). The geometry data is then undergoing different types of post-processing and preparation (see sec. 5.4

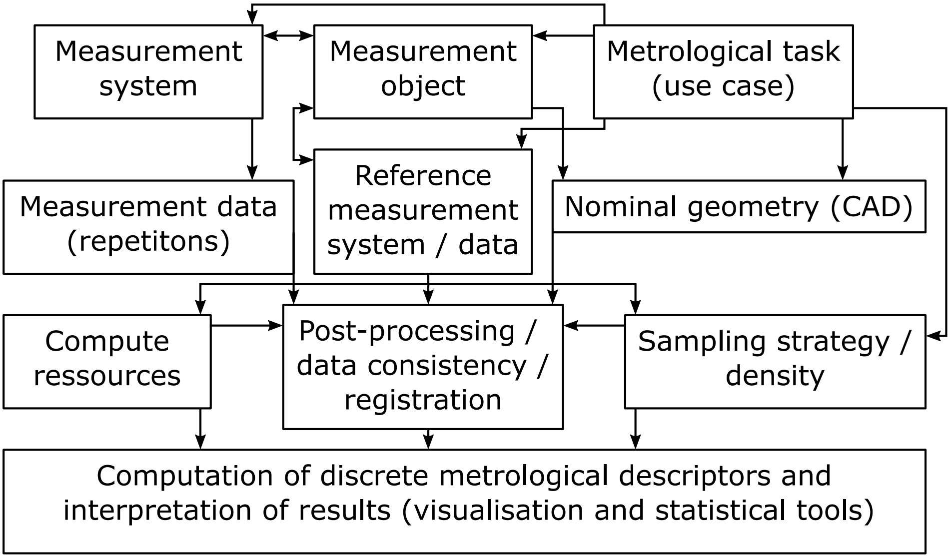

Figure 8: Starting with the definition of a metrological task the connection and sequence of operations is shown in order to acquire spatially discrete metrological descriptors. Arrows mark dependencies, e.g. the measurement object is dependent on the metrological task and measurement object and system are both dependent on each other. Based on the use case not all components need to be defined.

---

[53] The term ”primary measurement system” used in this thesis does explicitly not refer to a ”primary reference measurement procedure” described in VIM [10].

and 5.5), which ensures data consistency and respects user-given parameters (e.g. sampling strategy, sec. 5.3) and also performs the alignment of different coordinate systems (registration, sec. 5.6). The processing pipeline is concluded by the computation of the spatially discrete metrological descriptors and the interpretation of the results.

The following example illustrated in Figure 9 describes the fundamental relationship between the different types of geometries (nominal, reference measurement, measurement series) for a physical 1D length measurement (e.g. representing the results of gauge block height measurements). The same length measurement was performed with a primary measurement system $\mathcal{A}$ (red data points) as well as a secondary reference measurement system $\mathcal{B}$ (blue data points). The assigned meaning of primary and secondary measurement system, respectively, is solely based on user preference. However, it makes more sense in a metrological context to designate the more accurate (ideally traceable) system as the reference measurement system with respect to the primary systems[54]. The true value of the measurement is a theoretical value,

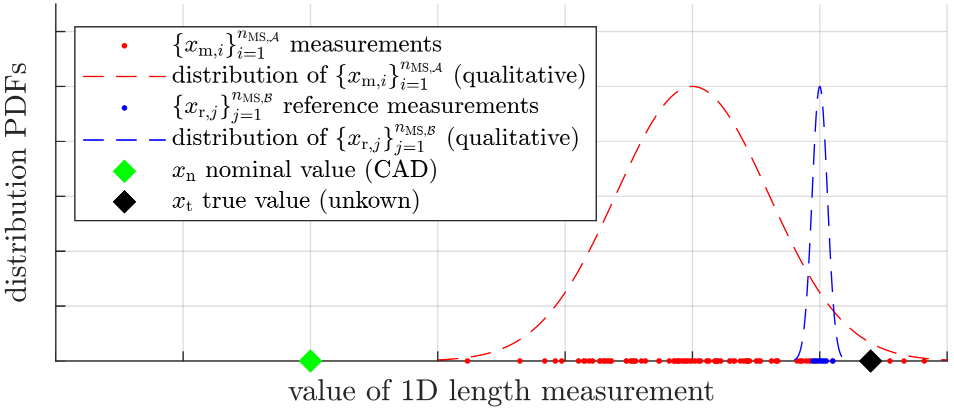

Figure 9: Illustration of possible components of a 1D length measurement of a physical object: $n_{\mathrm{MS},\mathcal{A}}$ measurements are performed with a primary measurement system $\mathcal{A}$ as well as $n_{\mathrm{MS},\mathcal{B}}$ measurements with a secondary reference measurement system $\mathcal{B}$. Both measurement series result in distinct distributions. The nominal measurement result (from CAD) are also shown, as well as the true value of the measurement which can never be exactly obtained.

---

[54] The international vocabulary of metrology (VIM) defines a reference measurement procedure as "measurement procedure accepted as providing measurement results fit for their intended use in assessing measurement trueness of measured quantity values obtained from other measurement procedures for quantities of the same kind, in calibration, or in characterizing reference materials". [10]

which can never be obtained by any measurement[55] [10]. The nominal value is the result of a (theoretically) perfectly manufactured measurement object and corresponds to the intended geometrical properties by the designer. Because of the fact that the reference measurement is expected to be both significantly more precise and accurate compared to the primary measurement series this thesis only considered reference measurement series of size 1. Consequently, it is assumed in this thesis, that the measurement errors (both systematic and random) of the reference measurement system are negligible. From this data, the following parameters can be obtained:

- The precision of a measurement series is represented by the dispersion of the data series $\{x_{\mathrm{m},i}\}_{i=1}^{n_{\mathrm{MS},\mathcal{A}}}$ and $\{x_{\mathrm{r},j}\}_{j=1}^{n_{\mathrm{MS},\mathcal{B}}}$ (typically the standard deviation).
- The systematic measurement error of the primary measurement series with respect to the secondary series as the difference of their arithmetic means $\frac{\sum x_{\mathrm{m},i}}{n_{\mathrm{MS},\mathcal{A}}} - \frac{\sum x_{\mathrm{r},j}}{n_{\mathrm{MS},\mathcal{B}}}$.
- The manufacturing deviations of the examined component as $\frac{\sum x_{\mathrm{r},j}}{n_{\mathrm{MS},\mathcal{B}}} - x_{\mathrm{n}}$, with x_{n} denoting the nominal value.

In this thesis, the task is to determine the mentioned parameters for geometries represented in 3D space, which requires a more sophisticated data processing pipeline. The next sections give detailed technical descriptions of the used geometry representation, the handling of various types of geometry data and the single processing steps required to determine the spatially discrete metrological descriptors.

Because of the fact that software has been shown to negatively contribute to the measurement uncertainty, which means that software uncertainty is cause for concern [167], special care was taken when designing the algorithms forming the data processing pipeline for spatially discrete metrological descriptors. This is reflected by the fact that all mathematical operations are described as accurately as possible in the following sub-sections.

5.1 Extended triangle mesh data structure

The STL format characterises a triangle mesh by storing a set of individual triangle faces (i.e. three vertices per face, see sec. 2.2.3), which does not explicitly represent the mesh connectivity and is therefore commonly referred to as triangle soup [87]. Consequently, this form of data structure contains redundant information, because within a mesh, vertices are shared between

---

[55] This limitation applies only to physical measurements of real objects because for many simulated (virtual) measurements the true value of the measurement is equal to the nominal value and is therefore well known.

faces. A simple and efficient and thus popular data structure for triangle meshes is the so-called indexed face set, which consists of two arrays [87]:

1. vertices: Each of the N_v (number of vertices) rows of the array contains three Cartesian coordinates of a single triangle vertex, such that $\mathtt{v} = [\mathtt{v}_{\mathtt{i,x}}\ \mathtt{v}_{\mathtt{i,y}}\ \mathtt{v}_{\mathtt{i,z}}]^{\mathrm{N_v}}$.
2. faces: Each of the N_f (number of faces) rows of the array contains three[56] indices, pointing to row numbers of the vertices array and thus each defining a single face consisting of three vertices, such that $\mathtt{f} = [\mathtt{k}_{\mathtt{i,1}}\ \mathtt{k}_{\mathtt{i,2}}\ \mathtt{k}_{\mathtt{i,3}}]^{\mathrm{N_f}}$.

The vertices $\hat{\mathtt{v}}$ corresponding to a set of faces with indices $\hat{\mathtt{i}}$ are then found by array indexing [168], such that $\hat{\mathtt{v}} = \mathtt{v}(\mathtt{f}(\hat{\mathtt{i}},:)',:)$. Both arrays `v` and `f` are constructed from the imported[57] vertices data (see Algorithm 1)[58] by finding the unique coordinate triplets and constructing the faces array from the original vertices order in the imported data.

```
function [faces,vertices] = GetFacesVerticesArrays(verticesImport)
    [vertices,~,idxInSorted] = unique(verticesImport,'rows');
    faces = reshape(idxInSorted',3,[])';
end
```

Algorithm 1: Generating faces and vertices arrays from the imported triangle data. This code snippet follows MATLAB [171] syntax.

Note that in this data structure, the order of the rows of `f` can be arbitrarily arranged, without changing the underlying geometry of the object. The columns of `f` can also be changed, as long as their ordering remains consistent. Because of data efficiency as well as consistency reasons, the face normal vectors $\{\boldsymbol{n}_{\mathrm{f},i}\}_{i=1}^{N_\mathrm{f}}$ are not imported from the STL file (see Table 3) but instead computed from `f` and `v`. The coordinates of a single triangle $\triangle_{\boldsymbol{abc}}$ are given as $\boldsymbol{a}$, $\boldsymbol{b}$ and $\boldsymbol{c}$ in that particular order according to `f`. A vector $\boldsymbol{r}$ is calculated using the vector product [18] of two edge vectors (29), such that the right-hand-rule (see sec. 2.2.3) is fulfilled.

$$\boldsymbol{r} = (\boldsymbol{b} - \boldsymbol{a}) \times (\boldsymbol{c} - \boldsymbol{a}) \tag{29}$$

The face normal vector $\boldsymbol{n}_\mathrm{f}$ and the triangle area $A_\triangle$ can be computed from $\boldsymbol{r}$ as (30), because the edge vectors $\boldsymbol{b} - \boldsymbol{a}$ and $\boldsymbol{c} - \boldsymbol{a}$ span a parallelogram with twice the triangle area [172]. In case of a degenerate triangle with two

---

[56] The number of indices per face can be changed accordingly if other types of meshes (e.g. quadrilateral or hexagonal) are represented.

[57] The file format is described in sec. 2.2.3.

[58] Function reference: `unique(...)` [169], `reshape(...)` [170].

(nearly) parallel edges, $\boldsymbol{r} \to [0\ 0\ 0]^{\mathrm{T}}$. That means that $\boldsymbol{n}_{\mathrm{f}}$ is undefined and is generated from random numbers[59].

$$\begin{aligned} A_{\triangle} &= \frac{\|\boldsymbol{r}\|}{2} = \frac{\sqrt{\boldsymbol{r} \cdot \boldsymbol{r}}}{2} \\ \boldsymbol{n}_{\mathrm{f}} &= \frac{\boldsymbol{r}}{2A} \quad \text{with } \|\boldsymbol{n}_{\mathrm{f}}\| = 1 \end{aligned} \tag{30}$$

Formally, the surface normal vector of a point $\boldsymbol{x}$ on the mesh surface Ω, $\boldsymbol{x} \in \Omega$, is a line which is perpendicular to the tangential plane of $\boldsymbol{x}$ [18]. The normal vector of $\boldsymbol{n}(\boldsymbol{x})$ is equivalent to the normalised gradient of $\nabla \boldsymbol{x}$ (31) [18], which is an alternative designation of the same concept in the context of scalar field theory.

$$\boldsymbol{n}(\boldsymbol{x}) = \frac{\nabla \boldsymbol{x}}{\|\nabla \boldsymbol{x}\|} = \nabla_{\mathrm{norm}} \boldsymbol{x} \tag{31}$$

Consequently, because a triangle mesh is a piecewise planar surface, normal vectors can be computed for three different surface regions: facets, edges and vertices. While it was straightforward and unambiguous to compute the triangle face normals $\boldsymbol{n}_{\mathrm{f}}$ (30), different approaches exist for determining the vertex normals $\boldsymbol{n}_{\mathrm{v}}$. This requires knowledge about which faces share a particular vertex. Geometrically, this information is embedded in the ”triangle fan” around one vertex, as demonstrated in Figure 10. These details are not directly available in the indexed face set consisting of `f` and `v` and must be calculated beforehand by creating the arrays `verticesPerVertex` (`vpv`) and `facesPerVertex` (`fpv`). Both arrays contain the vertex and face indices, respectively, connected to each vertex in the triangle mesh. Consequently, both arrays have N_{v} rows and their number of columns equals the maximum number of vertices / faces attached to one vertex. The valence of a vertex V_{v} (also called vertex degree) describes its number of neighbouring vertices (thus the number of incident edges), and its average value converges to six in closed, manifold meshes (this follows directly from the Euler formula (18)) [87]. A mesh is called regular, if all vertices have the same degree. In the example in Figure 10, the valence of $\boldsymbol{a}$ is $V_{\boldsymbol{a}} = 5$. Based on own experience, meshes typically exhibit a maximum valence of $V_{\max} < 10$, except for certain CAD to STL conversion results, where one vertex can be connected to hundreds of vertices with very thin triangle strips. Nonetheless, these special cases do not lead to memory bottlenecks because the overall number of vertices is relatively low whenever this special situation occurs. The value of $V_{\max}$ should be identical for both `vpv` and `fpv`, otherwise the triangle mesh is

---

[59] This is done for data structure consistency reasons. The methods described in sec. 5.2.1 ensure that degenerate triangles are removed.

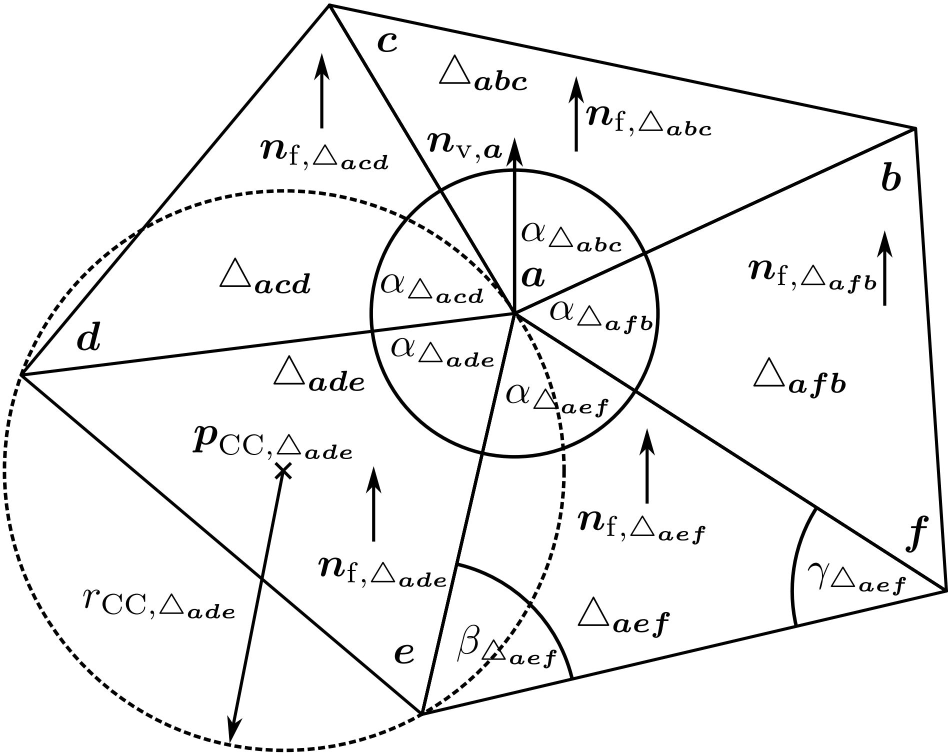

Figure 10: The local triangle fan around a vertex $\boldsymbol{a}$, resulting in a valence of five for vertex $\boldsymbol{a}$. From there, the calculation of the vertex normal of $\boldsymbol{n}_\mathrm{f}$ of $\boldsymbol{a}$ is possible by different weighting of the surrounding, consistently oriented face normals, e.g. by area or by their interior angles α, β and γ. For each triangle, its circumscribed circle, described by parameters CC_c and r_{CC} can be constructed.

inconsistent or defective. All measures taken in order to ensure a consistent triangle mesh geometry representation are described in sec. 5.2.1. Usually, not every vertex is connected with the same amount of vertices. Because of that, the remaining entries in the array are set to NaN[60], allowing straightforward handling in subsequent algorithms.

---

[60] The scalar double IEEE representation of ”not a number” (NaN) in hexadecimal representation is `fff8000000000000` [173] and represents one recommended way to represent missing data in numerical arrays according to [174].

From (30) directly follows that $\boldsymbol{r}$ is proportional to the triangle area. Consequently, (32) describes the calculation of the area-weighted vertex normal from all triangle faces containing that target vertex.

$$\boldsymbol{n}_{\mathrm{v}} = \frac{\sum_{i=1}^{V_{\mathrm{v}}} \boldsymbol{r}_i}{||\sum_{i=1}^{V_{\mathrm{v}}} \boldsymbol{r}_i||} \tag{32}$$

This represents a very popular method of calculating $\boldsymbol{n}_{\mathrm{v}}$ [175], however numerous alternative approaches have been described, e.g. using the mean of all $\boldsymbol{n}_{\mathrm{f}}$ or weighting each $\boldsymbol{n}_{\mathrm{f}}$ by its interior angle in the triangle fan [175–179] (see also Figure 10). In case of a triangle mesh with a homogeneous triangle size distribution, the methods produce very similar results. However, this condition of equally sized triangles can only be satisfied up to a certain degree. Because of the fact that vertex normals determined as weighted face normals $\boldsymbol{n}_{\mathrm{f},i}$ according to their respective interior angles α_i (33) [175] result in vertex normals $\boldsymbol{n}_{\mathrm{v}}$ independent of the local mesh structure, this method is preferred within the context of this thesis and was therefore used for all subsequent computations.

$$\begin{aligned} \boldsymbol{N} &= \sum_{i=1}^{V_{\mathrm{v}}} \alpha_i \boldsymbol{n}_{\mathrm{f},i} \\ \boldsymbol{n}_{\mathrm{v}} &= \frac{\boldsymbol{N}}{||\boldsymbol{N}||} \end{aligned} \tag{33}$$

The normal vector of an edge is either computed based on the normals of its two neighbouring facets or vertices, respectively[61]. The shown approaches for calculating normal vectors reflect the discontinuity of the represented surface in that sense, that a point very close to a triangle vertex is associated with a face normal vector which is possibly quite different from the vertex normal vector. A possibility to use smooth normal vectors is presented in sec. 5.3, which is based on interpolation of the calculated vertex normal vectors across the whole surface using barycentric coordinates [88].

The triangle centroid $\boldsymbol{c}$ is computed from the arithmetic mean of the triangle edge points $\boldsymbol{a}$, $\boldsymbol{b}$ and $\boldsymbol{c}$ as $3\boldsymbol{c} = \boldsymbol{a} + \boldsymbol{b} + \boldsymbol{c}$ [180].

The circumscribed circle of a triangle passes through all its vertices and is therefore embedded in the triangle plane with normal vector $\boldsymbol{n}_{\mathrm{f}}$. Consequently, no part of the triangle can be outside of that circle, which can be a useful property for collision tests. Using the notation introduced above, the

---

[61] Details are omitted for discontinuous edge normal vectors because of lacking relevance in the context of this thesis.

radius of a triangle circumscribed circle r_{CC} is calculated from the triangle vertices using (34) [181].

$$r_{\mathrm{CC}} = \frac{\|\boldsymbol{a} - \boldsymbol{b}\| \cdot \|\boldsymbol{b} - \boldsymbol{c}\| \cdot \|\boldsymbol{c} - \boldsymbol{a}\|}{4A} \tag{34}$$

The centre point $\boldsymbol{p}_{\mathrm{CC}}$ is then (35) [181]:

$$\begin{aligned} \boldsymbol{p}_{\mathrm{CC}} &= p\boldsymbol{a} + q\boldsymbol{b} + r\boldsymbol{c} \\ p &= \frac{\|\boldsymbol{b} - \boldsymbol{c}\|^2 \cdot (\boldsymbol{a} - \boldsymbol{b}) \cdot (\boldsymbol{a} - \boldsymbol{c})}{2(2A)^2} \\ q &= \frac{\|\boldsymbol{a} - \boldsymbol{c}\|^2 \cdot (\boldsymbol{b} - \boldsymbol{a}) \cdot (\boldsymbol{b} - \boldsymbol{c})}{2(2A)^2} \\ r &= \frac{\|\boldsymbol{a} - \boldsymbol{b}\|^2 \cdot (\boldsymbol{c} - \boldsymbol{a}) \cdot (\boldsymbol{c} - \boldsymbol{b})}{2(2A)^2} \end{aligned} \tag{35}$$

The extension from the circumscribed circle to the circumscribed sphere is trivial, it has the same centre point $\boldsymbol{p}_{\mathrm{CC}}$ and radius r_{CC}, respectively.

The Pythagorean theorem $c^2 = a^2 + b^2$ is a special case of the more general theorem relating the lengths of sides in any triangle, the law of cosines $c^2 = a^2 + b^2 - 2ab\cos\gamma$ [18]. Because all edge lengths of each triangles are known, this theorem can be used to determine the inner angles α, β and γ of the triangle (36) (Figure 10), such that $\alpha + \beta + \gamma = \pi$ [18].

$$\begin{aligned} \alpha &= \arccos\left(\frac{b^2 + c^2 - a^2}{2bc}\right) \\ \beta &= \arccos\left(\frac{a^2 + c^2 - b^2}{2ac}\right) \\ \gamma &= \arccos\left(\frac{a^2 + b^2 - c^2}{2ab}\right) \end{aligned} \tag{36}$$

Summarizing the above, every triangle mesh is represented by the properties listed in Table 4. The last property $\mathrm{BB}_{\mathrm{tf}}$ describes the tight-fitting bounding box, which can be calculated for every triangle mesh. It describes the size, position and orientation of the smallest possible cuboid, which completely encloses the targeted triangle mesh in its coordinate system. Its calculation and purpose in the context of the registration procedure is described in sec. 5.6.

Table 4: Overview over the main used triangle mesh properties.

identifier	description	array / struct size
N_v	number of vertices	$[1 \times 1]$
N_f	number of faces	$[1 \times 1]$
V	valence of each vertex	$[N_\text{v} \times 1]$
`f`	faces	$[N_\text{f} \times 3]$
`v`	vertices	$[N_\text{v} \times 3]$
`fpv`	faces (indices) per vertex	$[N_\text{v} \times V_\text{max}]$
`vpv`	vertices (indices) per vertex	$[N_\text{v} \times V_\text{max}]$
$\boldsymbol{n}_\text{f}$	face normal vectors	$[N_\text{f} \times 3]$
$\boldsymbol{n}_\text{v}$	vertex normal vectors	$[N_\text{v} \times 3]$
$\boldsymbol{c}$	triangle centroids	$[N_\text{f} \times 3]$
$A_\triangle$	triangle areas	$[N_\text{f} \times 1]$
α, β, γ	triangle interior angles	$[N_\text{f} \times 3]$
a, b, c	triangle edge lengths	$[N_\text{f} \times 3]$
r_CC	circumscribed circle radius	$[N_\text{f} \times 1]$
$\boldsymbol{p}_\text{CC}$	circumscribed circle centre point	$[N_\text{f} \times 3]$
BB_tf	tight fitting bounding box	$[1 \times 1]$ (struct)

5.2 Measurement data post-processing

Ideally, the triangle mesh representing a measurement result is a watertight 2-manifold (see sec. 2.2.3). Unfortunately, by experience, this is not the case for many measurements, thus routines must be provided to ensure these topological qualities of the measurement data. The process of removing artefacts from a geometric model in order to obtain certain qualitative properties of the output model for downstream applications is called model repair [87]. This processing step is described as one of the most enduring problems in the context of polygon mesh processing and is therefore critical for further streamlining of geometry processing pipelines [87].

In order to ensure that a triangle mesh conforms to the properties making it a watertight 2-manifold, it must pass the following five tests:

1. The mesh must contain at least four faces.
2. No corrupted triangles are allowed (see sec. 5.2.1).
3. Each (undirected) edge is shared by exactly two faces.

4. Each vertex is part of multiple edges and faces. Both these numbers must be equal such that $\texttt{fpv}_i = \texttt{vpv}_i$ is satisfied (see Table 4).
5. The mesh contains no self intersections, that means triangles ”touch” each other only at edges and vertices (see sec. 5.2.2).

The basic assumption for potentially required measurement data corrections is described as follows: Because of the fact that a measurement represents a physical object, it is expected and consequently enforced that the measurement data also correctly represents a physical object by being a watertight 2-manifold. Parts of the measurement data not conforming to this assumption are removed and potentially required replacements are subsequently added, as described in this section. The main reason for that requirement is the possibility of robust implementations of highly automated registration pipelines (sec. 5.6). Given the additional effort associated with (semi-)manual registration methods, this requirement could be relaxed.

5.2.1 Corrupted triangles

Corrupted triangles have in common that they add no useful surface information to the triangle mesh. They often are characterised by having no valid normal vector and are treated as follows:

1. Duplicate triangles are removed from the mesh.
2. Degenerate faces with two or three equal index entries or vertex positions, respectively, are removed from the mesh.
3. Faces with $\|\boldsymbol{r}\| < \epsilon$ (norm of cross product of edge vectors (see (29) on p. 50) below a small value ϵ): Each of those faces is removed using an edge collapse operation, which are selected such that they create the least amount of distortion in the mesh. Each edge collapse operation removes two faces and one vertex from the mesh.

5.2.2 Triangle mesh self intersections

Self intersections of triangle meshes are impossible to detect from the properties of the data structure itself. Consequently, each of the other 4 tests listed above can all be fulfilled, even though the mesh contains self intersections. A self intersection describes a condition where triangle facets are penetrating each other at any location, except at their edges. The only robust way to rule out any self intersections is to test each triangle pair against each other. This is demonstrated by the example given in Figure 11. Both images show the same consistent mesh, but vertex $[0\ 0\ -1]^\mathrm{T}$ was moved to $[0\ 0\ 2]^\mathrm{T}$ in the right image. This leads to self intersections in the triangle mesh, which need to be detected (and corrected) using the subsequently described triangle-triangle intersection tests.

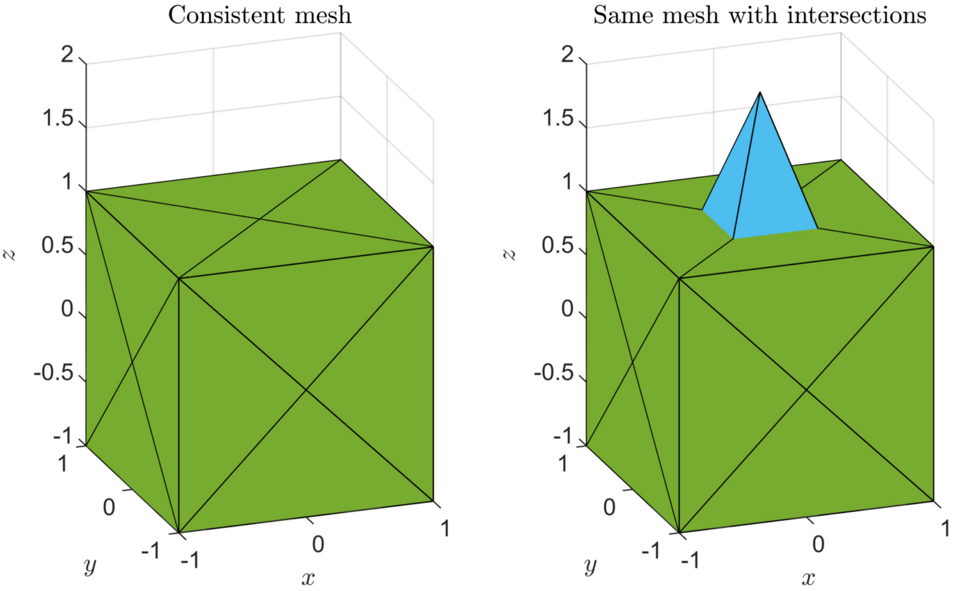

Figure 11: Two unit cubes meshes with a vertex in the centre of each side. Compared to the consistent mesh in the left image, the vertex $[0\ 0\ -1]^{\mathrm{T}}$ was moved to $[0\ 0\ 2]^{\mathrm{T}}$ in the right image which leads to mesh self intersections in the top cube side. The faces attached to that specific vertex were coloured blue for better clarity.

The implemented intersection test is based on the separating axis test, which follows from the separating hyperplane theorem [84]. According to the theorem, for two convex sets A and B either exists separating hyperplane P such that A and B are on different sides of P or A and B are intersecting [84]. A mathematically more rigorous definition including a proof of the theorem can be found in [182]. It can be shown, that if and only if P exists, the orthogonal projection of A and B onto a line L, perpendicular to P, results in two non-overlapping intervals (Figure 12) [84]. In practise it is better to test for separation on an axis instead of a plane, because it is computationally less demanding. In Figure 12, L is a separating axis of A and B, because the mathematical condition (37) is satisfied.

$$\neg(B_{\max} - A_{\min} > 0 \land A_{\max} - B_{\min} > 0) \tag{37}$$

The sub-conditions are intentionally chosen to be strictly greater than zero, because the cases where these intervals have a common value are treated separately, i.e. if two A and B share at least one common point. For all other cases touching of the intervals is regarded as an intersection.

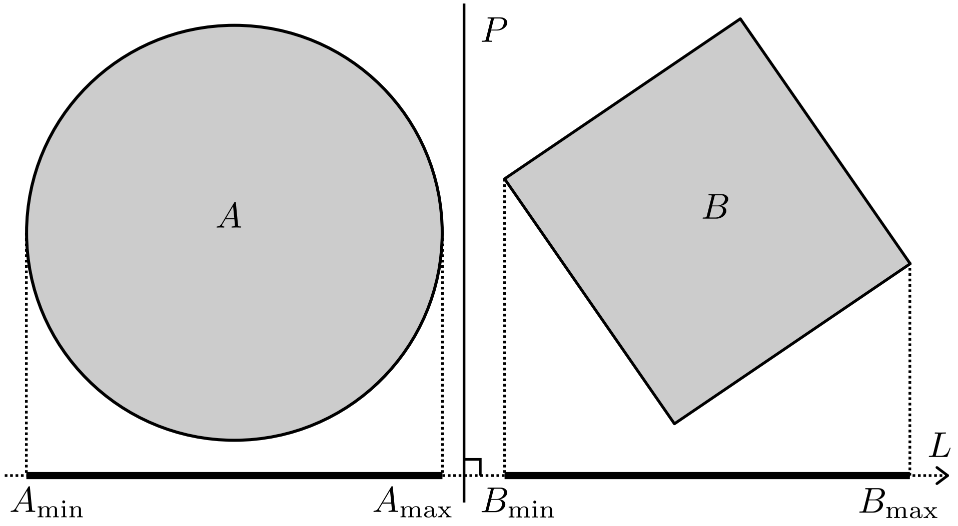

Figure 12: Two convex objects *A* and *B* are separated by a hyperplane *P*. Equivalently, *A* and *B* are non-overlapping in their projection onto the separating axis *L*. Figure redrawn from [84] with supplements.

For two triangles $\triangle_A$ and $\triangle_B$ with face normals $\boldsymbol{n}_{\mathrm{f},A}$ and $\boldsymbol{n}_{\mathrm{f},B}$ and edge vectors $\left\{\boldsymbol{e}_{A,i}\right\}_{i=1}^{3}$ and $\left\{\boldsymbol{e}_{B,j}\right\}_{j=1}^{3}$ at least the following 11 potential separating axes must be tested [84], remembering that the objects are guaranteed to not intersect as soon as one separating axis is found:

- 1 axis parallel to $\boldsymbol{n}_{\mathrm{f},A}$
- 1 axis parallel to $\boldsymbol{n}_{\mathrm{f},B}$
- 9 axes parallel to $\boldsymbol{e}_{A,i} \times \boldsymbol{e}_{B,j} \forall i, j \in \{1, 2, 3\}$

The problem of testing each possible triangle pair of the complete mesh containing n triangles is an "embarrassingly parallel" problem [183] (see chap. 7) with $(n^2-n)/2$ required tests[62] resulting in an algorithmic complexity of $O(n^2)$. Because of the first property the problem is well suited for execution on parallel processor architectures, such as GPUs, but also the robustness of the algorithm needs to be improved because of the potentially reduced floating point accuracy (see chap. 7). Consequently, additional tests have been introduced, specifically targeting intersection tests within a triangle mesh. If triangles $\triangle_A$ and $\triangle_B$ contain common vertices, these cases are treated separately and are thus resolved without explicit separating axis tests. Besides the desired solution "no intersection", the algorithm identifies the following intersection types:

---

[62] The intersection test of two triangles $\triangle_A$ and $\triangle_B$ is commutative.

1. Triangle is corrupted, such that $\|\boldsymbol{r}\| < \epsilon$ (see (29) on p. 50).
2. Triangle is a duplicate (same set of coordinates).
3. Triangle pair intersects with sub-case ”one common vertex”.
4. Triangle pair intersection with sub-case ”two common vertices” (triangles are coplanar).
5. Triangle pair with sub-case ”two common vertices” such that the angle between both face normal vectors is very small[63].
6. Triangle pair with sub-case ”two common vertices” and inconsistent orientation with respect to each other.
7. Triangle pair with true intersection (no separating axis found).

The first two tests are repeated from sec. 5.1 because they offer improved algorithm stability without additional cost. If a triangle pair with an intersection is found, it is in general not easily possible to determine if and which of both triangles could be removed in order to resolve that particular mesh inconsistency. Therefore, all triangles with an intersection condition are removed from the mesh. This can result in holes in the mesh (detected by edges only shared by one triangle), which are then closed again in the subsequent processing step described in the next section 5.2.3.

5.2.3 Volumetric model repair

Model repair describes a process of removing artefacts/errors[64] from a geometric model in order to create an output model conforming to certain quality requirements suitable for further processing [87]. Model repair algorithms can be separated in two groups ”surface-oriented” and ”volumetric” [87]. While solutions for correcting single occurrences of mesh errors can be robustly implemented as ”surface-oriented” algorithms (e.g. filling holes) it can become very difficult to correct mesh areas with a combination of problems. Surface-oriented algorithms, also classified as ”surface repair”, have been studied extensively, but remain elusive in practice, according to [184, 185]. Volumetric methods on the other hand convert the input model into an intermediate volumetric representation (e.g. Cartesian grid, Delaunay triangulation) from which a corrected output model can then be extracted [87].

Instead of trying to address every possible mesh artefact with a suitable ”surface-oriented” algorithm, this work implemented a ”volumetric” repair procedure, which is predominantly based on the work presented in [186].

---

[63] This condition is different from the previous one in the sense that the first one is regarded a mesh error, while the second one represents an unlikely condition in valid measurement data and is therefore also treated as a mesh error.

[64] This means violations of the watertight and connected 2-manifoldness of a mesh.

Here, the authors succeeded in presenting an automatic algorithm for producing volumetric meshes that fully contain the geometry of the input surface model. Their findings are also capable of robustly determining reasonable solutions for artefact affected mesh regions and are therefore summarised below.

At first, the triangle mesh $\mathcal{M}^\dagger$ representing the measurement data is prepared by removing corrupted triangles (see sec. 5.2.1) and self intersections (see sec. 5.2.2)[65]. This results in a triangle mesh with inconsistencies which must be removed in order to acquire the desired watertight 2-manifold representation of the measurement data. The core of the following correction method, which is first introduced for $\mathbb{R}^2$ and then generalised to $\mathbb{R}^3$, is the computation (38) of the scalar "winding number" $w(\boldsymbol{p})$ at coordinates $\boldsymbol{p} = [0\ 0]^\mathrm{T}$ with respect to a curve $\mathcal{C}$ in $\mathbb{R}^2$ [186].

$$w(\boldsymbol{p}) = \frac{1}{2\pi} \oint_{\mathcal{C}} d\theta = \frac{1}{2\pi} \sum_{i=1}^{n} \theta_i \tag{38}$$

The winding number can be described as the number of revolutions a observer placed at $\boldsymbol{p}$ needs to take by following a point moving along $\mathcal{C}$. If $\mathcal{C}$ is closed, $w(\boldsymbol{p})$ is a signed integer, with the sign indicating the direction in which the observer had to rotate. Consequently, the angle θ_i is the signed angle between the two vectors from $\boldsymbol{p}$ to each of two consecutive vertices $\boldsymbol{c}_i$ and $\boldsymbol{c}_{i+1}$ on $\mathcal{C}$. The discretisation of (38) is exact if $\mathcal{C}$ is piecewise linear. The properties are demonstrated in the left image of Figure 13. All points outside of the large square have a winding number of zero. Depending on the orientation of the curve segments (black arrows), an observer either needs two full revolutions (red small square) or zero revolutions (blue small square). In all other places inside the large square, the winding number is one. Because all curves are closed, the winding number shows a discontinuity jump of exactly ± 1 across each boundary. The special properties of the winding number with respect to inside-outside detection are demonstrated in the right image of Figure 13. If the curve is open (bottom), the winding number smoothly changes its value across the missing edge part. The method relies on consistent orientation, which is shown at the top part of the curve, where inconsistent orientation between edge segments leads to faulty inside-outside detection.

---

[65] Also triangle pairs with inconsistent orientation with respect to each other must be removed even though they might represent the correct boundaries of the object, because it is very hard to ensure that a finite number of face flips leads to an overall consistent mesh. Usually, any type of mesh artefacts is caused by "difficult" data and if one type of artefact is detected it is very likely that others might occur in the same mesh as well.

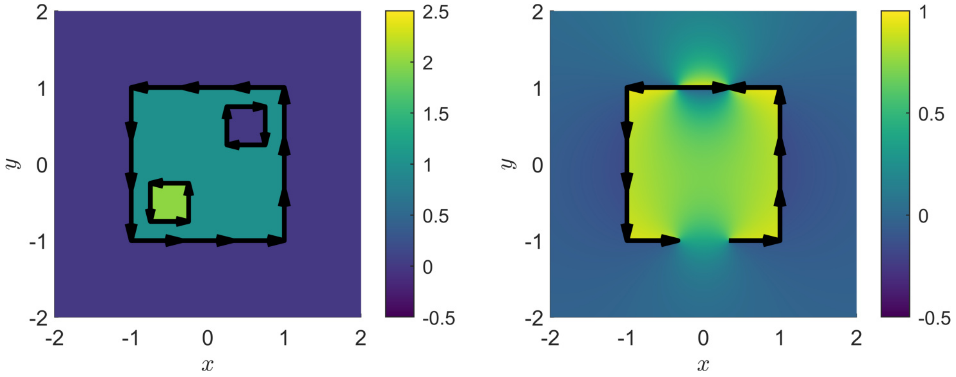

Figure 13: Colour-coded winding numbers $w(\boldsymbol{p})$ for a set of closed curves (left) and a curve with missing parts (right, bottom) and inconsistent orientation (right, top). The black arrows indicate the orientation of the linear curve segments.

The winding number $w(\boldsymbol{p})$ can be generalised to $\mathbb{R}^3$ (39)[66] by replacing the angle θ_i of a line segment in $\mathbb{R}^2$ with the solid angle Ω_f of a triangle face with vertices $\{\boldsymbol{u}, \boldsymbol{v}, \boldsymbol{w}\}$ in $\mathbb{R}^3$ [186][67]. In $\mathbb{R}^3$, the winding number now counts the (signed) total number of times the surface wraps around $\boldsymbol{p}$.

$$\begin{aligned} w(\boldsymbol{p}) &= \frac{1}{4\pi}\sum_{f=1}^{m} \Omega_\text{f}(\boldsymbol{p}) \\ \tan\left(\frac{\Omega_\text{f}(\boldsymbol{p})}{2}\right) &= \frac{\det([\boldsymbol{a}\ \boldsymbol{b}\ \boldsymbol{c}])}{\|\boldsymbol{a}\|\|\boldsymbol{b}\|\|\boldsymbol{c}\| + (\boldsymbol{a}\cdot\boldsymbol{b})\|\boldsymbol{c}\| + (\boldsymbol{b}\cdot\boldsymbol{c})\|\boldsymbol{a}\| + (\boldsymbol{c}\cdot\boldsymbol{a})\|\boldsymbol{b}\|} \\ \text{with:}\quad \boldsymbol{a} = \boldsymbol{u}-\boldsymbol{p},&\quad \boldsymbol{b} = \boldsymbol{v}-\boldsymbol{p},\quad \boldsymbol{c} = \boldsymbol{w}-\boldsymbol{p} \end{aligned} \tag{39}$$

Summarising the above, the winding number is a robust measure for inside-outside detection of a triangle mesh $\mathcal{M}^\dagger$, even if it is affected by artefacts, with the only two conditions being that the mesh exhibits consistent orientation with no self-intersections. The next step is to create a constrained Delaunay triangulation (CDT, see also sec. 2.2.4) of the input mesh $\mathcal{M}^\dagger$. The CDT was computed using TetGen from [188] with a technical publication available at [189]. TetGen requires mesh inputs free of self-intersections, which is ensured by the processing described in sec. 5.2.2. Now it is the goal to segment the "inside" of the mesh from its "outside" by assigning each tetrahedron to one of both regions. Each tetrahedron is classified according to the winding number

---

[66] The notation $[\boldsymbol{a}\ \boldsymbol{b}\ \boldsymbol{c}]$ means the concatenation of $\boldsymbol{a}$, $\boldsymbol{b}$, $\boldsymbol{c}$ resulting in $\boldsymbol{A} \in \mathbb{R}^{3\times3}$. Note that $\det(\boldsymbol{A}) = \det(\boldsymbol{A}^\text{T})$.

[67] Their work was later extended to triangle soups and point clouds by [187].

of its barycentre with respect to the input mesh $\mathcal{M}^\dagger$. The interface separating both sets of tetrahedra represents the sought-after surface. If $\mathcal{M}^\dagger$ represented a watertight 2-manifold free of ambiguities, a simple segmentation approach with a constant winding number threshold of 0.5 would yield the desired segmentation result between the ”inside” and the ”outside” of the resulting triangle mesh. However, that trivial case is not important, because then the whole routine would not be required. Because of the fact that mesh artefacts slightly distort the scalar winding number field for any $\boldsymbol{p}$ (see the smooth colour gradients in the right image of Figure 13), which is exaggerated by other types of artefacts, a more sophisticated segmentation approach based on the graphcut energy was proposed [186]. This problem is solved by addressing the maximum flow problem of the undirected graph constructed from the tetrahedra winding numbers, for technical details refer to [186, 190, 191]. Contrary to the original publication, for this work the algorithm was implemented in an iterative manner such that the weighting for the penalty factors between neighbouring tetrahedra is steadily rising from zero.

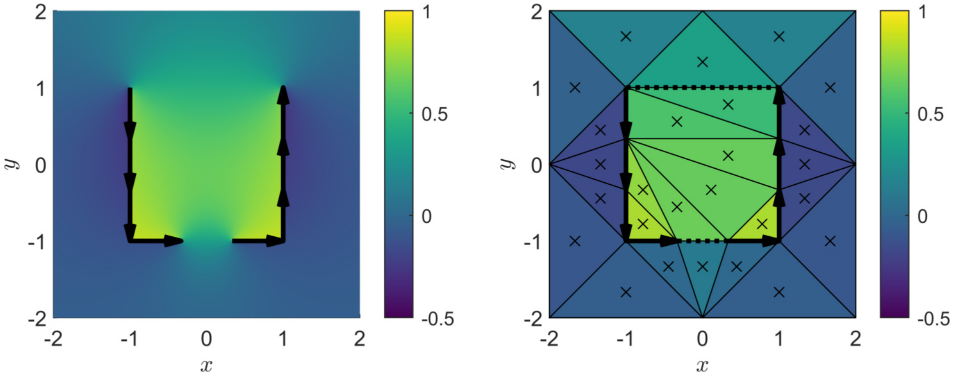

Figure 14: Visualisation of further processing steps, starting from the 2D example in the right image of Figure 13. First, inconsistent edges including the ones before and after are removed (top part of left image). The colour represents the winding number field. Then the constrained Delaunay triangulation (CDT) is constructed with the remaining edges indicated by black arrows (right image). The winding numbers of each triangle is evaluated at their barycentres (marked by black crosses) and each triangle is coloured with respect to that winding number. After that, the graphcut segmentation recovers the missing edges (dotted lines). In this case, the solution is exact with respect to the originating data, because the faulty regions exhibit no curvature.

The result of this approach is a watertight 2-manifold triangle mesh, which consists of the input triangles from $\mathcal{M}^\dagger$ in surface regions without artefacts. An example for 2D is shown in Figure 14. Even in this rather extreme case with one side of the square completely missing, a recovery of the desired edge curve is possible. In regions affected by mesh errors, new triangle facets are added conforming to a Delaunay triangulation. This can alter the input measurement data represented by $\mathcal{M}^\dagger$, however measurement data is considered invalid in erroneous regions (which are usually very small only affecting a few triangles at the same time) and the correction leading to a consistent data representation is therefore considered valid.

In Figure 14 the faulty edge curve is surrounded by another curve which defines the whole domain of the plot. Here, the solution in this thesis deviates from the work of [186] by means that the authors are using the convex hull of the object as outer domain boundary. However, this can lead to problems if mesh regions affected by artefacts are also part of the convex hull. Also, the size of the outer boundary with respect to mesh $\mathcal{M}^\dagger$ (here it is twice as large) and the discretisation of that outer boundary (here it is 2) can impact the quality of the observed results because the winding numbers of the element barycentres are the basis for the graph-cut segmentation procedure.

In the following it is expected that all measurement data represented by a triangle mesh are free of mesh artefacts and therefore represents a watertight 2-manifold geometry.

5.3 Distance metrics between two triangle meshes

The spatially discrete metrological descriptors are based on the similarity of geometries represented by triangle meshes. This section gives a technical description of the distance metrics (also called sampling strategy) used within the framework. The different sampling methods were chosen with respect to the following design principles:

- The sampling is conducted between two geometries, both represented by artefact-free triangle meshes. One of the geometries is the sampling start geometry $\mathcal{S}$ and the other is designated the target geometry $\mathcal{T}$.
- Both geometries are expected to be transferred into a common coordinate system, such that they ”lie on top of each other”. This process is called registration with detailed descriptions available in sec. 5.6.
- The sampling results as the local distance between both meshes are represented by vectors $\boldsymbol{d}_i$, which begin at a sampling start vertex $\boldsymbol{s}_i$ on $\mathcal{S}$ and end at an associated hit location $\boldsymbol{h}_i$ on the target geometry $\mathcal{T}$. That point is not required to represent a triangle edge vertex on the target surface, it can also be located anywhere on a triangle face, depending on which specific distance metric is applied.
- All $\boldsymbol{s}_i$ are represented by triangle edge points of $\mathcal{S}$. The reasons for this are that triangle meshes can be constructed without additional computation error at their edge vertices with respect to another geometry, even if this

underlying geometry exhibits local curvature (see sec. 5.1). The other reason is that visualisation methods, which are a very important aspect of the spatially discrete metrological descriptor framework, work best if additional colour information is either given per face or per vertex.

In the following the notation $i \in I = \{1, ..., N_{\mathcal{S},\mathrm{v}}\}$ and $j \in J = \{1, ..., N_{\mathcal{T},\mathrm{v}}\}$ with $N_{\mathcal{S},\mathrm{v}}$ and $N_{\mathcal{T},\mathrm{v}}$ equalling the number of triangle edge vertices in $\mathcal{S}$ and $\mathcal{T}$, respectively. The initial situation for calculating the local distance vectors $\boldsymbol{d}_i$ for each $\{\boldsymbol{s}_i\}_{i=1}^{N_{\mathcal{S},\mathrm{v}}}$ of the start geometry $\mathcal{S}$ with respect to the target geometry $\mathcal{T}$ described by $\{\boldsymbol{t}_j\}_{j=1}^{N_{\mathcal{T},\mathrm{v}}}$ is visualised in Figure 15. Their respective vertex normal vectors are $\{\boldsymbol{n}_{\mathcal{S},\mathrm{v},i}\}_{i=1}^{N_{\mathcal{S},\mathrm{v}}}$ and $\{\boldsymbol{n}_{\mathcal{T},\mathrm{v},j}\}_{j=1}^{N_{\mathcal{T},\mathrm{v}}}$. Both geometries represent the same object, but originate from different sources (e.g. nominal geometry and measurement result) and thus slightly deviate locally (which is exaggerated

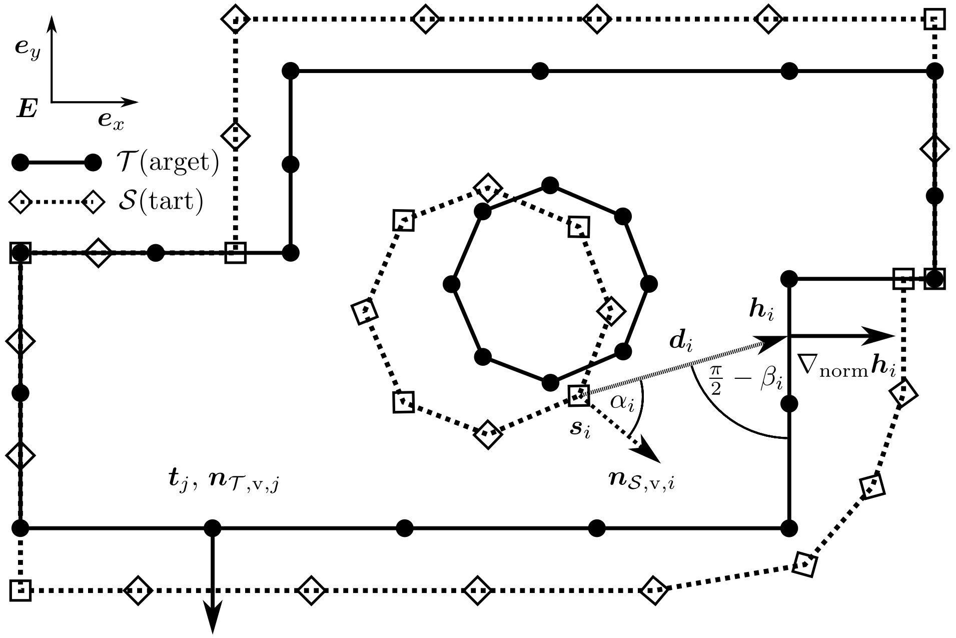

Figure 15: The image shows the contours of a sampling start mesh $\mathcal{S}$ (dashed line) and a target mesh $\mathcal{T}$ (solid line), which are both geometrically aligned in a common coordinate system $\boldsymbol{E}$. Both $\mathcal{S}$ and $\mathcal{T}$ represent the same object, but with small local differences, which are exaggerated here for a clearer visualisation. Both meshes are each characterised by edge points $\{\boldsymbol{s}_i\}_{i=1}^{N_{\mathcal{S},\mathrm{v}}}$ and $\{\boldsymbol{t}_j\}_{j=1}^{N_{\mathcal{T},\mathrm{v}}}$ with associated vertex normal vectors $\{\boldsymbol{n}_{\mathcal{S},\mathrm{v},i}\}_{i=1}^{N_{\mathcal{S},\mathrm{v}}}$ and $\{\boldsymbol{n}_{\mathcal{T},\mathrm{v},j}\}_{j=1}^{N_{\mathcal{T},\mathrm{v}}}$, respectively. A fictional hit location $\boldsymbol{h}_i$ associated with sampling start point $\boldsymbol{s}_i$ can be anywhere on $\mathcal{T}$ (and is deliberately placed at a non-intuitive location in this example), depending on the actual distance metric, with associated local normal vector $\nabla_{\mathrm{norm}}\boldsymbol{h}_i$.

in Figure 15 for improved clarity). The subsequent evaluations assume, that both $\mathcal{S}$ and $\mathcal{T}$ are aligned in a common coordinate system $\boldsymbol{E}$ as a result of previous registration (see sec. 5.6). Dependent on the concrete distance metric, a hit location $\boldsymbol{h}_i$ is determined for each $\boldsymbol{s}_i$.

The result of the sampling is a local (signed) distance measurement l_i associated with $\boldsymbol{s}_i$ as a function $\mathcal{F}$ of $\boldsymbol{d}_i$ (40).

$$l_i = \mathcal{F}(\boldsymbol{d}_i) \tag{40}$$

The angle between $\boldsymbol{d}_i$ and $\boldsymbol{n}_{\mathcal{S},\mathrm{v},i}$ is denoted α_i (41). The absolute value makes the resulting angle independent of the position of $\boldsymbol{h}_i$ relative to $\boldsymbol{n}_{\mathcal{S},\mathrm{v},i}$.

$$\alpha_i = \arccos\left(\left|\frac{\boldsymbol{d}_i \cdot \boldsymbol{n}_{\mathcal{S},\mathrm{v},i}}{\|\boldsymbol{d}_i\|}\right|\right) \tag{41}$$

Similarly, the angle β_i can be calculated between $\boldsymbol{d}_i$ and the local surface gradient at the hit location $\nabla_{\mathrm{norm}}\boldsymbol{h}_i$ (42). The exact normal vector depends on the distance metric and on which part of a triangle $\boldsymbol{h}_i$ is associated with. Thus, the value range of both α_i and β_i is $\left[0, \frac{\pi}{2}\right]$.

$$\beta_i = \arccos\left(\left|\frac{\boldsymbol{d}_i \cdot \nabla_{\mathrm{norm}}\boldsymbol{h}_i}{\|\boldsymbol{d}_i\|}\right|\right) \tag{42}$$

The surface normal vector of a hit coordinate on the target geometry $\mathcal{T}$ is equivalent to its normalised local gradient $\nabla_{\mathrm{norm}}\boldsymbol{h}_i$. Depending on the used distance metric, the calculated coordinate $\boldsymbol{h}_i$ on the target geometry $\mathcal{T}$, can either be a triangle vertex $\boldsymbol{t}_j$, or on a triangle edge, or inside a triangle face. In the first case $\nabla\boldsymbol{h}_i$ is equal to the vertex normal vector of $\boldsymbol{t}_j$. In the second case, $\nabla_{\mathrm{norm}}\boldsymbol{h}_i$ is determined by the weighted average of the vertex normal vectors of the hit triangle edge, depending on where the hit location is with respect to both vertices. In the third case (hit location is inside a triangle face), the normal vectors of the three triangle vertices $\boldsymbol{a}$, $\boldsymbol{b}$ and $\boldsymbol{c}$ are weighted according to the barycentric coordinates u, v, w of the hit coordinate $\boldsymbol{h}_i$. Barycentric coordinates in a triangle fulfil (43) [82, 88]. This approach gives continuous surface normal vectors, even though the positions are discontinuous (except for flat regions). Consequently, this results in slightly richer information provided by β_i and the distance metric SDHP (see sec. 5.3.4).

$$\begin{aligned} u + v + w &= 1 \\ \boldsymbol{h}_i &= u\boldsymbol{a} + v\boldsymbol{b} + w\boldsymbol{c} \end{aligned} \tag{43}$$

In the following subsections, different distance metrics are presented. A comparison of the results obtained from different distance metrics based on real world data is presented in sec. 6.2. From that perspective, the shortest distance metric (see section after next) is regarded as the most versatile and therefore regarded as the default choice for the spatially discrete metrological descriptor framework.

5.3.1 Closest edge point (CEP)

The mathematically simplest approach is to match the closest $\boldsymbol{t}_j$ for every $\boldsymbol{s}_i$, with respect to their shortest Euclidean distance, such that $\boldsymbol{d}_i$ can be determined by (44).

$$\begin{aligned} &\underset{x \in \{1,\ldots,N_{\mathcal{T},\mathrm{v}}\}}{\arg\min} \quad \|\boldsymbol{t}_x - \boldsymbol{s}_i\| \\ &\boldsymbol{d}_i = \boldsymbol{t}_x - \boldsymbol{s}_i \end{aligned} \tag{44}$$

The principle of "**C**losest **E**dge **P**oint sampling" (CEP) is visualised in Figure 16, where $\boldsymbol{d}_i$ is drawn for exemplary $\boldsymbol{s}_i$ as $\boldsymbol{d}_1$, $\boldsymbol{d}_2$, $\boldsymbol{d}_3$. For each $\boldsymbol{s}_i$ there is only one[68] $\boldsymbol{t}_j$ on or inside its circle with radius $\|\boldsymbol{d}_i\|$. By design, that kind of sampling is ignoring the local connectivity information between $\boldsymbol{t}_j$ (the triangulation), which leads to increased distance values for these sampling points (e.g. marker $\boxed{1}$ in Figure 16). The optimisation stated in (44) represents a special case of the well-known k-nearest neighbours problem (knn-search), with $k = 1$, for which efficient algorithms with complexity $O(kn\log(n))$ exist [192]. That kind of sampling is very robust, as it is always possible to find a nearest neighbour if the target geometry is non-empty. However, depending on the triangle sizes of the target geometry $\mathcal{T}$, the method can be rather inaccurate locally, e.g. for $\boldsymbol{d}_1$, $\boldsymbol{d}_2$ as well as at marker $\boxed{1}$ in Figure 16, because it can lead to large $\boldsymbol{d}_i$ even though the triangle meshes are very close to each other in that region. Furthermore, it is possible, that several $\boldsymbol{s}_i$ match the same coordinate $\boldsymbol{t}_j$, resulting in a high local correlation between the results. If $\boldsymbol{s}_i \in \{\boldsymbol{t}_j\}_{j=1}^{N_{\mathcal{T},\mathrm{v}}}$ (see marker $\boxed{3}$ in Figure 16) then $\|\boldsymbol{d}_i\| = 0$. In a special edge case, where the triangle sizes are much smaller for the target surface compared to the start surface, that kind of sampling represents a robust method for an efficient determination of the spatially discrete metrological descriptors because of its simple algorithm structure. Also, the method is well-suited for time-critical applications. In general however, this method should be avoided, compared to other methods discussed further below, especially if accurate results are required. This assessment was confirmed by real data comparison presented in sec. 6.2.

---

[68] Extremely unlikely (synthetic) edge cases where several $\|\boldsymbol{d}_i\|$ with equal lengths occur are decided algorithmically by chance such that only one result remains.

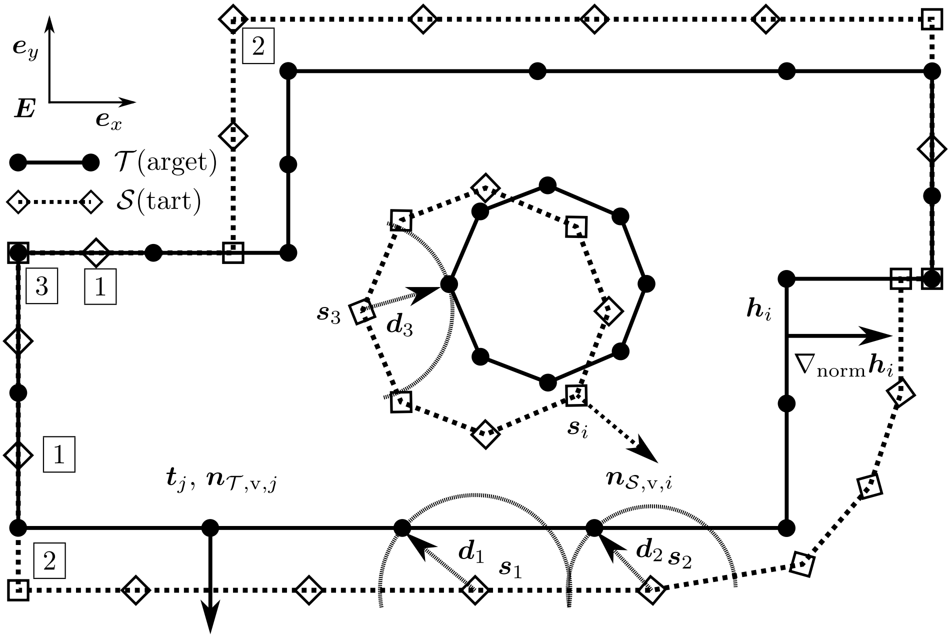

Figure 16: The principle of closest edge point sampling (CEP) is based on a nearest neighbour search. For each $\boldsymbol{s}_i$, only one $\boldsymbol{t}_j$ is on or inside its circle with radius $\|\boldsymbol{d}_i\|$ (examples given $\boldsymbol{d}_1$, $\boldsymbol{d}_2$, $\boldsymbol{d}_3$). The method is very robust because there is always a nearest neighbour to be found. Nonetheless, this method tends to overestimate the distance between $\boldsymbol{s}_i$ and $\mathcal{T}$, depending on the vertex density of $\mathcal{T}$, and especially if $\boldsymbol{s}_i$ lies on the surface of $\mathcal{T}$ (marker $\boxed{1}$), such that $\boldsymbol{s}_i \in T$. The method finds the shortest Euclidean distance from $\boldsymbol{s}_i$ to $\mathcal{T}$ in some cases (marker $\boxed{2}$). The result $\|\boldsymbol{d}_i\| = 0$ is only possible if $\boldsymbol{s}_i \in \{\boldsymbol{t}_j\}_{j=1}^{N_{\mathcal{T},\text{v}}}$ (marker $\boxed{3}$).

Each $\boldsymbol{s}_i$ is associated with a normal vector $\boldsymbol{n}_i$ with $\|\boldsymbol{n}_i\| = 1$ (see sec. 5.1), which is used to determine the sign of l_i according to (45).

$$l_i = \begin{cases} +\|\boldsymbol{d}_i\| & \text{if } \boldsymbol{d}_i \cdot \boldsymbol{n}_i \geq 0 \\ -\|\boldsymbol{d}_i\| & \text{otherwise} \end{cases} \tag{45}$$

The angular parameters α_i and β_i are calculated according to (41) and (42).

5.3.2 Shortest distance (SD)

The second method describing a distance metric between two triangle meshes is called "**S**hortest **D**istance sampling" (SD). It is based on finding the minimum (absolute) distance between each $\boldsymbol{s}_i$ and the target mesh $\mathcal{T}$. As visualised in Figure 17, the circles around each $\boldsymbol{s}_i$ with radius $\|\boldsymbol{d}_i\|$ touch the target ge-

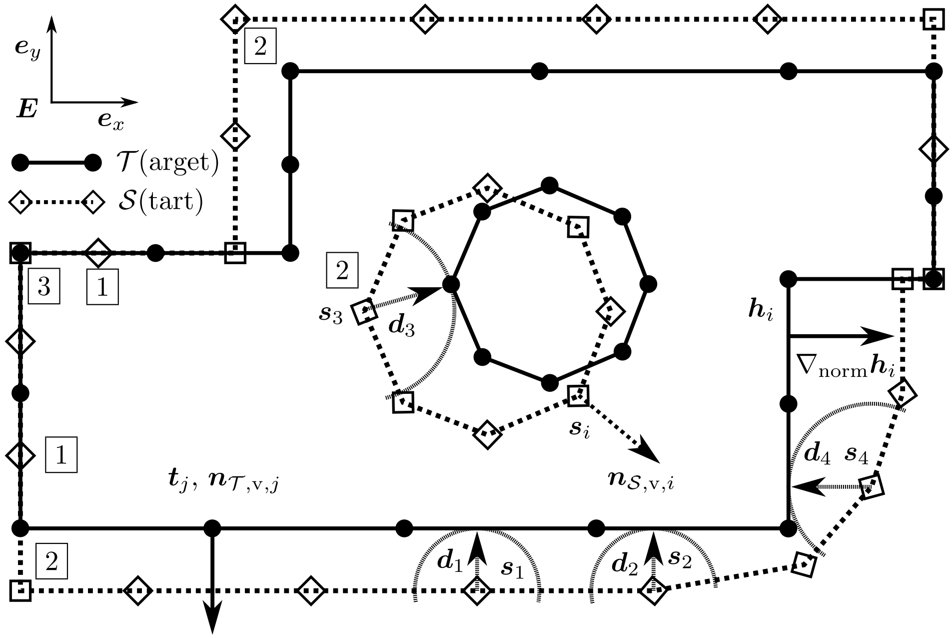

Figure 17: The principle of shortest distance sampling (SD) is to find the closest point on $\mathcal{T}$ with respect to $\boldsymbol{s}_i$. Each circle around $\boldsymbol{s}_i$ with radius $\|\boldsymbol{d}_i\|$ has exactly one touching point with the target mesh $\mathcal{T}$ (see $\boldsymbol{d}_1$, $\boldsymbol{d}_2$, $\boldsymbol{d}_3$, $\boldsymbol{d}_4$). That sought-after point can be either part of a facet, an edge or be equal to a triangle vertex. Cases $\boxed{1}$ are handled better, compared to CEP sampling, because their result is $\|\boldsymbol{d}_i\| = 0$. Cases $\boxed{2}$ with $\boldsymbol{h}_i \in \{\boldsymbol{t}_j\}_{j=1}^{N_{\mathcal{T},\mathrm{v}}}$ produce equal results.

ometry $\mathcal{T}$ at exactly one[69] point. Compared to CEP sampling (sec. 5.3.1) this method considers the complete triangle surface as potential target points and is therefore independent of the spatial discretisation of $\mathcal{T}$, which is a big advantage compared to CEP sampling. The method is guaranteed to produce a lower bound for the derived (conventional) metrological descriptors (see sec. 5.7). This however comes at the cost of increased computational demand. In this work, the algorithm described in [84] was implemented and is therefore briefly described in the following, however alternative approaches exist, e.g. [82]. The closest point on a triangle with edge points $\boldsymbol{a}$, $\boldsymbol{b}$ and $\boldsymbol{c}$ of $\mathcal{T}$ ($\triangle^{\mathcal{T}}_{\boldsymbol{abc}}$) with respect to $\boldsymbol{s}_i$ is calculated by first determining the Voronoi[70] regions of $\triangle^{\mathcal{T}}_{\boldsymbol{abc}}$ (see Figure 18) which a sampling start point $\boldsymbol{s}_i$ is associated with [84]. Therefore, depending on in which of the seven Voronoi regions of

---

[69] Comparable to the CEP distance metric rare edge cases with multiple results are resolved by chance.

[70] Voronoi diagrams are one of the most fundamental data structures in computational geometry. Given some number of points in a plane, the corresponding Voronoi diagram divides that plane such that each point is associated with the region closest to it. [193, 194]

$\triangle^{\mathcal{T}}_{\boldsymbol{abc}}$ $\boldsymbol{s}_i$ is positioned, the sought-after closest point $\boldsymbol{p}_k$ (one $\boldsymbol{p}_k$ for each of the triangles in the target mesh) to $\boldsymbol{s}_i$ on that triangle can either be one of the edge points $\boldsymbol{a}$, $\boldsymbol{b}$, $\boldsymbol{c}$, or located on one of the edges $\boldsymbol{a} \rightarrow \boldsymbol{b}$, $\boldsymbol{a} \rightarrow \boldsymbol{c}$, $\boldsymbol{b} \rightarrow \boldsymbol{c}$ or lie inside $\triangle^{\mathcal{T}}_{\boldsymbol{abc}}$. Therefore, the Voronoi region of $\boldsymbol{s}_i$ is calculated by (46), with $\boldsymbol{n}_{\mathrm{f}}$ denoting the face normal vector of $\triangle^{\mathcal{T}}_{\boldsymbol{abc}}$ (see Figure 18) [84].

$$\text{”?”} = \begin{cases} \boxed{1} & \text{if } \overrightarrow{\boldsymbol{as}_i} \cdot \overrightarrow{\boldsymbol{ab}} \leq 0 \wedge \overrightarrow{\boldsymbol{as}_i} \cdot \overrightarrow{\boldsymbol{ac}} \leq 0 \\ \boxed{2} & \text{if } \overrightarrow{\boldsymbol{bs}_i} \cdot \overrightarrow{\boldsymbol{ba}} \leq 0 \wedge \overrightarrow{\boldsymbol{bs}_i} \cdot \overrightarrow{\boldsymbol{bc}} \leq 0 \\ \boxed{3} & \text{if } \overrightarrow{\boldsymbol{cs}_i} \cdot \overrightarrow{\boldsymbol{cb}} \leq 0 \wedge \overrightarrow{\boldsymbol{cs}_i} \cdot \overrightarrow{\boldsymbol{ca}} \leq 0 \\ \boxed{4} & \text{if } \boldsymbol{n}_{\mathrm{f}} \cdot (\overrightarrow{\boldsymbol{s}_i\boldsymbol{a}} \times \overrightarrow{\boldsymbol{s}_i\boldsymbol{b}}) \leq 0 \wedge \overrightarrow{\boldsymbol{as}_i} \cdot \overrightarrow{\boldsymbol{ab}} \geq 0 \wedge \overrightarrow{\boldsymbol{bs}_i} \cdot \overrightarrow{\boldsymbol{ba}} \geq 0 \\ \boxed{5} & \text{if } \boldsymbol{n}_{\mathrm{f}} \cdot (\overrightarrow{\boldsymbol{s}_i\boldsymbol{b}} \times \overrightarrow{\boldsymbol{s}_i\boldsymbol{c}}) \leq 0 \wedge \overrightarrow{\boldsymbol{bs}_i} \cdot \overrightarrow{\boldsymbol{bc}} \geq 0 \wedge \overrightarrow{\boldsymbol{cs}_i} \cdot \overrightarrow{\boldsymbol{cb}} \geq 0 \\ \boxed{6} & \text{if } \boldsymbol{n}_{\mathrm{f}} \cdot (\overrightarrow{\boldsymbol{s}_i\boldsymbol{c}} \times \overrightarrow{\boldsymbol{s}_i\boldsymbol{a}}) \leq 0 \wedge \overrightarrow{\boldsymbol{cs}_i} \cdot \overrightarrow{\boldsymbol{ca}} \geq 0 \wedge \overrightarrow{\boldsymbol{as}_i} \cdot \overrightarrow{\boldsymbol{ac}} \geq 0 \\ \boxed{7} & \text{otherwise} \end{cases} \tag{46}$$

$$\text{with} \quad \overrightarrow{\boldsymbol{qg}} \equiv \boldsymbol{g} - \boldsymbol{q} \quad \text{and} \quad \boldsymbol{n}_{\mathrm{f}} = \overrightarrow{\boldsymbol{ab}} \times \overrightarrow{\boldsymbol{ac}}$$

The Voronoi regions extend to ±∞ in the direction of $\boldsymbol{n}_{\mathrm{f}}$. Once the associated Voronoi region for $\boldsymbol{s}_i$ is determined, the coordinates of points $\{\boldsymbol{p}_k\}_{k=1}^{N_{\mathcal{T},\mathrm{f}}}$, which are closest to that $\boldsymbol{s}_i$ for each of the $N_{\mathcal{T},\mathrm{f}}$ triangles of $\mathcal{T}$ can be com-

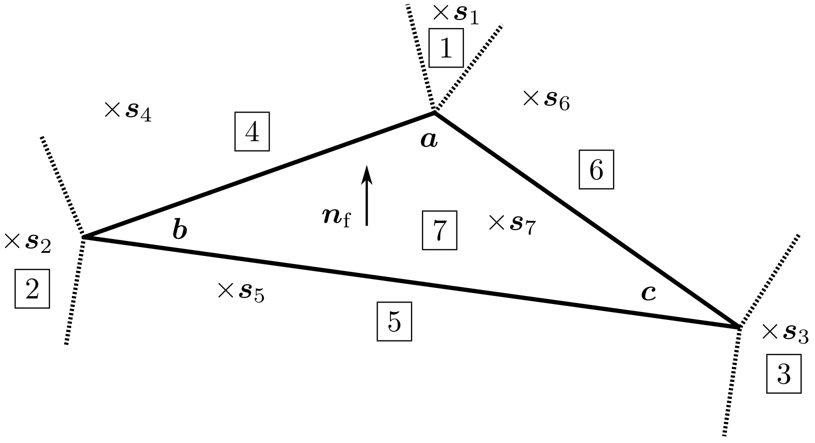

Figure 18: For a triangle $\triangle^{\mathcal{T}}_{\boldsymbol{abc}}$ (edge points $\boldsymbol{a}$, $\boldsymbol{b}$, $\boldsymbol{c}$) 7 Voronoi regions can be constructed. Depending on in which of the Voronoi regions a point $\boldsymbol{s}_i$ (exemplary $\boldsymbol{s}_k$ bing placed inside regions $\boxed{\mathrm{k}}$ with $k \in \{1, 2, \ldots, 7\}$) lies, it is determined which triangle element (edge point, edge or face) is closest to $\boldsymbol{s}_i$ (46). This computation step is required for the shortest distance calculation between $\boldsymbol{s}_i$ and $\triangle^{\mathcal{T}}_{\boldsymbol{abc}}$ in order to realise SD sampling. Dashed lines indicate the boarders of Voronoi regions $\boxed{\mathrm{k}}$, $k \in \{1, \ldots, 7\}$ which extend to ±∞ in the direction of $\boldsymbol{n}_{\mathrm{f}}$ and away from their individual start points $\boldsymbol{a}$, $\boldsymbol{b}$, $\boldsymbol{c}$, respectively.

puted. Similar to (44), the search for the solutions $\boldsymbol{d}_i$ can be formulated as an optimisation problem (47).

$$\begin{aligned} &\underset{x \in \{1,\dots,N_{\mathcal{T},\mathrm{f}}\}}{\arg\min} \quad \|\boldsymbol{p}_x - \boldsymbol{s}_i\| \\ &\boldsymbol{d}_i = \boldsymbol{p}_x - \boldsymbol{s}_i \end{aligned} \tag{47}$$

The (signed) distances l_i are computed according to (45). The intersection angle α_i is computed according to (41). The second angle β_i is depended on the type of triangle component representing the target for the shortest distance calculation. It is either computed (42) between $\boldsymbol{d}_i$ and the vertex normal vector (target is triangle vertex), or the edge vector (target is triangle edge) or the face normal vector (target is triangle face). Here, continuous normal vectors are used as described above.

SD sampling is by definition determining the shortest distance for all $\boldsymbol{s}_i$ with respect to $\mathcal{T}$ and is considering the complete surface while doing so. This kind of sampling shows to be very robust for the same reasons as for CEP sampling because the sought-after distances always[71] exist. Its computation is solely based on vector calculations (47) for which efficient compute solutions can be implemented (see chap. 7).

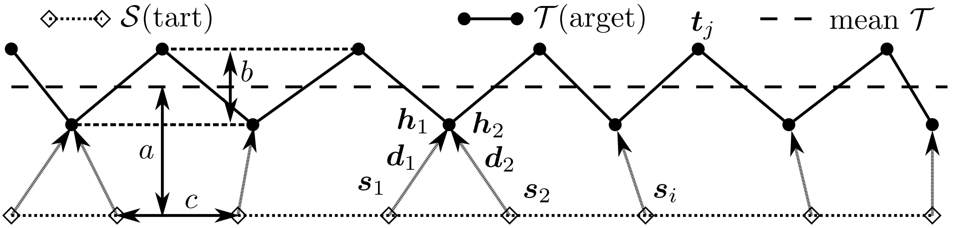

Figure 19: Sampling of $\mathcal{T}$ with large peak-to-valley heights b can lead to a systematic underestimation of $\|\boldsymbol{d}_i\|$ by about $\frac{b}{2}$ if the SD distance metric is used. The effect is magnified for larger distances a between $\mathcal{S}$ and the mean target surface profile. The SD distance metric allows for solutions $\boldsymbol{h}_i \in \{\boldsymbol{t}_j\}_{j=1}^{N_{\mathcal{T},\mathrm{v}}}$.

Nonetheless, this method can also show suboptimal results in certain edge cases involving spatial frequencies (waviness / roughness) of $\mathcal{T}$ similar to those of $\mathcal{S}$, as shown in Figure 19. The SD distance metric by design tends to capture the surface features closest to each $\boldsymbol{s}_i$, which could underestimate $\|\boldsymbol{d}_i\|$ by about $\frac{b}{2}$. This is especially the case for increased peak-to-valley heights b of $\mathcal{T}$ with at the same time increasing ratio $\frac{a}{b}$. This kind of behaviour can not be improved by increased point density c of $\mathcal{S}$, which is described in sec. 5.4,

---

[71] Assuming non-empty $\mathcal{T}$.

but can relatively easily be detected by increased scatter of α_i (see sec. 5.7) in case c is large enough. Alternatively, the vertex normal vector (VNV) distance metric (see sec. 5.3.5) can be applied. On the other hand, the effect is less problematic if at the same time $a \ll b$.

5.3.3 Shortest distance from the plane defined by the sampling start point and its vertex normal vector (SDSP)

The SD sampling method (sec. 5.3.2), results in distance vectors $\boldsymbol{d}_i$ as defined in (47). Two alternative sampling methods derived from SD sampling are described in this and the following section, respectively. The first one is set up by projecting $\boldsymbol{d}_i$ from (47) onto the vertex normal vector $\boldsymbol{n}_{\mathcal{S},\mathrm{v},i}$ associated with $\boldsymbol{s}_i$ (48). This effectively calculates the distance of the found hit location on the target mesh to the plane defined by $\boldsymbol{n}_{\mathcal{S},\mathrm{v},i}$ and containing the point $\boldsymbol{s}_i$ (Figure 20).

$$\begin{aligned} l_i &= \boldsymbol{d}_i \cdot \boldsymbol{n}_{\mathcal{S},\mathrm{v},i} \\ \boldsymbol{d}_{i,\mathrm{SDSP}} &= l_i \boldsymbol{n}_{\mathcal{S},\mathrm{v},i} \end{aligned} \tag{48}$$

However, the coordinate $\boldsymbol{s}_i + \boldsymbol{d}_{i,\mathrm{SDSP}}$ is not guaranteed to exist on the target

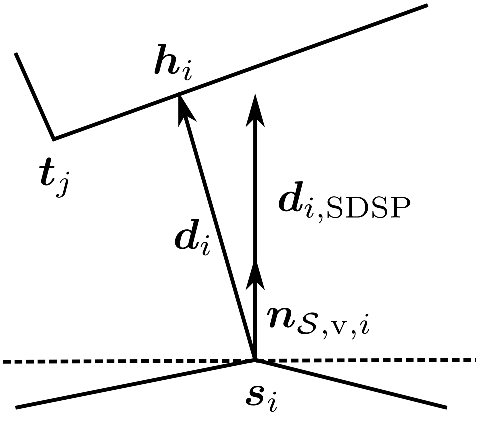

Figure 20: Geometrical visualisation of the distance metric SDSP. The vector $\boldsymbol{d}_{i,\mathrm{SDSP}}$ describes the shortest distance from $\boldsymbol{s}_i$ to $\boldsymbol{h}_i$ in the direction of $\boldsymbol{n}_{\mathcal{S},\mathrm{v},i}$. The underlying SD distance metric allows for solutions $\boldsymbol{h}_i \in \{\boldsymbol{t}_j\}_{j=1}^{N_{\mathcal{T},\mathrm{v}}}$ but $\boldsymbol{h}_i$ can also lie anywhere on a triangle, like in this visualisation example.

mesh $\mathcal{T}$, as it is the case for the previously introduced sampling methods. Nonetheless, this can be a helpful measure in some cases, as it ultimately determines l_i in the direction of $\boldsymbol{n}_{\mathcal{S},\mathrm{v},i}$, which can improve the comparability when sampling multiple geometries, because it is not affected by lateral components of $\boldsymbol{d}_i$ (see sec. 5.7 for more details). Furthermore, from (48) directly follows that $l_i(\text{SDSP}) \leq l_i(\text{SD})$ is always satisfied. The intersection angle β_i with the target surface is determined the same way as for SD sampling (42). The angle α_i between $\boldsymbol{n}_{\mathcal{S},\text{v},i}$ and $\boldsymbol{d}_{i,\text{SDSP}}$ is 0° by design (41).

This alternative sampling strategy measuring the shortest distance in the direction of the plane defined by $\boldsymbol{s}_i$ and its vertex normal vector $\boldsymbol{n}_{\mathcal{S},\text{v},i}$ is abbreviated as SDSP (**S**hortest **D**istance from **S**tart **P**lane).

5.3.4 Shortest distance to plane defined by the hit coordinate and its normalised gradient (SDHP)

The second alternative sampling method derived from SD sampling is set up similarly to SDSP sampling. However, instead of projecting the distance vector $\boldsymbol{d}_i$ onto the vertex normal vector $\boldsymbol{n}_{\mathcal{S},\text{v},i}$ of the start coordinate $\boldsymbol{s}_i$ (48), $\boldsymbol{d}_i$ is projected onto the surface normal vector $\nabla_{\text{norm}}\boldsymbol{h}_i$ of the hit location $\boldsymbol{h}_i$. This effectively measures the distance from $\boldsymbol{s}_i$ to the plane defined by the target coordinate $\boldsymbol{h}_i$ and $\nabla_{\text{norm}}\boldsymbol{h}_i$ (49) with $\boldsymbol{h}_i = \boldsymbol{s}_i + \boldsymbol{d}_i$ (see Figure 21).

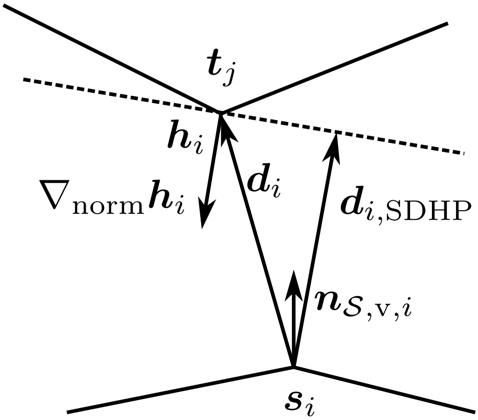

Figure 21: Geometrical visualisation of the distance metric SDHP. The vector $\boldsymbol{d}_{i,\text{SDHP}}$ describes the shortest distance from $\boldsymbol{s}_i$ to the plane defined by $\boldsymbol{h}_i$ and $\nabla_{\text{norm}}\boldsymbol{h}_i$. The underlying SD distance metric allows for solutions $\boldsymbol{h}_i \in \{\boldsymbol{t}_j\}_{j=1}^{N_{\mathcal{T},\text{v}}}$, like in this visualisation example, but $\boldsymbol{h}_i$ can also lie anywhere on a triangle, as shown in sec. 5.3.2.

$$\boldsymbol{d}_{i,\text{SDHP}} = (\boldsymbol{d}_i \cdot \nabla_{\text{norm}}\boldsymbol{h}_i)\nabla_{\text{norm}}\boldsymbol{h}_i \tag{49}$$

The parameter l_i is calculated according to (45). The method is referred to as SDHP (**S**hortest **D**istance to **H**it **P**lane). Importantly, the coordinate $\boldsymbol{s}_i + \boldsymbol{d}_{i,\text{SDHP}}$ is not guaranteed to lie on $\mathcal{T}$, which also applies for SDSP (see section above). The difference in results obtained between SD and SDHP can be very subtle, depending on the texture of the target geometry. The rougher that surface is, the larger is the expected difference in calculated hit distances because of the influence of the surface angle at the target location. The continuous interpolation of the local surface gradient from the surrounding vertices is described in sec. 5.3.2.

5.3.5 Vertex normal vector (VNV)

The fifth sampling strategy is based on a true orthogonal distance measurement from each $\boldsymbol{s}_i$ to the target mesh $\mathcal{T}$. The orthogonality is reflected by the vertex normal vector of $\boldsymbol{s}_i$, $\boldsymbol{n}_{\mathcal{S},\mathrm{v},i}$. The principle is illustrated in Figure 22. Mathematically, this problem can be formulated with a ray-triangle intersection algorithm. Each $\boldsymbol{s}_i$ defines a ray in both directions of its vertex normal vector $\boldsymbol{n}_{\mathcal{S},\mathrm{v},i}$. This ray is tested against all triangles, resulting in $k \in \{0, 2, 4, \dots\}$

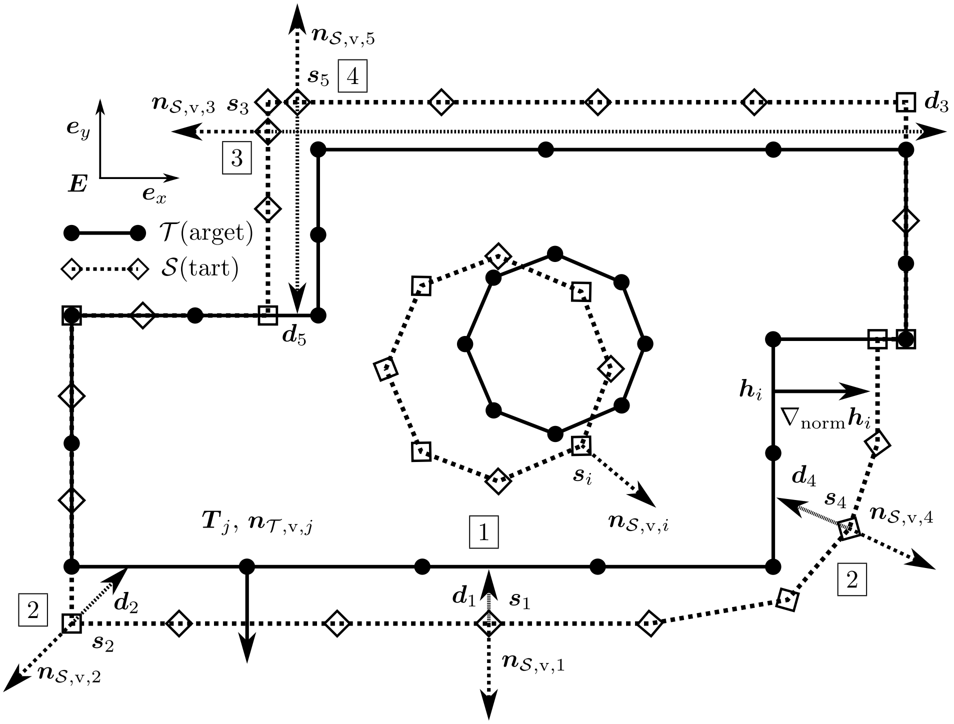

Figure 22: Vertex normal vector sampling is based on solving the ray-triangle intersection problem from $\boldsymbol{s}_i$ in both directions of $\boldsymbol{n}_{\mathcal{S},\mathrm{v},i}$ and selecting the shortest intersection distance of all possible intersections. The method represents a true orthogonal measurement with respect to $\boldsymbol{s}_i$. The image shows several exemplary solutions $\boldsymbol{d}_1$, $\boldsymbol{d}_2$, $\boldsymbol{d}_3 = \emptyset$ (it misses $\mathcal{T}$), $\boldsymbol{d}_4$, $\boldsymbol{d}_5$. One downside are the results associated with edge regions where either potentially increased distances are produced which could overestimate the calculated measurement errors ($\boxed{2}$, $\boxed{4}$), or no intersection is found at all ($\boxed{3}$).

intersections[72] of that ray with the target geometry $\mathcal{T}$, given $\mathcal{T}$ conforms to a closed 2-manifold, as described in sec. 5.2. The closest intersection point to $\boldsymbol{s}_i$ is the sought-after result. In this thesis, the popular ray-triangle intersection algorithm [195] of Tomas Möller and Ben Trumbore was implemented although numerous alternative approaches have been proposed [84, 196–199], because ray-tracing is a key problem in computer graphics [200][73].

The intersection between a ray $\boldsymbol{s}_i + L\boldsymbol{n}_{\mathcal{S},\mathrm{v},i}$ and a triangle $\triangle^{\mathcal{T}}_{\boldsymbol{abc}}$ in barycentric coordinates [201] u, v with $u \geq 0$, $v \geq 0$ and $u + v \leq 1$ is formulated as (50) [195]:

$$\boldsymbol{s}_i + L\boldsymbol{n}_{\mathcal{S},\mathrm{v},i} = (1 - u - v)\boldsymbol{a} + u\boldsymbol{b} + v\boldsymbol{c} \tag{50}$$

Solving the equation for the searched parameters L, u and v yields (51) [195]:

$$\begin{bmatrix} L \\ u \\ v \end{bmatrix} = \frac{1}{(\boldsymbol{n}_{\mathcal{S},\mathrm{v},i} \times (\boldsymbol{c} - \boldsymbol{a})) \cdot (\boldsymbol{b} - \boldsymbol{a})} \begin{bmatrix} ((\boldsymbol{s}_i - \boldsymbol{a}) \times (\boldsymbol{b} - \boldsymbol{a})) \cdot (\boldsymbol{c} - \boldsymbol{a}) \\ (\boldsymbol{n}_{\mathcal{S},\mathrm{v},i} \times (\boldsymbol{c} - \boldsymbol{a})) \cdot (\boldsymbol{s}_i - \boldsymbol{a}) \\ ((\boldsymbol{s}_i - \boldsymbol{a}) \times (\boldsymbol{b} - \boldsymbol{a})) \cdot \boldsymbol{n}_{\mathcal{S},\mathrm{v},i} \end{bmatrix} \tag{51}$$

Triangle intersections are only valid if the intersection is within the triangle according to the barycentric coordinates u and v (52).

$$L = \begin{cases} L & u \geq 0 \wedge v \geq 0 \wedge u + v \leq 1 \\ \infty & \text{otherwise} \end{cases} \tag{52}$$

$$\begin{aligned} &\underset{x \in \{1,\dots,N_{\mathcal{T},\mathrm{f}}\}}{\arg\min} \quad |L_x| \\ &l_i = L_x \\ &\boldsymbol{d}_i = l_i \boldsymbol{n}_{\mathcal{S},\mathrm{v},i} \end{aligned} \tag{53}$$

The sought-after intersection information is determined by testing the ray starting at $\boldsymbol{s}_i$ against all triangles in $\mathcal{T}$ and selecting the intersection with the smallest $|L_x|$ (53). The intersection angle α_i is always 0° by definition and β_i

---

[72] For every instance an infinite ray penetrates the hull of an object it also must leave it again at some point, resulting in intersection pairs. Due to the way the algorithm is implemented, mathematically possible tangential rays are avoided, in fact assuring the mentioned occurrence of intersection pairs.

[73] The mathematical foundation for ray-tracing were already developed a few decades ago, however only the development of modern computer hardware made its application possible in widespread graphics applications.

is determined by the alignment of $\boldsymbol{d}_i$ and the interpolated surface normal vector of the hit triangle[74] in the sense of (42).

Compared to CEP and SD sampling, **V**ertex **N**ormal **V**ector sampling (VNV) determines the closest intersection to $\boldsymbol{s}_i$ in the direction of its vertex normal vector $\boldsymbol{n}_{\mathcal{S},\mathrm{v},i}$. This is therefore an orthogonal measurement of the distance between the two geometries, which is often-times a desired property in dimensional 3D coordinate metrology. Unfortunately, VNV sampling can show some unfavourable behaviour in edge regions, as shown in Figure 22 at markers $\boxed{2}$, $\boxed{4}$: It is possible that certain $\boldsymbol{s}_i$ are associated with long intersection distances l_i, which could lead to an overestimation of the local measurement errors. In the worst case, rays from edge regions completely miss the target geometry $\mathcal{T}$, resulting in an undefined distance calculation ($\boxed{3}$). While the complete missing of the target ($\boxed{3}$) can be compensated for by applying a second sampling strategy, cases illustrated with markers $\boxed{2}$, $\boxed{4}$ are hard to detect and to fix. This behaviour is a great weakness of VNV sampling and represents one of its key characteristics. The results are especially problematic, if the examined geometries exhibit many strong discontinuities (sharp features) in combination with large geometrical deviations between both meshes.

In certain cases, it can be beneficial to use an alternative vertex normal vector instead of one calculated from the geometry data itself. One example would be that reference measurement data from a CMS is produced as described in sec. 5.5 and the following calculation of the local distance field utilises the local normal vector of the underlying nominal geometry (CAD). In this special case, the sampling strategy is referred to as VNVx.

5.3.6 Triangle mesh affinity (TMA)

In order to evaluate the affinity of two triangle meshes A and B in their current coordinate system (e.g. after registration, see sec. 5.6), the **T**riangle **M**esh **A**ffinity measure (TMA) is defined, using the SD distance metric defined in sec. 5.3.2 (54).

$$\mathrm{TMA}_{\mathcal{A},\mathcal{B}} = \sqrt{\frac{\sum_{i=1}^{n} w_i \cdot l_i^2}{\sum_{i=1}^{n} w_i}} \tag{54}$$

---

[74] The parametrisation of the possible solutions based on barycentric coordinates includes the intersection at edge points and edges, which are part of the triangle. This means, that no distinction between different components of a triangle (edge point, edge, faces) is made with this approach.

Here, the sampling is performed starting from mesh $\mathcal{A}$ and targeting mesh $\mathcal{B}$. The parameter w_i weights each summand according to one third of the area of the triangle fan (see also Figure 10) centred around that sampling point $\boldsymbol{s}_i$. In general it must be expected that $\mathrm{TMA}_{\mathcal{A},\mathcal{B}} \neq \mathrm{TMA}_{\mathcal{B},\mathcal{A}}$ holds.

5.4 Preparation of nominal geometry data

In the context of this thesis it is expected that manufactured parts in general can be associated with their respective nominal geometry in form of a CAD model. Otherwise, dimensional examinations of their geometry are of little use and so is the uncertainty of these measurements[75]. Therefore, the nominal geometry can potentially act as a sampling start surface $\mathcal{S}$, which means that its properties need to be controlled in order to ensure certain properties of the subsequently obtained descriptor estimates. As described in the previous section, distance metrics between two triangle meshes are computed such that one of both is defining the sampling points and consequently associates the distance field with its own data structure. Therefore ideally, the sampling start surface defines a dense and homogeneous spatial distribution of sampling points. Here, "dense" means enough sampling points per area with respect to a user defined (scalar) upper limit of spatial frequencies, which should be captured by the sampling process. The spatially discrete metrological descriptor framework profits a lot from various visualisation techniques, especially coloured triangle mesh plots and statistical methods. That is why the sampling points of the sampling start geometry are also strictly organised as a triangle mesh as opposed to a simple point cloud with no connectivity information between points. This, however, requires some effort in converting the nominal geometry $\mathcal{N}$ from a CAD model (this work uses the STEP interface, see sec. 2.2.2) to a triangle mesh $\mathcal{M}^{\mathrm{tri}}$, such that the following properties are satisfied:

- The edge points of $\mathcal{M}^{\mathrm{tri}}$ must lie exactly on $\mathcal{N}$ with zero positional error. This is only possible if the sampling points are represented by triangle edge points, because there is always some deviation inside the triangle facets if a surface with non-zero curvature is represented (a triangle mesh is a piecewise linear geometry).
- All geometric features of $\mathcal{N}$ must be captured by the resulting mesh $\mathcal{M}^{\mathrm{tri}}$. Therefore, a geometric feature which is smaller than the targeted sampling density must not be discarded.
- In case $\mathcal{M}^{\mathrm{tri}}$ is used as a sampling start surface $\mathcal{S}$, the complete surface of $\mathcal{N}$ must be represented by homogeneously sized triangles, depending on a user input. Ideally, depending on the use case, this value corresponds to at

---

[75] Exceptions can be found in the context of reverse engineering [8].

least half of the structural resolution of the examined measurement system. This sampling should be independent of the local surface curvature.

A first approach is to use the commercial CAD software Autodesk Inventor Professional 2021 for the conversion of the STEP model to a triangle mesh with a target triangle edge length. To examine this behaviour, the STEP CAD model of the "multi purpose specimen"[76] (technical drawings are given in Appendix, for a 3D view of the object in form of the "BREP" triangle mesh, see Figure 24 with additional explanations further below) was converted to a triangle mesh, targeting a triangle edge length of 100 µm. However, this results in suboptimal distribution of triangle edge lengths, as is visualised in the upper image in Figure 23. The cumulative density function estimate (CDF)

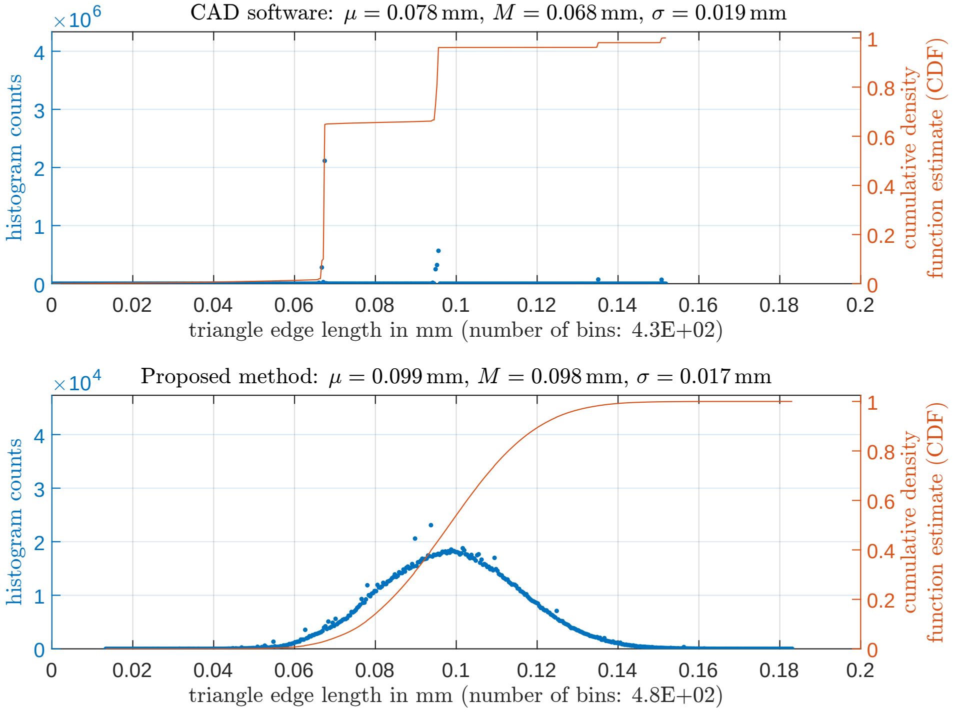
CAD software: $\mu = 0.078\,\mathrm{mm}$, $M = 0.068\,\mathrm{mm}$, $\sigma = 0.019\,\mathrm{mm}$

Proposed method: $\mu = 0.099\,\mathrm{mm}$, $M = 0.098\,\mathrm{mm}$, $\sigma = 0.017\,\mathrm{mm}$

Figure 23: Visualisation of triangle edge lengths statistics from an automatic conversion with commercial CAD software (top) and the result of the proposed solution (bottom) with a target edge length of 100 µm. The number of bins was determined according to (55) and CDF stands for cumulative density function estimate. The statistical parameters of the distributions are given in the individual titles as mean μ, median M and standard deviation σ. The number of (unique) triangle edges are approx. $1.3 \cdot 10^6$ and $7.4 \cdot 10^5$ (upper histogram and lower histogram, respectively).

---

[76] Design by Lorenz Butzhammer, FMT. Used with permission.

directly gives access to arbitrary percentiles of the distribution and therefore adds additional information. The number of bins was determined according to the Freedman-Diaconis rule, which computes the histogram bin width W as (55) based on the interquartile range of the input data $\mathrm{IQR}(\{x_i\}_{i=1}^{n})$[77] and the number of data points n [202, 203].

$$W = \frac{2 \cdot \mathrm{IQR}(\{x_i\}_{i=1}^{n})}{\sqrt[3]{n}} \tag{55}$$

The upper image of Figure 23 shows an inhomogeneous distribution of triangle edge lengths. Ideally, all triangles would have exactly the same size, however this is generally not possible. The result of the alternative approach (described further below) for creating a triangle mesh from a CAD model is shown in the bottom of Figure 23. The distribution of triangle edge lengths fairly accurately follows a Gaussian distribution. When conducting statistical evaluations about the distribution of spatially discrete metrological descriptors on a geometry (e.g. measurement precision), it is advantageous if the underlying distribution of triangle sizes is known, because their edge vertices represent the sampling starting points. Therefore, the Gaussian-shaped distribution is favourable compared to the first one because it shows a symmetrical distribution with known mean value μ. This is especially true when histogram plots of sampling results of the complete mesh surface are presented, because differences in the lateral sampling density (determined by the triangle edge lengths of the sampling start surface) are also reflected in the histogram bin counts.[78] Furthermore, most of the triangles produced by the direct CAD conversion are below the targeted edge length, resulting in significantly more triangles ($2.6 \cdot 10^6$) compared to the proposed solution ($1.5 \cdot 10^6$), which causes unnecessary computing requirements. Nonetheless, the first method is much easier to use, because it is offered by commercial software and is therefore also more robust compared to the proposed alternative. For high quality assessments, the subsequently presented method for producing such a triangle mesh from a STEP CAD model with good statistical properties is recommended and can be summarised with the following processing steps:

$\boxed{\text{Step 1:}}$ Create a coarse triangle mesh from the STEP CAD model using commercial CAD software, such that the geometry is represented by large triangles, with large local error at curved surfaces. This setting is often called ”BREP” (from boundary representation) and the result of that conversion is

---

[77] The IQR defines as the 75th percentile of $\{x_i\}_{i=1}^{n}$ minus its 25th percentile.

[78] This problem can only be partially mitigated by creating a histogram which counts area instead of discrete instances (”this much area of the surface is associated with a certain histogram distance bin”), because the distance information is missing nonetheless for large sampling point distances.

shown in Figure 24. The mesh is exact with respect to the underlying STEP CAD model at triangle edge points, but shows large deviations inside the triangle facets.

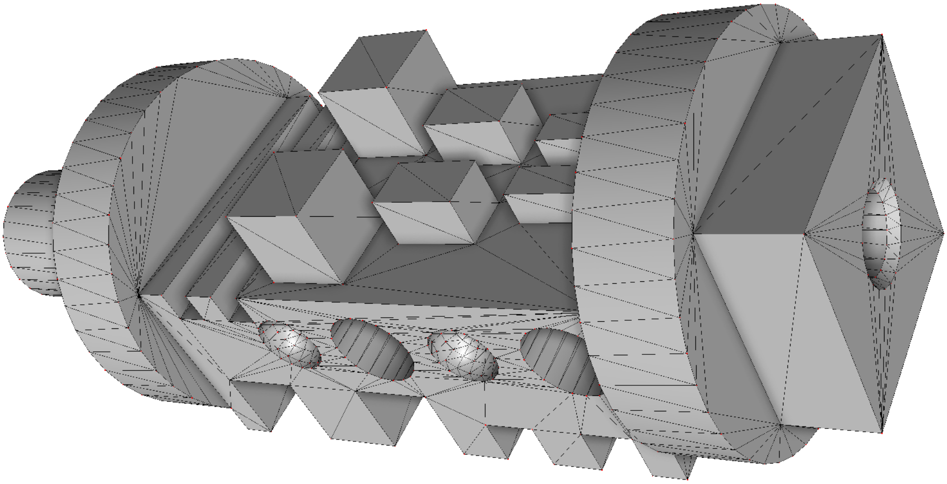

Figure 24: Geometry of the test specimen as a triangle mesh which was created with commercial CAD software using the "BREP" setting. Triangle vertices are placed based on the local curvature of the surface such that a certain error metric is satisfied. This representation is used as the start geometry for the generation of a triangle mesh conforming to the defined requirements of a sampling start surface. The specimen consists of different types of elementary surfaces: planes, cylinders, cones and spheres.

$\boxed{\text{Step 2:}}$ Generate a constrained Delaunay triangulation (CDT) from the BREP-mesh using TetGen [188, 189] and apply a scalar resize function to each tetrahedron with the same tool. During this volumetric mesh refinement procedure, neighbouring coplanar surfaces patches are subdivided while targeting a specific triangle edge length provided by the user. The input BREP-mesh is respected such that newly created triangle edge points lie exactly on the BREP geometry (with zero positional error). Furthermore, existing triangle edges between non coplanar facets are preserved.

$\boxed{\text{Step 3:}}$ Because of the way the CDT refinement procedure works, newly generated points from curved surface regions are not located exactly on the surface of the underlying CAD model (but exactly on the triangles of the BREP-mesh). Therefore, during this last step, all newly generated triangles are projected onto their originating geometry element, such that all points are then located on the CAD representation. For that, each CAD entity with curvature is examined and the points in question are shifted onto the ideal surface of the CAD entity. During this process, possible local mesh overlaps due to the shift operation are identified and corrected for. The process can be described for a limited spherical surface as follows:

1. Find all triangles from the BREP-mesh, which triangle vertices all lie exactly on the spherical surface.
2. Ensure by inspecting the boundaries of the spherical surface (in this case the boundary of a limited spherical surface is always a circle) that the planned shifting of mesh coordinates is not causing intersections with the neighbouring surfaces mesh due to "denting out" of local surface curvature. This is the most demanding processing step with regards to its algorithmic complexity, because the cutting lines of arbitrary geometry element combinations must be handled.
3. Find all triangles from the refined-mesh whose triangle vertices all lie exactly on the triangles of the BREP geometry selected in the first step. This results in an association of the CAD geometry with the refined mesh through the BREP mesh, which directly indicates which facets of the refined mesh represent a certain CAD entity (here a sphere).
4. Using this associating, project each vertex onto the spherical surface. This operation moves the vertices in the direction of the local normal vector of the spherical surface.

The results of the mesh refinement are visualised in Figure 25. The coarse BREP-mesh is converted to a mesh with the targeted triangle edge length and the newly generated vertices are projected onto their respective CAD elements. The surface of the geometry is represented by homogeneously sized triangles, according to the statistics shown in Figure 23.

Ideally, the target triangle edge length for the proposed geometry preparation is as large as possible (to reduce computation requirements) while being as small as required in order to reflect the capabilities of the used measurement system with respect to its capability to capture geometrical features. The relationship behaves quadratically, where bisecting of the targeted triangle edge length results in 4 times as many triangles. In recent years, numerous efforts to determine different resolution terms describing those metrological capabilities of a measurement system in the context of industrial X-ray computed tomography were published, especially with respect to the metrological structural resolution [204, 205] of a system [65, 206–212]. Ultimately, a goal is to determine performance limits of a measurement systems by using amplitude-wavelength maps (also named Stedman diagrams after their inventor Margaret Stedman [213–215]). A method to determine amplitude-wavelength maps for industrial X-ray computed tomography was reported in [216, 217]. However, no such characterisation was yet successfully conducted for any of the measurement systems used in this

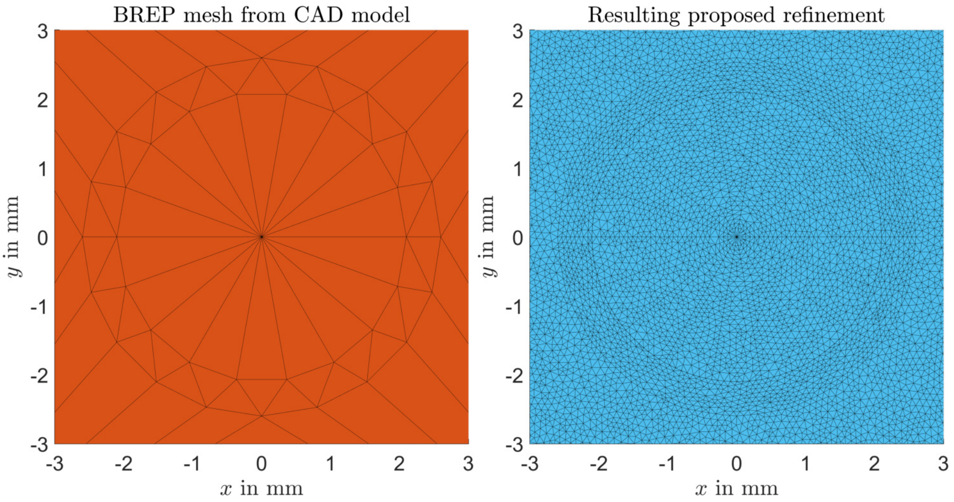

Figure 25: Studies of the BREP-mesh and the result of the proposed mesh refinement methodology. The plots show the hole on top of the specimen, visible in right side of Figure 24. Note that the vertices on the circular edges lie all exactly on the circle in both images.

thesis (see Appendix). Therefore, the values for the structural metrological resolution for arbitrary measurement tasks are unknown and were thus estimated and then applied to the mesh refinement algorithm with respect to the Nyquist-Shannon sampling theorem [218, 219].

5.5 Preparation of reference measurement data

This thesis follows the definitions given by [10] about ”reference measurement data” meaning the ”reference quantity values” obtained with a ”reference measurement procedure”. The spatially discrete metrological descriptor framework, however, does not assess the correctness of a user-defined relationship between two measurement systems with respect to one of the systems acting as a reference to the other. Instead, the obtained metrological descriptors are calculated based on a given assignment, without actively defining it. A primary[79] measurement system captures a measurement series, which is then evaluated with respect to a potentially[80] provided reference

---

[79] Not to be confused with the ”primary reference measurement procedure” described in VIM [10].

[80] A reference measurement is not necessarily required but its absence is limiting the determination of certain metrological descriptors, e.g. the systematic measurement error of the primary measurement system.

measurement. As such, it is expected that a reference measurement offers negligible[81] measurement errors compared to the primary system.

In order to estimate both the systematic and random spatially discrete measurement error, respectively, reference measurement data of the same measurement object is required. Like the other types of geometry data (nominal geometry and measurement series data) the reference measurement must also be represented by a closed 2-manifold triangle mesh. Depending on the use case (see sec. 5.7), the reference geometry can act as the sampling start surface, thus associating the calculated measurement metrological descriptors with its data structure. In that case, the triangle mesh should also show a favourable distribution of triangle sizes (see discussion in sec. 5.4). The main scenario covered in this thesis is the provision of reference measurement data from tactile coordinate measurement systems (CMS), which represent the state of the art for high accuracy coordinate measurements for a wide range of industrial applications (see sec. 2.1.1).

5.5.1 Tactile CMS reference measurement represented by a point cloud

Tactile coordinate measurement systems (TCMS, tactile CMS) are well understood and offer high-accuracy measurement data. Therefore, measurements with these types of systems are well-suited for the application in the spatially discrete metrological descriptor framework. However, due to the properties of TCMS measurements, their data cannot be used directly and their information about the measured geometry must first be adequately prepared. The following typical features of a TCMS measurement are important with respect to the intent of providing a triangle mesh representation of such a measurement:

- A TCMS measurement of an object is typically based on the nominal geometry (CAD) of that object such that the resulting measurement points are each associated with exactly one geometric feature.
- The result of a TCMS measurement is a point cloud (including meta data, e.g. probing vectors) and thus unfortunately not an areal representation of the measured geometry. Furthermore, that point cloud has no consistent shape as it is a product of the user-defined probing strategy of each geometric feature (e.g. a plane or cylindrical surface).
- In geometry, an edge is a cutting line between two intersecting surfaces. Therefore, edges are typically not probed by TCMS measurements. Another

---

[81] In case of significant calibration uncertainty (which would require another measurement system), the framework can be easily adapted such that these uncertainty contributions are propagated through the measurement chain.

reason is the technical requirement of safety margins in order to avoid collision of the probing element with neighbouring geometry elements.
- Not all geometrical features of an object are physically accessible to TCMS probing. Examples are regions covered by clamping equipment and undercuts. Consequently, a closed geometry mesh must substitute these parts of the object surface with suitable information from other sources.

The developed method respecting the listed properties is described in the following and was previously published in [P12]. The underlying design principles were chosen as:

- A high fidelity triangle mesh created from the same nominal geometry used for the TCMS measurement (CAD model) with the method described in sec. 5.4 represents the basis for the local adjustments with respect to the TCMS measurement data.
- The nominal geometry of an object is represented by surface elements, such as e.g. planes, cylindrical surfaces, conical surfaces, B-spline surfaces, and more. Each of these features can be associated with its available TCMS measurement data as well as with the triangle sub-mesh representing that part of the geometry.
- Surface regions without associated TCMS measurement data are unaltered, this includes by design all feature edges.

Each geometric feature is represented in its own local coordinate system and points on that feature can be parametrised as $\sigma(u, v)$ (see sec. 2.2.2). The signed orthogonal distance w from a measurement point with coordinates (u, v) to the surface of that feature can then be formulated as a function F of u and v (56).

$$w = F(u, v) \tag{56}$$

Because w is measured in the direction of the normal vector $\boldsymbol{n}(u, v)$ (see (12) p. 23), $\{u, v, w\}$ form an orthogonal basis. From (56) an interpolation function F is defined, such that each of the triangle mesh vertices $\boldsymbol{v_i}$ can be shifted according to their interpolated $w = F(u', v')'$ values (57).

$$\boldsymbol{v}_i' = \boldsymbol{v_i} + \boldsymbol{n}(u', v') \cdot F(u', v') \tag{57}$$

The reverse transformations of triangle coordinates $\{X, Y, Z\}$ to the coordinate system of different geometry elements $\{u', v'\}$ are given in sec. 2.2.2. The amount of shift is determined by $w = F(u', v')$, where F is based on "natural neighbour interpolation" (also called "Voronoi interpolation") between data points (method explained below). First, the triangle sub-mesh representing a feature is extracted exploiting the fact that triangle vertices are guaranteed to lie exactly on the nominal geometry (see sec. 5.4). An example for a geometry

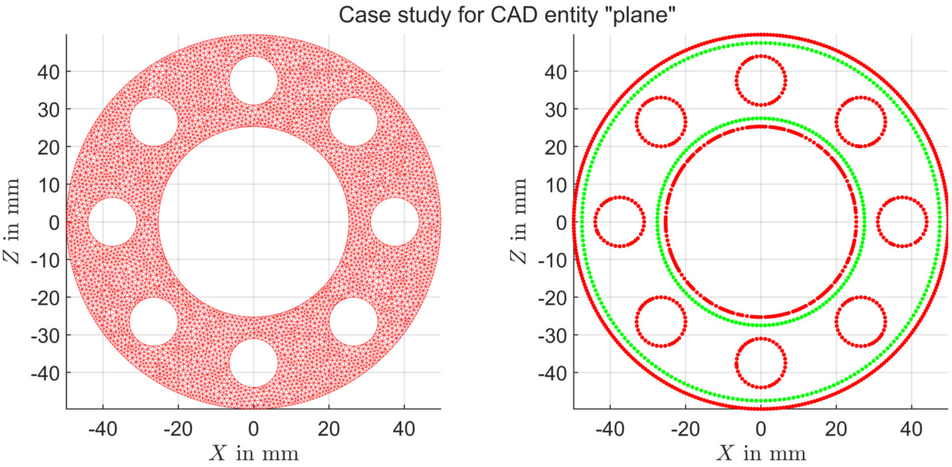

Figure 26: Left: Extracted sub-mesh for a geometry element of type "plane". The edges of that sub-mesh represent the measurement domain for that particular element, thus all measurement points are guaranteed to reside inside that domain. The edges (red) are plotted together with the TCMS measurement data for that geometry element (green) in the right image. The w value of edge vertices is zero by definition for the described method.

element of type "plane" is shown in Figure 26, left image[82]. As explained above, the edges of that sub-mesh restrict the domain in which TCMS measurement data is captured. Therefore, $w(u, v) = 0$ for edge vertices, meaning that they remain unaltered. The coordinates defining those edges are extracted and plotted (red) together with the captured TCMS measurment data (green) Figure 26, right image. The w value of the measurement points (green) is dependent on their particular measurement result. The task is now to interpolate the value $w(u', v')$ for all triangle vertices extracted in the left image.

$$w'(P) = \frac{w(A)S(A \cap P)}{S(P)} + \frac{w(B)S(B \cap P)}{S(P)} + \frac{w(C)S(C \cap P)}{S(P)} + \frac{w(D)S(D \cap P)}{S(P)} \tag{58}$$

Voronoi interpolation is based on the weighted mean of w values depending on the covered areas of neighbouring cells of a query point P. For the example in Figure 27 it is calculated according to (58) with $S(X)$ denoting the area of a Voronoi cell X [221]. It shows four Voronoi cells A, B, C and D (each constructed around a measurement point which are associated with their individual w value) and eight surrounding edge vertices (with $w = 0$). Additional technical details about this interpolation method can be found in

---

[82] The measurement object is the aluminium specimen "Multi-Feature-Check" from eumetron GmbH, Germany [220].

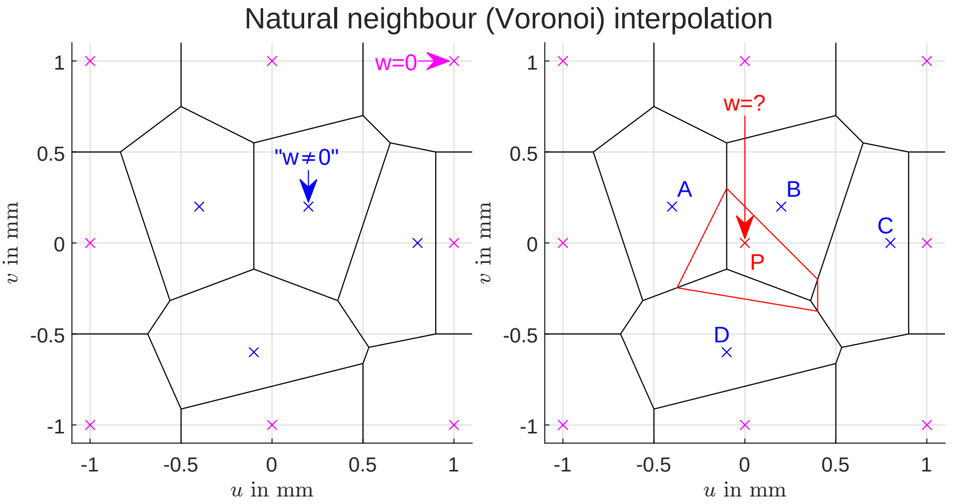

Figure 27: The principle of Natural neighbour interpolation is to generate the Voronoi diagram for data points in the u, v coordinate frame. Each data point is associated with its own w value. Interpolation of $w(P)$ is performed based on the weighted mean of the surface shares the Voronoi region of P (red) is ”stealing” from its surrounding Voronoi regions (here from A, B, C and D) (58).

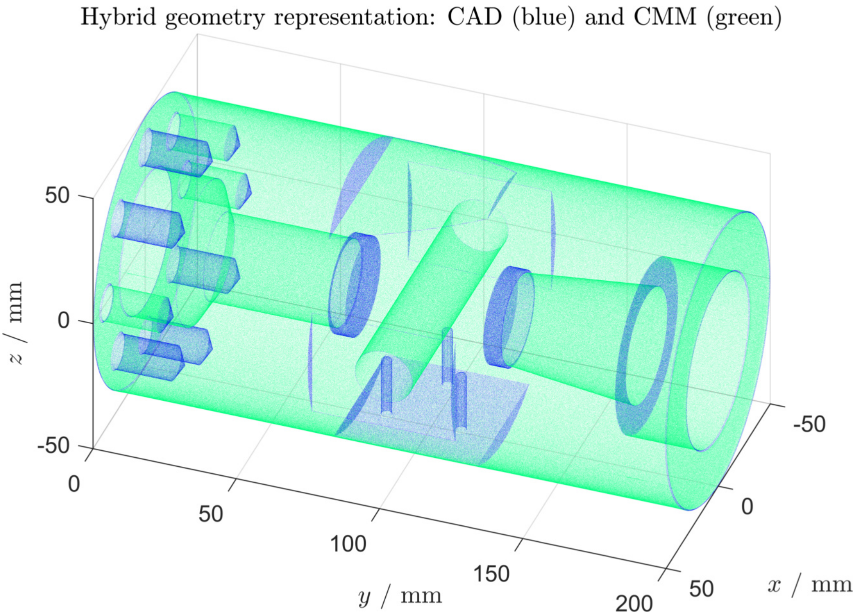

Figure 28: Hybrid geometry representation, where unaffected geometry elements (including edge vertices) are coloured blue and modified elements are marked green.

[194, 221]. Figure 29 shows an exemplary result for the integration of TCMS measurement data into a triangle mesh representing the nominal geometry, resulting in a hybrid CMS/CAD triangle mesh of the ”Multi-Feature-Check” [220] (see Figure 28). For more technical details refer to [P12], where the method presented in this section was previously published.

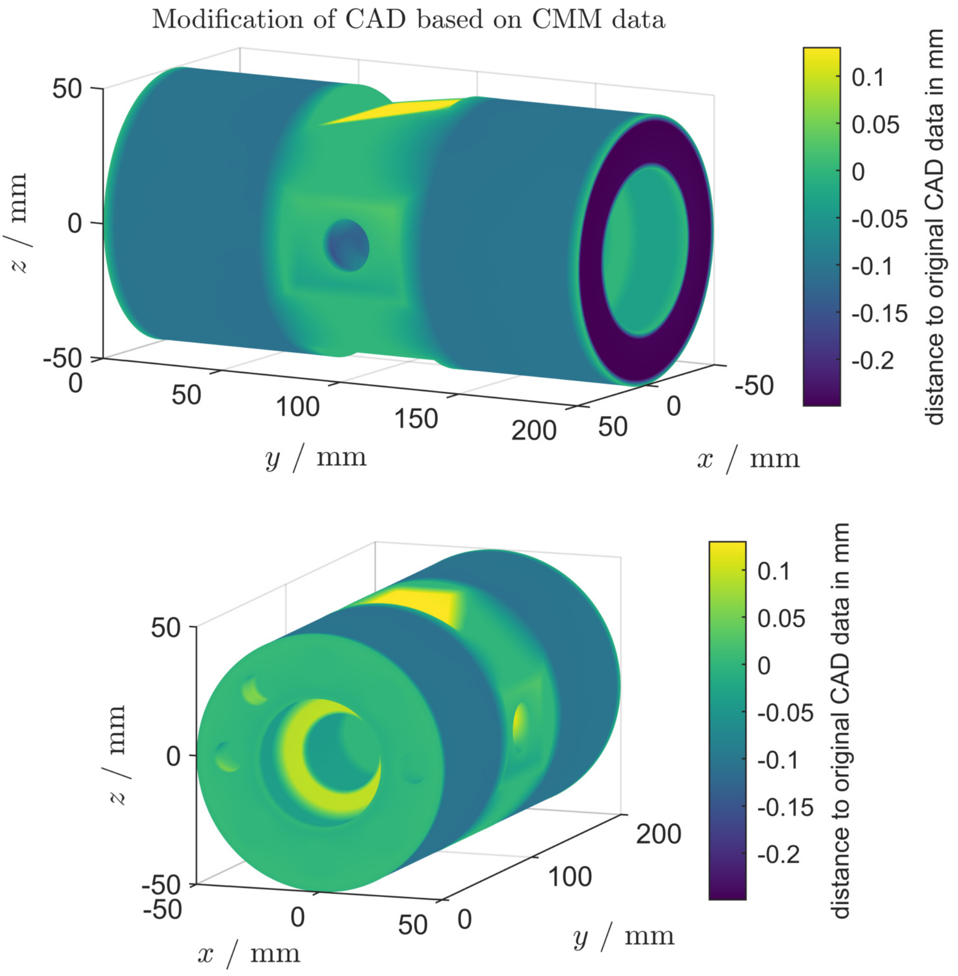

Figure 29: Resulting hybrid CAD/CMS triangle mesh after consideration of a set of measurement data. The shift values w' for each triangle vertex are visualised using false colours. Image partly reused from [P12] with minor modifications.

5.5.2 Reference measurement represented by a triangle mesh

In a second case, the reference measurement data is already represented by a triangle mesh. Here, the requirement of additional processing is strongly dependent on the structure and quality of the mesh, which is typically the case for optical CMS and industrial X-ray computed tomography (CT) measurements. If the mesh does not meet the expectations regarding the triangle size distribution, a resampling can be performed as follows if the nominal geometry of the object also exists: First, convert the nominal geometry into a mesh with the desired properties as described in sec. 5.4. In a second step, project that mesh onto the mesh representing the reference measurement, such that the triangle vertices lie exactly on the surface of the reference mesh. For this, SD sampling yields good results in practice, however an iterative approach alternating with mesh repair routines (removing resulting degenerate triangles) might be required, depending on the local differences between both meshes. The preferred reference measurement data originates from a TCMS and is subsequently processed as described in the previous section.

5.6 Alignment of coordinate systems (registration)

The spatially discrete metrological descriptor framework processes geometries from different sources which all represent the same object (nominal geometry, reference measurement and repeated measurements). These geometries have to be transferred into a common coordinate system, such that their features are aligned with each other as accurately as possible, according to a certain error metric. This alignment process is called registration. Depending on the particular science field, the terms ”image registration” [222] and ”point set / point cloud registration” [223, 224] are preferably used. One of the possible results of this framework is the determination of the spatially discrete measurement uncertainty, which is based on independent distance measurements between two different objects in 3D (see sec. 5.7). Consequently, these results are dependent on the unknown position and orientation of both geometries with respect to each other, which means that the lowest possible uncertainty of this distance measurement is dependent on the determination uncertainty of the ”optimal” transformation between both geometries. That is why the alignment of the coordinate systems of both objects is of central importance in the context of this work.

Mathematically, the representation of geometry in Euclidean space is always associated with a coordinate system, also referred to as a basis. The standard Euclidean basis in $\mathbb{R}^3$ is denoted by the unit vectors $\boldsymbol{e}_x = [1\ 0\ 0]^\mathrm{T}$, $\boldsymbol{e}_y = [0\ 1\ 0]^\mathrm{T}$ and $\boldsymbol{e}_z = [0\ 0\ 1]^\mathrm{T}$, thus forming the base $\boldsymbol{E} \in \mathbb{R}^3 \times \mathbb{R}^3 = \left[\boldsymbol{e}_x, \boldsymbol{e}_y, \boldsymbol{e}_z\right]$. The base vector of index k of the coordinate system (also called ”base” or ”observer”) $\boldsymbol{E}$ is denoted by $\boldsymbol{E}_k$. A base is called orthonormal in case its unit vectors are orthogonal to each other, such that $\boldsymbol{e}_x \cdot \boldsymbol{e}_y = \boldsymbol{e}_x \cdot \boldsymbol{e}_z = \boldsymbol{e}_y \cdot \boldsymbol{e}_z = 0$ holds. A coordinate system (base) is referred to as right-handed if its determinant $\det(\boldsymbol{E}) > 0$ and left-handed if $\det(\boldsymbol{E}) < 0$. Within the context of this thesis, coordinate systems are expected to be orthonormal and right-handed. The mathematical relationship of two observers $\boldsymbol{A}$ and $\boldsymbol{B}$, each representing an orthonormal base and both describing an object $\mathcal{O}$ consisting of coordinates $\boldsymbol{p}$ is shown in Figure 30. Here, both observers are placed within a global coordinate frame, represented by the standard basis $\boldsymbol{E}$. The following notation assumes $k = 3$ dimensional Euclidean space and is derived from [82, 225].

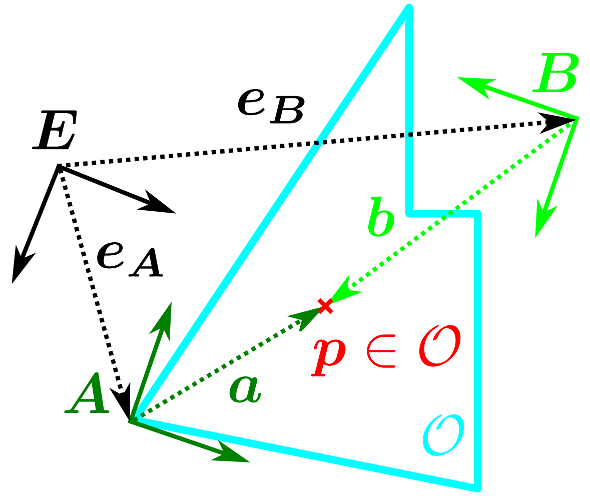

Figure 30: Two orthonormal observers $\boldsymbol{A}$ and $\boldsymbol{B}$ are placed with respect to the world coordinate system $\boldsymbol{E}$ and describe the same coordinate $\boldsymbol{p} \in \mathcal{O}$.

$$\begin{aligned} \boldsymbol{p} &= \boldsymbol{e_A} + \sum_{i=1}^{k} a_i \boldsymbol{A}_i \\ \boldsymbol{p} &= \boldsymbol{e_B} + \sum_{i=1}^{k} b_i \boldsymbol{B}_i \end{aligned} \tag{59}$$

In the global coordinate system $\boldsymbol{E}$, a point $\boldsymbol{p}$ has two different representations (59). This relationship can be written down using 4x4 matrices as (60) [225].

$$\begin{bmatrix} \boldsymbol{A} & \boldsymbol{e_A} \\ 0\ 0\ 0 & 1 \end{bmatrix} \begin{bmatrix} \boldsymbol{a} \\ 1 \end{bmatrix} = \begin{bmatrix} \boldsymbol{p} \\ 1 \end{bmatrix} = \begin{bmatrix} \boldsymbol{B} & \boldsymbol{e_B} \\ 0\ 0\ 0 & 1 \end{bmatrix} \begin{bmatrix} \boldsymbol{b} \\ 1 \end{bmatrix} \tag{60}$$

The conversion between both coordinate systems is then possible using the transformation matrix $\boldsymbol{C}$ (61) [225].

$$\begin{aligned}
\begin{bmatrix} \boldsymbol{a} \\ 1 \end{bmatrix} &= \boldsymbol{C} \begin{bmatrix} \boldsymbol{b} \\ 1 \end{bmatrix} \\
\begin{bmatrix} \boldsymbol{b} \\ 1 \end{bmatrix} &= \boldsymbol{C}^{-1} \begin{bmatrix} \boldsymbol{a} \\ 1 \end{bmatrix} \\
\boldsymbol{C} &= \begin{bmatrix} \boldsymbol{A} & \boldsymbol{e_A} \\ 0\ 0\ 0 & 1 \end{bmatrix}^{-1} \begin{bmatrix} \boldsymbol{B} & \boldsymbol{e_B} \\ 0\ 0\ 0 & 1 \end{bmatrix} = \begin{bmatrix} \boldsymbol{A}^{-1}\boldsymbol{B} & \boldsymbol{A}^{-1}(\boldsymbol{e_B} - \boldsymbol{e_A}) \\ 0\ 0\ 0 & 1 \end{bmatrix} \\
\boldsymbol{C}^{-1} &= \begin{bmatrix} \boldsymbol{B} & \boldsymbol{e_B} \\ 0\ 0\ 0 & 1 \end{bmatrix}^{-1} \begin{bmatrix} \boldsymbol{A} & \boldsymbol{e_A} \\ 0\ 0\ 0 & 1 \end{bmatrix} = \begin{bmatrix} \boldsymbol{B}^{-1}\boldsymbol{A} & \boldsymbol{B}^{-1}(\boldsymbol{e_A} - \boldsymbol{e_B}) \\ 0\ 0\ 0 & 1 \end{bmatrix}
\end{aligned} \tag{61}$$

In this example, the relationship between $\boldsymbol{A}$ and $\boldsymbol{B}$ is known because of their common coordinate system $\boldsymbol{E}$. However, a registration problem can be formulated if this relationship is unknown. In coordinate metrology, measurement results are always primarily represented in the coordinate system of the measurement system. Consequently, the three-dimensional measurement volume is located within the coordinate frame of the physical axes of the system and the measurement result is reported with respect to that frame. During the design of an object using CAD, the features of the object are defined with respect to a user-given coordinate system. Therefore, if that nominal geometry needs to be compared against a measurement of the manufactured part, the following circumstances require consideration:

- Both geometry representations (CAD model and measurement data) describe the same object, but nonetheless differ locally because of both manufacturing deviations and measurement errors.
- Both geometries are represented in different coordinate systems.
- For real measurements, the relationship between the coordinate systems of both objects is typically unknown[83].

The registration problem is defined as finding the 3D affine transformation matrix $\boldsymbol{C} \in \mathbb{R}^4 \times \mathbb{R}^4$, such that the relationship between coordinates $\boldsymbol{a}$ and $\boldsymbol{b}$ describing the same feature on both geometry representation can be described (61). The unknown matrix $\boldsymbol{C}$ can be determined by matching corresponding features in both geometry representations and calculating the sought-after transformation from that. However it is important to know that in the context of metrology the calculated $\boldsymbol{C}$ is usually only an approximation

---

[83] This usually does not apply to virtual (simulated) measurements.

of the true transformation, no matter which registration method is used. The reason for that is that both geometries are not only represented in different coordinate systems, but they also differ more or less locally, due to possible manufacturing and measurement errors, respectively.

In principle, $\boldsymbol{C}$ can represent any combination of translation, rotation, scaling, reflections and shears. However, in the context of 3D coordinate metrology, only translation and rotation are considered in the final transformation, which is then referred to as a rigid registration problem. Mathematically, this problem is characterised by six degrees of freedom (three rotational and translational parameters, respectively). Therefore, an affine transformation $\boldsymbol{C}$ can be described by six independent parameters $\boldsymbol{x} = [x_1, x_2, x_3, x_4, x_5, x_6]$, e.g. by combining[84] three rotation matrices $\boldsymbol{R_X}$, $\boldsymbol{R_Y}$, $\boldsymbol{R_Z}$ and one translation matrix $\boldsymbol{T}$ (62)[85] (adapted from [18]).

$$\boldsymbol{T} = \begin{bmatrix} 1 & 0 & 0 & x_1 \\ 0 & 1 & 0 & x_2 \\ 0 & 0 & 1 & x_3 \\ 0 & 0 & 0 & 1 \end{bmatrix}; \qquad \boldsymbol{R_X} = \begin{bmatrix} 1 & 0 & 0 & 0 \\ 0 & \cos(x_4) & \sin(x_4) & 0 \\ 0 & -\sin(x_4) & \cos(x_4) & 0 \\ 0 & 0 & 0 & 1 \end{bmatrix}$$

$$\boldsymbol{R_Y} = \begin{bmatrix} \cos(x_5) & 0 & -\sin(x_5) & 0 \\ 0 & 1 & 0 & 0 \\ \sin(x_5) & 0 & \cos(x_5) & 0 \\ 0 & 0 & 0 & 1 \end{bmatrix}; \qquad \boldsymbol{R_Z} = \begin{bmatrix} \cos(x_6) & -\sin(x_6) & 0 & 0 \\ \sin(x_6) & \cos(x_6) & 0 & 0 \\ 0 & 0 & 1 & 0 \\ 0 & 0 & 0 & 1 \end{bmatrix}$$

$$\boldsymbol{C} = \boldsymbol{C}(\boldsymbol{x}) = \boldsymbol{R_X} \cdot \boldsymbol{R_Y} \cdot \boldsymbol{R_Z} \cdot \boldsymbol{T} \tag{62}$$

The research published over the last few decades dealing with or related to the registration problem is extensive. The focus in this thesis lies on providing a feasible solution to the registration problem in the context of the existing boundary conditions (closed manifold triangle meshes, rigid transformation). Furthermore, it is aimed at determining the influence of various registration methods on the determined spatially discrete metrological descriptors, ultimately quantifying its potential influence on the measurement uncertainty. At first, commonly used methods based on the (semi-)manual selection of object feature correspondences are described. Nonetheless, fully automatable

---

[84] Importantly, matrix multiplications are not commutative, the order of operations is read from right to left (here first $\boldsymbol{T}$ and last $\boldsymbol{R_X}$).

[85] With this convention, positive rotation angles cause a counter-clockwise rotation about an axis in the sense that one looks inward from a point on the positive axis towards the origin.

solutions are also described and preferred in order to preserve the otherwise fully-automated data processing pipeline.

5.6.1 Manual registration based on geometry elements

A commonly used method to align two related[86] geometries is to manually solve the correspondence problem by assigning coherent geometry features to suitable geometry elements of the same type. The principle is depicted in

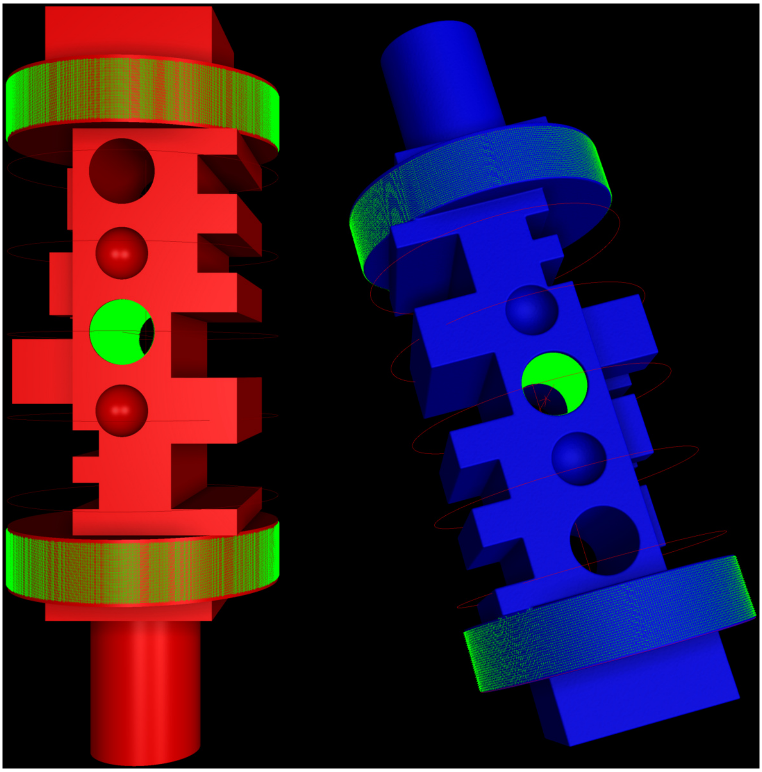

Figure 31: Solving the correspondence problem by manual assignment of geometry elements between the nominal geometry (red) and a measurement (blue). For both geometries, two cylinders (large outer cylinder surfaces, and the bore hole in the centre of the object) are fitted to the underlying data, with fit-points shown in green colour. The alignment is then possible by sequentially aligning corresponding cylinders with each other. Image created with VGStudio MAX 3.5.

---

[86] This means the presence of two geometry objects both representing the same object but possibly affected by local differences caused by external influences. This influences are not limited to metrological effects but also include purely mathematical and algorithmic factors, e.g. such arising when converting a CAD geometry into a triangle mesh.

Figure 31: Two representations of the same object (CAD in red and measurement in blue) are placed in a common coordinate system. The transformation $\boldsymbol{C}$ aligning both surfaces with each other, such that corresponding features match each other locally, is unknown. In most cases, $\boldsymbol{C}$ can only be determined approximately, which is denoted by $\boldsymbol{C}_{\text{approx}}$. One possibility is to apply a sequential registration, where corresponding features are matched sequentially until all six degrees of freedom are covered. In the first step, a cylinder covering both surface regions of the large outer diameter is constructed in both geometries with fit[87] points marked in green. Then both geometries can be transformed such that both cylinders align by matching their respective axes. After that, only one rotational and one translational degree of freedom are still unrestricted, which is then locked by a second cylinder covering the hole in the centre of the object. After that, both geometries are aligned with each other, based on the geometry information covered by both cylinders. This kind of regression is extremely robust because a human solves the correspondence problem. Furthermore, the procedure is applicable for almost any type of geometry. However, there are also some drawbacks, which include the aforementioned required human interaction and the fact, that the used geometry information is restricted to the regions covered by geometry elements. Therefore, it is possible that an unfavourable selection of surface regions covered by geometry elements can impact the registration result negatively. Within the ISO GPS framework, it is the responsibility of the designer to define metrologically robust reference frames consisting of datums. In reality however, it can be difficult to anticipate the degree to which coordinate systems can be affected by local measurement errors. Besides the described sequential registration, similar alternatives exist, most notably the feature-based registration, which determines $\boldsymbol{C}_{\text{approx}}$ in one step based on multiple corresponding geometry elements (as opposed to a sequential approach). This type of registration is also part of any modern TCMS measurement, because the transformation $\boldsymbol{C}_{\text{approx}}$ between the workpiece coordinate system and the coordinate system of the CMS must be determined ("determination of the workpiece coordinate system" [29]) in order to probe the measurement object based on the measurement task defined in the geometrical specification (see also sec. 2.1.1). Here, the machine operator manually probes defined features of the measurement object and thus defines a new local coordinate system before the actual measurement. The spatially discrete metrological descriptor framework does support geometry element based registration, e.g. datums and datum systems by application of DIN EN ISO 5459:2013-05 [226], but typically automated methods are applied (see next section), be-

---

[87] This type of procedure is also called "fitting" because it fits the parameters of a geometry object such that it matches the targeted data (here cylinder surface).

cause many use cases of the developed framework can be applied without the preparation of geometrical product specifications.

Ideally, the alignment of the different geometries can be performed in a fully automated way. As mentioned earlier, at least 20 measurement repetitions are recommended to ensure a large enough sample size from which the spatially discrete metrological descriptors are estimated. Therefore, also semi-manual approaches are assessed as unsuitable, due to expensive user interaction, and only options based on fully automated computations are considered in the following. Nonetheless it is important to note that for certain geometries with numerous symmetry axes or only very small symmetry breaking features, automated methods have limited capabilities (e.g. gear wheels or heavily cylindrical objects). Then, the only way to align two geometries robustly with each other is to use manual methods, as described above.

5.6.2 Automated global ”best fit” registration

The automated methods demonstrated below are called ”global” because all data points are used to solve the registration problem. These kinds of registration algorithms are also referred to as ”best-fit” methods, because they typically solve an optimisation problem in a least-squares sense. The goal is to estimate the affine transformation $\boldsymbol{C}_{\text{approx}} \in \mathbb{R}^4 \times \mathbb{R}^4$ from all possible transformations $\mathbb{A}$ between the data triangle mesh $\mathcal{M}^{\text{tri}}_{\text{data}}$ and a template[88] triangle mesh $\mathcal{M}^{\text{tri}}_{\text{template}}$ such that a distance function $\text{dist} = \text{dist}(\mathcal{M}^{\text{tri}}_{\text{data}}, \mathcal{M}^{\text{tri}}_{\text{template}}, \boldsymbol{C}_{\text{approx}})$ is minimised (63).

$$\underset{\boldsymbol{C}_{\text{approx}} \in \mathbb{A}}{\arg\min} \quad \text{dist}(\mathcal{M}^{\text{tri}}_{\text{data}}, \mathcal{M}^{\text{tri}}_{\text{template}}, \boldsymbol{C}_{\text{approx}}) \tag{63}$$

For the following, it is assumed, that the correspondences between both geometries (template $\mathcal{M}^{\text{tri}}_{\text{template}}$ and data $\mathcal{M}^{\text{tri}}_{\text{data}}$) are unknown (which points in both geometries represent the same geometric features). Then, the solution of such an optimisation problem typically converges to the ”closest” optimum, depending on the initial solution parameters and the distance function $\text{dist}(\mathcal{M}^{\text{tri}}_{\text{data}}, \mathcal{M}^{\text{tri}}_{\text{template}}, \boldsymbol{C}_{\text{approx}})$. In order to provide an optimal initial set of solution parameters, the registration problem is typically divided into two distinct stages: Coarse and fine alignment, respectively. For both, numerous variants have been proposed in literature, especially for solutions based on the Iterative Closest Point (ICP) method [228] (see further below). Therefore, this thesis focuses on the comparison of several popular variants, in order to

---

[88] Naming adopted from [227]. The data geometry is ”registered against” the template geometry.

provide enough flexibility for all intended use cases and an estimation of the introduced error of each variant with respect to other solutions (including commercial ones).

Coarse alignment using tight-fitting bounding boxes

The implemented method is based on the computation of the tight-fitting bounding box $\mathrm{BB}_{\mathrm{tf}}$ of both geometries $\mathcal{M}_{\mathrm{data}}^{\mathrm{tri}}$ and $\mathcal{M}_{\mathrm{template}}^{\mathrm{tri}}$ and aligning those boxes for a good initial estimate of the searched for transformation matrix $\boldsymbol{C}_{\mathrm{approx}}$. A $\mathrm{BB}_{\mathrm{tf}}$ is a cuboid with minimal volume completely enclosing an object. The basic idea is to enclose two geometries with their respective $\mathrm{BB}_{\mathrm{tf}}$ and then align both $\mathrm{BB}_{\mathrm{tf}}$ with each other. The method is roughly described by the following steps:

1. Compute the convex hull of both $\mathcal{M}_{\mathrm{data}}^{\mathrm{tri}}$ and $\mathcal{M}_{\mathrm{template}}^{\mathrm{tri}}$, which results in two triangle meshes [84, 229].
2. Using singular value decomposition, compute the eigenvectors of each of the covariance matrices of both convex hulls represented by triangle meshes, exploiting mathematical advantages compared to computing the covariance matrices on the triangle vertices alone [84, 229]. Each decomposition yields three eigenvectors which form an orthonormal base centred in its bounding box.
3. Find the transformation aligning both bounding boxes with each other, such that corresponding eigenvectors match each other, depending on the size of their associated eigenvalues [84]. Resolve possible ambiguities (also caused by partial symmetries) by allowing only right-hand coordinate systems and matching internal asymmetries.

Figure 32 shows the construction of a $\mathrm{BB}_{\mathrm{tf}}$ for an object in two different coordinate systems. Even though a bounding box itself inherently has three symmetry planes, the correct orientation can be found as long as the object itself shows symmetry breaking features.

Although the application of this method results only in an approximation of the $\mathrm{BB}_{\mathrm{tf}}$ for a given object, its use can be justified compared to the known exact but complicated algorithm with a high algorithmic complexity by [230], because the result is only used as an estimation of the initial registration parameters. A technical discussion of the algorithm based on the construction of the covariance matrices can be found in [229]. A positive assessment with respect to alternative approaches is published in [84]. An review of other methods for coarse registration can be found in [231].

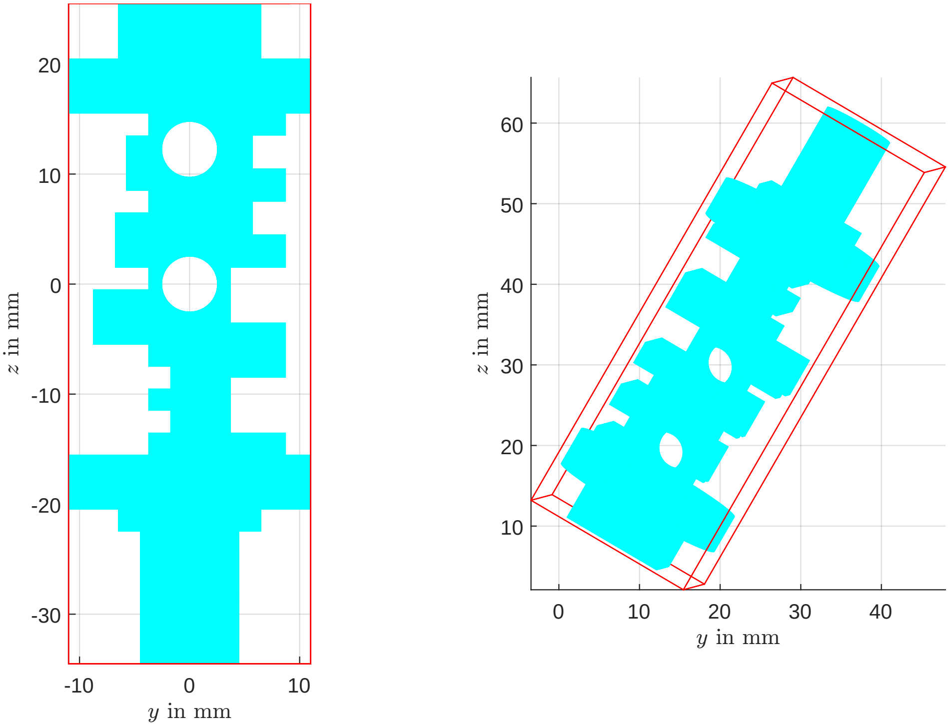

Figure 32: Tight-fitting bounding box for the same object with two different coordinate systems. A coarse registration can be performed by matching the bounding boxes with each other. Furthermore, the correct orientation with respect to the symmetry planes of the bounding box itself can be found by exploiting symmetry breaking features of the object itself.

Examined Iterative Closest Point (ICP) variants for fine alignment

After the previous step of coarse alignment, it is expected that both geometries $\mathcal{M}^{\mathrm{tri}}_{\mathrm{template}}$ and $\mathcal{M}^{\mathrm{tri}}_{\mathrm{data}}$ are aligned well enough with each other, that the following methods of fine alignment will converge to an adequate combined solution, i.e. the closest error function minimum the algorithm converges to is the global minimum. A very popular approach for obtaining this solution is the Iterative Closest Point (ICP) algorithm, originally proposed by both [232] and [233]. Its conceptual simplicity and high customisation potential have significantly contributed to its widespread success. The method was initially developed for the registration of point cloud data, however, the adaption for the support of triangle mesh data is possible, if the meshes show favourable properties. Representing geometry data as triangle meshes offers the possibility of controlling their mesh properties (see sec. 5.4) in a way that profits the use of ICP variants. The main steps of the implemented variants are the following, which are a subset of the set of steps formally listed by [234]:

1. **Matching** points in both meshes with each other, thus estimating corresponding point pairs, from which the required transformation can be computed. The matching can either be performed with reference to $\mathcal{M}^{\text{tri}}_{\text{template}}$ or $\mathcal{M}^{\text{tri}}_{\text{data}}$, which is decided by the user.
2. **Weighting** corresponding point pairs. In the following, point pairs are weighted according to the mesh area covered by the vertex of the sampling start surface, which can be determined from the triangle fan centred around each vertex.
3. Defining an **error metric** and solving the **optimisation problem**. The metrics used here are "point-to-point" (64), "point-to-plane" (66) and "DOF7" (67).

After the last step, the calculated solution is applied and the process starts again, thus exposing the iterative character of the algorithm. The process is terminated based on user-defined criteria (e.g. number of iterations or very small change in solution parameters such as residuals).

Within the context of this thesis, all data points of both geometries are considered at all times, thus no additional selection takes place with respect to a potential filtering of outliers. This approach is justified by the fact that the consistency of the used geometry data was already assured as described in sec. 5.2. Importantly, registration based on ICP variants is strongly dependent on the assignment of the data geometry $\mathcal{M}^{\text{tri}}_{\text{data}}$ and template geometry $\mathcal{M}^{\text{tri}}_{\text{template}}$ to both roles "sampling start geometry ($\mathcal{S}_{\text{reg}}$)" and "sampling target geometry ($\mathcal{T}_{\text{reg}}$)" (similar to the allocation used for the distance metrics for spatially discrete metrological descriptors in sec. 5.3)[89]. That means that $\mathcal{M}^{\text{tri}}_{\text{data}}$ can either be assigned to represent $\mathcal{S}_{\text{reg}}$ or $\mathcal{T}_{\text{reg}}$. The decision which object is selected as $\mathcal{S}_{\text{reg}}$ and $\mathcal{T}_{\text{reg}}$, respectively, is very important for the obtained quality of the alignment and is strongly dependent on the structure of the used triangle mesh (see section further below). Consequently, the processing step of matching is described by the search for a corresponding point $\boldsymbol{h}_{\text{reg},i} \in \mathbb{R}^3$ on the $\mathcal{T}_{\text{reg}}$ for every triangle vertex $\boldsymbol{s}_{\text{reg},i} \in \mathbb{R}^3$ in the $\mathcal{S}_{\text{reg}}$. In this thesis, the algorithms used for matching coincide with the distance metrics described in sec. 5.3: CEP, SD, SDSP, SDHP and VNV. The sampling start geometry can either be the data geometry $\mathcal{M}^{\text{tri}}_{\text{data}}$ or the template geometry $\mathcal{M}^{\text{tri}}_{\text{template}}$. This choice can influence certain mathematical characteristics of the solution finding process but does not restrict the application of the solution by defining which object is transformed and which one remains static. The reason for that is that the obtained transformation matrix can simply be inverted in order to exchange the direction of the operation. In the following, different registration error metrics are described.

---

[89] Different abbreviations are introduced to clarify the registration context.

One of the key characteristics of the point-to-point error metric is its closed solution and that it estimates the rotational parameters (represented by a rotation matrix $\boldsymbol{R} \in \mathbb{R}^3 \times \mathbb{R}^3$) independently of the translational ones (translation vector $\boldsymbol{t} \in \mathbb{R}^3$). For $n_{\mathcal{S}_{\text{reg,v}}}$ points $\boldsymbol{s}$ with associated (optional) scalar weights w, the error metric $E_{\text{point-to-point}}$ can be formulated as (64), which is an adaptation (additional weights) of the originally proposed algorithm by [232].

$$
\begin{aligned}
E_{\text{point-to-point}} &= \sum_{i=1}^{n_{\mathcal{S}_{\text{reg,v}}}} w^{\triangle}_{\mathcal{S}_{\text{reg}},i} \|\boldsymbol{R}\boldsymbol{s}_{\text{reg},i} + \boldsymbol{t} - \boldsymbol{h}_{\text{reg},i}\|^2 \overset{!}{=} \min \\
\bar{\boldsymbol{s}} &= \frac{1}{\sum_{i=1}^{n_{\mathcal{S}_{\text{reg,v}}}} w^{\triangle}_{\mathcal{S}_{\text{reg}},i}} \sum_{i=1}^{n_{\mathcal{S}_{\text{reg,v}}}} w^{\triangle}_{\mathcal{S}_{\text{reg}},i} \boldsymbol{s}_{\text{reg},i} \\
\bar{\boldsymbol{h}} &= \frac{1}{\sum_{i=1}^{n_{\mathcal{S}_{\text{reg,v}}}} w^{\triangle}_{\mathcal{S}_{\text{reg}},i}} \sum_{i=1}^{n_{\mathcal{S}_{\text{reg,v}}}} w^{\triangle}_{\mathcal{S}_{\text{reg}},i} \boldsymbol{h}_{\text{reg},i} \\
\boldsymbol{Z} &= \frac{n_{\mathcal{S}_{\text{reg,v}}}}{\sum_{i=1}^{n_{\mathcal{S}_{\text{reg,v}}}} w^{\triangle}_{\mathcal{S}_{\text{reg}},i}} [\boldsymbol{s} - \bar{\boldsymbol{s}}] \cdot \operatorname{diag}(w) \cdot \left[\boldsymbol{h} - \bar{\boldsymbol{h}}\right]^{\mathrm{T}} \\
\boldsymbol{Z} &= \boldsymbol{U}\boldsymbol{S}\boldsymbol{V}^{\mathrm{T}} \\
\boldsymbol{R} &= \boldsymbol{V}\boldsymbol{U}^{\mathrm{T}} \\
\boldsymbol{t} &= \bar{\boldsymbol{h}} - \boldsymbol{R}\bar{\boldsymbol{s}}
\end{aligned}
\tag{64}
$$

The point-to-point metric minimises the weighted error function $E_{\text{point-to-point}}$ (64). Both sets $\{\boldsymbol{h}_{\text{reg},i}\}_{i=1}^{n_{\mathcal{S}_{\text{reg,v}}}}$ and $\{\boldsymbol{s}_{\text{reg},i}\}_{i=1}^{n_{\mathcal{S}_{\text{reg,v}}}}$ are centred in $\bar{\boldsymbol{h}}$ and $\bar{\boldsymbol{s}}$, respectively, in order to calculate their weighted covariance matrix $\boldsymbol{Z} \in \mathbb{R}^3 \times \mathbb{R}^3$ (obtained from matrix multiplication). Then singular value decomposition SVD (also named principal component analysis PCA) is applied to $\boldsymbol{Z}$, from which $\boldsymbol{R}$ and $\boldsymbol{t}$ und subsequently $\boldsymbol{C}_{\text{approx}}$ (65) can be computed.

$$
\boldsymbol{C}_{\text{approx}} = \begin{bmatrix} \boldsymbol{R} & \boldsymbol{t} \\ 0\;0\;0 & 1 \end{bmatrix} \tag{65}
$$

The weighted centroids are intentionally computed based on $\boldsymbol{s}_{\text{reg},i}$ and $\boldsymbol{h}_{\text{reg},i}$ with the same area-based weights $w^{\triangle}_{\mathcal{S}_{\text{reg}},i}$, dependent on how much triangle mesh area is attributed to a single point $\boldsymbol{s}_{\text{reg},i}$. This is done instead of treating $\boldsymbol{s}_{\text{reg},i}$ and $\boldsymbol{h}_{\text{reg},i}$ as point clouds without weights, because, based on own examinations, that approach yielded better convergence behaviour. Detailed mathematical discussions of the solution of the point-to-point error metric can be found elsewhere [235].

The point-to-plane error metric minimises the function $E_{\text{point-to-plane}}$ formulated in (66) and originally proposed (without weights) by [233].

$$E_{\text{point-to-plane}} = \sum_{i=1}^{n_{\mathcal{S}_{\text{reg},\text{v}}}} w^{\triangle}_{\mathcal{S}_{\text{reg}},i} \left[\left(\boldsymbol{C}_{\text{approx}} \boldsymbol{s}_{\text{reg},i} - \boldsymbol{h}_{\text{reg},i} \right) \cdot \boldsymbol{n}_{\mathcal{S}_{\text{reg}},\text{v},i} \right]^2 \overset{!}{=} \min \tag{66}$$

Because $\boldsymbol{C}_{\text{approx}}$ is an affine 4×4 transformation matrix, which describes 3 rotational and 3 translational degrees of freedom, respectively, $\boldsymbol{s}_{\text{reg},i}$ and $\boldsymbol{h}_{\text{reg},i}$ are expanded vectors, such that $\boldsymbol{s}_{\text{reg},i} = \left[s_{i,x}\ s_{i,y}\ s_{i,z}\ 1 \right]^{\text{T}}$. Furthermore,the surface normal vector at $\boldsymbol{h}$ is denoted as $\boldsymbol{n}_{\mathcal{S}_{\text{reg}},\text{v},i} = \left[n_{i,x}\ n_{i,y}\ n_{i,z}\ 0 \right]^{\text{T}}$. This non-linear least squares optimisation problem can be solved in different ways, e.g. by linearisation of the rotation matrix. Technical discussions regarding the ICP point-to-plane error metric can be found in [236].

The third ICP variant DOF7 is formulated by (67) and characterised by the fact that isotropic scaling by the factor $c = x_7$ is additionally allowed during the optimisation (hence the name "seven degrees of freedom"), which will then be compensated again in the final affine transformation matrix $\boldsymbol{C}_{\text{approx}}$ by using $\det(c\boldsymbol{X}) = c^k \cdot \det(\boldsymbol{X})$ for $k = 3$ dimensional space as well as (62).

$$\begin{aligned}
E_{\text{DOF7}} = E_{\text{DOF7}}(\boldsymbol{x}) &= \sum_{i=1}^{n_{\mathcal{S}_{\text{reg},\text{v}}}} w^{\triangle}_{\mathcal{S}_{\text{reg}},i} \| \boldsymbol{B} \boldsymbol{s}_{\text{reg},i} - \boldsymbol{h}_{\text{reg},i} \|^2 \overset{!}{=} \min \\
\boldsymbol{x} &= [x_1, x_2, x_3, x_4, x_5, x_6, x_7] \\
\boldsymbol{S} &= \begin{bmatrix} x_7 & 0 & 0 & 0 \\ 0 & x_7 & 0 & 0 \\ 0 & 0 & x_7 & 0 \\ 0 & 0 & 0 & 1 \end{bmatrix} \\
\boldsymbol{B} = \boldsymbol{B}(\boldsymbol{x}) &= \boldsymbol{S} \cdot \boldsymbol{R}_X \cdot \boldsymbol{R}_Y \cdot \boldsymbol{R}_Z \cdot \boldsymbol{T} \\
\boldsymbol{C}_{\text{approx}} &= \frac{1}{\sqrt[k]{\det(\boldsymbol{B})}} \cdot \boldsymbol{B}
\end{aligned} \tag{67}$$

The additional degree of freedom (isotropic scaling) is represented by parameter x_7 and results in an additional scaling matrix $\boldsymbol{S}$, which can then be combined with the other matrices presented in (62). The same vector expansion applies here (as shown above). The optimisation problem is iteratively solved using Matlab's non-linear least squares solver [237] based on the trust-region-reflective algorithm enabled by additionally providing the corresponding Jacobian $J_i = \frac{\partial E_{\text{DOF7}}}{\partial x_i}$.

All ICP variants have in common that the convergence to the global minimum out of all possible transformations is not guaranteed. Instead, the optimum closest to the initial position and orientation of both meshes with respect to each other is found. Therefore, this method has a distinct path dependency, which means that it is possible to obtain different results from different start conditions (determined by coarse registration). However, the enforcement of consistent triangle meshes in combination with the fact that reasonable measurement data can be expected (it makes no sense to determine measurement uncertainty for corrupted measurements) lead to favourable behaviour of the algorithm in practice.

Fine alignment based on kernel correlation

The ICP variants discussed above all have in common that they define a ”single-linked” registration cost function. That means that for every point in the sampling start geometry ($\mathcal{S}_{\text{reg}}$), a single matching partner in the sampling target geometry ($\mathcal{T}$) is found. This matching pair is then considered in the error metric. In contrast to that, the alternative approach of kernel correlation developed by [238, 239] represents a ”multiply-linked” [239] registration cost function by interaction of all points of both geometries with each other. The method defines a closeness measure between two coordinates $\boldsymbol{a} \in \mathbb{R}^3$ and $\boldsymbol{b} \in \mathbb{R}^3$ based on a Gaussian kernel with variance σ as (68) [239].

$$K_{\text{Gauss}}(\boldsymbol{a}, \boldsymbol{b}) = (2\pi)^{\frac{3}{2}} \exp\left(\frac{\|\boldsymbol{a} - \boldsymbol{b}\|^2}{2\sigma^2}\right) \tag{68}$$

Then, a cost function $E_{\text{KC}} = E_{\text{KC}}(\mathcal{S}_{\text{reg}}, \mathcal{T}_{\text{reg}}, \boldsymbol{C}_{\text{approx}})$ is defined (69) based on the correlation of two kernel density estimates $\text{KDE}_{\mathcal{S}_{\text{reg}}}$ and $\text{KDE}_{\mathcal{T}_{\text{reg}}}$ for both sampling start geometry $\{\boldsymbol{s}_{\mathcal{S}_{\text{reg}}}\}_{i=1}^{N_{\text{v},\mathcal{S}_{\text{reg}}}}$ and sampling target geometry $\{\boldsymbol{s}_{\mathcal{T}_{\text{reg}}}\}_{i=1}^{N_{\text{v},\mathcal{S}_{\text{reg}}}}$, both point clouds. The kernel density estimates are a function of a set of grid coordinates $g = \{\boldsymbol{g}_k\}_{k=1}^{N_{\text{grid}}} \wedge \boldsymbol{g} \in \mathbb{R}^3$, which are located inside the spatial domain. They represent the coordinates at which the error function E_{KC} is evaluated. Additionally $\{\boldsymbol{s}_{\mathcal{S}_{\text{reg}}}\}_{i=1}^{N_{\text{v},\mathcal{S}_{\text{reg}}}}$ are a function of the sought-after transformation $\boldsymbol{C}_{\text{approx}}$, which is dependent on six parameters $\boldsymbol{x}$ defining a rigid transformation, as shown in (62). The variables m and n denote the number of coordinates of $\boldsymbol{s}_{\mathcal{T}_{\text{reg}}}$ and $\boldsymbol{s}_{\mathcal{S}_{\text{reg}}}$, respectively.

$$\begin{aligned}
\text{KDE}_{\mathcal{T}_{\text{reg}}}(\boldsymbol{g}) &= \sum_{i=1}^{N_{\text{v},\mathcal{T}_{\text{reg}}}} K_{\text{Gauss}}(\boldsymbol{g}, \boldsymbol{s}_{\mathcal{T}_{\text{reg}},i}) \\
\text{KDE}_{\mathcal{S}_{\text{reg}}}(\boldsymbol{g}, \boldsymbol{C}_{\text{approx}}) &= \sum_{i=1}^{N_{\text{v},\mathcal{S}_{\text{reg}}}} K_{\text{Gauss}}(\boldsymbol{g}, \boldsymbol{C}_{\text{approx}} \cdot \boldsymbol{s}_{\mathcal{S}_{\text{reg}},i}) \\
E_{\text{KC}} = E(\mathcal{S}_{\text{reg}}, \mathcal{T}_{\text{reg}}, \boldsymbol{C}_{\text{approx}}) &= -\int_{g} \text{KDE}_{\mathcal{S}_{\text{reg}}}(\boldsymbol{g}, \boldsymbol{C}_{\text{approx}}) \cdot \text{KDE}_{\mathcal{T}_{\text{reg}}}(\boldsymbol{g})\, dg \overset{!}{=} \min
\end{aligned} \tag{69}$$

The searched for affine transformation matrix $\boldsymbol{C}_{\text{approx}}$ with six parameters defining a rigid transformation is then found by solving the optimisation problem (69) [239].

The work of [238] unfortunately does not give clear recommendations for the consideration of the free parameters of the algorithm. These are the size of the Gaussian kernel σ and the definition of the grid points g, over which the cost function is evaluated. A large σ means that many neighbouring points have a significant contribution and the smoothing character of the multiply-linked approach is increased. However, if the position and orientation of $\mathcal{S}_{\text{reg}}$ and $\mathcal{T}_{\text{reg}}$ with respect to each other is not very good (in the early iterations), a small σ leads to incomplete gradient information because the contribution of distant points to the error function E_{KC} is too small. Within this thesis, the implementation of the kernel correlation registration algorithm is based on the following decisions:

- The grid points g are chosen to be the coordinates of the sampling target geometry. That means that $\text{KDE}_{\mathcal{T}_{\text{reg}}}(\boldsymbol{g})$ (69) can be directly computed.
- The value for σ decreases with each iteration by a factor of 2, starting from σ_s. The algorithm is terminated after k iterations. That means, that for the last iteration $\sigma_l = \sigma_s(\frac{1}{2})^{k-1}$, leading to a reasonable $\sigma_l \approx 0.031\,\text{mm}$ for $\sigma_s = 1\,\text{mm}$ in the context of commonly observed registration problem definitions in this thesis.
- The solution is acquired using MATLAB's non-linear programming solver `fminunc` [240] with its trust-region algorithm. The Jacobian $\boldsymbol{j}_i = \frac{\partial E_{\text{KC}}}{\partial x_i}$ and Hessian $\boldsymbol{H}_{ik} = \frac{\partial^2 E_{\text{KC}}}{\partial x_i \partial x_k}$ (first and second derivates of the objective function, respectively) are computed in advance.

The overall arithmetical complexity of registration based on the kernel correlation algorithm is high, which is why its calculations are mainly executed by a GPU (see sec. 7).

Error weights and geometry role assignment

The used ICP variants define scalar weights $w^{\triangle}_{\mathcal{S}_{\text{reg}},i}$ for each matched coordinate pair $\boldsymbol{s}_{\text{reg},i}$, $\boldsymbol{h}_{\text{reg},i}$. The weights are calculated as one third of the area of the triangle fan surrounding each $\boldsymbol{s}_{\text{reg},i}$ because within a triangle each of its 3 edge points is associated with the same fraction ($\frac{1}{3}$) of the complete triangle area. This can improve the convergence behaviour if the sampling start geometry ($\mathcal{S}_{\text{reg}}$) containing points $\boldsymbol{s}_{\text{reg},i}$ features an inhomogeneous triangle size distribution. However, the weights can not mitigate the requirement of a high quality $\mathcal{S}_{\text{reg}}$ in terms of mesh structure in order to ensure an uniform sampling of the point-wise distances between both geometries. For the computation of the solution (affine transformation matrix $\boldsymbol{C}_{\text{approx}}$) it does not matter which of both surfaces is assigned to $\mathcal{S}_{\text{reg}}$ and $\mathcal{T}_{\text{reg}}$, respectively (because $\boldsymbol{C}_{\text{approx}}$ can simply be inverted for the reverse transformation). However, for an accurate sampling and thus a more accurate registration result, it makes sense to choose that geometry as $\mathcal{S}_{\text{reg}}$ which mesh properties can be controlled without changing the underlying geometry information. If the nominal geometry is available for registration, it is always possible to generate a mesh conforming to favourable properties, as described in sec. 5.4. The same applies if a TCMS reference measurement is available and prepared according to sec. 5.4. This approach is preferable compared to modifying the triangle mesh of the measurement data, because it contains the uncertainty information of the examined measurement system. Therefore, registration as part of the spatially discrete metrological descriptor framework is conducted such that the template geometry $\mathcal{M}^{\text{tri}}_{\text{template}}$ (the data geometry d is "registered onto" the template geometry) is set as the $\mathcal{S}_{\text{reg}}$.

5.6.3 Performance evaluation for different methods

In order to evaluate the quality of the results obtained from different registration algorithms, the methods described above were implemented and tested. Furthermore, results from commercial software products were gathered in order to provide a reference for the other methods. The measurement data consists of 20 repeated (simulated) CT measurements from [P13]. This data set is considered as a best case scenario[90], because the systematic measure-

---

[90] The registration of two identical objects against each other (but with different starting coordinate systems) yielded results within the numerical precision.

ment errors are small with respect to the size of the object. The template geometry $\mathcal{M}^{\text{tri}}_{\text{template}}$ is equal to the input geometry for the simulation (the geometry which was measured), but with altered triangle mesh properties, such that a Gaussian-shaped triangle edge length distribution with a mean value of approx. 250 µm (resulting in roughly 240 000 triangles) was obtained. The commercial software products use the unaltered geometry, which was generated from the CAD file by Autodesk Inventor 2019 (the exact mesh that was used as input for the simulation), because potentially required additional mesh processing is the responsibility of the software product. Additionally, due to the offered CAD interface, both examined commercial products were tested also using the original CAD file as input for the registration[91]. Each of the 20 measurement was registered individually against $\mathcal{M}^{\text{tri}}_{\text{template}}$. The quality of the registration result was judged identically for all examined methods with the triangle mesh affinity measure defined in (54) using the same geometry as $\mathcal{M}^{\text{tri}}_{\text{template}}$ (target mean triangle edge length of 250 µm). For each pair-wise registration, two scalar TMA values can be determined by exchanging the sampling start surfaces: $\text{TMA}_{A,B}$ and $\text{TMA}_{B,A}$. Two scenarios were tested: $\mathcal{M}^{\text{tri}}_{\text{template}}$ as $\mathcal{S}_{\text{reg}}$ and $\mathcal{M}^{\text{tri}}_{\text{data}}$ as $\mathcal{T}_{\text{reg}}$ and vice versa. The following 25 different registration procedures were examined:

- **VGSseqReg**: VGStudio Max 3.5 sequential registration using two cylinders as described above.
- **VGSbestFit**: VGStudio Max 3.5 ”best fit” registration against $\mathcal{M}^{\text{tri}}_{\text{template}}$.
- **VGSbestFitCAD**: VGStudio Max 3.5 ”best fit” registration against $\mathcal{M}^{\text{tri}}_{\text{template}}$ represented as STEP CAD file.
- **VGSbestFitVol**: VGStudio Max 3.5 ”best fit” registration against $\mathcal{M}^{\text{tri}}_{\text{template}}$ using the CT volume data instead of the measurement data in form of a triangle mesh. This can improve the result because a measurement triangle mesh is possibly already a simplification compared to the original CT data.
- **PWbestFit**: PolyWorks 2020 ”best fit” registration against $\mathcal{M}^{\text{tri}}_{\text{template}}$. Here, automatic processing was not possible and additional manual steps for a better pre-alignment were requested by the software user interface.
- **PWbestFitCAD**: PolyWorks 2020 ”best fit” registration against $\mathcal{M}^{\text{tri}}_{\text{template}}$ represented as STEP CAD file.
- **mlClosed, mlPoint2Plane**: MATLAB’s registration functionality provided by `pcregistericp` [241] based on point cloud objects (`pointCloud` [242]). The required vertex normal vectors were provided from the triangle mesh, however, the algorithms are not able to consider weights.
- **cepClosed**: CEP sampling with the closed solution of the point-to-point error metric (64)

---

[91] The CAD file and an extracted triangle mesh do not represent exactly the same geometry (for objects with regions of finite curvature), because of approximation errors.

- **cepPoint2Plane**: CEP sampling with the point-to-plane error metric (66)
- **cepDOF7**: CEP sampling with the DOF7 error metric (67).
- All other 12 combinations between the described name error metrics (”closed”, ”point2plane” ”DOF7”) and the different sampling methods VNV, SD, SDSP and SDHP.
- **KC1**: Kernel correlation with $\sigma_s = 1$ mm and six iterations.
- **KC05**: Kernel correlation with $\sigma_s = 0.5$ mm and six iterations.

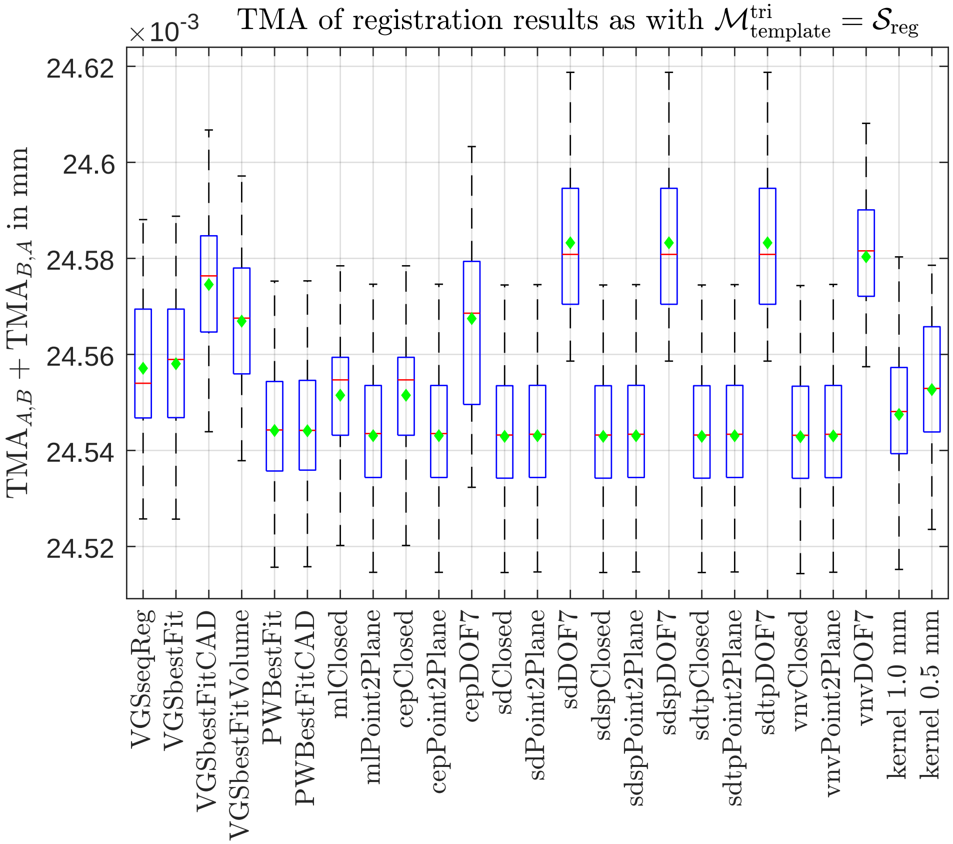

Figure 33: Comparing 25 different registration methods and variants for 20 single measurements. The figure shows the sum of $\text{TMA}_{A,B}$ and $\text{TMA}_{B,A}$. The median and mean values are shown by red lines and green diamonds, respectively. Overall, the differences between the examined methods are very small. The exact ranking of results is given in (70).

Overall, 20 measurements were registered against the same template geometry $\mathcal{M}^{\text{tri}}_{\text{template}}$ using the 25 different methods described above. The results are visualised in Figure 33. The exact ranking (lower values are better) with respect to $\mathrm{TMA}_{A,B} + \mathrm{TMA}_{B,A}$ is listed in (70).

$$\begin{aligned}
&\text{vnvClosed} \leq \text{sdClosed} \leq \text{sdspClosed} \leq \text{sdtpClosed} \leq \text{vnvPoint2Plane}\\
&\leq \text{sdPoint2Plane} \leq \text{sdspPoint2Plane} \leq \text{sdtpPoint2Plane}\\
&\leq \text{mlPoint2Plane} \leq \text{cepPoint2Plane} \leq \text{PWBestFitCAD} \leq \text{PWBestFit}\\
&\leq \text{kernel } 1.0\text{ mm} \leq \text{cepClosed} \leq \text{mlPoint2Point} \leq \text{kernel } 0.5\text{ mm}\\
&\leq \text{VGSseqReg} \leq \text{VGSbestFit} \leq \text{VGSbestFitVolume} \leq \text{cepDOF7}\\
&\leq \text{VGSbestFitCAD} \leq \text{vnvDOF7} \leq \text{sdDOF7} \leq \text{sdspDOF7} \leq \text{sdtpDOF7}
\end{aligned} \tag{70}$$

The ICP variant based on the closed solution (64) produces the smallest mean TMA value, followed by the point2Plane error function (66). The method using 7 degrees of freedom (67) performs slightly worse, which is generally also the case for CEP sampling. The commercial solutions tend to perform slightly worse, which can be caused by different methods/data (e.g. sequential registration, registration against STEP CAD file and the requirement of manual interaction) as well as the additional introduction of weights within the own implementations. Registration based on kernel correlation performs inconspicuous, however the sensitivity towards the internal parameter selection (σ_s and therefore the dependency on the number of performed iterations) becomes clear. It is important to note that the ranking is created based on the proposed TMA, which might not be optimal for different use cases. In general, it can be expected that the tested commercial products are more robust and offer more flexibility compared to the own implementations, especially when considering, that the presented benchmark is close to a "best case" due to the low geometrical deviations between the geometries.

The shown results rate the different algorithms by their capability of reaching low TMA values. This reflects the intended behaviour of the underlying optimisation problems. That means that local geometric differences between the processed geometries (here simulated measurement results and the simulation input geometry) affect the registration result with respect to the optimisation tasks. The mean $\mathrm{TMA}_{A,B} + \mathrm{TMA}_{B,A}$ when applying the true transformation (as given to the simulation) is $24.605 \cdot 10^{-3}$ mm. Therefore, it is important to be aware of how "best-fit" registration works when using these results within the data processing pipeline of the spatially discrete descriptor framework.

5.6.4 Simultaneous registration of multiple geometries

The previous chapters described pairwise registration methods, which are performed independently of each other, such that for example each single measurement of a measurement series is registered against a second geometry (nominal or reference geometry, respectively). Therefore, evaluations based on that kind of registration implicitly assume that location and orientation of repeated measurement data inside the coordinate system of the measurement system with respect to each other are not important for the characterisation of the observed local geometry interaction. This is due to the fact that drift effects could be partially compensated by that kind of registration, because the determined spatially discrete metrological descriptors are only dependent on the best possible matching, found by the described registration. There are however use cases where the location and orientation of repeated measurements with respect to each other are of special interest. Then, the registration task changes from an $\mathrm{REG}_{1\rightarrow 1}$ pairwise registration to a $\mathrm{REG}_{1\rightarrow n}$ registration problem, where the optimal position and orientation of a single geometry (nominal or reference geometry, respectively) is simultaneously determined against all n measurements of the complete measurement series. In other words, the position and orientation of repeated measurements with respect to each other is unaffected by this kind of registration. Therefore, the spatially discrete metrological descriptor framework additionally offers functionality for simultaneous $\mathrm{REG}_{1\rightarrow n}$ registration. Mathematically, the $\mathcal{S}_{\mathrm{reg}}$

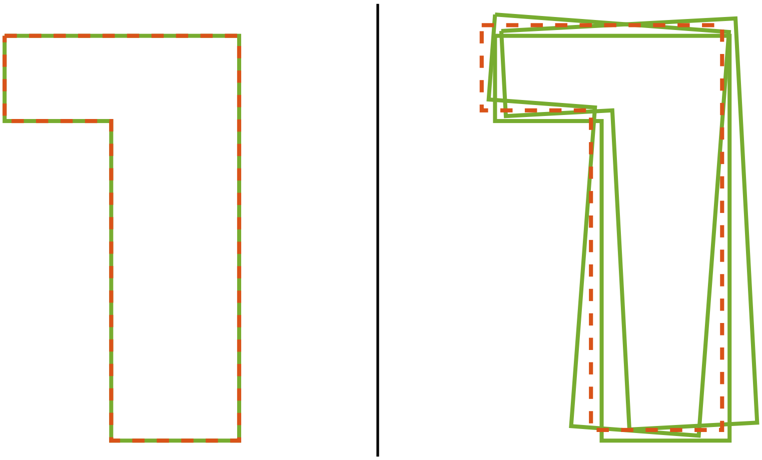

Figure 34: Comparing $\mathrm{REG}_{1\rightarrow 1}$ registration (left) with $\mathrm{REG}_{1\rightarrow n}$ registration (right) with a measurement series consisting of 3 measurements (green) and a secondary geometry (red). The relative position and orientation is preserved for $\mathrm{REG}_{1\rightarrow n}$ registration which can be a desired behaviour, depending on the use case.

is fixed to be the template geometry $\mathcal{M}^{\text{tri}}_{\text{template}}$ and the coordinate $\boldsymbol{h}_{\text{reg},i}$ is then the result of an averaging of the matching results of n surfaces (64), (66), (67). Otherwise, the method remains unchanged and the approach is (currently) not supported for registration based on kernel correlation. The principle is visualised in Figure 34, where a measurement series of 3 repeated measurements (green) is registered against a secondary geometry. The registration compensates relative differences in position and orientation of the single measurements with respect to each other when $\text{REG}_{1\rightarrow 1}$ registration is used (left side), compared to $\text{REG}_{1\rightarrow n}$ registration (right side). This kind of registration ($\text{REG}_{1\rightarrow n}$) is usually not supported directly by commercial software. One possible workaround can be to merge all n measurements into one single triangle mesh and perform the registration using this file. However, it is not guaranteed that the sampling will be performed correctly, moreover, the resulting mesh does not represent a physical object.

5.6.5 Alternative registration methods

A popular alternative approach to registration is called ”Random Sample Consensus (RANSAC)”, originally proposed by [243]. It is based on repeated random minimal subset sampling and model fitting, such that the result most strongly supported by the conducted trials (random samples) yields the desired solution [244]. However, complex algorithmic details need to be figured out (robust termination criteria while dealing with a high number of iterations), which is reflected by the fact that many variants exist [245]. The method was not tested within the context of this thesis because of its random nature, which can limit the reproducibility of the results, contributing to unwanted method uncertainty.

5.6.6 Summary of the registration decision tree

This section summarises the main options available in the registration pipeline.

Type: By default, $\text{REG}_{1\rightarrow 1}$ registration is applied, or if only 2 geometries should be aligned with each other (e.g. for a nominal-actual comparison). However, it can be beneficial to choose $\text{REG}_{1\rightarrow n}$ registration over $\text{REG}_{1\rightarrow 1}$ if:

- Position and orientation of individual measurements of a measurement series should be preserved with respect to each other.
- Potential drifts during the measurement should contribute to the measurement error.
- Repeatability of a measurement should be defined with respect to the coordinate system of the measurement system.

- The object has one or more symmetry planes (e.g. a gear wheel).

$\mathcal{S}_{\text{reg}}$ **(sampling start geometry):** Choose the $\mathcal{S}_{\text{reg}}$ either as template $\mathcal{M}^{\text{tri}}_{\text{template}}$ or measurement $\mathcal{M}^{\text{tri}}_{\text{data}}$, depending on:

- $\mathcal{S}_{\text{reg}}$ should be primarily that geometry whose mesh properties are easier to control, without introducing changes affecting the metrological characteristics of a measurement.
- If the shapes of $\mathcal{M}^{\text{tri}}_{\text{data}}$ and $\mathcal{M}^{\text{tri}}_{\text{template}}$ deviate strongly from each other and if $\mathcal{M}^{\text{tri}}_{\text{data}}$ shows high surface roughness, it can be advantageous to choose $\mathcal{M}^{\text{tri}}_{\text{data}}$ as $\mathcal{S}_{\text{reg}}$ because of the effects explained in Figure 19.
- If both the nominal geometry and the reference geometry are available, it is better to select the reference measurement as $\mathcal{S}_{\text{reg}}$ because it can be assumed that it reflects the geometry measured by the primary system better than the nominal geometry (because of manufacturing deviations between the nominal and the reference geometry, respectively).
- In case of 1:n registration, the $\mathcal{S}_{\text{reg}}$ is by design always $\mathcal{M}^{\text{tri}}_{\text{template}}$.

Error metric / sampling: Consider the following for choosing an error metric:

- If the data processing pipeline allows for sufficient automation and if $\text{REG}_{1\to 1}$ registration is targeted, use commercial products for increased robustness and reliability.
- If automated best fit registration is required within the processing pipeline or if $\text{REG}_{1\to n}$ registration is needed, choose vnvClosed or sdClosed by default.
- Expert users might choose other metric / sampling combinations for special applications.

In case the registration should be performed based on external datums and datum systems, the looked-for transformation must be determined using external (commercial) software. The results $\boldsymbol{C}_{\text{approx}}$ can then be imported and considered for the following determination of the metrological descriptors (see following section).

5.7 Determination of metrological descriptors

This section puts all of the previous steps together to form the spatially discrete metrological descriptor framework. Due to its great flexibility regarding its use cases, the data processing pipeline differs slightly depending on the available inputs and targeted metrological descriptors. The three possible geometry input types are:

- $\mathcal{N}$: Nominal geometry representation of the examined measurement object in form of a triangle mesh as described in sec. 5.4.
- $\mathcal{R}$: Single[92] reference measurement of the examined measurement object in form of a triangle mesh, as described in sec. 5.5.
- $\mathcal{M} = \{M_j\}_{j=1}^{n_{\text{MS}}}$: Measurement series consisting of at least $n = 20$ measurement repetitions (following the recommendation in DIN EN ISO 15530-3:2018-09 [43] and VDI/VDE 2630:2015-06 Part 2.1 [139]) of the examined measurement object represented as triangle meshes and satisfying the repeatability condition of measurement defined in VIM [10].

The measurement series $\mathcal{M}$ is captured with that (primary) measurement system for which the metrological characteristics should be determined. The reference measurement $\mathcal{R}$ is a (single) measurement with a second system that should act as a reference with respect to the first system. The actual classification of systems is a choice made by the user of the spatially discrete metrological descriptor framework and impacts the meaningfulness of the results in a metrological context.

The metrological characterisations are based on the pairwise computation of the distance fields between surfaces, as described in sec. 5.3. Depending on their availability, the three geometry input types $\mathcal{N}$, $\mathcal{R}$ and $\mathcal{M}$ are classified as sampling start surface (SS), primary sampling target (PST) or secondary sampling target (SST). The exact classification depends on the intended use case and hence the type of information intended to be obtained by the application of the spatially discrete metrological descriptor framework. All sampling targets (PST/SST) are sampled starting from the only sampling start surface (SS) and the resulting distance metrics (e.g. t_i for each point on the sampling start surface $\boldsymbol{s}_i$) are captured for each of the sampling targets. Therefore, all sampling information is associated with the data structure of SS, meaning that for each $\boldsymbol{s}_i$, n_{MS} t_i are captured, which are expressed in the following as $\{t_{i,j}\}_{j=1}^{n_{\text{MS}}}$ (same applies for α_i and all other parameters obtained by the distance field calculations). Based on that information both conventional and unconventional metrological descriptors can be computed as described in the next chapters.

In the following, the functions `mean`$(\boldsymbol{x})$ and `std`$(\boldsymbol{x})$ denote the arithmetic mean and the standard deviation of a data vector $\boldsymbol{x} = \{x_k\}_{k=1}^{N}$ of length N. In the same way, the median is denoted as `median`$(\boldsymbol{x})$.

---

[92] Although the framework is in principle capable of processing reference measurement series in the form of $\mathcal{R} = \{R_j\}_{j=1}^{m}$ of size m, this scenario is highly unlikely in the context of practical applications because of the high effort required for the additional measurements and the limited additional benefits. Therefore, the following descriptions assume the processing of a single reference measurement $\mathcal{R}$.

5.7.1 Conventional metrological descriptors

The conventional metrological descriptors of the spatially discrete metrological descriptor framework based on distance measurements are defined as follows for each sampling point $\boldsymbol{s}_i$:

- E_{sys}: The estimation of the local systematic measurement error.
- E_{rand}: The estimation of the local random measurement error.
- Δ_{cmp}: The estimation of the local geometric deviations of the examined component.
- $\Delta_{\text{cmp}}^{E_{\text{sys}}}$: The estimation of the superimposition of the local systematic measurement error and the geometric deviations of the examined component.

The possibility to determine the named conventional metrological descriptors is dependent on the available types of geometry and their specific calculation relies on the applied use case (UC), as collectively shown in Table 5.

Table 5: Different use cases (UC) of the spatially discrete metrological descriptor framework depending on the availability of each of the three geometry input types "nominal geometry ($\mathcal{N}$)", "reference measurement ($\mathcal{R}$)" and "measurement series ($\mathcal{M}$)". There are 9 different types of use cases, each distinguished by different combinations of "sampling start surface (SS)", "primary sampling target surface (PST)" and "secondary sampling target surface (SST)", resulting in varying opportunities to determine the dimensional metrological descriptors "systematic measurement errors (E_{sys})", "random measurement errors (E_{rand})", "component deviations (Δ_{cmp})" and the "superimposition of component deviations and systematic measurement errors ($\Delta_{\text{cmp}}^{E_{\text{sys}}}$)". $\mathcal{M}^*$ means the selection of one measurement of $\mathcal{M}$ based on a criterion described further below in this section. Generally, it is assumed that $\mathcal{M}$ consists of at least 20 measurement repetitions, however the edge case of a single measurement is denoted by $\mathcal{M}^\dagger$.

UC	SS	PST	SST	E_{sys}	E_{rand}	Δ_{cmp}	$\Delta_{\text{cmp}}^{E_{\text{sys}}}$
1a	$\mathcal{N}$	$\mathcal{R}$	$\mathcal{M}$	yes	yes	yes	yes
1b	$\mathcal{R}$	$\mathcal{N}$	$\mathcal{M}$	yes	yes	yes	yes
2a	$\mathcal{N}$	$\mathcal{M}$	-	no	yes	no	yes
2b	$\mathcal{R}$	$\mathcal{M}$	-	yes	yes	no	no
3	$\mathcal{M}^*$	$\mathcal{M}$	-	no	yes	no	no
4a	$\mathcal{N}$	$\mathcal{R}$	-	no	no	yes	no
4b	$\mathcal{R}$	$\mathcal{N}$	-	no	no	yes	no
5a	$\mathcal{N}$	$\mathcal{M}^\dagger$	-	no	no	no	yes
5b	$\mathcal{R}$	$\mathcal{M}^\dagger$	-	yes	no	no	no
5c	$\mathcal{M}^\dagger$	$\mathcal{N}$	-	no	no	no	yes
5d	$\mathcal{M}^\dagger$	$\mathcal{R}$	-	yes	no	no	no

The following rules apply:

1. The systematic measurement errors are calculated with respect to the reference measurement $\mathcal{R}$. If $\mathcal{R}$ is undefined, E_{sys} is also undefined.
2. The estimation of the random measurement errors is always calculated as $E_{\text{rand}} = \texttt{std}(\{t_{i,j}\}_{j=1}^{n_{\text{MS}}})$. If $n < 2$, E_{rand} is undefined.
3. The component deviations Δ_{cmp} are calculated with respect to the nominal geometry $\mathcal{N}$. If $\mathcal{N}$ is undefined, Δ_{cmp} can not be determined.
4. The superimposition of E_{sys} and Δ_{cmp} is determined as $\Delta_{\text{cmp}}^{E_{\text{sys}}}$. It can be either computed as $\Delta_{\text{cmp}}^{E_{\text{sys}}} = E_{\text{sys}} + \Delta_{\text{cmp}}$ if both E_{sys} and Δ_{cmp} are defined. Alternatively, it can be calculated by sampling $\mathcal{M}$ with $\mathcal{N}$ defined as sampling start surface SS.

The interpretation of Table 5 is done as follows at the example of the use case $\text{UC}_{4\text{a}}$: The nominal geometry $\mathcal{N}$ and a single reference measurement ($\mathcal{R}$) are compared against each other, with the $\mathcal{N}$ representing the sampling start surface (SS). In this configuration, the measurement series $\mathcal{M}$ is missing. Therefore, only the component deviations Δ_{cmp} can be calculated. The signed distances t_i are determined with respect to the SS. Consequently, Δ_{cmp} for each $\boldsymbol{s}_i$ with are calculated as $\Delta_{\text{cmp}}(\text{UC}_{4\text{a}}) = -t_i$. Thinking further, $\Delta_{\text{cmp}}(\text{UC}_{4\text{b}}) = t_i$. Here, the same descriptor was determined, but with the sampling start surface (SS) and the primary sampling target (PST) exchanged with each other. Although there are exceptions (e.g. sampling two parallel surfaces), in general $\Delta_{\text{cmp}}(\text{UC}_{4\text{a}}) \neq \Delta_{\text{cmp}}(\text{UC}_{4\text{b}})$ holds. The reason for that lies in the nature of the geometric sampling (see sec. 5.3).

The calculation rules for obtaining E_{sys} (71), E_{rand} (72), Δ_{cmp} (73) and $\Delta_{\text{cmp}}^{E_{\text{sys}}}$ (74) depending on the available data and sampling start surface are listed below. Here $\texttt{mean}(\{t(\text{SST})_{i,j}\}_{j=1}^{n_{\text{MS}}})$ is the mean t_i resulting from sampling of SST for each sampling point $\boldsymbol{s}_i$. Other parameters are used equivalently.

$$E_{\text{sys}} = \begin{cases} \texttt{mean}(\{t(\text{SST})_{i,j}\}_{j=1}^{n_{\text{MS}}}) - t(\text{PTS})_i & \text{UC}_{1\text{a}} \\ \texttt{mean}(\{t(\text{SST})_{i,j}\}_{j=1}^{n_{\text{MS}}}) & \text{UC}_{1\text{b}} \\ \texttt{mean}(\{t(\text{PST})_{i,j}\}_{j=1}^{n_{\text{MS}}}) & \text{UC}_{2\text{b}} \\ t(\text{PTS})_i & \text{UC}_{5\text{b}} \\ -t(\text{PTS})_i & \text{UC}_{5\text{d}} \\ \emptyset & \text{otherwise} \end{cases} \tag{71}$$

The approach to define the sign of the metrological descriptors is shown for the use case $\text{UC}_{1\text{a}}$ in Figure 35. Here the nominal geometry $\mathcal{N}$ is the sampling start surface (SS), thus it defines the common coordinate frame because the

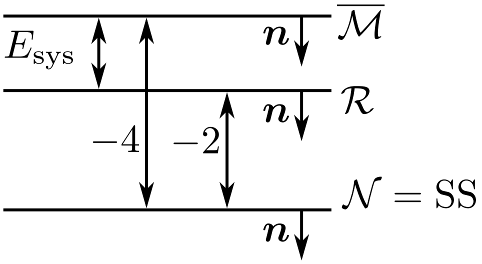

Figure 35: Calculating E_{sys} for use case 1a. Applying the numbers shown in the example, $E_{\text{sys}} = (-4) - (-2) = -2$. The sign of the distances values depends on the surface normal vector of the sampling start surface (here $\mathcal{N}$).

distance are calculated with respect to that surface. The mean surface of the measurement series $\mathcal{M}$ is shown as $\overline{\mathcal{M}}$ in order to simplify the figure. The visualisation shows that the correct value for E_{sys} evaluates according to (71) as $E_{\text{sys}} = (-4) - (-2) = -2$. $\overline{\mathcal{M}}$ lies ”behind” the surface of $\mathcal{R}$ with respect to its normal vector[93]. Consequently, the sign must be negative because E_{sys} is determined with respect to the reference value $\mathcal{R}$. The same reasoning is applied for the other cases demonstrated in (71), (72), (73) and (74).

$$E_{\text{rand}} = \begin{cases} \texttt{std}(\{t(\text{SST})_{i,j}\}_{j=1}^{n_{\text{MS}}}) & \text{UC}_{1a} \lor \text{UC}_{1b} \\ \texttt{std}(\{t(\text{PST})_{i,j}\}_{j=1}^{n_{\text{MS}}}) & \text{UC}_{2a} \lor \text{UC}_{2b} \lor \text{UC}_{3} \\ \emptyset & \text{otherwise} \end{cases} \tag{72}$$

$$\Delta_{\text{cmp}} = \begin{cases} t(\text{PST})_i & \text{UC}_{1a} \lor \text{UC}_{4a} \\ -t(\text{PST})_i & \text{UC}_{1b} \lor \text{UC}_{4b} \\ \emptyset & \text{otherwise} \end{cases} \tag{73}$$

$$\Delta_{\text{cmp}}^{E_{\text{sys}}} = \begin{cases} E_{\text{sys}} + \Delta_{\text{cmp}} & \text{UC}_{1a} \lor \text{UC}_{1b} \\ \texttt{mean}(\{t(\text{PST})_{i,j}\}_{j=1}^{n_{\text{MS}}}) & \text{UC}_{2a} \\ t(\text{PST})_i & \text{UC}_{5a} \\ -t(\text{PST})_i & \text{UC}_{5c} \\ \emptyset & \text{otherwise} \end{cases} \tag{74}$$

The special cases UC_{5a} and UC_{5b} listed in Table 5 represent two types of classical nominal-actual comparisons, where a single measurement is compared against the nominal geometry or a reference measurement, respectively. The

---

[93] In this example, this approach requires the normal vectors $\boldsymbol{n}$ of $\mathcal{R}$ and $\mathcal{N}$ to locally point into the same half space. Except for some rare (theoretical) edge cases, this condition is satisfied for practical situations.

cases with UC_{4a} and UC_{5a} both feature $\mathcal{N}$ as SS, which samples a single primary sampling target (PST). The differentiation is justified by the different significance of $\mathcal{R}$ and $\mathcal{M}^\dagger$ in the context of this framework, because a $\mathcal{R}$ expects the (imaginary) presence of a measurement series MS for which it acts as a reference. Interestingly, in case UC_{5b} it is possible to mathematically[94] estimate E_{sys} but not E_{rand} from a measurement series of size one $\mathcal{M}^\dagger$. UC_{5c} and UC_{5d} are special cases of UC_{5a} and UC_{5b}, respectively, by uniquely selecting the measurement data as sampling start surface. This allows for the realisation of nominal actual comparison with direct false-colour representation of local geometry deviations.

The use cases UC_{1a}, UC_{1b} and UC_{2b} are uniquely capable of determining the (expanded) measurement uncertainty U_{exp}, because they provide both E_{sys} and E_{rand}. The associated calculation rule (75) [246] is similar to (25), but assumes that $u(E_{\mathrm{sys}}) = 0$, because there was no reasonable data available[95]. Typically, a coverage factor $k = 2$ is applied in practice.

$$U_{\mathrm{exp}} = k\sqrt{(E_{\mathrm{sys}})^2 + (E_{\mathrm{rand}})^2} \tag{75}$$

Lastly, the use case with UC_3 is special because it estimates the random measurement errors (E_{rand}) purely from a set of repeated measurements $\mathcal{M}$. The surface $\mathcal{M}^*$ is one surface selected from $\mathcal{M}$ by evaluation of an optimisation problem, such that $\mathcal{M}^*$ lies between all other surfaces of $\mathcal{M}$ resulting in the smallest sum of errors. Starting from $\mathcal{M}^*$, all other $n_{\mathrm{MS}} - 1$ surfaces in $\mathcal{M}$ are then sampled, and the evaluation of the distance fields can be done with the already described calculation rules. A detailed description of the methodology can be found in [P11].

5.7.2 Unconventional metrological descriptors

The previously described conventional metrological descriptors are complemented by a set of unconventional ones. They are mainly dependent on the applied sampling strategy and evaluate the angles α_i and β_i, as well as the vectors $\boldsymbol{d}_i$ connecting a sampling start point $\boldsymbol{s}_i$ with its hit location on the target geometry (see sec. 5.3). For each of the following metrological descriptors $\exists\mathcal{M}$ is assumed and it is not relevant for their definition, if $\mathrm{SS} = \mathcal{N}$ or $\mathrm{SS} = \mathcal{R}$.

---

[94] It possible to calculate the mean value of a sample of size one but not its empirical standard deviation.

[95] Given another reference measurement for the used reference measurement (with even lower measurement uncertainty), this is something that can be determined using the spatially discrete metrological descriptor framework.

Statistics regarding α_i and β_i

The parameter α_i was defined as the smallest angle between the normal vector $\boldsymbol{n}_{\mathcal{S},\mathrm{v},i}$ of each sampling start point $\boldsymbol{s}_i$ and $\boldsymbol{d}_i$, which connects $\boldsymbol{s}_i$ with the hit location $\boldsymbol{h}_i$ on the target surface. $\alpha_i = 0$ applies by definition for sampling strategies "shortest distance to plane (SDP)" and "vertex normal vector (VNV)". However, for the sampling methods "closest edge point (CEP)" and "shortest distance (SD)", the values $\{\alpha_{i,j}\}_{j=1}^{n_{\mathrm{MS}}}$ are expected to fluctuate for repeated measurements. The metrological descriptors $\alpha_{\mathrm{sys}} = \mathtt{mean}(\{\alpha_{i,j}\}_{j=1}^{n_{\mathrm{MS}}})$ and $\alpha_{\mathrm{rand}} = \mathtt{std}(\{\alpha_{i,j}\}_{j=1}^{n_{\mathrm{MS}}})$ provide information about the statistics of the tilting of $\{\boldsymbol{d}_{i,j}\}_{j=1}^{n_{\mathrm{MS}}}$ with respect to $\boldsymbol{n}_{\mathcal{S},\mathrm{v},i}$ of the sampling start surface (SS). Large values for α_{sys} suggest larger local differences between the surface pair, while large values for α_{rand} can indicate a high surface roughness.

Similar examinations can be defined for the opposing angle β_i, which is calculated by the surface normal vector at the target location and the connection vector $\boldsymbol{d}_i$ from $\boldsymbol{s}_i$ to that target location. The corresponding metrological descriptors are defined as $\beta_{\mathrm{sys}} = \mathtt{mean}(\{\beta_{i,j}\}_{j=1}^{n_{\mathrm{MS}}})$ and $\beta_{\mathrm{rand}} = \mathtt{std}(\{\beta_{i,j}\}_{j=1}^{n_{\mathrm{MS}}})$.

Construction of deviation ellipsoids from $\boldsymbol{d}_i$

The covariance matrix of $\{\boldsymbol{d}_{i,j}\}_{j=1}^{n_{\mathrm{MS}}}$ can be used to construct an error ellipsoid for each $\boldsymbol{s}_i$ describing the variance of the intersection results in different directions. This applies only to the sampling methods CEP and SD, because the other methods SDP, SDHP and VNV determine intersections solely in the direction of a constant vector. The singular value decomposition (SVD) of the diagonal 3×3 covariance matrix yields three eigenvalues $\lambda_1 \geq \lambda_2 \geq \lambda_3$ and three eigenvectors $\{\boldsymbol{\Lambda}_1, \boldsymbol{\Lambda}_2, \boldsymbol{\Lambda}_3\}$ which form an orthogonal base. This information can be used to describe an ellipsoid, which is defined by three pairwise perpendicular axes of symmetry (eigenvectors of the covariance matrix) of lengths corresponding to the aforementioned eigenvalues. From that, two parameters are derived:

$$\lambda_{\mathrm{ratio},i} = \log_{10}\left(\frac{\lambda_1}{\sqrt{\lambda_2^2 + \lambda_3^2}}\right) \tag{76}$$

The parameter $\lambda_{\mathrm{ratio},i}$ (76) determines the ratio of the largest eigenvalue compared to the other two and therefore describes the shape of the ellipsoid. If all eigenvalues are equal, the ellipsoid can be described by a sphere.

$$\gamma_i = \arccos(|\boldsymbol{\Lambda}_1 \cdot \boldsymbol{n}_{\mathcal{S},\mathrm{v},i}|) \tag{77}$$

The second parameter γ_i (77) describes the orientation of the main axis of the ellipsoid (described by $\boldsymbol{\Lambda}_1$) with respect to the vertex normal vector $\boldsymbol{n}_{\mathcal{S},\mathrm{v},i}$ of the corresponding sampling point $\boldsymbol{s}_i$.

Identification of drifts

In case the examined measurement system reports the measurement result with respect to its base coordinate system, the measurement data can be examined for possible drifts. That is, the position of the measurement object within the coordinate system of the measurement system changes from the first to the last measurement, which can be caused by thermal effects or especially in industrial X-ray CT if elastic clamping based on styrofoam is used. This kind of examination requires a specific targeting during the measurement registration (non-pairwise 1:n registration, see sec. 5.6) or the application of use case UC_3 (because no coordinate transformation is applied here).

$$\mathrm{Drift} = \frac{1}{n-1} \sum_{k=1}^{n-1} T_{k+1} - T_k \tag{78}$$

The calculation is laid out in (78) with T denoting the values $\{t_{i,j}\}_{j=1}^{n_{\mathrm{MS}}}$ for $\boldsymbol{s}_i$. The values T are consecutively summed up. However, their values only have meaning with respect to each other. Ideally, the determined values for the drift are zero. This parameter is especially well suited for visual inspection using false-colour plots.

5.7.3 Spatial correlation of metrological descriptors

Each sampling point $\boldsymbol{s}_i$ is associated with a set of conventional and unconventional metrological descriptors. Their determination is strictly independent of each other. Therefore, statements about the lateral correlation of metrological descriptors is only possible implicitly due to visual inspection of the results. However, there are scenarios where numerical statements about the correlation of neighbouring $\boldsymbol{s}_i$ with respect to their metrological descriptors are required. At first, the spatial domain has to be determined, which can be done in two different ways (Figure 36). For each $\boldsymbol{s}_i$, x-ring neighbourhoods can be defined, with $x = \{1, 2, \ldots, x_{\mathrm{max}}\}$. The 1-ring neighbourhood R_1 contains all $\boldsymbol{r}_{1,j}$ (red, without $\boldsymbol{s}_i$), the 2-ring neighbourhood R_2 contains both $\boldsymbol{r}_{1,j}$ and $\boldsymbol{r}_{2,k}$ (blue), and so forth. Using these sets, the scalar parameter $\mathrm{SpatCorr}_{t_i,R_k}$ can be determined for each $\boldsymbol{s}_i$ (79).

$$\mathrm{SpatCorr}_{t_i,R_x} = \frac{\texttt{mean}(\{t(\boldsymbol{s}_i)_k\}_{k=1}^{n_{\mathrm{MS}}}) - \texttt{mean}(\{t(R_x)_k\}_{k=1}^{n_{\mathrm{MS}}})}{\texttt{std}(\{t(R_x)_k\}_{k=1}^{n_{\mathrm{MS}}})} \tag{79}$$

Here, $\texttt{mean}(\{t(R_x)_k\}_{k=1}^{n_{\text{MS}}})$ results in a scalar value (mean over all values, same applies for `std(...)`). The correlation of other (scalar) parameters (e.g. α_i) can be calculated equivalently. The absolute value of the metrological descriptor $\text{SpatCorr}_{t_i,R_k}$ is high if the difference between the mean value of the parameter associated with $\boldsymbol{s}_i$ and those in its x-ring neighbourhood is large compared to the dispersion of values within the domain. This approach used the mesh connectivity to establish the local domain around $\boldsymbol{s}_i$. Alternatively, the domain can be constructed based on an user defined search radius, as shown in Figure 36 for two exemplary radii r_a and r_b. Here, both types of domains are equal, because of the very regular mesh structure in this example. Typically, this property is not satisfied for larger x.

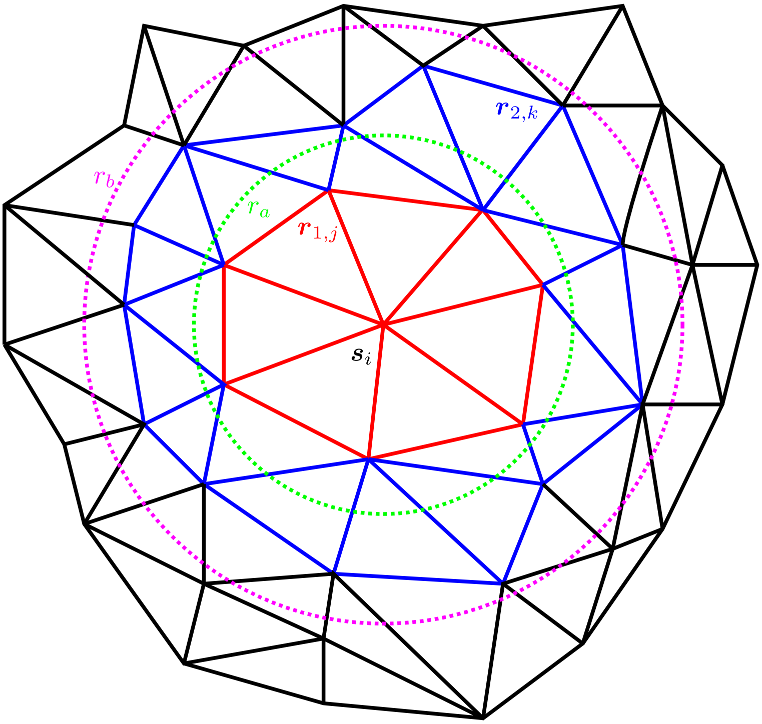

Figure 36: Defining different domains for the evaluation of the spatial correlation of metrological descriptors. The first method is to define the x-ring neighbourhoods around each $\boldsymbol{s}_i$ (here R_1 and R_2 are shown). Alternatively, the domain is constructed based on a search radius, for which examples r_a and r_b are drawn. All points within a specific domain contribute to the evaluation of the spatial correlation with respect to $\boldsymbol{s}_i$ according to (79).

5.7.4 More statistical properties of the distributions $\{t_{i,j}\}_{j=1}^{n_{\mathrm{MS}}}$

Within this framework, typically $n_{\mathrm{MS}} = 20$ measurement repetitions are recommended. In case this number can be increased, the accuracy of estimated statistical parameters increases with respect to the underlying unknown statistical population. If n increases, also other parameters, besides `mean(...)` and `std(...)`, which are based on the evaluation of the distribution $\{t_{i,j}\}_{j=1}^{n_{\mathrm{MS}}}$ (and related), can be expressed meaningfully. One example is the skewness of the distribution Skw at the example of Pearson's second skewness coefficient (median skewness), which is defined for $\{t_{i,j}\}_{j=1}^{n_{\mathrm{MS}}}$ in (80) [247].

$$\mathrm{Skw} = 3\frac{\mathtt{mean}(\{t_{i,j}\}_{j=1}^{n_{\mathrm{MS}}}) - \mathtt{median}(\{t_{i,j}\}_{j=1}^{n_{\mathrm{MS}}})}{\mathtt{std}(\{t_{i,j}\}_{j=1}^{n_{\mathrm{MS}}})} \tag{80}$$

Especially for larger n any deviations of the distribution of $\{t_{i,j}\}_{j=1}^{n_{\mathrm{MS}}}$ from a Gaussian distribution can hint at unknown systematic measurement errors. The reason for that can be found in the central limit theorems, which state that the sum of a large number of independent random numbers asymptotically follow a stable distribution (which is normally distributed for finite, positive variance) [248]. However, the opposite is not necessarily true, because the presence of a perfect Gaussian distribution does not mean that $E_{\mathrm{sys}} = 0$.

5.8 Summary of the data processing pipeline

The foundation of the data processing pipeline is a clean specification of a data structure (see sec. 5.1). Conditions satisfying a closed 2-manifold triangle mesh are strictly enforced on all three supported geometry data sources (nominal, reference and measurement series) in order to ensure consistent results enabled by robust algorithms. The preparation routines with regards to the measurement data are described in sec. 5.2. The spatially discrete metrological descriptor framework defines several distance metrics between triangle meshes, which offer different characteristics, depending on the intent of the examinations (see sec. 5.3). In most cases, SD sampling produces the most robust and yet versatile results. In case the nominal geometry is available, routines for accurately modifying the configuration of its triangle mesh structure are provided and described in sec. 5.4. Tactile 3D coordinate measurement systems (TCMS) are the industry standard for providing traceable reference measurement data. A versatile procedure for the conversion of their point cloud data into a triangle mesh satisfying the requirements of the framework with a minimal set of boundary conditions is documented in sec. 5.5. Geometry data from different sources requires transfer into a common coordinate system (see sec. 5.6). Finally a set of so called conventional and unconventional metrological descriptors can be computed. They lay the foundation for diverse visualisations and statistical analyses of different metrological characteristics (see sec. 5.7).

6 Selected applications of the spatially discrete metrological descriptor framework

This chapter demonstrates a selection of possible applications of the spatially discrete metrological descriptor framework, which was derived in the previous chapters. The most basic utilisation are different types nominal-actual comparisons (UC_{4a}, UC_{4b}, UC_{5a} and UC_{5b} described in Table 5), which differ in the meaning and interpretation of their results. Each of these variants is a useful tool for measurement data evaluation in various contexts, however they do not offer statistical statements. This chapter begins with the main application of the framework, which is measurement system analysis. After that, other use cases such as weighted geometry element regression, improvements for tolerance specifications and the influence of the chosen distance metric on the observed results are discussed.

Some of the work presented in this chapter is taken from previous publications, dating back until 2016, where the determination of the measurement noise for points on a CT measurement surface was first described [P19]. Naturally, those earlier publications describe different stages of work in progress and can therefore differ slightly with respect to the used methods as well as their designation / notation compared to the findings described in this thesis. In case of doubt, the latter represents the latest status.

6.1 Analysis of measurement systems and tasks

Measurement system analysis is the main application for the spatially discrete metrological descriptor framework. Results for TCMS and optical structured-light scanner are presented, however the main focus lies on use cases for industrial CT. The following sections show a selection of a variety of possible applications. They all have in common that they provide additional (sometimes non-trivial) information about a measurement task, which can ultimately be used to improve the measurement results by reducing the measurement uncertainty in case appropriate measures were taken. For example, the framework was used to evaluate the calibration of complex 3D scan trajectories for an industrial computed tomography setup [P15].

6.1.1 Evaluating the precision of TCMS measurements

The method described in sec. 5.5 makes it possible to generate a triangle mesh from TCMS point cloud measurement results with a minimal set of boundary conditions. This procedure was subsequently used to examine the precision of repeated TCMS measurements. For these investigations, the ”multi purpose specimen” (see Appendix) made out of aluminium was repeatedly measured using a TCMS. The details of the pipeline configuration are listed in Table 6.

Table 6: Pipeline configuration for the determination of the spatially discrete metrological descriptors for repeated TCMS measurements.

Measurement object geometry	”multi purpose specimen”, see Appendix
Measurement object material	aluminium
Measurement system	Zeiss UPMC 1200, see Appendix
Tactile probe	ruby, diameter 1 mm
Number of measurement points per measurement	3659 (single point probing)
Size of measurement series	20
Mesh pitch for conversion of the CMS data to mesh	100 µm
Registration	Zeiss Calypso (semi-manual based on geometry elements)
Sampling start geometry ($\mathcal{S}_{\text{reg}}$)	nominal geometry, pitch 50 µm
Distance metric	vertex normal vector (VNV)
Framework use case	UC_{2a} (see Table 5)

The repeated measurements were compared against the nominal geometry (CAD) of the specimen. Therefore, the use case UC_{2a} applies here, with the limitations regarding the observable metrological descriptors listed in Table 5. The conversion of the point cloud of the TCMS measurement data into a triangle mesh requires a prepared triangle mesh with a target pitch of 100 µm. The same procedure (sec. 5.4) was applied to generate the mesh representing the sampling start geometry, here with a pitch of 50 µm.

The spatial distribution of the metrological descriptors $\Delta_{\text{cmp}}^{E_{\text{sys}}}$ and E_{rand} are visualised in Figure 37. Nearly the complete surface was measured, only the top and bottom bore holes were excluded from the measurement. The metrological descriptors for these surface regions are set to zero. By design, feature edges are always associated with zero deviations, because it is not possible to probe them reliably with a TCMS (see sec. 5.5). The superposition of work piece deviations and systematic measurement error $\Delta_{\text{cmp}}^{E_{\text{sys}}}$ (left image) ranges from ≈ -20 µm to ≈ 40 µm, with the largest absolute values observed in both spherical calottes. The random measurement error E_{rand} (right image) are

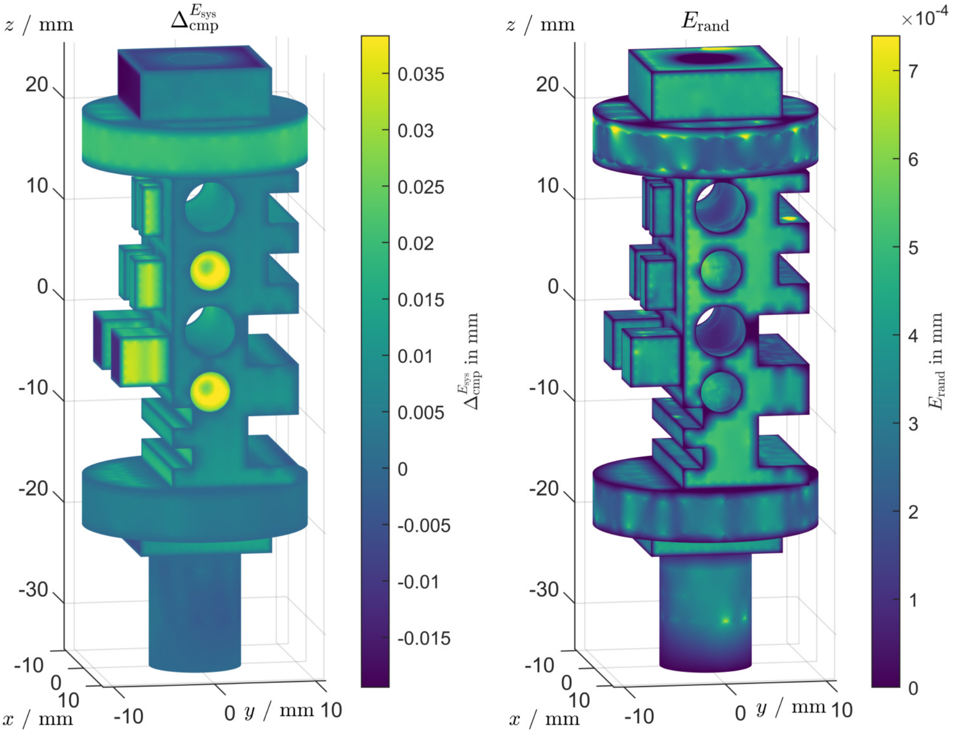

Figure 37: Visual evaluation of the spatially discrete metrological descriptors obtained from 20 repeated TCMS measurements of an aluminium test specimen using the TCMS Zeiss UPMC 1200 (see Appendix). The left image shows the superposition of local component deviations Δ_{cmp} and systematic measurement error E_{rand}, $\Delta_{\text{cmp}}^{E_{\text{sys}}}$. The right image shows the local random measurement error which were at least partially caused by drifts of unknown source (see text). Colour map limits represent the data percentiles $P_{0.1}$ and $P_{99.9}$, respectively. The parameter values of surface regions without associated measurement data (top and bottom bore holes) are set to zero.

mostly around or below 0.5 µm, however larger values can be observed for certain measurement points (deep red). Besides $\Delta_{\text{cmp}}^{E_{\text{sys}}}$ and E_{rand}, the drift was examined (Figure 38). One side of the workpiece systematically shows slightly negative values (Figure 38, left) and the opposite side shows positive values (Figure 38, right). Because of the fact, that for CMS measurements, the coordinate system of the workpiece is determined at the beginning of each measurement, the observed values do not correspond to physical drift of the object within the measurement volume of the CMS (the measurement coordinates are represented in the coordinate system of the nominal geometry $\mathcal{N}$). Instead, the observed effect hints at imperfect repeatability of the aforementioned process of determining the local workpiece coordinate system. This has no effect on common ISO GPS based dimensional evaluations

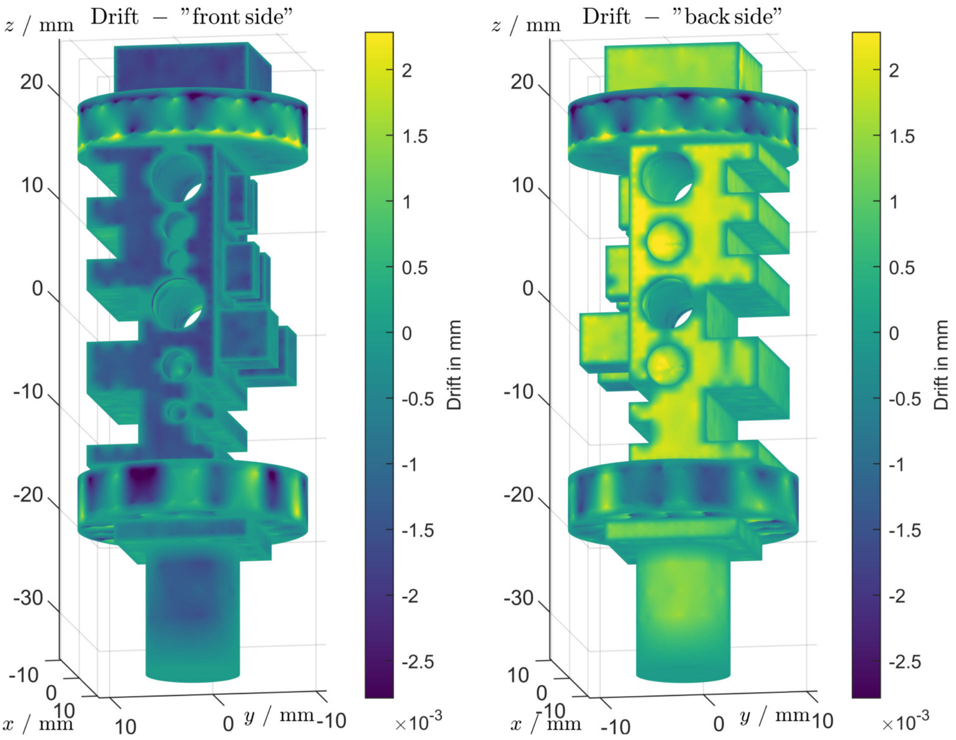

Figure 38: The measurement series shows the effects of potentially thermal drift. The central bore hole at $z \approx 0$ is unaffected by that systematic effect, as well as both large cylindrical surfaces, because that feature was part of the coordinate system alignment during the measurement. The drift is given with respect to the local surface normal vector which is reflected by different signs of the observed drift on the upper (positive sign) and lower (negative sign) of the surfaces in the right sides of each image. Colour map limits represent the data percentiles $P_{0.1}$ and $P_{99.9}$, respectively.

based on a single measurement because all measurement points are measured within one stable coordinate frame and all further data evaluations happen within their own constant coordinate frame[96]. It also does not mean, that the measurement system is inaccurate, but it is possible that the stability of the determination of the workpiece coordinate system was negatively affected by the chosen measurement strategy. Additionally, the effect could be caused by the surface roughness of the workpiece within the context of registration, because probing locations do not hit exactly the same physical spot for

---

[96] The GPS standards define the "duality principle", which states that both specification and verification are defined as virtual and real measurements [9]. Consequently, the relationship between $\mathcal{N}$ and a single measurement $\mathcal{M}^\dagger$ is not required to be known for GPS conformance testing. The spatially discrete metrological descriptor framework behaves differently, because the key parameters are determined based on the comparison of geometries in 3D.

each measurement repetition. Consequently, imperfect determination of the workpiece coordinate system with respect to $\mathcal{N}$ increases the dispersion of measurement data around $\mathcal{N}$ other, which also contributes partially to E_{rand}.

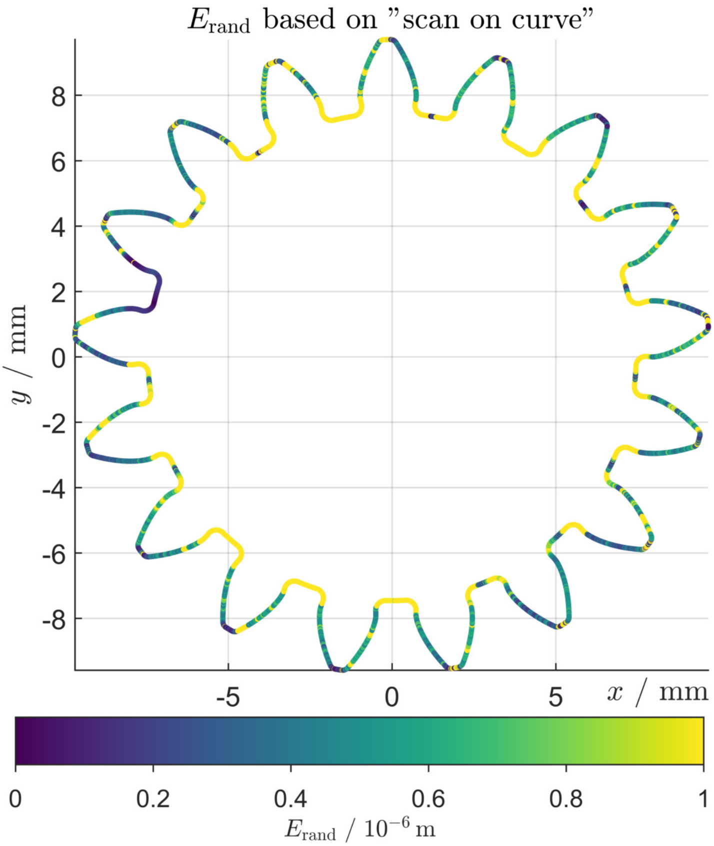

Figure 39: Visualisation of E_{rand} from repeated "scan on curve" gear wheel measurements. Besides the tooth root regions, the observed precision is below 1 µm. Image reprinted from [P10] with minor modifications.

Lastly, an alternative approach based on scanning measurements is presented. During the design of the method of creating triangle mesh reference measurements from TCMS measurement data (see sec. 5.5) an intermediate development step was taken. Instead of the final areal description based on the conversion of CMS point cloud data into a triangle mesh, the metrological descriptors were directly computed from repeated and connected line scans. With respect to a gear wheel case study, the measurement points nominally lie all in a plane, consequently the sampling problem could be (approximately) simplified to two dimensions instead of three[97]. After alignment, the local E_{rand} values could be calculated. A detailed description of procedures for determining the measurement precision from tactile scanning measurements at the example of metal gear wheels can be found in [P10, P27]. The results of repeated "scan on curve" measurements are visualised in Figure 39. Here, the observed values are mostly below 1 µm, except in the tooth root regions, where physical probing is more difficult. Overall, the results show strong fluctuations of precision values, which could be caused by unfavourable surface roughness of the gear surface. Compared to the method using an areal description of geometry based on triangle meshes, evaluating the metrological descriptors based on scans in plane is clearly inferior because they yield much less information about the measurement. Also, additional error was introduced by the applied dimension reduction, however the rough estimation of the achieved measurement precision was possible.

6.1.2 Spatially discrete metrological descriptors for optical measurements

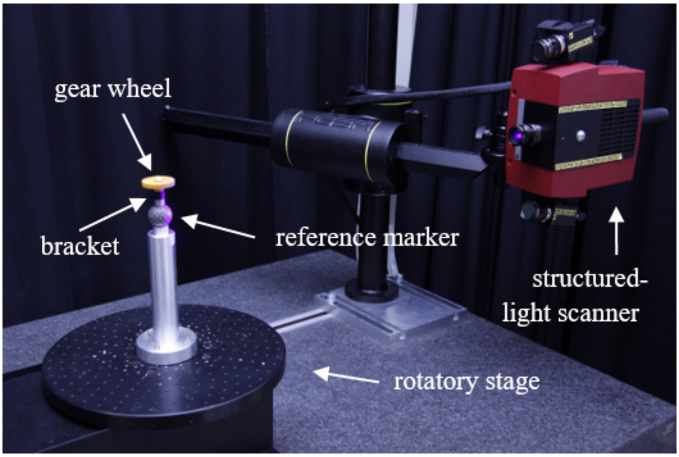

Figure 40: Optical set up for gear measurements, consisting of a structured-light scanner (GOM ATOS Compact Scan 2M/300) in combination with a rotatory stage. Image reprinted from [P9]. The bracket was designed by [S4].

In the following, results based on optical fringe-projection measurements of a polymer gear wheel are summarised from previous publications [P9, P28]. A gear wheel was mounted on a rotatory stage (Figure 40) and measured in

---

[97] The used distance metric is comparable to Shortest Distance (SD, see sec. 5.3.2), although implemented differently because instead of triangles, line segments were targeted.

800 single positions (2 sensor positions slightly below and above the gear wheel plane with 400 positions for one full stage rotation). The measurement data processing was handled by the measurement system (GOM ATOS Compact Scan 2M/300 / GOM ATOS Professional 2018, see Appendix) and 20 measurement repetitions were performed. The uncertainty of the optical measurement setup was then computed in reference to a CT measurement of the same object[98]. Therefore, the framework use case was UC_{2a} (see Table 5). Technical details regarding the data processing pipeline can be found in [P9, P28].

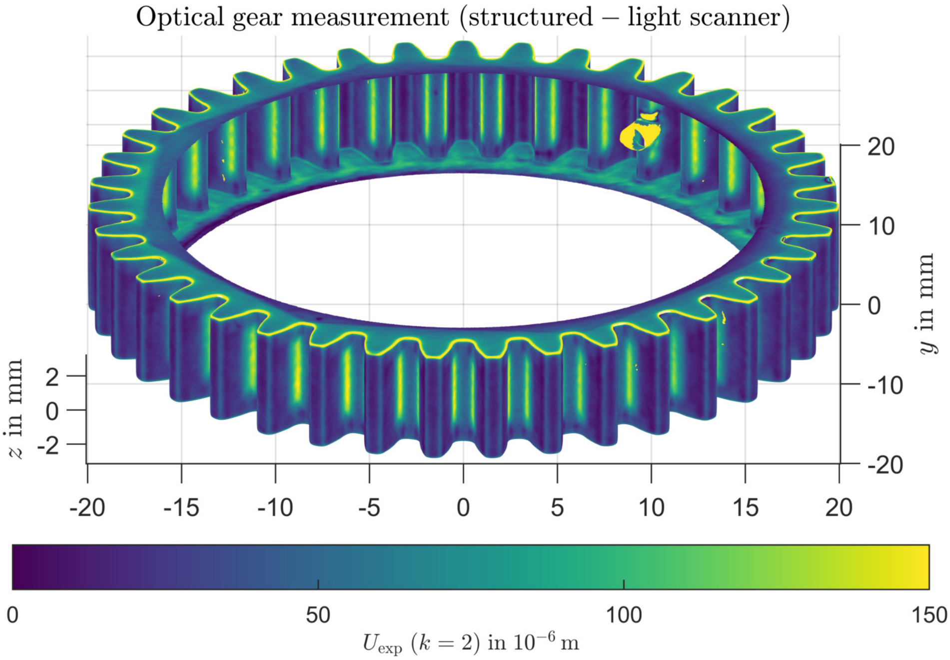

Figure 41: Visualisation of the expanded measurement uncertainty from repeated gear measurements using an optical structured-light scanner. The reference measurement was obtained by CT. The yellow region in the inner top right part of the gear is caused by an additional bore hole in the measurement object which was used to break the periodic symmetry properties of the gear wheel. Image reprinted from [P9] with minor modifications.

The results of the evaluations are shown in Figure 41 using false-colour imaging of the resulting expanded measurement uncertainty U_{exp} (75) with $k = 2$. Relatively speaking, the observed uncertainty is lower in the tooth head and

---

[98] As stated earlier, the suitability of a certain measurement system (here CT) to act as a reference for another system (here structured-light scanner) must be ensured by the user of the framework. In this particular case, it is arguably debatable if the used CT system is really accurate/precise enough in comparison in order to act as a reference measurement system in the sense of the VIM [10].

tooth base regions, respectively, and higher at the tooth flanks. This result can be expected due to the different optical accessibility and the fact that tooth flanks are only measured at relatively steep angles. The sides of the gear wheel also show slightly higher uncertainties, because they are also measured at an angle and additionally only captured by a single sensor position.

Aiming at investigating a different type of optical areal measurements, the influence of a tilt of the optical axis with respect to an object surface in case of optical surface measurements (measurement principle focus variation) was examined in [P31]. Optical surface measurements differ from 3D coordinate metrology insofar that they represent a height measurement where z is a function of a xy grid (camera pixels) such that $z = f(x, y)$. The results demonstrated that the method is also applicable for optical surface measurements, however they are admittedly less relevant in that field.

An estimation of the optical measurement accuracy of partially reflective objects was reported in [P20].

6.1.3 Validating surface point quality parameters for CT

In recent years a method for evaluating, visualising and harnessing the quality of measurement points in CT was developed at FMT, with the first publication dating back to 2015 [P1, P3, P7, P8, P17–P19, P33]. One patent associated with that method was applied for in several countries [249–254]. Similar work was also reported elsewhere [255–259]. This section briefly summarises these findings and shows how the spatially discrete metrological descriptor framework could contribute to further developments. Characteristic for CT measurements is the intermediate measurement result in form of a voxel grid (volume data consisting of volumetric elements) each representing the measured X-ray absorption in that particular part of the measurement volume. The 3D coordinates describing the surface of the measurement object lie in regions of increased volume data gradient, which represent the interface between two materials, one of which is the atmosphere. This can be confirmed in Figure 42 (left side), where the volume data centred around a surface coordinate is sampled in both directions of its normal vector (starting at zero): The maximum (absolute) gradient (red curve) is located exactly in the centre of the profile (at zero). The aforementioned method determines the surface point quality (SPQ) from analysing the volume data around each of the measured surface coordinates, e.g. from the one visualised in Figure 42. From these profiles, different quality parameters can be derived based on the varying mathematical properties of volume data profiles with respect to each other, e.g. rating the symmetry of the curve. It was shown that the SPQ is well suited for the classification of artefact-affected surface regions,

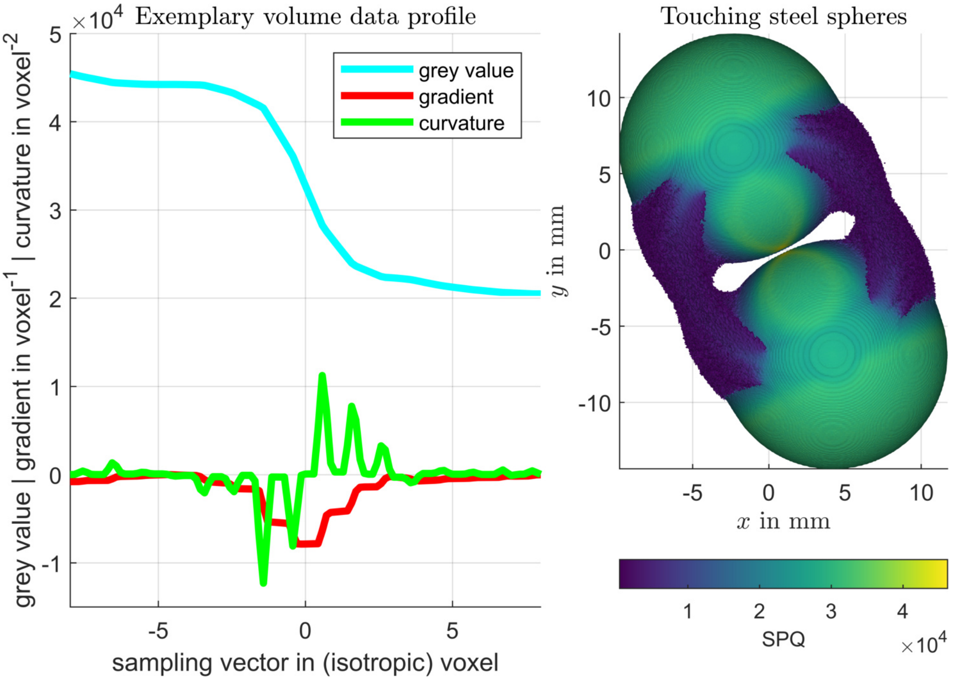

Figure 42: SPQ values can be obtained by evaluating the volume data transition in both direction around each measured coordinate sampled in the direction of its normal vector (left image). Suitable SPQ parameters can be used to classify artefact-affected surface regions with respect to other regions. This also includes more subtle examples than the shown case featuring two touching steel spheres (right image). Images reprinted from [P7] with minor modifications.

as shown in the right image of Figure 42, where the measurement artefacts correspond to lower SPQ values than the rest of the surface. Here, the effects of severe beam hardening artefacts are shown (regions between the spheres coloured red), for which in principle different correction methods exist, e.g. [P29]. The biggest drawback of the method is the abstract nature of the quality parameters, with no direct relationship to a traceable dimensional unit (metre). Consequently, because both the SPQ method as well as the spatially discrete metrological descriptor framework determine point-wise parameters, it was straightforward to compare both with each other in order to observe a possible correlation. If that were the case, statements about dimensional properties of a measurement (e.g. local random measurement error) could directly be derived from a single CT measurement (instead of a complex series of measurements), based on the SPQ. In order to investigate that possible connection, a polymer gear measurement was evaluated (a single measurement for SPQ and 20 measurements for the spatially discrete random measurement error evaluation) and compared against each other visually (see Figure 43). The measurement object was positioned inside the measurement volume such that the rotation axis of the gear wheel was aligned parallel to the rotation axis of the CT system, provoking a change between larger and smaller X-ray penetration lengths that way. It turns out that within the context of a visual comparison, there is a qualitative correlation between both methods observable in Figure 43 (further details for this particular study are provided in [P7]). However, the relationship is most likely not linear and its concrete nature requires further research. Nonetheless, it could already be shown additionally that weighting measured coordinates according to their respective SPQ value in the context of geometry element regression yields potential for improving dimensional measurements (see sec. 6.3). Therefore, the spatially discrete metrological descriptor framework can assist in exploring such quality parameters by providing a method to connect these parameters calculated from measurement meta data with a metrological unit.

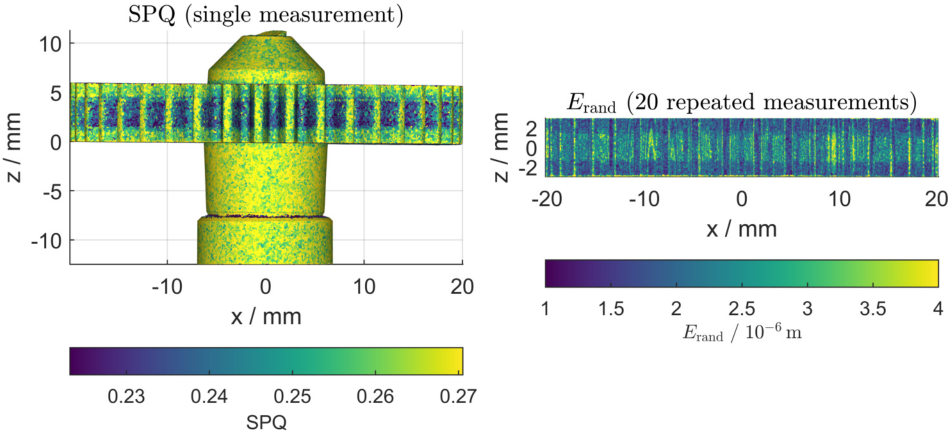

Figure 43: Qualitative comparison between SPQ (single measurement) and its corresponding E_{rand} values (based on a measurement series) for a polymer gear wheel. The images show a qualitative correlation between both methods, however further development of the SPQ method might be required before reliable statements about the local random measurement error can be derived. Images reprinted from [P7] with minor modifications.

6.1.4 Measurement duration vs. uncertainty for CT

One of the key criteria for the industrial application of any measurement system is the duration of a single measurement. Lower measurement durations increase the number of examined parts per time and thus decrease the associated costs per measurement. The impact of potentially time-saving continuous[99] CT scans compared to usually applied "stop and go" measurement data acquisition was examined with respect to their impact onto different types of measurement errors [P14]. CT measurements are generally affected by the superimposition of noise of different sources (e.g. quantum noise, readout noise), which means that countermeasures often include some form of data averaging (e.g. increased projection integration time, averaging of multiple projections or detector binning) in order to increase the statistical stability of the measurement results. The essential connections between measurement duration and uncertainty, respectively, are as follows:

- Higher image integration duration[100] reduces image noise and thus uncertainty[101], but also increases the measurement duration.
- The averaging of multiple projections for each angular position reduces image noise, but also increases the measurement duration.
- Higher X-ray tube current increases the number of photons and therefore reduces noise. However this also increases the required X-ray focal spot size, which itself tends to contribute to higher uncertainty due to additional blurring.
- All recorded X-ray intensity values must lie within the linear window of the detector. If not, the measurement uncertainty typically increases significantly, due to the introduction of measurement deviations with respect to the X-ray intensity [260, 261].

Therefore, the following study was conducted in order to quantitatively investigate the trade-off between measurement duration and uncertainty, respectively. It consists of several measurement series, which were configured as described in Table 7. Additionally, the X-ray intensity reaching the detector was within its linear value range for all listed measurement configurations.

The following figures show cumulated density function estimates for each setting as coloured curves between their 2.5 and 97.5 percentile, respectively. The vertical lines (referred to as index "|" in the following) show the weighted mean value of the complete data, with weights corresponding to the mesh area captured by each sampling point[102]. The second textbox (besides the

---

[99] Here, projections are recorded with a constant rotation speed of the rotary stage.

[100] Also called integration time.

[101] In some cases, it is possible that the systematic measurement errors correlate positively with the measurement duration which in turn increases the uncertainty of the measurement. However in practise within reasonable machine settings the uncertainty reducing effect of higher integration times largely outweighs the uncertainty contributions of potentially increasing systematic errors.

[102] This can be computed by evaluation of the triangle fan surrounding each vertex within a mesh. Each vertex takes one third of the area of each face it is a part of. See also the definition of the triangle mesh affinity (TMA) in sec. 5.3.6.

Table 7: Measurement parameters for the investigation of the influence of the integration time onto the measurement uncertainty.

Measurement object geometry	”multi purpose specimen”, see Appendix
Measurement object material	aluminium
Measurement system	Zeiss Metrotom 1500, see Appendix
Reference measurement system	Zeiss UPMC 1200, see Appendix
X-ray tube	$150\,\mathrm{kV} \cdot 267\,\mu\mathrm{A} \approx 40\,\mathrm{W}$, focal spot size as $1\,\mu\mathrm{mW}^{-1} \approx 40\,\mu\mathrm{m}$
Geometric magnification	5×, resulting voxel size 40 µm
Integration times in ms	400, 500, 667, 1000 and 2000
Images averaged per projection	1
Detector gain settings	16, 16, 16, 16 and 8
Number of projections	2050, VAST scan
Size of measurement series	20
Surface determination	VGStudio Max (VGS), export mesh as ”precise with simplification”
Registration	VGS best-fit ($\mathrm{REG}_{1\rightarrow n}$ later, see text)
Sampling start geometry ($\mathcal{S}_{\mathrm{reg}}$)	reference geometry, pitch 40 µm ($\approx 7.6 \cdot 10^6$ triangles)
Distance metric	shortest distance (SD)
Framework use case	$\mathrm{UC}_{1\mathrm{b}}$ (see Table 5)

legend), shows additional statistical data, which is coded as described in Table 8.

The first figure visualising different key observations is showing the random measurement error E_{rand} (Figure 44). The random measurement error increases with lower integration times. This is an expected result, i.e. the trade-off follows the mathematical model of the signal-to-noise ratio (SNR) of Poisson-distributed X-ray sources with quantum number Q, where $\mathrm{SNR} \propto \sqrt{Q}$ [262]: Increasing the integration time by a factor of 5 (from 400 ms to 2000 ms) increases the weighted mean random measurement error by a factor of 2.172, and $\sqrt{5} = 2.236$. The spacing between each of the weighted mean values (vertical lines) is almost identical and 97.5 % of all random measurement errors (E_{rand}) are below 2.5 µm for an integration time of 2000 ms.

Table 8: Decoding of additional statistical information given in the result plots.

Symbol	Meaning
$\varnothing_{\vert}$	mean value of all curve means
$\leftrightarrow_{\vert}$	the range of all curve means
$\uparrow_{\vert}$ / $\downarrow_{\vert}$	ratio between max. and min. mean value
$\uparrow_{\vert}=\{a\}; \downarrow_{\vert}=\{b\}$	curve indices a, b of the max. and min. mean values

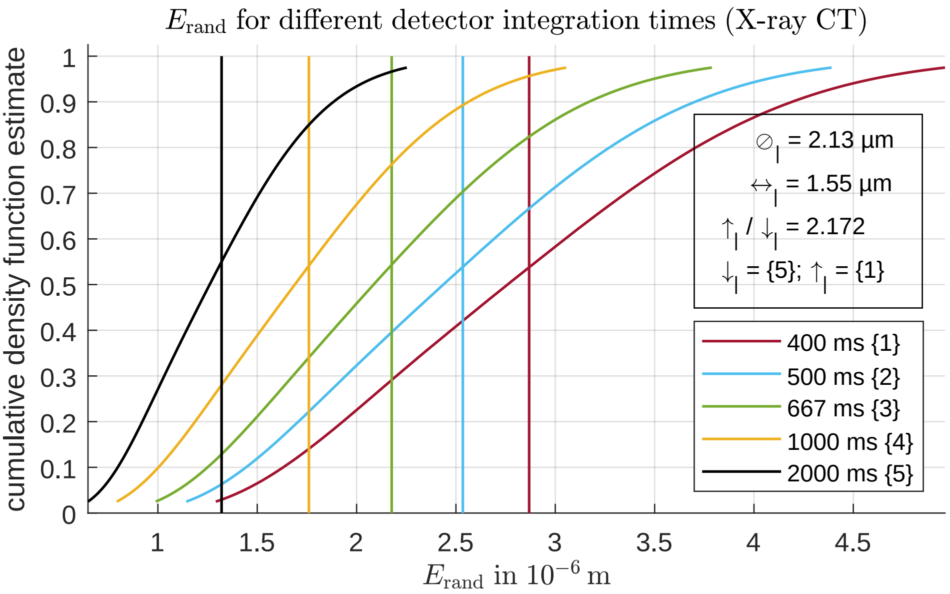

Figure 44: Evaluation of the random measurement error E_{rand} for each of the 5 measurement series described in Table 7. Higher integration times consistently result in lower random measurement error. Between the highest and lowest mean curve value lies a factor of just 2.172. Vertical lines indicate the area weighted mean value of their respective distribution.

The systematic measurement error E_{sys} is shown in Figure 45. The larger negative numbers are mainly caused by the rounding of edges by any CT measurement, e.g. due to blurring because of the non-zero X-ray focal spot size [56]. Due to the way the mesh is generated from TCMS reference data (edge regions are not corrected see, sec. 5.5) the systematic measurement errors are slightly overestimated in these regions. However, the observed E_{sys} are nearly constant for all examined measurement settings, with the measurement series ”667 ms” showing slightly different values. The $\varnothing_{\vert}$ and the related parameters show very low deviations, which are however caused by the mutual cancellation of positive and negative deviations. Nonetheless, the values are valid for a comparison of the curves with each other. Because of the fact that the E_{sys} are significantly larger than E_{rand}, the expanded measurement uncertainty U_{exp} $(k = 1)$ is also dominated by E_{sys} (Figure 46).

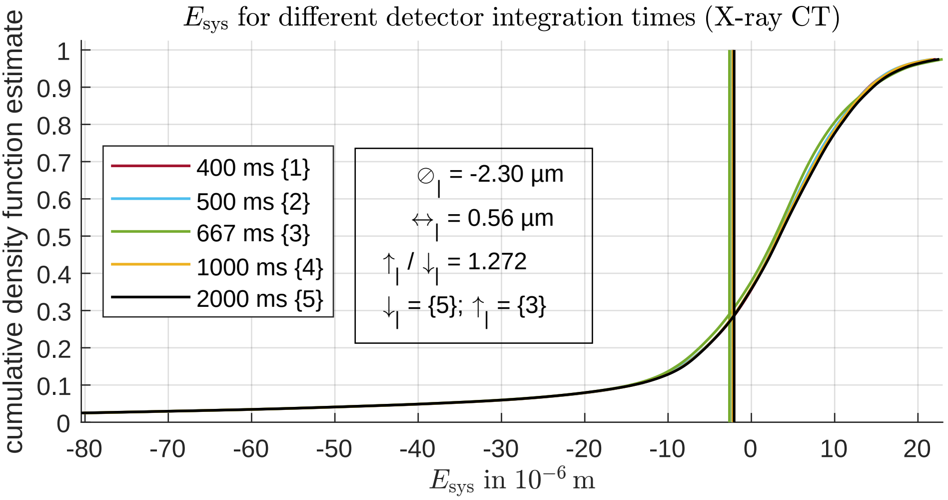

Figure 45: Systematic E_{sys} for different measurement series described in Table 7. The different integration times show little effects on E_{sys}.

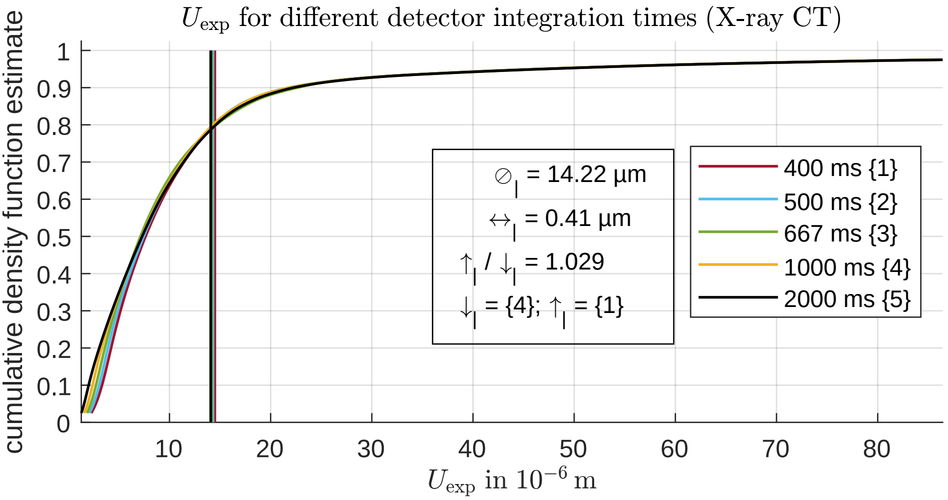

Figure 46: Evaluation of the expanded measurement uncertainty U_{exp} $(k = 1)$ for measurement series described in Table 7. Because the measurement is dominated by systematic error, U_{exp} shows very little correlation with the used integration times.

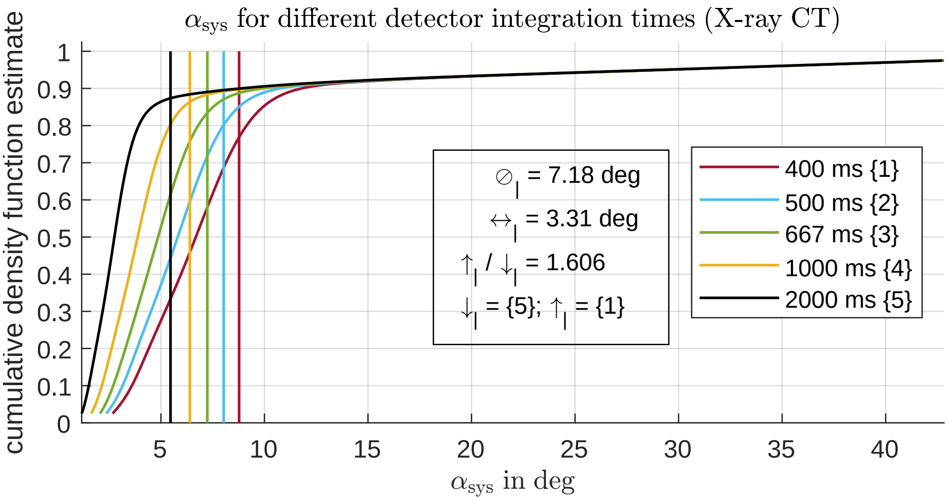

Figure 47: The unconventional metrological descriptor α_{sys} is consistently increased with lower integration times, suggesting increased surface roughness on the measured surface.

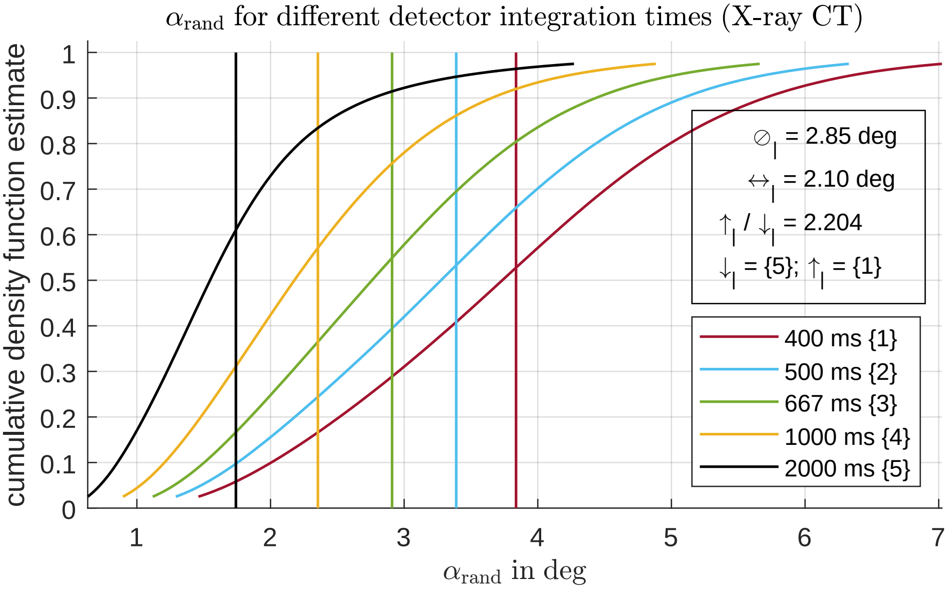

Figure 48: The dispersion of α (described by α_{rand}) is increased for lower integration times, suggesting increased surface roughness of the measured surface.

Inspecting these results, the first conclusion was that there is only little difference between these settings with respect to the measurement uncertainty and that in this particular example the setting corresponding to the fastest measurement should be chosen. However, the unconventional metrological descriptors (see sec. 5.7.2) clearly show distinct differences in the surface texture of the measurements. As an example, α_{sys} and α_{rand} are described in Figure 47 and Figure 48, respectively. These parameters describe the statistics of the angle α between the sampling point normal vector and the connection between the sampling point and its target location. If the distribution is shifted towards higher values, the targeted surface is affected by more high frequency roughness. Those plots show, that both the mean angle α_{sys} and the scatter of that angle α_{rand} are increased by lower integration times. The parameters β_{sys}, β_{rand} (the angle of the connection vector with the target surface) show very similar behaviour, as well as the parameters γ and λ_{ratio} (without figure).

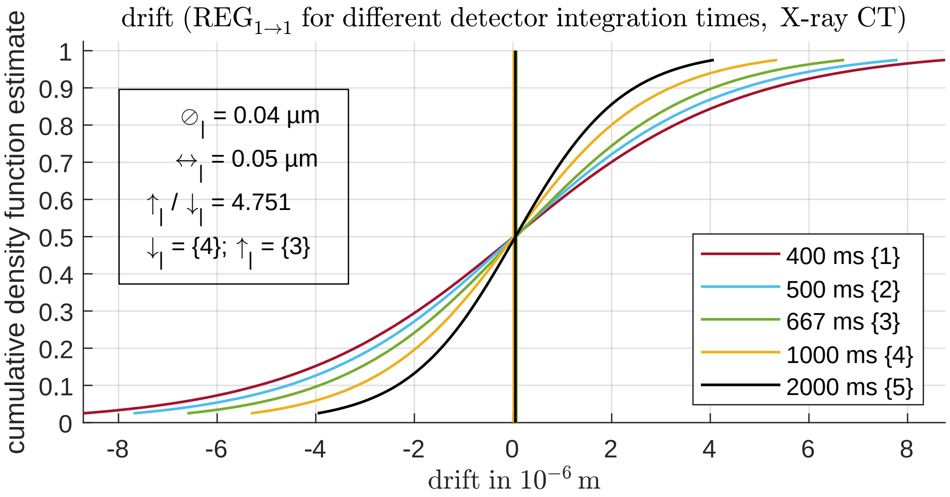

Figure 49: The evaluation of the drift for each measurement series shows no anomalies. Both mean and median values are meeting at zero indicating no relevant drift within each series. Importantly, these values are affected by the used registration algorithm.

Finally, the drift between each measurement series is examined in order to ensure the consistency of the presented results. The weighted mean values and the median values of all curves meet at zero, indicating that there is no relevant drift between the measurements of each series (Figure 49). Of course, due to the way this parameter is calculated, the curves are affected by noise. Therefore, lower image noise leads to steeper curves. It is important to note that these results are affected by the registration routine (REG$_{1\to1}$). This means that each individual surface was registered against one common geometry, thus eliminating the relative position and orientation of the single measurements with respect to each other. This causes the set of measurements be become tightly packed, within the limits of the applied registration error metric. Because of that, REG$_{1\to n}$ registration was proposed

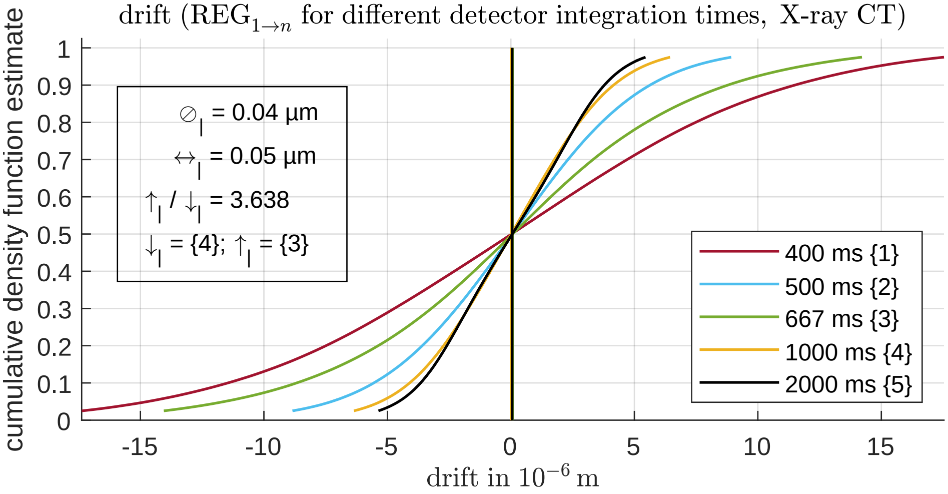

Figure 50: Drift with REG$_{1\to n}$ registration applied instead of VGS best-fit. Compared to Figure 49, larger both positive and negative values are observed but mean value and median are still centred around zero.

(see sec. 5.6.4), where all measurements are registered against the same geometry at once, therefore keeping their relative position and orientation with respect to each other. This effect can be observed by comparison of Figure 49 with Figure 50, where the drift for REG$_{1\to n}$ registration is shown. These curves are also centred at zero, but show higher positive and negative values at the edges of the distributions. This means that the "mesh cloud" of measurements is spread wider in case their relative position and orientation is unaffected compared to when REG$_{1\to 1}$ registration is applied. Nevertheless, there is no drift, because the mean values are centred at zero. These results are consistent with higher E_{rand} in case of REG$_{1\to n}$ registration (not shown). Thus, the somewhat philosophical questions arises, if a change of the measured coordinates with respect to the machine coordinate system, which can be observed when repeating measurements, is actually part of the measurement uncertainty as defined in this framework. In typical applications, this is not the case, because the geometric properties of an object are defined with respect to its own basis, therefore a measurement of an object in different locations of the measurement volume is obviously not affecting the dimensional results. Consequently, the used type of registration (REG$_{1\to 1}$ or REG$_{1\to 1}$) affects the observed uncertainty.

Summarising this section, the effect of different integration times can be observed using the spatially discrete metrological descriptor framework. The results of this specific investigation suggest that dimensional measurands should remain mostly unaffected by reduced integration times, as long as they are not sensitive to different surface textures caused by increased noise. Consequently, for the examined measurements, time savings up to a factor of 5 can be realised nearly without any impact on the observed measurement uncertainty.

6.1.5 The impact of projection averaging[103] settings for CT

The results presented in the previous section showed that the spatially discrete metrological descriptor framework can successfully distinguish between measurement series recorded with only small differences in their respective measurement parameters. The subsequently presented examinations evaluate how a given measurement time budget (here 2000 ms) is best spent using different measurement parameters. The settings are identical to those presented in Table 7, resulting in the 7 different measurement series listed in Table 9. All measurements require 2 s per projection except series #2 and #7, which take 4 s each. With respect to the overall measurement duration, it is irrelevant if more projections are recorded with less integration time or vice versa. However, with respect to the measurement error, this non-trivial connection is targeted with these examinations.

Table 9: Settings for the measurement series conducted for the image averaging studies. All other settings are identical to those given in Table 7. Measurement series 6 was reused from the previous section 6.1.4.

#	integration time	number of images averaged per projection	duration per projection	detector gain
1	400 ms	5	2 s	16×
2	400 ms	10	4 s	16×
3	500 ms	4	2 s	16×
4	667 ms	3	2 s	16×
5	1000 ms	2	2 s	16×
6	2000 ms	1	2 s	8×
7	2000 ms	2	4 s	8×

Inspecting Figure 51, the measurements featuring a total projection duration of 2 s show lower random measurement error E_{rand} the higher their integration time per projection is (2000 ms with 1 img is better than 1000 ms with 2 img, etc.). Therefore, the results suggest that a higher integration time should be

---

[103] The averaging of k projections into one X-ray image is denoted k img.

preferred over higher image averaging. Furthermore, increasing the total time per projection from 2 s to 4 s further reduces E_{rand}, but higher integration time beats higher image averaging also for these settings. The difference between these two settings with 4 s is smaller than between the best and worst setting for a total time budget of 2 s. This means that the distribution between integration time and number of images averaged gets less important with higher durations per projection. The worst result (weighted means) only exceeds E_{rand} of the best one by a factor of 1.472. Spending a total duration per projection of 4 s means that E_{rand} can be kept below 2 µm for the complete work piece surface (> 98 %).

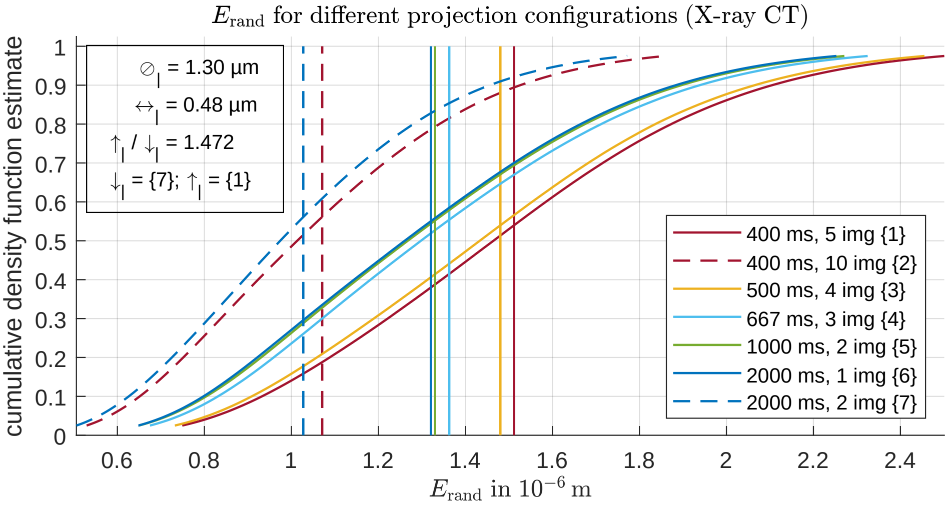

Figure 51: The random measurement error E_{rand} can be further decreased by increasing the total measurement time per projection from 2 s to 4 s. The setting 2000 ms is preferred over those featuring the same total time per projection in combination with image averaging.

The parameter λ_{ratio} describes the shape of the error ellipsoid associated with a sampling point. Their curves corresponding the image averaging studies are printed in Figure 52. The results for a total projection time of 2 s are closely aligned with each other but nonetheless exactly ordered with respect to their integration time. Same as for E_{rand}, increasing the total projection time significantly improves the logarithmic parameter λ_{ratio} even more. Higher values indicate a more narrow error ellipsoid and thus a smoother target surface. Parameters β_{sys}, BetaRnd, α_{sys} and α_{rand} show results perfectly consistent with λ_{ratio} (not shown). The expanded measurement uncertainty behaves invariantly with respect to the examined parameters, the maximum value exceeds the minimum value by less than 2 % (not shown). The reason for that is that the measurement is dominated by systematic error, which is unaffected by the investigated parameter combinations.

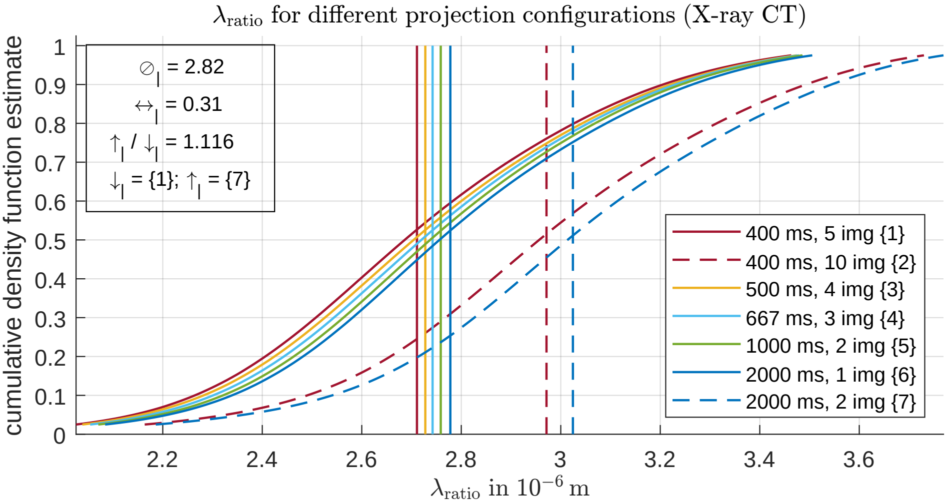

Figure 52: Results for the logarithmic parameter λ_{ratio}, which describes the shape of the error ellipsoid associated with a sampling point. Higher total projection time significantly improves the smoothness of the targeted surface.

Consequently, the spatially discrete metrological descriptor framework is consistently able to detect very subtle differences in measurement settings. Increasing the total time per projections further than 2 s is only helpful in scenarios where the systematic measurement errors are unimportant compared to the measurement precision. It is expected that the precision can be further improved by increasing the total measurement time per projection even more, however at significant costs with regards to the duration of the complete measurement. For most measurement tasks, the setting 2000 ms, 1 img can be expected to produce the best results from those examined in this section.

6.1.6 The impact of FBP reconstruction filters and binning

In order to reconstruct CT volume data from a stack of projections, filtered back projection (FBP) is a widely used method (FDK in case of a cone beam CT). One important mathematical property of FBP is the implicit linear weighting of the (Radon and Fourier) transformed projection data based on their spatial frequency, which effectively represents a high-pass filter [262]. This filter has therefore noise amplifying characteristics, which are often problematic for CT measurements. It is also called a ramp filter. In order to compensate for that behaviour, additional data windowing techniques in the frequency domain are applied [262]. Figure 53 shows the frequency response of commonly used filters, which describes the weight of these frequencies

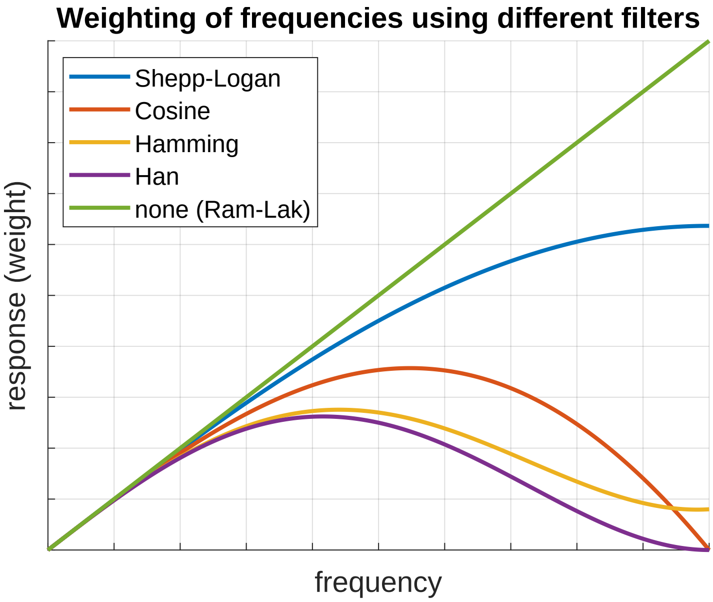

Figure 53: Altered frequency weighting due to the application of additional windowing in the frequency domain. The mathematical descriptions of the filters were taken from [262].

during FBP. With no additional filter applied (none), the mentioned linear ramp filter characteristics are unchanged during reconstruction. While their mathematical properties can be discussed extensively [65, 262], their concrete impact on a specific measurement task is difficult to estimate from a theoretical analysis. Therefore, the spatially discrete metrological descriptor framework was used in the following to examine different FBP filters with respect to their impact on the measurement error. Additionally, 2×2 detector binning was examined with respect to its noise suppression characteristics. Here, the measured intensity of 4 pixels is combined into one pixel value, which results in less measurement noise at the expense of potentially reduced measurement resolution. The measurement chain configuration is documented in Table 10. Two measurement series (binning 1×1 and 2×2), each consisting of 20 single measurement were recorded and the listed 5 different reconstruction filters were applied onto those data sets. The default FBP reconstruction filter of the used CT system is ”Shepp-Logan”, which offers the least amount of high frequency suppression of all additional filters (see Figure 53). On the other hand, ”Han” is expected to produce the smoothest measurement results. Thus, the biggest difference in results can be expected between the combinations ”binning 1x1, Shepp-Logan” and ”binning 2x2, Han”, which is visualised in Figure 54 for the metrological descriptor β_{sys}. This descriptor represents the mean angle the VNV search ray forms with the

Table 10: Measurement parameters for the investigation of the influence of the integration time onto selected metrological descriptors. Note: The ”Han” filter is also called ”Hanning” [262], however this work uses the identifier given in Zeiss Metrotom OS.

Measurement object	cylindrical indexable insert for turning, ISO-code RNGN 120700 (diameter 12 mm, height 7.94 mm), ceramic
Measurement system	Zeiss Metrotom 1500, see Appendix
X-ray tube	$225\,\text{kV} \cdot 95\,\mu\text{A} \approx 21\,\text{W}$, focal spot size as $1\,\mu\text{m}\text{W}^{-1} \approx 21\,\mu\text{m}$, pre-filter 0.25 mm Cu
Geometric magnification	$20\times$, resulting voxel size 10 µm
Integration time	2000 ms
Detector	$16\times$ gain, binning 1×1 (none) or 2×2
Number of projections	2050, VAST scan
Size of measurement series	20
FBP reconstruction filters (using Zeiss Metrotom OS)	Shepp-Logan, Cosine, Hamming, Han, none (Ram-Lak)
Surface determination	VGStudio Max (VGS), export mesh as ”precise with simplification”
Registration	$\text{REG}_{1\to n}$ ”SD-closed”
Sampling start geometry ($\mathcal{S}_{\text{reg}}$)	nominal geometry, pitch 25 µm ($\approx 2.2 \cdot 10^6$ triangles)
Distance metric	vertex normal vector (VNV)
Framework use case	UC_{2a} (see Table 5)

target surface normal vector. The figure clearly shows large difference with respect to the surface roughness of both settings.

The comparison of β_{sys} for all examined reconstruction settings is shown in Figure 55. The different filters qualitatively reflect the theoretical predictions with respect to their noise suppression characteristics. Other metrological descriptors (E_{rand}, β_{rand}) confirm these observations.

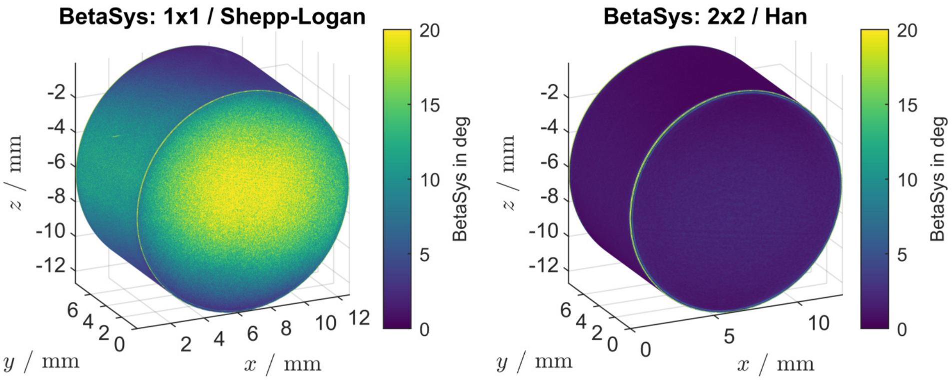

Figure 54: Comparison of β_{sys} for the most opposite settings of these examinations between ”binning 1x1, Shepp-Logan” and ”binning 2x2, Han”.

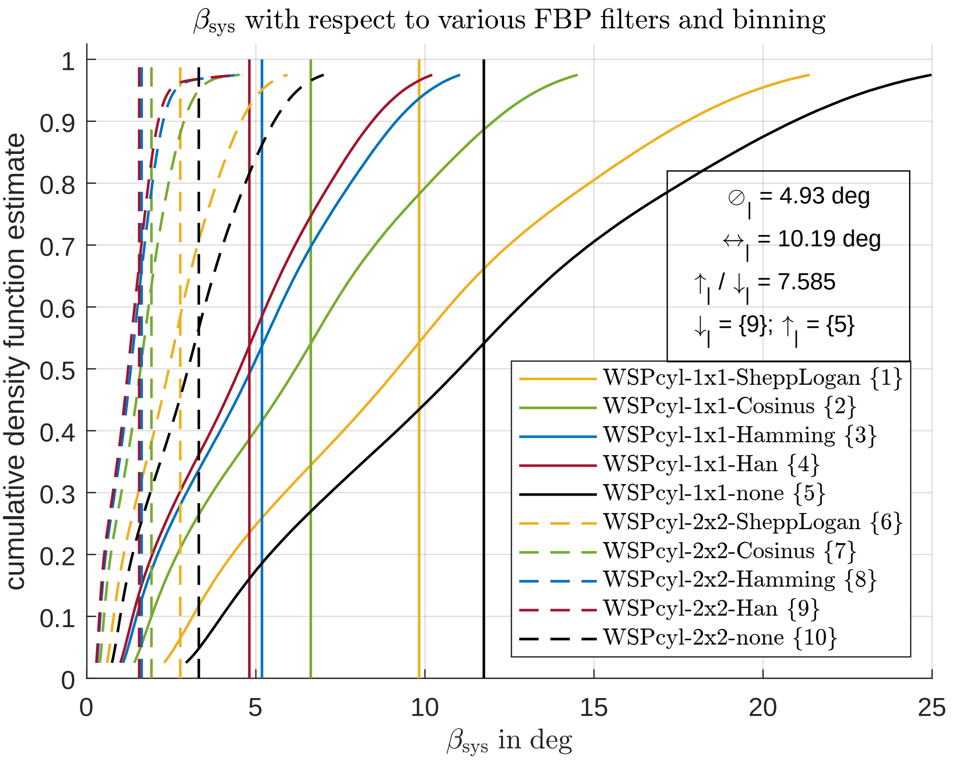

Figure 55: Comparison of β_{sys} for all examined reconstruction settings. The curves follow the theoretical predictions qualitatively exactly.

6.1.7 Accuracy of digital twins for metrological CT systems

In recent years, computational methods based on simulation tools and aimed at providing information about the measurement uncertainty with regards to a single (real) measurement were developed. One known representative is the context of coordinate metrology the ”Virtual CMM” (VCMM) for TCMS [35, 36]. These approaches simulate the measurement process (often incorporating Monte Carlo methods) and subsequently derive information about the accuracy of the measurement. Analytical models for physically and mathematically complex CT systems are hard to design, but the simulation of the underlying physical and technical interactions are in principal doable with suitable software solutions. Substantial research effort has been and currently is spent on developing digital twins for industrial CTs, which map the behaviour of a real system as accurately as possible. It was conceptualised that digital twins can be used to estimate the measurement uncertainty of a real measurement by contemporaneous simulation of the measurement task at hand [P21]. For that, the simulation must accurately depict individual aspects of the complete CT system, e.g. the X-ray focal spot [P16]. Given an accurate digital twin of a CT measurement system, systematic errors could be corrected. This was demonstrated with an early development version of the spatially discrete metrological descriptor framework [P25]. The required corrections are determined from repeated virtual measurements and applied to a real measurement of an object with sufficient similarity to the simulated scenario (e.g. the nominal geometry). While this method is capable in principle, the lack of accurate digital twins for arbitrary measurement tasks is still hindering its serious application. Currently, the main problem is to configure the parameters of simulation software such that a realistic counterpart to a real measurement can be obtained[104] in reasonable computation time. While the first part is generally well known, the required complexity of a physics based and thus accurate simulation currently typically still exceeds the duration of a real measurement.

The design of a digital twin is usually an iterative process, where model parameters are adjusted dependent on how well a target quantity of the simulation matches the corresponding reference values. For example, additional blurring is introduced into an X-ray image, depending on the effective X-ray spot size, which means that these characteristics must be determined for a real system [P6] and subsequently be respected adequately within the simulation. The technical details about the process of creating a metrologically capable digital

---

[104] Individual reports claiming the opposite have not passed independent testing and / or only cover very specific use cases. This observation is backed up by substantial funding spent in current and future research projects aiming to contribute to solving this problem.

twin in the context of the research project AdvanCT [263] were published in [264]. In the following, the results of that design process are evaluated using the spatially discrete metrological descriptor framework by comparing one virtual measurement series against a real one[105]. These series describe the measurement results of both systems with measurement parameters matching each other as closely as possible. The measurement object (hole plate) showed little manufacturing deviations, which was confirmed by a TCMS reference measurement, which was processed into a reference triangle mesh, as described in sec. 5.5. Consequently, the framework use case for the real measurement series was UC_{1b}. For the computation of the spatially discrete measurement uncertainty, the reference geometry was represented by a triangle mesh with nominal mean edge length of 50 μm consisting of

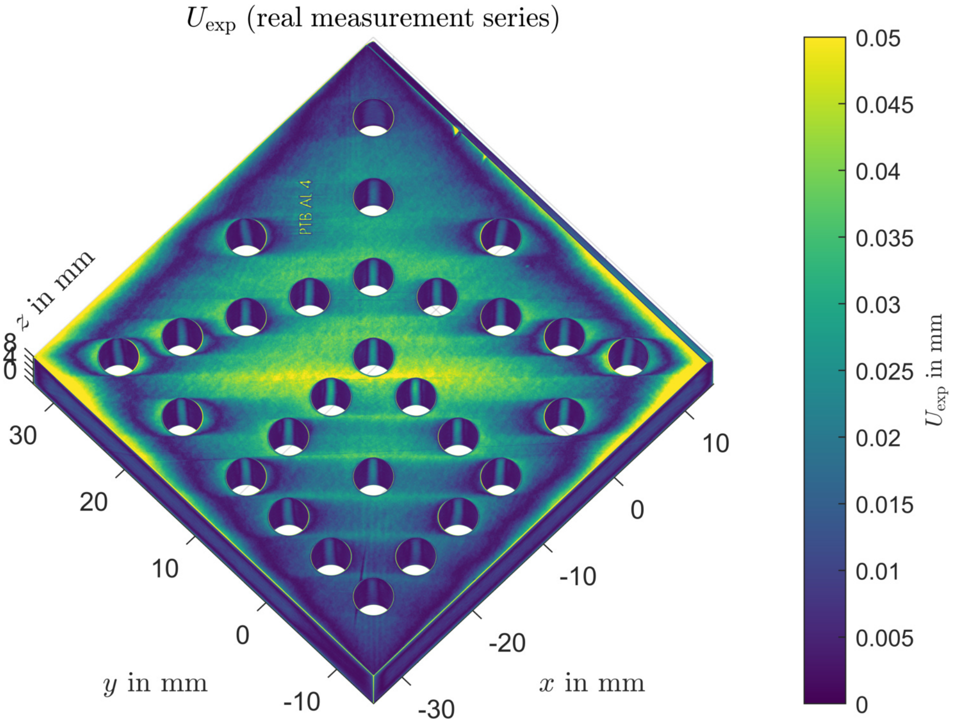

Figure 56: U_{exp} of the real measurement series, with respect to the given nominal geometry. Colour map limits represent the 2.5thand 97.5th percentiles of U_{exp}, respectively. The measurement series show larger measurement uncertainty in the centre of the hole plate, compared to the outer regions. The bore holes contain surface regions affected by cone beam artefacts.

---

[105] Thus, knowledge about the exact approach for generating the digital twin is not required for the following examinations. For the same reason, no details about measurement settings are given here, they are the responsibility of the respective researchers.

$\approx 6.9 \cdot 10^6$ triangles. The measurement object of the corresponding simulated measurement series is represented by the nominal geometry of the hole plate. Because of the fact that there are no manufacturing deviations in case of a simulated measurement, there is no difference[106] between the nominal and the reference geometry, respectively, and the framework use case was therefore UC_{2b}. The corresponding triangle mesh representing the sampling start geometry was prepared with the same nominal mean edge length of 50 µm, resulting in the same number of triangles ($\approx 6.9 \cdot 10^6$)[107].

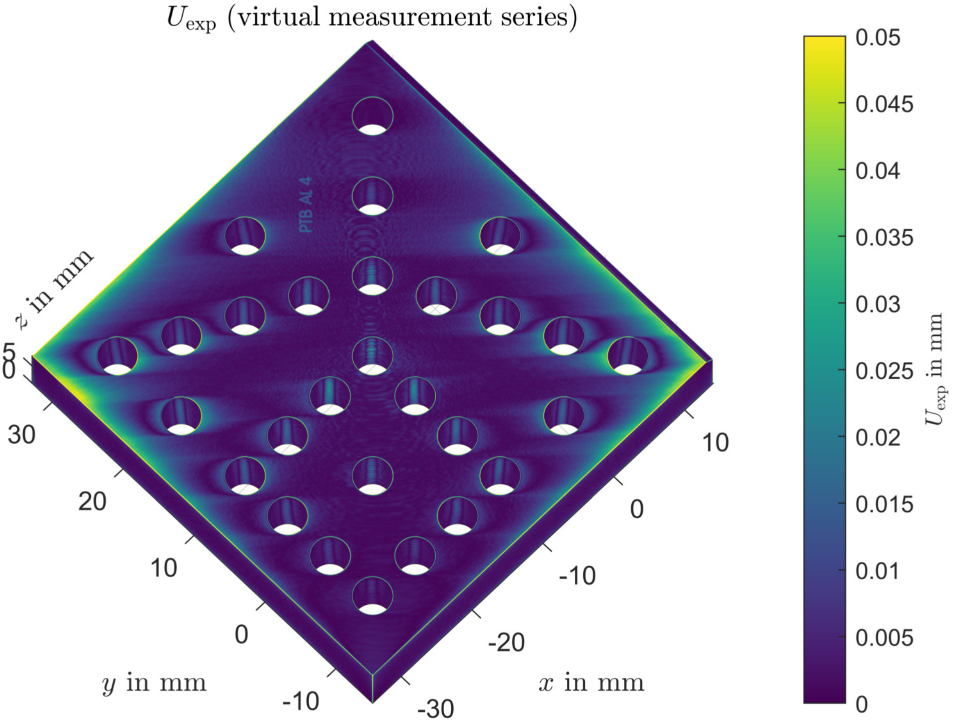

Figure 57: U_{exp} of the simulated measurement series, with respect to the given input geometry. Colour map limits represent the 2.5thand 97.5th percentiles of U_{exp}, respectively. Most of the surface shows low measurement uncertainty. The bore holes show the effects of cone beam artefacts.

---

[106] This assumes, that the conversion of the nominal CAD geometry into a triangle mesh (the used simulation software provides an STL geometry interface), was done with negligible approximation error.

[107] The number is triangles is equal, because they originate from the same mesh, with the only difference being that the reference mesh was additionally altered according to the TCMS measurement data.

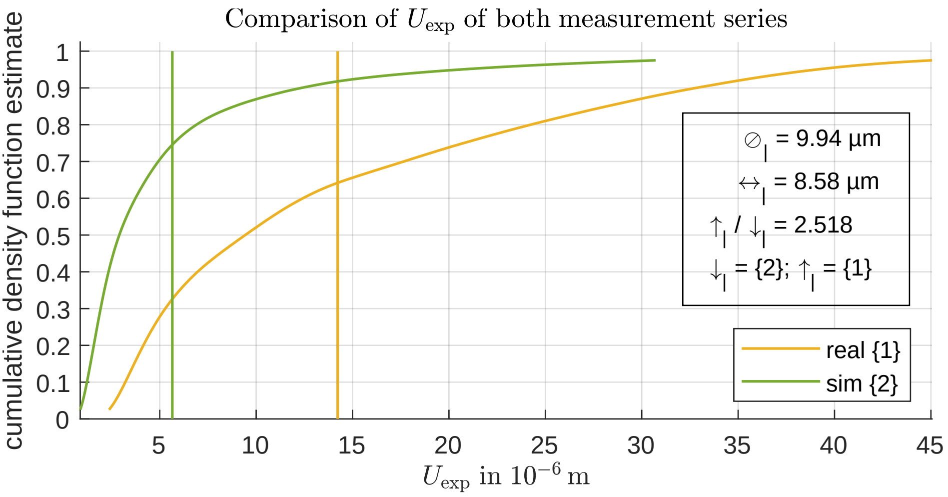

Figure 58: The statistical comparison between the measurement uncertainty of the simulated and the real measurement series confirms that the simulation is underestimating the uncertainty by a factor of ≈2.5.

The comparison between U_{exp} of the real (Figure 56) and the simulated (Figure 57) measurement series, respectively, shows substantial differences. The visual inspection reveals less uncertainty in the centre of the hole plate and overall the uncertainty seems to be lower compared to the real measurement series. This first impression is confirmed by the statistical evaluation shown

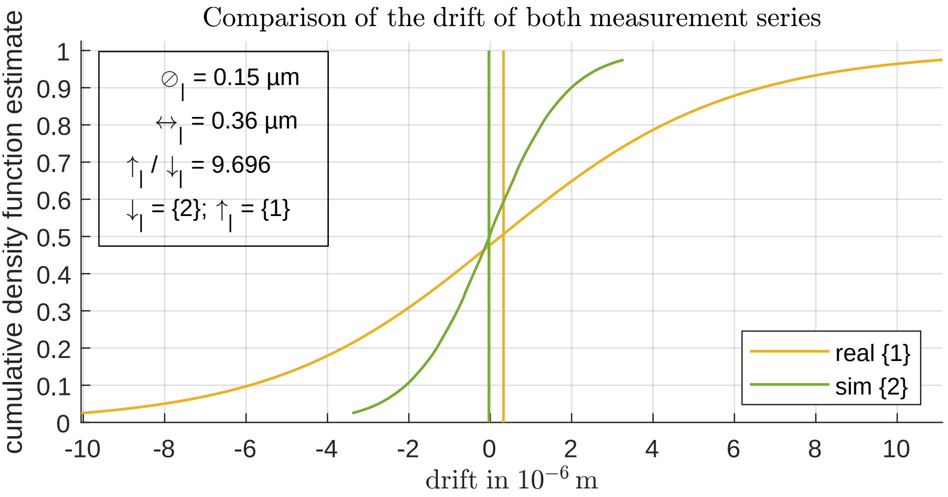

Figure 59: The real measurement series shows some drift, which can be recognised by both non-zero mean and median values of the orange curve.

in Figure 58. The results give reason to believe that the goal of creating a digital twin, which accurately describes the metrological behaviour of a real CT system, could not yet be fully met and further research may be required. It is worth mentioning that the real measurement series was affected by a small drift (Figure 59), which could at least partially contribute to the observed differences between both systems. Drifts in CT systems are commonly caused by imperfect clamping and especially styrofoam relaxation can cause this, if not used with caution.

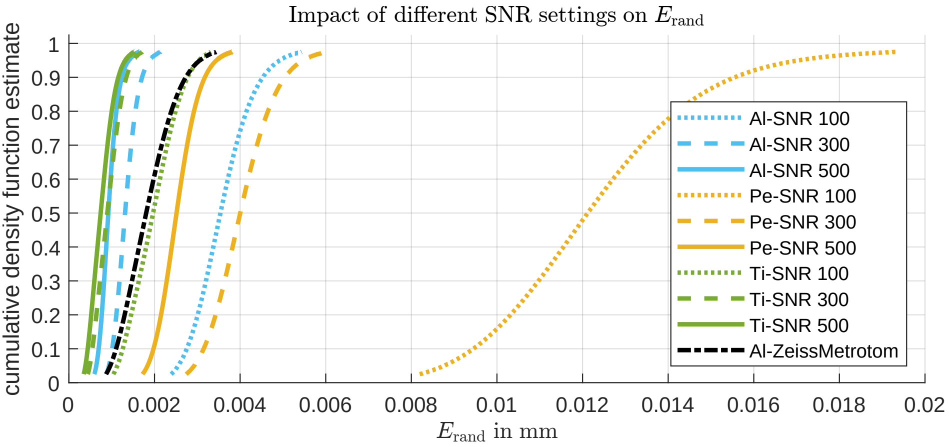

Figure 60: Comparison of the random measurement error E_{rand} occurring for measurement series with different object material and SNR settings against those of a real measurement. The examined simulation method of representing measurement noise based on the observed signal-to-noise ratio (SNR) in real measurements produces rather unrealistic results, which is also indicated by the large differences between the three PE measurement series. Image reprinted from [P13].

Besides the examination of that specific digital twin, the method of representing noise based on the signal-to-noise ratio (SNR) in CT simulation software was investigated and published in [P13]. For that study, three different materials (polyethylene, aluminium and titanium) were virtually measured with three different SNR (100, 300 and 500) and compared with a real measurement of the examined part made out of aluminium. It turned out that the examined method of simulating noise was rather unsuited for creating accurate digital twins, because it both underestimated and overestimated the random measurement error E_{rand} for different measurement scenarios compared to a real measurement (Figure 60). The main reason for that was the used sub-optimal virtual detector model with respect a real device. More details can be found in the corresponding publication [P13].

6.1.8 Investigating VGS mesh export presets

For CT measurements, the volume data reconstruction is followed by the surface determination, which produces the data foundation for dimensional evaluations. For conventional dimensional validation based on the ISO GPS standards, it is sufficient to process point cloud geometry data, the same as it is performed by default in the case of tactile measurements. The computation of the spatially discrete metrological descriptors however is based on triangle mesh geometry data, which requires a conversion of the result of the CT surface determination into surface geometry data. The same concepts of only approximative representation of curved data as for the representation of CAD geometry data apply here. Therefore, higher triangle counts tend to mean more accurate representation of curved surface regions at the cost of higher associated computation expenses. Ideally, the geometry is represented with the least amount of triangles but without altering the represented measurement results. The CT software VGStudio Max (VGS) offers 8 different presets for exporting CT measurement data as a triangle mesh (Table 11). These settings vary in the amount of triangles they produce for a given measurement. The suffix "with simplification" means, that the triangle count of a mesh resulting from a certain setting is further reduced by removing triangles which offer little additional information, based on certain thresholds. This can include triangles with a very small interior angle, or multiple neighbouring triangles lying approximately within a common plane, which offers the possibility to represent that planar region with less triangles. For this examination, the measurement data presented in a previous section (see sec. 6.1.4) was reused, but with different mesh export settings. The measurements of series "400 ms, 1 img" are consistently represented by more triangles, because the measurements are noisier compared to "2000 ms, 1 img", which caused the requirement of more triangles in order to depict the underlying geometry.

The reason why mesh export settings are examined is that geometry representations differing with regards to the amount of information they contain (file size) should also differ with respect to how accurately they can describe the underlying geometry. If that is the case different measurement error is computed from these measurements just by changing the file export settings. The amount of that influence was investigated by calculating the spatially discrete metrological descriptors using the same reference geometry as sampling start geometry as described in Table 7. For that, the distance metric "vertex normal vector (VNV)" was applied, because for that distance metric, the calculated intersections are not influenced by the surface roughness of the target geometry. Both measurement series "400 ms, 1 img" and "2000 ms, 1 img" were exported with all 8 presets. It shows, that E_{sys} and U_{exp} are nearly

Table 11: Comparison of the mean mesh sizes resulting from different mesh export quality settings by VGS for the measurement series ”400 ms, 1 img” and ”2000 ms, 1 img” (see Table 7). In the binary STL file format, 1 face corresponds to 50 B of file size.

name	mean number of triangles ”400 ms”	mean number of triangles ”2000 ms”
very fast	$1.2\cdot10^6$	$1.1\cdot10^6$
fast	$1.7\cdot10^6$	$1.7\cdot10^6$
fast with simplification	$0.8\cdot10^6$	$0.5\cdot10^6$
normal	$3.5\cdot10^6$	$3.4\cdot10^6$
normal with simplification	$2.5\cdot10^6$	$1.6\cdot10^6$
precise	$4.6\cdot10^6$	$3.9\cdot10^6$
precise with simplification	$3.2\cdot10^6$	$1.7\cdot10^6$
precise watertight	$13.6\cdot10^6$	$13.3\cdot10^6$

unaffected by different export settings, with the range between the mean values $\leftrightarrow_{|}$ being below 1 µm for both series. The parameter E_{rand} consistently shows higher values, the more triangles the setting produced, but the absolute differences between the mean E_{rand} are also below 1 µm for both series. The scatter of the target surface normal vector β_{rand} for series ”400 ms, 1 img” is visualised in Figure 61. It shows that β_{rand} generally increases with higher triangle count. That means that measurements dependent on the surface roughness are surely influenced by the mesh export settings. Especially work considering CT in the context of surface measurements (e.g. [265]) must take that influence factor into account. Now, the order of magnitude of the influence of the mesh export settings can be assessed with respect to the observed descriptors and the targeted use case of the spatially discrete metrological descriptor framework. For measurements where the magnitude of systematic measurement errors are more closely matching these of the random ones, the mesh export settings could influence the observed U_{exp} more. For other cases, a good compromise is the setting ”precise with simplification” especially against the background that unnecessarily large measurement files also increase the computation costs. Consequently, that setting was used for most other evaluations.

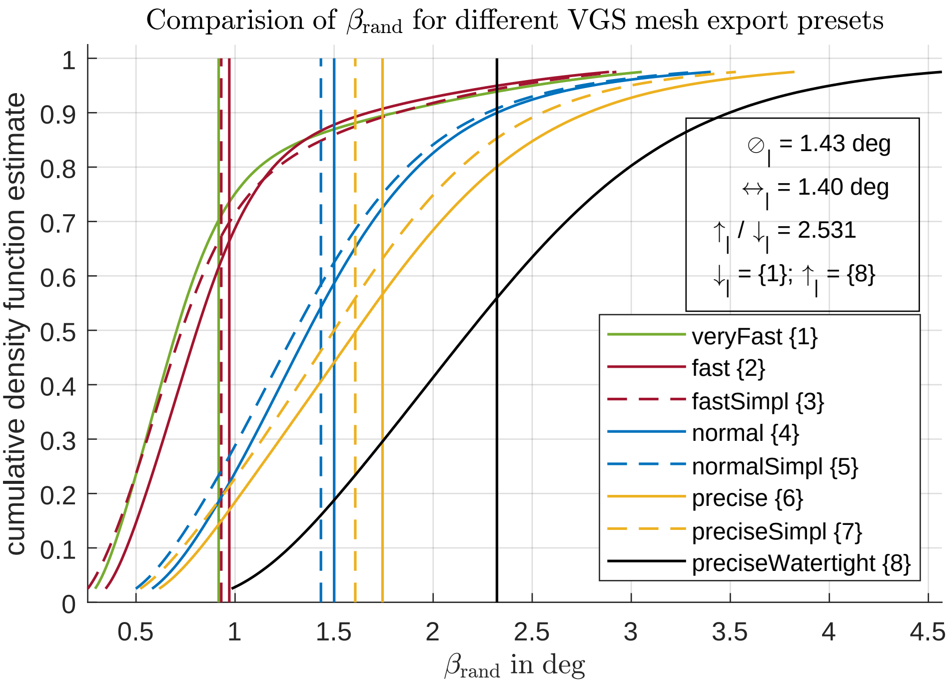

Figure 61: Visualisation of differences between mesh export settings by inspecting the resulting β_{rand} values of series ”400 ms, 1 img”. Higher triangle mesh count (see also Table 11) results in higher β_{rand} values, confirming that more high frequency shares are represented then. The highest and lowest weighted mean value of the distributions deviate up to a factor of 2.531.

6.2 Differences between the available distance metrics

In sec. 5.3, different distance metrics where introduced, each of them offering individual characteristics with respect to the obtained results. The exact anticipation of their different behaviour can be abstract, that is why a practical comparison is given in this section. For that, the measurement series ”400 ms, 1 img” (Table 7) was exported using the ”precise watertight” export setting (Table 11) and the spatially discrete metrological descriptors were computed using the reference measurement named in the first table. For the following purpose, the metrological implications are less important than a comparison of the different distance metrics with respect to each other. Therefore, the absolute E_{sys} values were presented in Figure 62. As expected, the CEP metric produces the largest results, which is caused by only considering intersections at triangle vertex points. For the majority of sampling points, the results of the other metrics show very little differences with respect to each other. The SD metric is guaranteed to find the smallest possible (existing) distance from a sampling point to the target surface. Both SDSP and SDHP are derived from

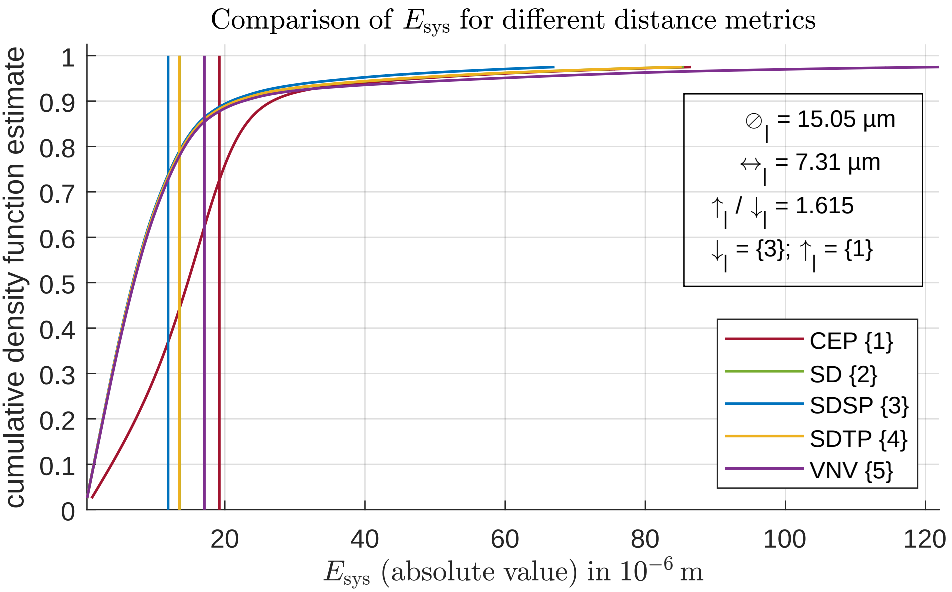

Figure 62: Comparison of absolute E_{sys} values of measurement series ”400 ms, 1 img” exported with setting ”precise watertight”. Observing the weighted mean values of the distributions, different distance metrics deviate up to 61 % from each other. The curves for SD and SDHP lie nearly exactly on top of each other.

that, additionally considering the vertex normal of the sampling start surface and the sampling target surface, respectively. Therefore, these two metrics must produce smaller results than SD. Especially in case the target surface is noisy, such as it was chosen here, the SDSP metric is expected to deviate noticeable from SD. The ”vertex normal vector (VNV)” metric produces larger intersection distances in edge regions, because of its direction constraint. This example shows that it is very important that the implications of choosing a certain distance metric must be well understood in advance, in order to be able to correctly interpret the obtained results. In [P4] a comparison between the SD and VNV distance metric, respectively, was presented, alongside technical implementation details. The determination of E_{rand} purely based on measurement repetitions (UC$_3$, see 5) was published in [P11].

6.3 Weighted geometry element regression analysis and data fusion

An important aspect of derived point-wise quality/uncertainty information from measurement data is the possibility to potentially improve mathematical operations that further process that measurement points. One example is the association operator of the ISO GPS framework (see sec. 1.1), where the measurement points describing a distinct geometric feature are associated with a model of that feature (e.g. coordinates representing a bore hole are associated with a cylinder). The model parameters of the cylinder (e.g. radius) that "fits-best", according to a user-defined auxiliary condition (e.g. Gaussian or minimum circumscribed [6]), represent a possible basis for dimensional measurands of the measurement object. Because of the fact that multiple measurement points are used for that regression analysis, it makes sense to assume that some measurement points are affected more by measurement error than others. Logically, consideration of various points within that mathematical optimisation procedure according to their respective uncertainty, such that "good" points are weighted more than "bad" ones, could yield an improvement of the dimensional measurement. However, this assumption only holds if the correlation between the parameter used for weighting and the measurement uncertainty is large enough. This theory was tested in three different ways, which are briefly presented in the following.

The first one is based on combining several measurement of the same object, which only differ with respect to their object placement within the measurement volume of an industrial CT system. Each measurement was affected by severe beam-hardening artefacts, however the different orientations caused different surface regions to be affected by that artefacts for each measurement. A weighted data fusion approach of all measurements, where the SPQ of each surface point determined its weight, showed favourable results compared to the individual measurements without data fusion. A detailed description of the method can be found in the corresponding publications. [P2, P3]

The second use case deals with the introduction of SPQ values into weighted geometry element regression analysis. For that, a calibration artefact consisting of 27 spheres was measured with an industrial CT system (see Appendix). Additionally disturbing bodies were introduced into the scene, such that the sphere surfaces were locally affected by measurement artefacts (Figure 63, left side). In the following, distances between sphere centres with sphere positions obtained from four different regression methods ("Chebyshev - miniumum zone", "Gauss - least squares", "Maximum inscribed" and "Minimum circumscribed" [266]) were compared against their respective reference measurement values obtained from a TCMS. For that, measurement coordinates with an unfavourable SPQ were removed from the measurement data, consequently only points with a "better" SPQ were taken into account for the regression analysis. It could be shown that improvements towards the reference measurement values could be obtained for almost all examined use cases, comparing the unweighted with the weighted results, respectively. Detailed explanations can be found in previously published work. [P33]

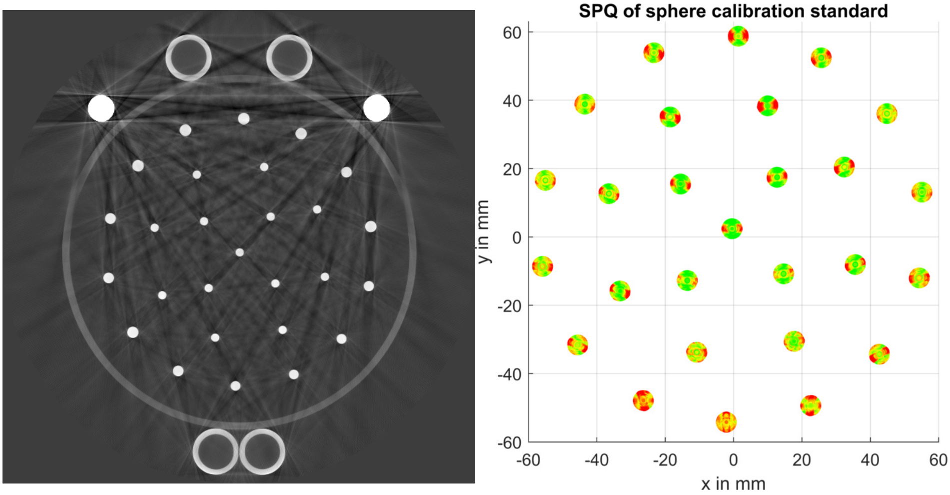

Figure 63: A measurement of a sphere calibration standard with additional disturbing bodies (4 times aluminium, 2 times steel) placed around the object. The left image shows a cut through the volume data of the measurement. The SPQ of the sphere surface points shows different qualities, depending how much they are locally affected by measurement artefacts (right image). Note, that the spheres centres do not lie in a common plane. Images reprinted from [P33] with minor modifications.

In the third example, weighted geometry regression analysis based on determined spatially discrete metrological descriptors (E_{rand}) was examined for cylinders in a hole plate. The precision information was directly introduced into the optimisation problem associated with geometry regression analysis. Here, improvements with respect to the results obtained from the commercial software VGStudio Max could be observed, however these were not consistent for all evaluations. A potential reason for that could be the unfavourable setup of the Monte Carlo simulation for generating random measurement samples from the obtained local spatially discrete metrological descriptors, which did not take into account geometrically local correlation between neighbouring points. [P5]

6.4 FORTol: Improving tolerance specifications

The research group ”FOR 2271: process-oriented tolerance management based on virtual computer-aided engineering tools”[108],[109] conducted fundamental scientific research with regards to how to design a holistic approach

---

[108] German project title: ”Prozessorientiertes Toleranzmanagement mit virtuellen Absicherungsmethoden”.

[109] Funding by the German Research Foundation (DFG) is acknowledged [268].

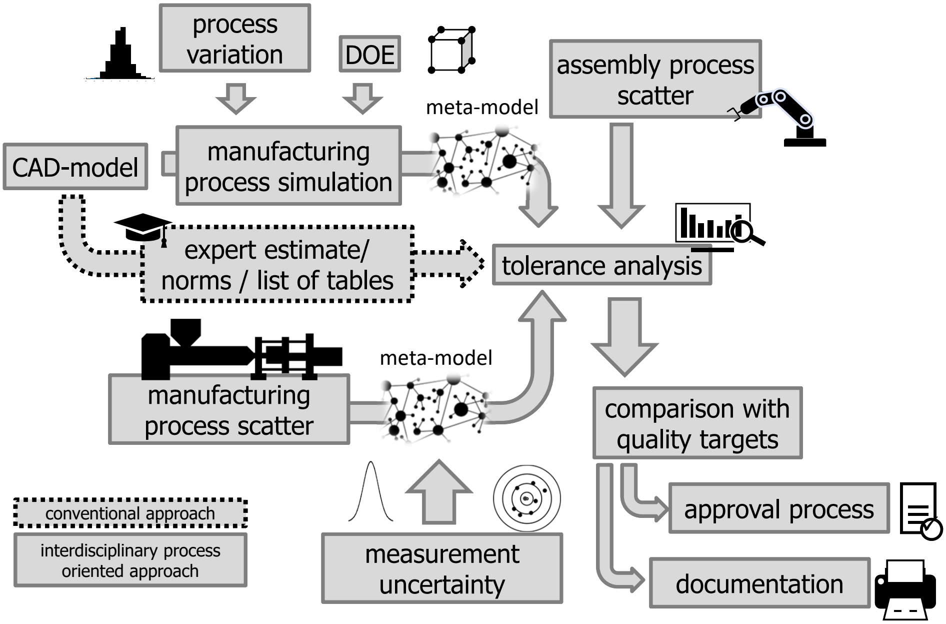

Figure 64: Image reprinted from [P30] (originally based on [267]) with minor modifications.

and efficient tools for the comprehensive control of geometric deviations in the product development process and validates these using a model factory. The conventional approach was to conduct a tolerance analysis based on expert estimates, standards and historical data (Figure 64). From the point of view of metrology, the process of specifying tolerances during the design can be improved if information about the expected measurement uncertainty during validation of the associated product specification is taken into account. The basic idea that tolerances are connected to the measurement uncertainty was already well known in form of the Golden Rule of metrology (see sec. 2.3), however a description of the uncertainty for any point on a workpiece surface enabled new opportunities. These included the determination and implementation of a parametrised description of the local measurement uncertainty (e.g. for certain surfaces relevant for the function of the part) into tolerance simulation tools, both with and without the creation of performant meta-models [P22–P24, P26, P30, P32]. The vision of the research group was to enable systematic cooperation between product development, manufacturing and metrology in computer-aided tolerance allocation (Figure 64). Thus, besides the aforementioned measurement uncertainty, also manufacturing process scatter as well as assembly process scatter were considered[110]. This close cooperation was intended to allow early identification of production process-related causes of subsequent functional limitations and quality reductions and ultimately lead to the joint development of tolerances that are suitable for production, testing and function. Due to the developed capability of the estimation of the local measurement uncertainty of a workpiece based on different tactile, optical and tomographic measurements, an important building block to improving the specification of tolerances could be contributed to an overall successful research project [P34].

---

[110] Additionally, wear effects were taken into account in a later project phase.

7 Heterogeneous computing for data parallel problems

The core functionality of the spatially discrete metrological descriptor framework is the local comparison of two meshes using different distance metrics, as described in sec. 5.3. The more sampling points are defined on the sampling start geometry, the more the results converge to a spatially continuous description of the metrological descriptors over the complete surface. This would be the ideal case mathematically, however it involves an infinite amount of computation. From a metrological point of view, the sampling density should reach at least half of the best metrological structural resolution of the measurement system for that particular measurement. On the other side, the targeted geometry mostly represents measurement data, which ideally contains the complete spatial frequency spectrum of the measurement system. It turned out that special care with regards to the implementation of the used algorithms was required in order to provide enough computational performance to realise a broad spectrum of applications of the spatially discrete metrological descriptor framework. This chapter gives insight on the reasoning and implementation as well as performance key figures of the proposed solution based on the use of at least one general purpose graphical processing unit (GPGPU) [269].

7.1 Problem size and algorithmic properties

Within the data processing pipeline, typically the majority ($\geq 90\,\%$) of the computational work is required for the following operations:

- The distance metrics (CEP, SD, SDSP, SDHP, VNV) are used within the error metrics of the geometric registration as well as for the computation of the distance fields between two triangle meshes from which the descriptor information is computed.
- Ideally, the measurement data is error-free and is represented by watertight 2-manifolds. In case triangle mesh repair is needed, the test for inconsistencies based on triangle-triangle intersection tests as wells as the computation of winding numbers used for volumetric mesh repair are operations with increased computational demand.

The search for triangle mesh inconsistencies tests all triangles of a mesh against each other, which requires $\frac{n(n-1)}{2}$ triangle-triangle intersection tests. All other algorithms listed above have the same structure: For each $\boldsymbol{S}_i$, a sought-for distance is selected from all possible solutions with respect to the target geometry, which consists of a multitude of triangles. In order to obtain that required result, each primitive (triangle) must be tested for a potentially correct solution. The desired result can be obtained in two different ways:

1. Explicitly test all possible combinations (e.g. test each ray against each triangle) and select the correct intersection. This technique is called exhaustive search or brute-force search [270]. For each ray, n tests are required at all times.
2. Implicitly test all possible combinations through the application of spatial partitioning methods, e.g. k-dimensional (k-d) trees. Vividly explained[111], the searched domain (e.g. coordinates in 3D) is split into volume elements (e.g. cubes) and each of these cubes is again subdivided into 8 cubes [84]. This process can be repeated until a user defined depth. Then, all target elements (e.g. triangles) are associated with this tree structure. The test for all possible intersection of ray with the triangles of the target mesh first tests for hits of the tree structure (cubes) and only then tests against the remaining possible triangle candidates associated with the deepest cube level. For each ray between $\log(n)$ and n tests are required but additional cost is introduced due to tree construction and traversal. This approach can be adapted to CEP and SD-related distance metrics.

The problem size is dependent on the following three factors: The number of $\boldsymbol{S}_i$, m, the number of target elements in the target geometry (points or triangles) n, and the size of the measurement series, which was fixed to 20 for this thesis. From a metrological point of view, it makes sense to expect $m = n$ for the following algorithmic discussions. Consequently, the described methods show theoretical asymptotic complexities [272] between $O(n\log(n)$ and $O(n^2)$. The required performance is ultimately determined by the triangle count of the processed geometry data. This in turn is dependent on the effective resolution capabilities of the used measurement systems, which was not exactly known. The overarching goal was to realise enough computational performance even for large tasks, which might currently exceed requirements of the demonstrated use cases, in order to provide additional potential for future research. The associated design choices are described in the following section.

7.2 Fundamental design choices

As described above, the primary goal was to enable the processing of high triangle count geometry data within reasonable time scales. The initial aim

---

[111] This specific approach is called an octree which can be formally generalised to k-d trees [192, 271].

was to be able to process triangle mesh geometry data with triangle edge length in the typical range of the voxel size of the specific CT system Zeiss Metrotom 1500 (see Appendix), which is about 20 µm to 100 µm for typical objects[112]. This decision replaced the missing information about the metrological structural resolution of that system, whose determination is subject to current research. Furthermore, there were some auxiliary conditions which influenced the decision making with regards to the implemented software solution:

- MATLAB should be used as primary programming language, because it enables short development cycles for software prototypes. The fastest solution is not useful if it cannot be programmed within the given time constraints.
- The potentially achievable speed-ups justify the increased development times. In this context, it is also important to estimate beforehand how much additional optimisation is required after the first prototype is built.
- The developed solution must provide enough flexibility for further adjustments due to slightly changed requirements. In general flexibility and specialisation (i.e. solving a specific problem in the best possible way) work in opposite directions, which means that the right balance must be found.

Considering all facts, the decision was made to implement the numerically intensive program parts with the CUDA programming model (introduced by Nvidida in 2007 [273]) and thus to outsource the execution of critical program parts to specialised hardware, the graphics processing unit (GPU). As opposed to central processing units (CPU), which are by design latency-oriented, GPUs are designed as parallel, throughput-oriented computing engines [273]. GPUs were invented to perform computation of graphics applications in the context of a fast growing video game industry, which require a massive number of floating-point calculations per video frame [273]. Since the early 2000s, a variety of applications has greatly benefited from building applications in CUDA, often in the range of several orders of magnitude compared to previous state of the art implementations [274–279]. In order to balance implementation efforts against potential benefits in computation speed, the decision was made to implement the algorithm without additional acceleration methods. These are typically based on spatial partitioning techniques [84], e.g. k-dimensional trees (k-d trees) [192, 271]. Such data structures offer a superior theoretical asymptotic complexity of $O(n \log n)$ plus the cost of creating and traversal of the search data structure. However, different search structures are required for different problems, which means that the ”closest

---

[112] The number of triangles is thus dependent on the voxel size and the surface area of the measurement object which both indirectly correlate with each other due to the relationship between measurement volume and magnification.

point on triangle" problem requires a different search structure than ray-triangle intersection tests. Furthermore, it is not trivial to find the optimal tree parameters (e.g. tree depth) and deviations from the most efficient tree negatively impact performance. Instead, the algorithms were implemented using exhaustive search (explicitly test all possible combinations) in combination with GPU acceleration, which overall required less development time, offered more flexibility and ultimately resulted in sufficient performance for the targeted computation tasks. One additional reason for the decision to work with GPUs was the introduction of hardware-accelerated ray-tracing in form of specialised processor cores with the Turing architecture in 2018 by Nvidia [280, 281]. Therefore, it was foreseeable that the best possible performance for the spatially discrete metrological descriptor framework would be achieved using the associated OptiX ray-tracing engine [282] for the computation of the VNV distance metric[113]. The reason for that is that with OptiX, specialised chips on the GPU are used to accelerate the ray-triangle intersection calculations directly on the hardware level.

Even though the application of GPGPU methods overall offers the best performance for the relevant problem size scales, the framework is additionally equipped with a performant CPU implementation of the SD distance metric. The functionality is based on MATLAB's nearest-neighbour search [283], which can be adopted for the solution of the "closest point to triangle" problem. Even though the performance is in general lower than the GPU implementation, it provides the possibility to use the framework without specialised additional GPU hardware. A detailed description of the algorithm was published in [P4].

7.3 The basics of parallel programming

The observation made by Gordon Moore in 1965 that the number of transistors integrated on silicon chips were doubling about every 2 years is commonly known as Moore's law [284, 285]. This exponential growth led to automatically faster sequential applications through faster microprocessors [285]. In 2005, further advancement in the development of single core processors was limited by technical restrictions, which caused a shift to new processor designs using multiple cores [285]. These barriers are also referred to as "three walls" and are briefly introduced as [285, 286]:

- Power wall: Exponential growth in power usage with increasing clock rate.

---

[113] The current implementation is not using OptiX but an own implementation of the ray-triangle intersection algorithm (see sec. 5.3.5) in CUDA.

- Instruction-level parallelism wall: Limits to available low-level parallelism [287].
- Memory wall: Discrepancy between processor and memory speeds, respectively [288].

The combination of these factors is also called the ”brick wall” [286]. This lead to two main trajectories for designing microprocessors: The multicore trajectory, where the execution speed of sequential programs is maintained while moving into multiple cores, and the many-thread trajectory, which focuses on the execution throughput of parallel applications [273]. This results in two distinct strengths for each of the architectures, such that CPUs are generally latency (time to complete a task) optimised processors and GPUs being throughput-oriented (rate at which a series of tasks can be completed) [285]. The reason for that lies in the different design of CPUs and GPUs, as illustrated in Figure 65. The GPU devotes more transistors to data processing rather than data caching and flow control [289]. This is beneficial for highly parallel computations, because the GPU can hide memory access latencies with computation this way, instead of relying on large data caches and complex control flow to improve memory access latencies [289]. Consequently, the best overall performance can be achieved by heterogeneous computing by assigning computational tasks to each microprocessor type, depending on their computational profile [285, 290].

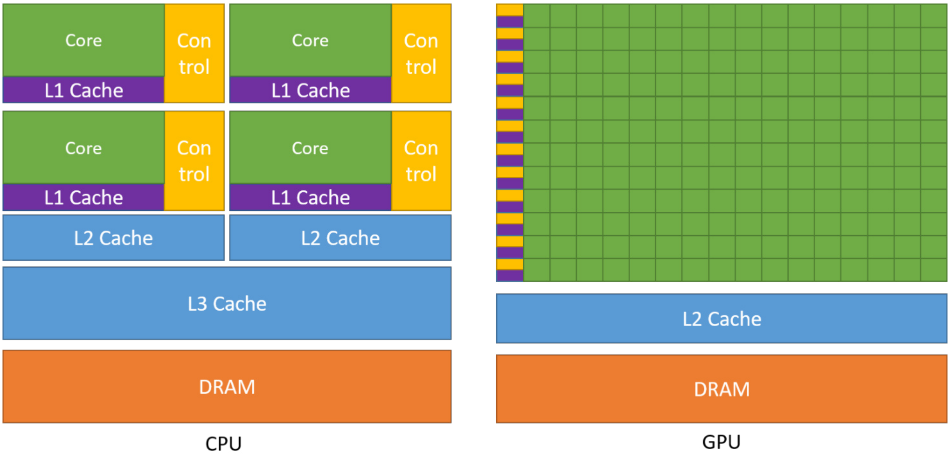

Figure 65: Differences in architectural design choices for CPUs and GPUs: Because a GPU is specialised for highly parallel computation, it devotes more transistors to data processing rather than data caching and flow control [289]. Image reprinted from [289].

There exists a theoretical limit (called Amdahl’s law) how much an application can be sped up by a factor S (Figure 66) dependent on the number of workers (cores / threads) $k \in \mathbb{N}^+$ and the fraction of serial program parts $p \in [0,1]$, which cannot be parallelised and thus benefit from multiple workers (81) [291].

$$S = \frac{1}{p + \frac{1-p}{k}} \tag{81}$$

Clearly, parallelisation efforts show diminishing returns fast, if the serial fraction of the program increases. Amdahl's law, also referred to as strong scaling, assumes a fixed problem size and gives an upper limit of the potential speedup with respect to the number of processors used. Weak scaling on the other hand was introduced as Gustafson-Barsis' law (Figure 67), which assumes that the parallel part of a program scales linearly with the amount of resources, which means that the serial part remains constant (82) [292].

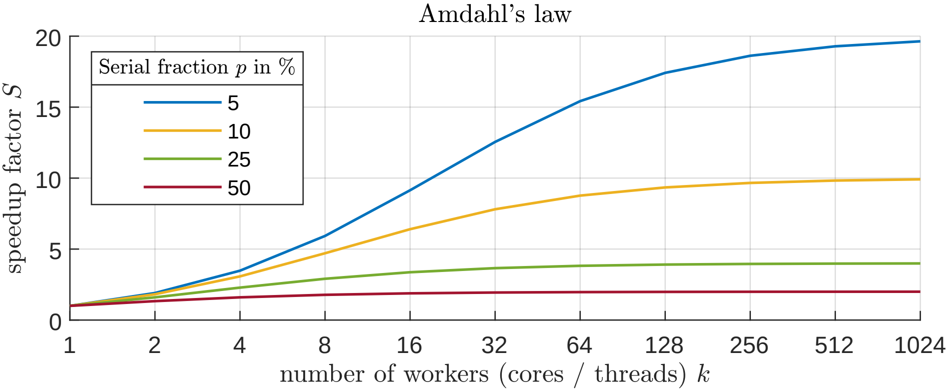

Figure 66: Amdahl's law is describing the potential speedup factor due to the application of parallelisation as a function of the number of workers k and the serial fraction p of the executed program.

$$S = k + (1-k) \cdot p \tag{82}$$

Both Amdahl's and Gustafson-Barsis' laws are correct, however Gustafson-Barsis' observations fit the historical trend better [285]. Both models show linear speedup with the number of processors, in case $p = 0$. Therefore, it is clear, that the targeted problem needs to show certain properties in order to obtain high speed-up factors and thus high efficiency with respect to the used computing resources. The best strategy to achieve scalable parallelism is data parallelism [273, 285, 293]. Data parallelism is observed when a task can be broken down into many smaller computations that can be performed independently of each other [273, 279]. If that is the case and given that the data is large enough, perfect parallel scaling can be achieved, because

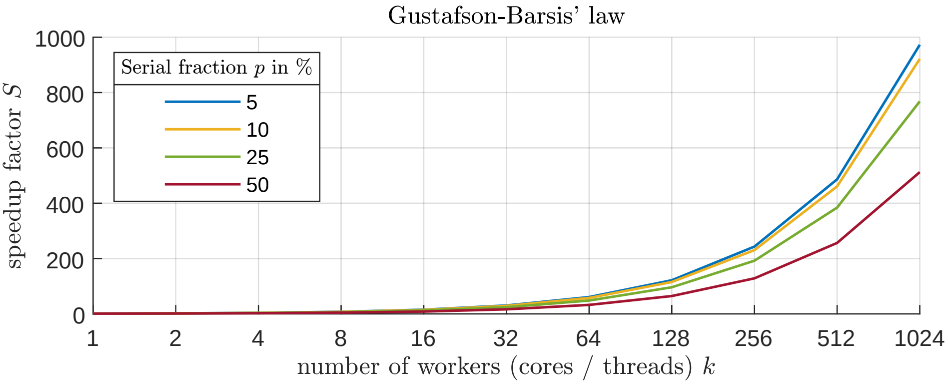

Figure 67: Gustafson-Barsis' law assumes that the parallel fraction of a program increases with the number of workers, resulting in a linear scaling with respect to k. (Note the logarithmic scale for better comparison with Figure 66).

the serial fraction converges to zero. This behaviour is in fact the case when applying the distance metrics to two triangle meshes: The computations required to obtain the distance data for different sampling points is completely independent of each other and scales therefore perfectly with the available resources. A computational problem is called ”embarrassingly parallel” if it can easily be divided into components that can be executed concurrently [183].

7.4 Building heterogeneous solutions with CUDA

On a hardware level, the NVIDIA GPU architecture is built around a scalable array of multithreaded Streaming Multiprocessors (SMs), which are designed to execute hundreds of threads concurrently. CUDA threads execute on at least one physically separate device, that operates as a coprocessor to the host (CPU) running a C++ program. Both host and device have their own separate memory (RAM and VRAM as well as on-chip caches). The CUDA programming model exposes the hardware functionality to the user. It consists of a minimal set of extensions to the C++ programming language and a runtime library. The user can define own C++ functions, called kernels, that are executed in parallel by a number of user-defined threads. Threads are organised in equally-shaped thread blocks, which are themselves organised in a grid. Thread blocks must execute independently of each other in any order, in parallel or in series. Threads within a block can cooperate by synchronising their execution with regards to coordinating memory accesses. CUDA exposes a memory hierarchy with per-block shared memory, per-thread local memory and all threads having access to global memory (GPU-RAM). [289]

MATLAB can not execute C++ code directly, but it provides interfaces between both programming languages (C Matrix API [294], Data API for C++ [295] and GPU MEX API [296]). With these APIs, so-called MEX files containing the CUDA functionality can be compiled into mex functions, which can then be directly called like ordinary functions in MATLAB.

A simple example is shown in Algorithm 2, p. 163. Here, different code key words are coloured according to their origin: C++ (blue), CUDA (red) and MATLAB C Matrix API (olive). The goal of this program is to add the values of two equally sized vectors on the GPU and return the result vector to the host. This program is called in MATLAB and its entry point of the program is `mexFunction`[114] (line 10) with its fixed signature. At first, both input arrays are copied to the GPU (lines 13/14) and device pointers are created (lines 17/18). A result array and its device pointer are created (lines 21/22) followed by the definition of the grid parameters by setting the number of blocks and threads per block (lines 25-27). Here, each thread performs an addition, which might not be optimal in practise. Then the `Add` kernel[115] is called (line 28) with the given grid and input and return parameters, respectively, and the computations are executed in parallel on the GPU. The host CPU thread is meanwhile stalling at the CPU/GPU synchronisation barrier (line 29) until all computations are completed. The results of the computation are returned to MATLAB (line 30) and only temporary required memory is freed again (lines 32-34). Inside the kernel (lines 1-8), the programmer has access to different built-in variables, which specify the grid and block dimensions and the block and thread indices. These themselves can have multiple dimensions x, y and z. Here, `threadIdx.x`, `blockIdx.x` and `blockDim.x` are used to determine the array index for the addition of both input arrays.

The following design principles can help to achieve the best overall performance of the implemented heterogeneous programs as well as reveal potential weaknesses of GPU accelerated algorithms:

- The computation task must be large enough in order to fully saturate the GPU (at least several thousand parallel threads) and to satisfy the additional cost of data transfers to and from the GPU.
- The task should expose high degrees of data parallelism, such that individual data elements can be processed independently of each other.

---

[114] It fulfils the equivalent purpose of a C/C++ `main` function.

[115] Kernels are GPU functions, that are marked with the `__global__` keyword and callable from host code.

```
__global__ void Add(float* a, float* b, float* c, int n)
{
    int i = threadIdx.x + blockIdx.x * blockDim.x;
    if(i < n)
    {
        c[i] = a[i] + b[i];
    }
}

void mexFunction(int nlhs, mxArray* plhs[], int nrhs,
                            const mxArray* prhs[])
{
    const mxGPUArray* a = mxGPUCreateFromMxArray(prhs[0]);
    const mxGPUArray* b = mxGPUCreateFromMxArray(prhs[1]);
    int n = mxGPUGetNumberOfElements(a);

    float* d_a = (float*)mxGPUGetData(a);
    float* d_b = (float*)mxGPUGetData(b);

    int N[] = { n, 1 };
    mxGPUArray* c = mxGPUCreateGPUArray(2, N, mxSINGLE_CLASS,
                            mxREAL, MX_GPU_INITIALIZE_VALUES);
    float* d_c = (float*)mxGPUGetData(c));

    int blockSize = 1024;
    dim3 blocks((n + blockSize - 1) / blockSize);
    dim3 threads(blockSize);
    ADD<<<blocks, threads>>>(d_a, d_b, d_c, n);
    cudaDeviceSynchronize();
    plhs[0] = mxGPUCreateMxArrayOnCPU(c);

    mxGPUDestroyGPUArray(a);
    mxGPUDestroyGPUArray(b);
    mxGPUDestroyGPUArray(c);
}
```

Algorithm 2: CUDA program for adding two vectors on the GPU (device) and return the result array to the host. This function is callable from MATLAB, through the entry point `mexFunction` by using its C Matrix API. Key words are given in different colours for C++ (blue), CUDA (red) and C Matrix API (olive). This is an exemplary code snippet, actual implementations might vary.

- Control flow instructions (`if`, `switch`, `do`, `for`, `while`) can significantly impact the effective instruction throughput if threads of the same warp[116] diverge. The reason for that is that if threads of a warp diverge via data-

---

[116] The multiprocessor creates, manages, schedules, and executes threads in groups of 32 parallel threads called ”warps” [289].

dependent conditional branches, the warp executes each branch path taken, disabling threads that are not on that path. Consequently, control flow instructions should be small or otherwise the program must be structured around them, such that thread divergence is avoided. [289]
- In general, the programmer must optimise memory usage to achieve maximum memory throughput, which is often the main performance limiting factor. This is also the case for the implemented algorithms in this thesis, because they are programmed around an exhaustive search (see sec. 7.2), which are typically limited by memory performance. Effective measures include optimal memory access patterns and the use of user-managed caches via shared memory.
- One of the main differences[117] of GPUs compared to CPUs that they mostly perform floating point operations[118] in single-precision instead of double-precision. Although most Nvidia GPUs can also perform double-precision operations, their capabilities to that regard can be reduced significantly compared to single-precision ($1:64$ for the used GPU, see Appendix). Because ray-triangle intersection tests can be affected by reduced floating-point precision, the tests were performed in two stages: Valid intersections were selected from a wider window of barycentric coordinates with single-precision and then re-tested with double-precision. This effectively results in a double-precision ray-tracing algorithm, which provides more robust results in the context of dimensional metrology.
- The example in Algorithm 2 utilised only one GPU, but the extension to multi-GPU setups can be done by calling the kernel with both GPUs and additionally providing them with individual index ranges for the input/output data. For optimal performance, it is generally recommended to use GPUs dedicated for kernel execution (without active monitor output), which can then be operated with a specialised GPU driver mode (TCC).

7.5 Performance evaluation of the GPU implementations

This section starts by examining the theoretical and practical performance differences between a GPU and a CPU implementation of the algorithm behind the CEP distance metric, which is based on a nearest neighbour search in Euclidean space: The closest edge point of the target geometry must be determined for each sampling point $\boldsymbol{S}_i$. The own GPU implementation uses an exhaustive search, which tests each $\boldsymbol{S}_i$ against all edge points on the target geometry, resulting in a theoretical asymptotic complexity of $O(n^2)$.

---

[117] Exceptions exist for further specialised GPU hardware.

[118] All CUDA compute devices follow the IEEE 754 standard for binary floating-point representation, with a few exceptions which are documented in [289].

The CPU implementation is based on MATLAB's `knnsearch` [283] and has a superior theoretical asymptotic complexity of $O(n \log n)$. The performance

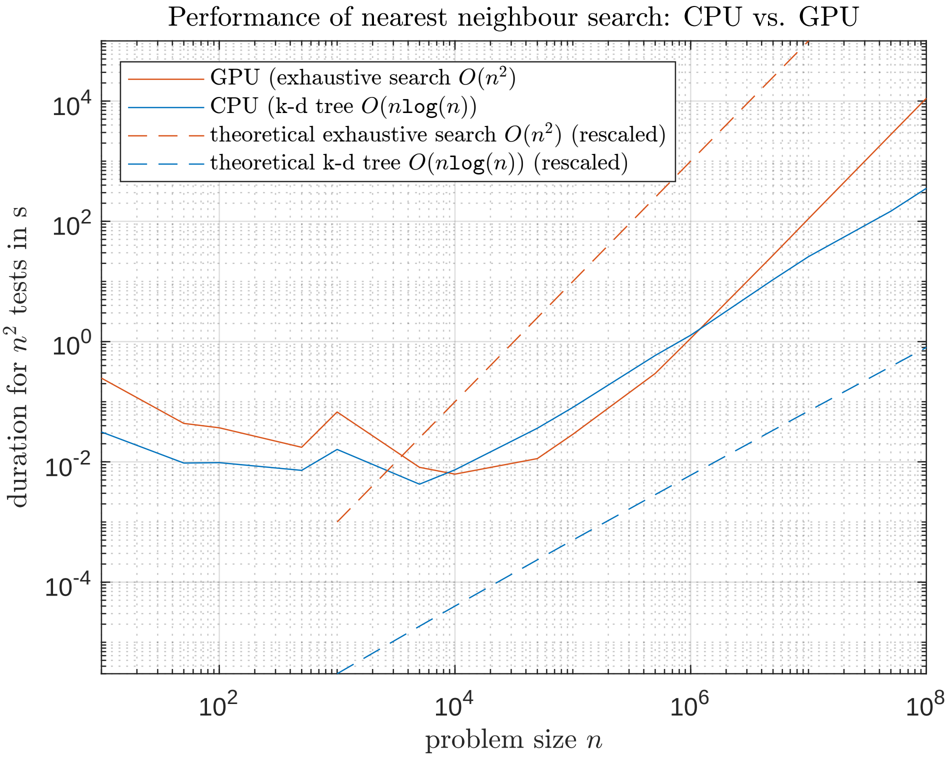

Figure 68: Performance comparison of a nearest neighbour search in 3D Euclidean space between a GPU and a CPU (for hardware see Appendix), using an own implementation of exhaustive search and MATLAB's kd-tree implementation [283], respectively. The GPU shows competitive performance up to a problem size of $n = 10^7$, only beyond that point the CPU solution is clearly preferred.

for different problem sizes n (for each point in set A, its closest point in set B is determined, with both sets having size n) is visualised in Figure 68. The GPU and CPU algorithms were run on the hardware devices described in Appendix. The differences for small problem sizes ($n < 10^4$) are very small but nonetheless reflect the additional overhead associated with GPU solutions (e.g. memory transfers). In the range $10^4 < n < 10^6$, the GPU implementation is faster, because the overhead associated with k-d trees are not yet fully compensated by the reduced computational demand. After that, the GPU implementation is slower with 110 s for $n = 10^7$ compared to the 25 s of the CPU. From this point on, the GPU matches the slope of its theoretical complexity curve (red dashed line). The CPU reaches this point earlier, at around $n = 10^4$. This problem size of $n = 10^7$ corresponds to the processing of two triangle meshes[119] with ≈1 GiB[120] each, which approximately represents the amount of triangles needed to cover the surface of a cube with 50 mm edge lengths with equilateral triangles with an edge length of 40 µm. STL files this large are currently clearly untypical with respect to metrological geometry representation. The largest observed CT measurement data STL file size with respect to this to work was ≤ 650 MiB (CT measurement with VGS mesh export preset "precise watertight"). This dense triangle meshes also clearly exceed the capabilities of visual inspection with false-colour plots, because the triangle sizes are far smaller than a screen pixel. Furthermore, the visual render engines (e.g. MATLAB) reach their limits, which results in stuttering handling in the graphical user interface. Consequently, problem sizes of $n^2 > 10^{14}$ are unlikely to provide further advantages in practise.

In the following, the performance of the implemented GPU algorithms is presented, in order to demonstrate their capabilities with respect to typical problem sizes. The performance indicators were measured with the hardware components described in Appendix. Figure 69 shows the number of "elementary tests" (e.g. 1 ray-triangle intersection test) performed per second of program run-time[121]. The mainly used distance metrics VNV and SD perform clearly more than 10^{11} elementary tests per second. The algorithm used for the distance metric CEP nearly manages 10^{12} elementary tests per second, nonetheless other distance metrics are preferred in practise because of their metrological properties. The CPU implementation of the same algorithm for the calculation of the winding numbers used for volumetric mesh repair in MATLAB (based on vectorisation and `parfor` [297]) performs worse by a factor of more than 400 compared to the own GPU implementation. Part of this performance difference can be attributed to the fundamentally different programming languages MATLAB (CPU) and C++ (GPU). Nonetheless, it confirms the statement made above, that an alternative implementation was necessary in order to provide sufficient computing capabilities for the spatially discrete metrological descriptor framework.

An estimation for expected computation times is given in Table 12. Here, the approximate processing duration for different operations is given with regards to the (file) size of the processed geometry. The presented durations are given with respect to the processing of a full measurement series, consisting of

---

[119] This assumes that the number of faces in the mesh equals twice its number of vertices, such that $N_f = 2N_v$.

[120] In the STL file format, the amount of data required to represent one triangle is 50 B.

[121] These performance metrics are also dependent on the overall duration of the program because of heat management mechanisms by the GPU itself. Typically, the chip frequency is slightly reduced with increasing chip temperature caused by the computations until an equilibrium is reached.

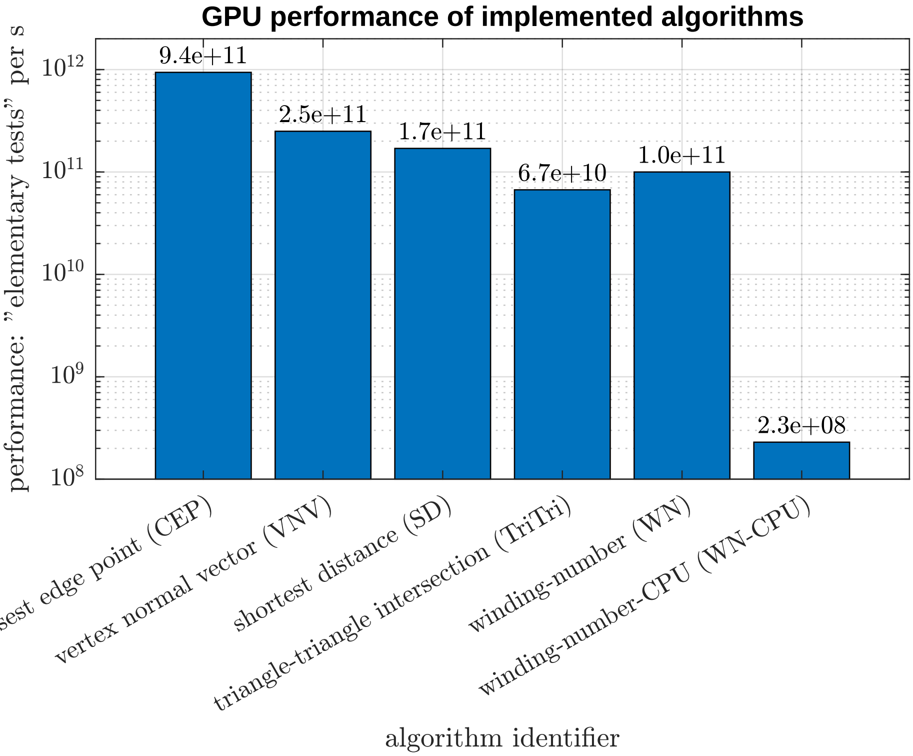

Figure 69: Performance evaluation of the implemented GPU algorithms in "elementary tests" per second. Such a test is e.g. one ray-triangle intersection test. The MATLAB implementation (using vectorisation and `parfor` [297]) of the same algorithm for the calculation of winding numbers (see sec. 5.2.3) is slower by a factor of about 400 compared to the own GPU implementation. Part of this difference is caused by the programming languages themselves (MATLAB vs. C++).

20 measurement repetitions. For example, CEP sampling for each of the 20 measurements with a file size of 50 MiB against a single sampling start geometry of equal size takes about 6 s with the hardware listed in Appendix. The listed algorithms (CEP, VNV, SD, TriTri) have different complexities with respect to file size. The STL file format represents each triangle with 50 B of data. The number of faces in a closed 2-manifold mesh equals twice the number of vertices such that $N_f = 2N_v$. The number of tests of CEP sampling with respect to the number of triangles n is therefore $\frac{n^2}{4}$, because it considers only the triangle edge vertices of both the sampling start geometry and the sampling target geometry. The distance metrics VNV and SD on the other hand also use the vertices of the sampling start geometry but additionally the full triangle faces on the target geometry, resulting in $\frac{n^2}{2}$ required tests.

Table 12: Expected durations for the processing of a measurement series consisting of 20 measurement repetitions of a specific (file) size and an equally sized sampling start geometry. The number of required elementary tests depends on the algorithm, e.g. for CEP, only the triangle vertices are processed, thus the total number of required elementary tests is $\frac{n^2}{4}$, using $N_f = 2N_v$. The exception TriTri is marked with †, because here the data structure applies the elementary tests (triangle-triangle intersection) against itself. Assuming no additional registration is required, the values shown in this table represent about 90 % of the overall computation time.

STL file size	50 MiB	100 MiB	250 MiB	500 MiB	1 GiB
# triangles (n)	$1.0\cdot 10^6$	$2.1\cdot 10^6$	$5.2\cdot 10^6$	$1.0\cdot 10^7$	$2.1\cdot 10^7$
20 × CEP $(\frac{n^2}{4})$	6 s	23 s	2 min	10 min	39 min
20 × VNV $(\frac{n^2}{2})$	44 s	3 min	18 min	73 min	5 h
20 × SD $(\frac{n^2}{4})$	65 s	4 min	27 min	108 min	7 h
20 × TriTri† $(\frac{n(n-1)}{2})$	3 min	11 min	68 min	5 h	18 h

The triangle-triangle intersection algorithm TriTri tests a mesh against self intersection, which means that in Table 12, the overall duration of the self intersection tests for each of the 20 measurement is reported. Here, the number of required tests is $\frac{n(n-1)}{2}$ because each triangle has to be tested against all other triangles exactly once, but not against itself. This table shows that the GPU implementations provide sufficient performance for both current and future applications.

In conclusion, the underlying design choices are revisited. It was clear that additional effort was needed in order to handle the computational requirements of the spatially discrete metrological descriptor framework. There were two possibilities: Either implement k-d tree search algorithms for an acceleration of the distance metric calculations or specifically exploit the data-parallel properties of that task. Although the first approach would have resulted in asymptotically superior complexity $n\log(n)$, different kinds of acceleration search structures would have been required for different distance metrics. Furthermore, these kinds of algorithms are technically more challenging and would have required more time to implement. On the other hand, GPU accelerated exhaustive search algorithms are conceptually simpler and very similar to each other with respect to their algorithm structure. This overall led to a higher efficiency during the development of the framework. It was shown, that the performance is very good and also high fidelity geometry data can be processed within a reasonable time frame. Additional performance improvements can be achieved today by using several GPUs (linear scaling) or in the future by the adoption of hardware product advancements.

8 Discussion

The spatially discrete metrological descriptor framework is based on the local comparison of triangle meshes in three-dimensional space. One of these geometries serves as a reference frame for all calculated results (the sampling start surface). Typically, some relationships between the coordinate systems of the different geometry types are unknown and must be calculated from error-affected data with mathematical tools (registration). This can be critically evaluated as follows:

- The geometry data processing of triangle meshes is significantly more demanding than that of point cloud data. Universal algorithms for creation, modification and evaluation of triangle meshes, especially in combination with faulty measurement data, do not (yet) exist. Therefore, universal robustness is hard to achieve, which also applies to the proposed methods and solutions.
- The local comparison operators (distance metrics) require consistent geometry data in order to produce reliable results. Otherwise, besides from increased algorithmic difficulties, the geometry data does not represent physical objects. These conditions corresponding to watertight 2-manifolds, are in practice not always possible to comply. This is especially true for tactile and optical measurements, where it is common to only measure parts of the complete geometry due to accessibility reasons (also caused by clamping). This problem is not as dominant for CT measurements because the complete measurement of the object is an inherent requirement[122] of the measurement principle. In cases where this condition cannot be met, this requirement can partially be lifted, if suitable (manual) registration methods in combination with adequate additional descriptor results post processing is applied. Nonetheless, the general requirement of watertight 2-manifolds partly limits the application of the spatially discrete metrological descriptor framework with respect to the possibility of a fully automated data processing pipeline.
- It is unclear which distance metric produces the ”most correct” results, because all of them show specific properties that can be disadvantageous in certain scenarios. A perpendicular measurement is usually preferred in metrology, however that distance metric (VNV) is not guaranteed to produce intuitively correct results, because their search rays can miss the targeted geometry in edge regions and if features are not aligned locally with each other for both geometries. The SD distance metric on the other

---

[122] Depending on the system, this condition can partially be lifted for special measurement setups.

hand might slightly underestimate the local uncertainty (especially in case of target surface roughness in the range of relevant spatial wavelengths), nonetheless this method is guaranteed to give the smallest possible uncertainty assessment, which is based on real intersection/hit data. The methods SDHP and SDSP are mostly reserved for special applications. The use of CEP should generally be avoided, however its computational demand is the lowest of the described distance metrics.

- The true coordinate transformation between the involved geometries is unknown and can only be estimated. Any deviations remaining from that true transform after the registration globally affect the metrological descriptors calculated for each discrete sampling point. Additionally, the chosen global registration approach can lead to relatively large contributions of small surface regions on the registration result. The alternative of manual registration based on geometry elements might produce more stable results in certain cases, however this method only considers a part of the geometry for determining the alignment. Even though the usability of the framework is reduced due to time consuming manual data processing steps, it is possible to consider datum systems from ISO GPS specifications (using third-party software) in order to solve the registration problem.
- The calculated spatially discrete uncertainty does not allow for function-oriented verification of geometric specifications (apart from some academic cases). The local metrological descriptors are determined based on time-consuming measurement repetitions. The obtained results require expert knowledge for interpretation and the generation of added value in the context of dimensional metrology is not trivial.
- In the absence of knowledge about the metrological structural resolution of a specific measurement task, it is currently not possible to apply minimum-requirement triangle mesh statistics in order to prevent sampling of spatial wavelengths beyond the capabilities of the system. In other words, the used sampling start surface triangle meshes might exhibit too few or too many triangles.
- Because of the made design choices, the framework currently relies on the availability of specialised hardware (CUDA compatible GPUs) in order to execute the computationally demanding comparison operators.

If these points can be managed for an application of interest, there are several distinct characteristics which make the method a powerful tool in the context of dimensional 3D coordinate metrology:

- Besides the requirement of complete measurements, the method requires no additional knowledge about the used measurement system and object, respectively. Therefore, no metrological test plans need to be created.

- The method is very sensitive to small changes in local measurement accuracy.
- It is straightforward to identify drifts in the measurement data.
- The main computation tasks (registration, mesh comparison and report generation) are fully automatable and thus require no user interaction. Thus, large scale investigations leaning on the field of ”big data” are very well possible.
- The results obtained with the implemented conventional metrological descriptors are traceable to the metre if traceable reference measurements were used. Furthermore, it is possible to determine a lower limit of the observed measurement uncertainty over the complete geometry of the workpiece (e.g. as area-weighted mean uncertainty). This is the case because the global[123] registration approach finds the tightest alignment of both geometries (according to the used error metric) and because the SD distance metric determines the smallest possible distances for each sampling point.
- Results obtained from different measurement series or systems, respectively, are directly comparable with each other and these comparisons yield metrological value. This distinguishes the spatially discrete metrological descriptor framework substantially from the surface point quality method for CT measurements.

If the mostly technical difficulties can be managed, the following applications and use cases are possible in the context of research and development:

- Testing and evaluating the effect of mathematical correction algorithms within the measurement chain aimed at reducing the measurement uncertainty, e.g. targeting measurement artefacts.
- Calibrating a digital twin with respect to its real world counter part. This includes the process of selecting mathematical models (e.g. which approximative physics model should be used weighting computational demand vs. accuracy) and especially evaluating their interaction over the full length of the measurement chain. This approach might be more promising compared to the configuration of simulation tools based on the accuracy of conventional measurement results (based on ISO GPS).
- Because of the fact that the spatially discrete metrological descriptor framework behaves system-agnostic, it can be used to compare the measurement results obtained from different measurement principles. This can be especially helpful for optical methods, which often cannot provide consistent results with respect to each other [298–305].

---

[123] The application of coordinate transforms obtained from different sources (e.g. registration based on geometry elements) is also possible.

Targeting the context of industrial applications, these key applications can improve the quality of metrological examinations:

- In case the conformity of mass produced products should be ensured, the spatially discrete metrological descriptor framework can be used to determine the measurement method and parameters, respectively, that best fit that specific measurement task. Especially the impact of the measurement duration can be part of the decision making, because the associated impact onto the measurement uncertainty is objectively measurable.
- Point-wise systematic measurement errors can be determined for a sample part and their correction applied to measurements of subsequently produced parts. Implemented carefully, this can expand the applicability of measurement systems for otherwise unsuited measurement tasks.
- Already during the design of an object, the definition of datums used for referencing the object within a coordinate frame can be optimised with regards to the used measurement system and the expected local measurement uncertainty.

Overall, the spatially discrete metrological descriptor framework is to be understood as a metrological toolbox in the context of 3D coordinate metrology. The mechanisms of each tool were accurately described, which allows for technical evaluation of each single processing step.

This work was mainly based on (dimensional) industrial X-ray computed tomography (both physical and virtual via simulation tools) because that measurement method is capable of capturing the complete (outer) surface of a measurement object with a single scan. Additionally, the causal connections between the measurement setup (measurement object and machine parameters) and the observed measurement error are generally well understood but large enough for reasonable correction efforts. Nonetheless, the presented method is not limited to X-ray computed tomography, as it was also successfully used for optical structured-light 3D scanners. The metrological traceability of the calculated results could be achieved by using reference measurements captured by tactile coordinate measurement systems.

9 Summary and outlook

3D coordinate metrology is widely used for the validation of geometrical properties of technical workpieces. The traditional ISO GPS language lacks sufficient capability of determining truly local measurement uncertainty at arbitrary geometry locations, because of its approach to evaluate measurements based on geometrical features. Although such a measurement task can strictly speaking be defined with the provided language tools, the ISO GPS standards are focused on the definition of measurands based on the interaction of many individual measurement points. The spatially discrete metrological descriptor framework evaluates the metrological relationships between nominal geometry, reference measurement geometry and repeated measurements of an object at arbitrary locations on its geometry. All geometry data is strictly represented by an areal representation, the triangle mesh. This geometry representation provides additional information, compared to commonly used point clouds. The data processing pipeline consists of different components, which allow a fully automated generation of conventional

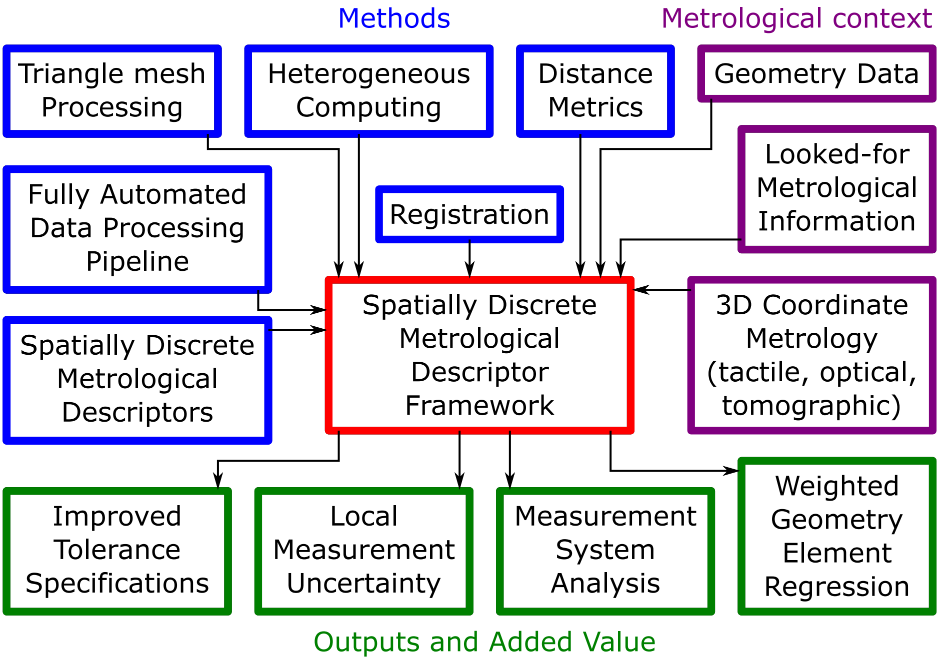

Figure 70: The spatially discrete metrological descriptor framework provides added value within a certain metrological context by the application of a collection of methods.

and unconventional metrological descriptors from repeated measurements. These quantities were successfully applied in various contexts, of which the measurement system analysis can especially benefit from localised metrological descriptor data. The method is very sensitive and thus able to detect subtle changes in the measurement chain, which makes it well suited for the optimisation of real and virtual measurement systems. The lateral sampling density should be oriented to the metrological structural resolution of the examined measurement system. In this thesis, the exact value of this parameter for the used measurement systems was estimated. Due to the implementation of an heterogeneous computing model, very high density geometry data can be processed within a competitive time frame. The different building blocks of the framework are visualised in Figure 70. The provided methods are capable of providing substantial added value within a user-defined metrological context of 3D coordinate metrology.

Finally, this work is concluded with a series of suggestions on how to further explore and use the spatially discrete metrological descriptor framework:

- Further extensions can be implemented which cover more specialised use cases, e.g. targeting the metrological descriptors associated with the characterisation of geometry edges (for an example see Appendix). The introduction of additional distance metrics which also consider the geometrical specification of an edge could potentially result in a way to evaluate the uncertainty of edge characterisations in the context of 3D coordinate metrology.
- The concept of skin model shapes in the context of tolerance analysis and geometrical variations modelling, proposed by [306], employs point-based models of product geometry considering shape variability. A fusion with the work presented in this thesis could yield an interesting application for tolerance analysis approaches.
- This work could potentially benefit from the introduction of statistical models based on Gaussian random fields, as proposed by [158]. This method is capable of estimating the local correlation of descriptor data obtained from neighbouring sampling coordinates. With the possibility of generating accurate local metrological descriptor data, those statistical models can become more accurate, which could increase the quality of the estimation of probability distributions of specific feature sizes in the context of ISO GPS.
- In case spatially discrete measurement uncertainty U_{exp} was obtained, these findings should additionally be validated, following DIN EN ISO/IEC 17025 [114]. For that, suitable methods need to be developed and validated in future work.

Appendix

Used measurement systems

Table 13: Tactile 3D coordinate measurement system

Name	Zeiss UPMC 1200 CARAT S-ACC
Construction year	1999
Design type	stationary table, moveable bridge
Measurement modes	single point probing, scanning
Operating software	Zeiss Calypso 5.6
Measuring range	1200 mm × 1500 mm × 1000 mm
Measurement resolution of Cartesian coordinate axes	0.08 µm
Maximum permissible error, probing - according to ISO 10360-2 [32]	MPE_E1 = 0.9 µm + L/500 µm mm^{-1} MPE_E3 = 1.5 µm + L/500 µm mm^{-1}
Maximum permissible probe deviation, size - according to ISO 10360-5 [307]	MPE_PS = 1.5 µm
Location	Measurement centre FMT, Erlangen

Table 14: Structured-light 3D scanner

Name	GOM ATOS Core 200 5M
Construction year	2014
Design type	photogrammetric structured-light scanner with rotary stage
Operating software	GOM Inspect
Measuring range	195 mm × 143 mm × 158 mm
Lateral measurement resolution	80 µm
Vertical measurement resolution	80 µm
Location	Laboratory NB FMT, Erlangen

Table 15: Industrial X-ray computed tomograph

Name	Zeiss Metrotom 1500G2
Construction year	2017
Design type	cone beam CT with fixed-position X-ray source and flat panel detector
Nominal source-detector distance	1370 mm
Operating software	Zeiss Metrotom OS (including reconstruction)
CT data evaluation software (surface determination and mesh generation)	Volume Graphics VGStudio Max 3.5
X-ray tube voltage, max. power	30 kV to 225 kV, 500 W
Default FBP reconstruction filter	Shepp-Logan
Measuring range (cylindrical $D \times H$)	305 mm × 260 mm 570 mm × 550 mm (raster tomography)
Detector resolution	2048 pixel × 2048 pixel
Detector pixel size	200 µm × 200 µm
System accuracy MPE according to VDI/VDE 2630 Part 1.3 [204]	length E_TS = 9 µm + L/50 µm mm^{-1} probing deviation PS_TS = 3 µm sphere centre distance deviation SD_TS = 4.5 µm + L/50 µm mm^{-1}
Location	Measurement centre FMT, Erlangen

Multi purpose specimen

The multi purpose specimen used as a demonstrator object was developed by Lorenz Butzhammer (FMT) and some of its important features are visualised in Figure 71 and Figure 72. Its tight-fitting bounding box has the size 60 mm × 22 mm × 22 mm.

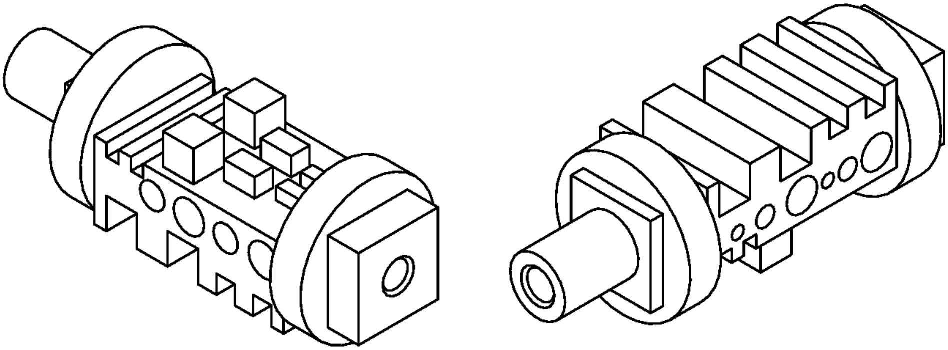

Figure 71: 3D views of the multi purpose specimen.

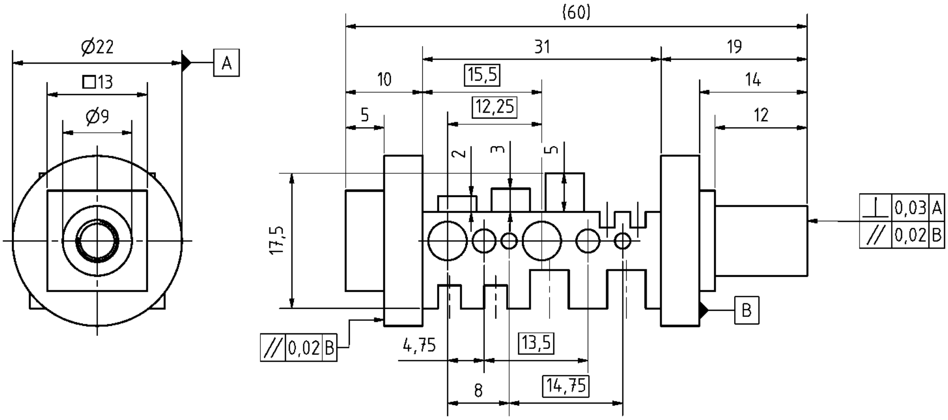

Figure 72: Technical drawing of the multi purpose specimen with some important features.

Specification of the used computer system

Table 16: Hardware and software components of the used computer system.

Operating system (OS)	Windows Server 2019
Central processing unit (CPU)	AMD Ryzen Threadripper Pro 3975WX 32 cores, Octo-Channel memory
Random Access Memory (RAM)	256 GiB DDR4-3200 with ECC
Graphics Processing Unit (GPU)	2× Nvidia RTX A6000, 48 GiB VRAM, TCC driver, 768 GiB s^{-1} peak memory bandwidth, 39 TFLOPS peak FP32, FP32 : FP64 = 64 : 1, (performance measurements in this work with respect to 1 GPU)
MATLAB	R2022a
CUDA	11.6
C++ Compiler	Visual Studio Community 2019

Special application: Spatially discrete metrological descriptors for component edges

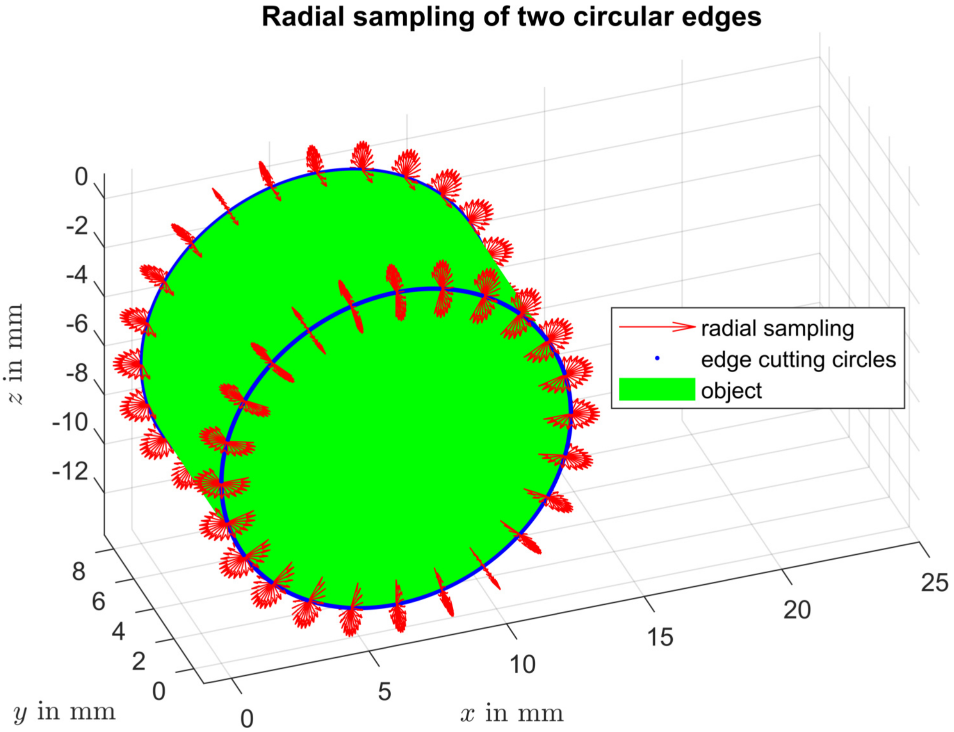

Figure 73: Radial sampling of edge circles (blue) results in a toroidal shape for sampling lines (red). Sampling density is reduced for improved visibility.

The following example intends to inspire alternative applications where the spatially discrete metrological descriptor framework can offer benefits with respect to metrological examinations. Up to now, the defined sampling tasks were coupled to a sampling start geometry (typically nominal or reference geometry, respectively) which means that the location (and direction) of the sampling points $\boldsymbol{S}_i$ was defined by these geometries. As was demonstrated, this coupling can lead to unsatisfactory sampling results especially in work piece edge regions. Therefore, a way to define alternative sampling patterns is demonstrated with the intention of the characterisation of edge regions. In sec. 6.1.6, cylindrical indexable inserts for turning (ISO-code RNGN 120700) were examined using a CT system (for settings see Table 10). The function of that object is cutting which means that the geometry of the cutting edge is of central importance. Therefore, the dependence between the shape of the cutting edge and the application of different CT reconstruction filters (see sec. 6.1.6) is targeted in the following examinations. A cylinder surface

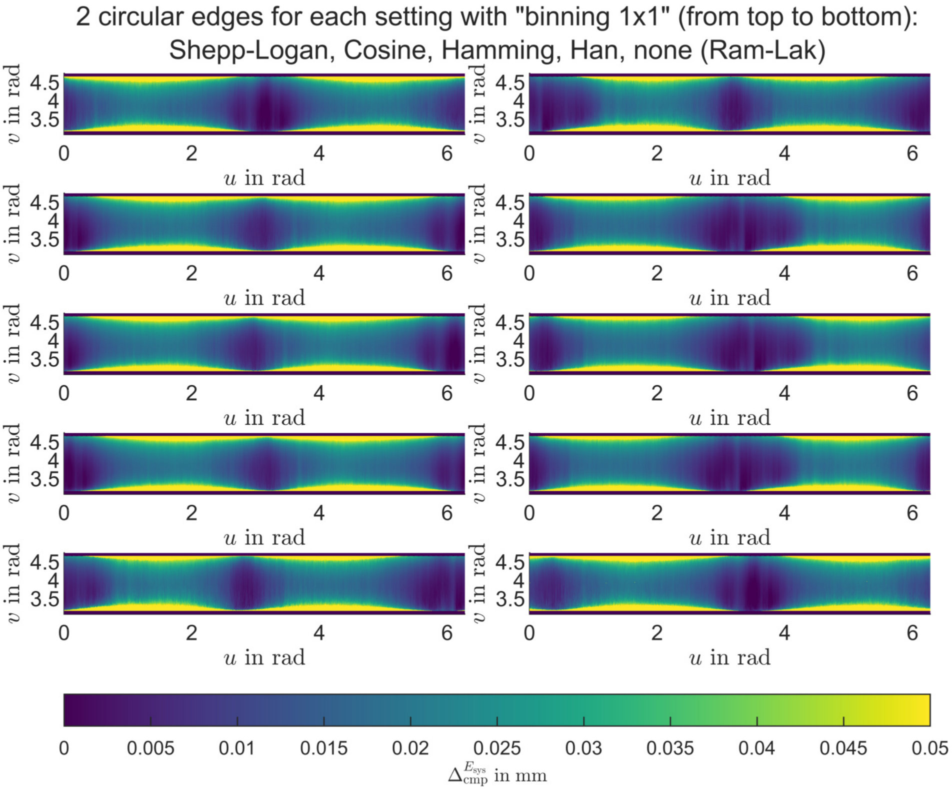

Figure 74: Result of sampling in toroidal angular parameter u and v for the measurement series with 1x1 binning using reconstruction filters Shepp-Logan, Cosine, Hamming, Han, none (Ram-Lak) from top to bottom.

is bound by two circles. Those circles represent the cutting line between the cylinder-mantel and both cover planes. Next, radial sampling originating from points on the circles can be applied such that the edge profile is captured. The principle is visualised in Figure 73: The sampling points are defined based on the location of the blue edge cutting circles (instead of the nominal/reference surface of the object, green) and radial sampling (red) is applied in order to capture the geometrical shape of the edges. This sampling only reports positive hit distances in the outer direction and is parametrised by the two angular parameters u and v of a toroidal shape (see sec. 5.4). The reported descriptor $\Delta_{\mathrm{cmp}}^{E_{\mathrm{sys}}}$ is defined as the mean intersection distance minus the distance to the nominal geometry: $\Delta_{\mathrm{cmp}}^{E_{\mathrm{sys}}} = \mathtt{mean}(\|\{\boldsymbol{d}_i\}_{i=1}^{n}\|) - \|\boldsymbol{d}_{\mathrm{nominal}}\|$. The results can then be visualised in the toroidal parameter space with the already familiar false-colour plots, as presented in Figure 74 for the five reconstruction settings featuring different filters and 1x1 binning. The results for 2x2

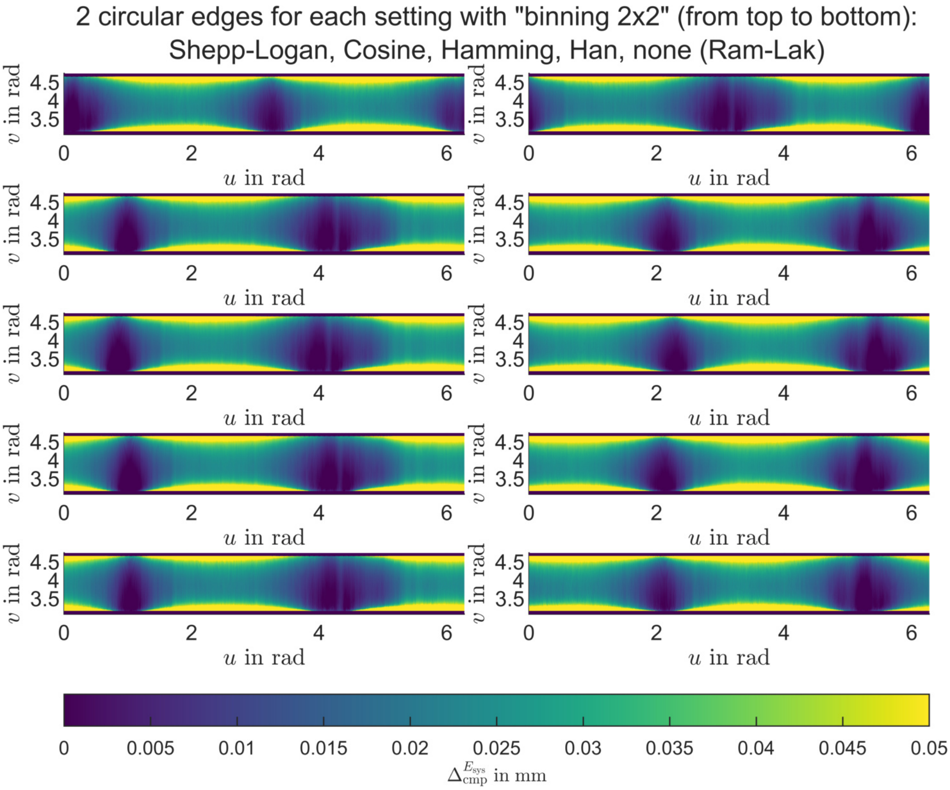

Figure 75: Result of sampling in toroidal angular parameter u and v for the measurement series with 2x2 binning using reconstruction filters Shepp-Logan, Cosine, Hamming, Han, none (Ram-Lak) from top to bottom.

binning are given in Figure 75. All measurement show the same pattern where the shape of the edge changes with two sharper and two smoother regions. This is caused by the different average penetration lengths for different edge regions. Overall, only minor differences are observable between the different measurement settings with slightly more rounding for measurements with 2x2 binning.

With additional customisation of this approach, it is in principle possible to consider specific standards which describe edges of defined shape (DIN EN ISO 21204:2022-01 [308]) and undefined shape (DIN EN ISO 13715:2020-01 [309]), as well as broken edges defined as general tolerances (DIN ISO 2768-1:1991-06 [310]) in these examinations. In that context, it could be beneficial to explicitly model sharp edges as generously rounded features in order to improve the sampling results obtained with the ”traditional” framework described in the previous chapters. This would represent a hybrid approach where the sampling start geometry is deliberately altered with respect to the nominal geometry in order to provide more robust sampling results (e.g. for the VNV distance metric).

Bibliography

[1] Robertson, Kristel and Swanepoel, Jan. “The economics of metrology”. *Australian Government, Department of Industry, Science, Energy and Resources, Office of the Chief Economist* 6 (2015). (Visited on 05/13/2022).

[2] *Metrology - in short: EURAMET project no. 1011*. 3. ed. Albertslund: Schultz Grafisk, 2008.

[3] *DIN EN ISO 14638:2015-12, Geometrical product specifications (GPS) - Matrix model (ISO 14638:2015); German version EN ISO 14638:2015*.

[4] Nielsen, Henrik S. *The ISO geometrical product specifications handbook: Find your way in GPS*. Charlottenlund: Danish Standards, 2012.

[5] Gröger, Sophie. “Funktionsgerechte Spezifikation geometrischer Eigenschaften mit dem System der Geometrischen Produktspezifikation und -verifikation”. Habilitation. Chemnitz: Technische Universität Chemnitz, 2013. https://nbn-resolving.org/urn:nbn:de:bsz:ch1-qucosa-120294 (visited on 08/17/2021).

[6] *DIN EN ISO 17450-1:2012-04, Geometrical product specifications (GPS) - General concepts - Part 1: Model for geometrical specification and verification (ISO 17450-1:2011); German version EN ISO 17450-1:2011*.

[7] *DIN EN ISO 22432:2012-03, Geometrical product specifications (GPS) - Features utilized in specification and verification (ISO 22432:2011); German version EN ISO 22432:2011*.

[8] Keferstein, Claus P.; Marxer, Michael, and Bach, Carlo. *Fertigungsmesstechnik*. Wiesbaden: Springer Fachmedien Wiesbaden, 2018.

[9] *DIN EN ISO 8015:2011-09, Geometrical product specifications (GPS) - Fundamentals - Concepts, principles and rules (ISO 8015:2011); German version EN ISO 8015:2011*.

[10] *JCGM 200:2012 (E/F): International vocabulary of metrology - basic and general concepts and associated terms (VIM) - Vocabulaire international de métrologie - concepts fondamentaux et généraux et termes associés (VIM) - 3rd edition, 2008 version with minor corrections*. https://www.bipm.org/en/committees/jc/jcgm/publications (visited on 12/03/2021).

[11] Krystek, Michael. *Berechnung der Messunsicherheit: Grundlagen und Anleitung für die praktische Anwendung*. 3. erweiterte Ausgabe. Praxis. Berlin, Wien, and Zürich: Beuth, 2020.

[12] *ISO/IEC GUIDE 98-3:2008 (E): Uncertainty of measurement - Part 3: Guide to the expression of uncertainty in measurement (GUM:1995)*. https://isotc.iso.org/livelink/livelink/Open/8389141.

[13] Sładek, Jerzy A. *Coordinate Metrology*. Berlin, Heidelberg: Springer Berlin Heidelberg, 2016.

[14] *DIN EN ISO 14253-1:2018-07, Geometrical product specifications (GPS) - Inspection by measurement of workpieces and measuring equipment - Part 1: Decision rules for verifying conformity or nonconformity with specifications (ISO 14253-1:2017); German version EN ISO 14253-1:2017*.

[15] Audette, Michel A.; Ferrie, Frank P., and Peters, Terry M. "An algorithmic overview of surface registration techniques for medical imaging". *Medical Image Analysis* 4.3 (2000), pp. 201–217.

[16] Linares, J. M.; Goch, G.; Forbes, A.; Sprauel, J. M.; Clément, A.; Haertig, F., and Gao, W. "Modelling and traceability for computationally-intensive precision engineering and metrology". *CIRP Annals* 67.2 (2018), pp. 815–838.

[17] CASRAI. *CRediT - Contributor Roles Taxonomy*. 2022. https://casrai.org/credit/ (visited on 04/26/2022).

[18] Bronštejn, Ilja N.; Semendjaev, Konstantin A.; Musiol, Gerhard, and Mühlig, Heiner. *Taschenbuch der Mathematik*. 7., vollst. überarb. und erg. Aufl. Frankfurt am Main: Deutsch, 2008.

[19] Moreland, Kenneth. "Diverging Color Maps for Scientific Visualization". *Advances in Visual Computing*. Ed. by Hutchison, David; Kanade, Takeo; Kittler, Josef; Kleinberg, Jon M.; Mattern, Friedemann; Mitchell, John C.; Naor, Moni; Nierstrasz, Oscar; Pandu Rangan, C.; Steffen, Bernhard; Sudan, Madhu; Terzopoulos, Demetri; Tygar, Doug; Vardi, Moshe Y.; Weikum, Gerhard; Bebis, George; Boyle, Richard; Parvin, Bahram; Koracin, Darko; Kuno, Yoshinori; Wang, Junxian; Pajarola, Renato; Lindstrom, Peter; Hinkenjann, André; Encarnação, Miguel L.; Silva, Cláudio T., and Coming, Daniel. Vol. 5876. Lecture Notes in Computer Science. Berlin, Heidelberg: Springer Berlin Heidelberg, 2009, pp. 92–103.

[20] Moreland, Kenneth. "Why We Use Bad Color Maps and What You Can Do About It". *Electronic Imaging* 28.16 (2016), pp. 1–6.

[21] Crameri, Fabio; Shephard, Grace E., and Heron, Philip J. "The misuse of colour in science communication". *Nature communications* 11.1 (2020), p. 5444.

[22] Bujack, Roxana; Turton, Terece L.; Samsel, Francesca; Ware, Colin; Rogers, David H., and Ahrens, James. “The Good, the Bad, and the Ugly: A Theoretical Framework for the Assessment of Continuous Colormaps”. *IEEE transactions on visualization and computer graphics* 24.1 (2018), pp. 923–933.

[23] The MathWorks, Inc. *Jet colormap array - MATLAB jet*. 2022. https://www.mathworks.com/help/matlab/ref/jet.html (visited on 05/16/2022).

[24] Liu, Yang and Heer, Jeffrey. “Somewhere Over the Rainbow”. *Proceedings of the 2018 CHI Conference on Human Factors in Computing Systems*. Ed. by Mandryk, Regan; Hancock, Mark; Perry, Mark, and Cox, Anna. New York, NY, USA: ACM, 2018, pp. 1–12.

[25] Hunter, John; Darren, Dale; Eric, Firing; Michael, Droettboom, and Matplotlib development team. *Colormap reference — Matplotlib 3.5.2 documentation*. 2022. https://matplotlib.org/stable/gallery/color/colormap_reference.html (visited on 05/16/2022).

[26] Moreland, Kenneth. *Color Map Advice for Scientific Visualization*. 2022. http://www.kennethmoreland.com/color-advice/ (visited on 05/16/2022).

[27] Hocken, Robert J. and Pereira, Paulo H. *Coordinate Measuring Machines and Systems*. CRC Press, 2016.

[28] Carl Zeiss Industrial Metrology, LLC. *100 Years Industrial Metrology at ZEISS: Zeiss UMM 500: High precision three-coordinate measuring machine: 1973*. https://www.zeiss.com/metrology/about-us/history.html (visited on 03/14/2023).

[29] Weckenmann, Albert, ed. *Koordinatenmesstechnik: Flexible Strategien für funktions- und fertigungsgerechtes Prüfen*. 2., vollständig überarb. Aufl. München and Wien: Hanser, 2012.

[30] Christoph, Ralf and Neumann, Hans Joachim. *Multisensor-Koordinatenmesstechnik: Dimensionelles Messen mit Optik, Taster und Röntgentomografie*. Vol. 352. Die Bibliothek der Technik. Landsberg/Lech: Verl. Moderne Industrie, 2013.

[31] *DIN EN ISO 10360-1:2003-07, Geometrical Product Specifications (GPS) - Acceptance and reverification tests for coordinate measuring machines (CMM) - Part 1: Vocabulary (ISO 10360-1:2000 + Corr 1:2002) (includes Corrigendum AC:2002); German version EN ISO 10360-1:2000 + AC:2002.*

[32] *DIN EN ISO 10360-2:2010-06, Geometrical product specifications (GPS) - Acceptance and reverification tests for coordinate measuring machines (CMM) - Part 2: CMMs used for measuring linear dimensions (ISO 10360-2:2009); German version EN ISO 10360-2:2009.*

[33] Weißgerber, Marco. “Bestimmung der spezifischen, oberflächenbedingten Scanning-Antastabweichungen für taktile 3D-Koordinatenmessgeräte”. Dissertation. Chemnitz: Technische Universität Chemnitz, 2019.

[34] Imkamp, Dietrich; Schmitt, Robert, and Berthold, Jürgen. “Blick in die Zukunft der Fertigungsmesstechnik”. *teme* 79.10 (2012), pp. 433–439.

[35] Trenk, Michael; Franke, Matthias, and Schwenke. “The “Virtual CMM” a software tool for uncertainty evaluation – practical application in an accredited calibration lab”. *ASPE Summer Topical Meeting on Uncertainty Analysis in Measurement and Design*. 2004.

[36] Wäldele, Franz and Schwenke, Heinrich. “Automatische Bestimmung der Messunsicherheiten auf KMGs auf dem Weg in die industrielle Praxis (Automated Calculation of Measurement Uncertainties on CMMs – Towards Industrial Application)”. *teme* 69.12 (2002), p. 550.

[37] *VDI/VDE 2617 Part 7:2008-09, Accuracy of coordinate measuring machines - Parameters and their checking - Estimation of measurement uncertainty of coordinate measuring machines by means of simulation*. https://www.vdi.de/richtlinien/details/vdivde-2617-blatt-7-genauigkeit-von-koordinatenmessgeraeten-kenngroessen-und-deren-pruefung-ermittlung-der-unsicherheit-von-messungen-auf-koordinatenmessgeraeten-durch-simulation (visited on 12/10/2022).

[38] *ISO/IEC GUIDE 98-3/Suppl.1:2008 (E): Uncertainty of measurement - Part 3: Guide to the expression of uncertainty in measurement (GUM:1995) - Supplement 1: Propagation of distributions using a Monte Carlo method*. https://isotc.iso.org/livelink/livelink/Open/8389141.

[39] *ISO/IEC GUIDE 98-3/Suppl.1:2008/Cor.1:2009 (E): Uncertainty of measurement - Part 3: Guide to the expression of uncertainty in measurement (GUM:1995) - Supplement 1: Propagation of distributions using a Monte Carlo method - Technical corrigendum 1*. https://isotc.iso.org/livelink/livelink/Open/8389141.

[40] Franke, Matthias; Kistner, Thomas; Hausotte, Tino; Heißelmann, Daniel; Schwehn, Carsten, and Wendt, Klaus. “Bestimmung der Messunsicherheit für Koordinatenmesssysteme”. *teme* 84.5 (2017), pp. 325–335.

[41] Heißelmann, Daniel; Franke, Matthias; Rost, Kerstin; Wendt, Klaus; Kistner, Thomas, and Schwehn, Carsten. “Determination of measurement uncertainty by Monte Carlo simulation”. *Advanced Mathematical and Computational Tools in Metrology and Testing XI*. Ed. by Forbes, Alistair B.; Zhang, Nien-Fan; Chunovkina, Anna; Eichstädt, Sascha, and Pavese, Franco. Vol. 89. Series on Advances in Mathematics for Applied Sciences. WORLD SCIENTIFIC, 2018, pp. 192–202.

[42] *VDI/VDE 2617 Part 11:2011-03, Accuracy of coordinate measuring machines - Characteristics and their checking - Determination of the uncertainty of measurement for coordinate measuring machines using uncertainty budgets*. https://www.vdi.de/richtlinien/details/vdivde-2617-blatt-11-genauigkeit-von-koordinatenmessgeraeten-kenngroessen-und-deren-pruefung-ermittlung-der-unsicherheit-von-messungen-auf-koordinatenmessgeraeten-durch-messunsicherheitsbilanzen (visited on 12/10/2022).

[43] *DIN EN ISO 15530-3:2018-09, Geometrical product specifications (GPS) - Coordinate measuring machines (CMM): Technique for determining the uncertainty of measurement - Part 3: Use of calibrated workpieces or measurement standards (ISO 15530-3:2011); German version EN 15530-3:2011*.

[44] Gühring, Jens. “3D-Erfassung und Objektrekonstruktion mittels Streifenprojektion”. Dissertation. Stuttgart: Universität Stuttgart, 2002.

[45] Geng, Jason. “Structured-light 3D surface imaging: a tutorial”. *Advances in Optics and Photonics* 3.2 (2011), pp. 128–160.

[46] Hartley, Richard and Zisserman, Andrew. *Multiple view geometry in computer vision*. 2. ed., 10. printing. Cambridge: Cambridge Univ. Press, 2013.

[47] Luhmann, Thomas; Robson, Stuart; Kyle, Stephen, and Harley, Ian. *Close-range photogrammetry: Principles, methods and applications*. Dunbeath: Whittles, 2006.

[48] *VDI/VDE 2634 Part 1:2002-05, Optical 3D measuring systems - Imaging systems with point-by-point probing*. https://www.vdi.de/richtlinien/details/vdivde-2634-blatt-1-optische-3d-messsysteme-bildgebende-systeme-mit-punktfoermiger-antastung (visited on 12/10/2022).

[49] *VDI/VDE 2634 Part 2:2012-08, Optical 3-D measuring systems - Optical systems based on area scanning*. https://www.vdi.de/richtlinien/details/vdivde-2634-blatt-2-optische-3-d-messsysteme-bildgebende-systeme-mit-flaechenhafter-antastung (visited on 12/10/2022).

[50] *VDI/VDE 2634 Part 3:2008-12, Optical 3D-measuring systems - Multiple view systems based on area scanning*. https://www.vdi.de/richtlinien/details/vdivde-2634-blatt-3-optische-3-d-messsysteme-bildgebende-systeme-mit-flaechenhafter-antastung-in-mehreren-einzelansichten (visited on 12/10/2022).

[51] Ntregka, A; Georgopoulos, A, and Quintero, M Santana. “Photogrammetric exploitation of HDR images for cultural heritage documentation”. *ISPRS Annals of the Photogrammetry, Remote Sensing and Spatial Information Sciences* II-5/W1 (2013), pp. 209–214.

[52] De Chiffre, L.; Carmignato, S.; Kruth, J. P.; Schmitt, R., and Weckenmann, A. “Industrial applications of computed tomography”. *CIRP Annals* 63.2 (2014), pp. 655–677.

[53] Kruth, J. P.; Bartscher, M.; Carmignato, S.; Schmitt, R.; De Chiffre, L., and Weckenmann, A. “Computed tomography for dimensional metrology”. *CIRP Annals* 60.2 (2011), pp. 821–842.

[54] Krieger, Hanno. *Grundlagen der Strahlungsphysik und des Strahlenschutzes*. 4., überarb. und erw. Aufl. Studium. Wiesbaden: Springer-Spektrum, 2012. http://swbplus.bsz-bw.de/bsz364358319cov.htm.

[55] Maaß, Clemens; Knaup, Michael; Sawall, Stefan, and Kachelrieß, Marc. “ROI-Tomografie (Lokale Tomografie)”. *The e-Journal of Nondestructive Testing* 16.6 (2010). https://www.ndt.net/article/ctc2010/papers/251.pdf (visited on 04/14/2024).

[56] Carmignato, Simone; Dewulf, Wim, and Leach, Richard. *Industrial X-Ray Computed Tomography*. Cham: Springer International Publishing, 2018.

[57] Feldkamp, L. A.; Davis, L. C., and Kress, J. W. “Practical cone-beam algorithm”. *Journal of the Optical Society of America A* 1.6 (1984), p. 612.

[58] Herold, Frank. “Die 10 Modellannahmen der Computertomographie”. *teme* 87.2 (2020), pp. 93–100.

[59] Tuy, Heang K. “An Inversion Formula for Cone-Beam Reconstruction”. *SIAM Journal on Applied Mathematics* 43.3 (1983), pp. 546–552. http://www.jstor.org/stable/2101324.

[60] Bartolac, Steven; Clackdoyle, Roll; Noo, Frederic; Siewerdsen, Jeff; Moseley, Douglas, and Jaffray, David. “A local shift-variant Fourier model and experimental validation of circular cone-beam computed tomography artifacts”. *Medical physics* 36.2 (2009), pp. 500–512.

[61] Hoheisel, M.; Bernhardt, P.; Lawaczeck, R., and Pietsch, H. “Comparison of polychromatic and monochromatic X-rays for imaging”. *Medical Imaging 2006: Physics of Medical Imaging*. Ed. by Flynn, Michael J. and Hsieh, Jiang. SPIE Proceedings. SPIE, 2006, p. 614209.

[62] Hoag, M. L. and Krahmer, R. L. *Polychromatic X-ray attenuation characteristics and wood densitometry applications*. Vol. 23. Wood and fiber science : journal of the Society of Wood Science and Technology. 1991.

[63] Sackewitz, Michael, ed. *Leitfaden zur industriellen Röntgentechnik: Zerstörungsfreie Prüfung mit Bildverarbeitung*. 2., vollständig aktualisierte und erweiterte Auflage. Vol. 15. Vision-Leitfaden. Stuttgart: Fraunhofer Verlag, 2015. http://www.vision.fraunhofer.de/de/publikationen/leitfaeden/band-15.html.

[64] Lifton, Joseph J.; Malcolm, Andrew A., and McBride, John W. “A simulation-based study on the influence of beam hardening in X-ray computed tomography for dimensional metrology”. *Journal of X-ray science and technology* 23.1 (2015), pp. 65–82.

[65] Carmignato, Simone; Pierobon, Anna; Rampazzo, Paola; Parisatto, Matteo, and Savio, Enrico. “CT for Industrial Metrology - Accuracy and Structural Resolution of CT Dimensional Measurements”. *The e-Journal of Nondestructive Testing* 17.12 (2012). https://www.ndt.net/article/ctc2012/papers/173.pdf (visited on 04/19/2022).

[66] Carmignato, Simone. “Accuracy of industrial computed tomography measurements: Experimental results from an international comparison”. *CIRP Annals* 61.1 (2012), pp. 491–494.

[67] Kobbelt, Leif and Botsch, Mario. “A survey of point-based techniques in computer graphics”. *Computers & Graphics* 28.6 (2004), pp. 801–814.

[68] Otepka, Johannes; Ghuffar, Sajid; Waldhauser, Christoph; Hochreiter, Ronald, and Pfeifer, Norbert. “Georeferenced Point Clouds: A Survey of Features and Point Cloud Management”. *ISPRS International Journal of Geo-Information* 2.4 (2013), pp. 1038–1065.

[69] Xu, Xun; Nee, Andrew Y.C., and Nee, Andrew Y. C., eds. *Advanced Design and Manufacturing Based on STEP*. 1. Aufl. Springer Series in Advanced Manufacturing. Dordrecht: Springer, 2009. http://www.loc.gov/catdir/enhancements/fy1109/2009935947-b.html.

[70] Step Tools, Inc. *The STEP Standard - ISO 10303: STEP Application Protocols*. 2021. https://www.steptools.com/stds/step/step_2.html (visited on 11/15/2021).

[71] Step Tools, Inc. *The STEP Standard - ISO 10303: STEP for Geometric Dimensioning and Tolerancing*. 2021. https://www.steptools.com/stds/step/step_3.html (visited on 11/08/2021).

[72] Library of Congress. *STEP-file, ISO 10303-21*. 2017. https://www.loc.gov/preservation/digital/formats/fdd/fdd000448.shtml (visited on 11/08/2021).

[73] *ISO 10303-42:2019(E), Industrial automation systems and integration — Product data representation and exchange, Part 42: Integrated generic resource: Geometric and topological representation, ISO 10303-42:2019(E)*. https://www.steptools.com/stds/smrl/data/resource_docs/geometric_and_topological_representation/sys/cover.htm.

[74] *The Britannica guide to geometry*. 1st ed. Math explained. New York, NY: Britannica Educational Pub. in association with Rosen Educational Services, 2011. https://ebookcentral.proquest.com/lib/kxp/detail.action?docID=514074.

[75] G. Requicha, A. and Voelcker, H. “Solid Modeling: Current Status and Research Directions”. *IEEE Computer Graphics and Applications* 3.7 (1983), pp. 25–37.

[76] Hoffmann, Christoph Martin. *Geometric and solid modeling: An introduction*. 2nd. print. Morgan Kaufmann series in computer graphics and geometric modeling. San Mateo, Calif.: Morgan Kaufmann, 1993.

[77] SIMON, Vincent. *CAD Interop - Different Geometry Types and Formats in CAD*. 2021. https://www.cadinterop.com/en/your-needs/step/different-geometry-types-and-formats-in-cad.html (visited on 11/08/2021).

[78] Lipman, Robert. *STEP File Analyzer and Viewer User Guide (Update 7)*. 2021. https://tsapps.nist.gov/publication/get_pdf.cfm?pub_id=933550.

[79] AHO, Alfred V. “Algorithms for Finding Patterns in Strings”. *Algorithms and Complexity*. Elsevier, 1990, pp. 255–300.

[80] Step Tools, Inc. *The STEP Standard - ISO 10303: AP242: Managed Model-Based 3D Engineering*. 2021. https://www.steptools.com/stds/step/ (visited on 11/09/2021).

[81] Piegl, Les. *The NURBS Book*. Monographs in Visual Communications. Berlin and Heidelberg: Springer, 1995.

[82] Schneider, Philip and Eberly, David H. *Geometric Tools for Computer Graphics*. 1. Aufl. The Morgan Kaufmann Series in Computer Graphics. s.l.: Elsevier professional, 2002. http://gbv.eblib.com/patron/FullRecord.aspx?p=293539.

[83] Botsch, Mario; Pauly, Mark; Rossl, Christian; Bischoff, Stephan, and Kobbelt, Leif. “Geometric Modeling Based on Triangle Meshes”. *ACM SIGGRAPH 2006 Courses*. SIGGRAPH ’06. New York, NY, USA: Association for Computing Machinery, 2006.

[84] Ericson, Christer. *Real-time collision detection*. [Nachdr.] Morgan Kaufmann series in interactive 3D technology. Amsterdam: Elsevier Morgan Kaufmann, 2008.

[85] Kobbelt, Leif; Bischoff, Stephan; Botsch, Mario; Kähler, Kolja; Rössl, Christian; Schneider, Robert, and Vorsatz, Jens. “Geometric Modeling Based on Polygonal Meshes”. *Tutorials of the European Association for Computer Graphics 21st Annual Conference (Eurographics-00)*. Interlaken, Switzerland: Eurographics, 2000, pp. 1–47. http://www.eg.org/EG/DL/Conf/EG2000/tutorials/tutorial4.pdf.

[86] Aghda, Nima; Younesy, Hamid, and Zhang, Hao. “5-6-7 meshes”. *Proceedings of Graphics Interface 2012*. GI 2012. Toronto, Ontario, Canada: Canadian Human-Computer Communications Society, 2012, pp. 27–34.

[87] Botsch, Mario; Kobbelt, Leif; Pauly, Mark; Alliez, Pierre, and Lévy, Brunjo. *Polygon mesh processing*. Natick, Mass. and Boca Raton: Peters and CRC Press, 2010.

[88] Coxeter, Harold S. M. *Introduction to geometry*. 2. ed. Wiley classics library. New York: Wiley, 1989.

[89] Stutz, David. *A Formal Definition of Watertight Meshes*. 2018. https://davidstutz.de/a-formal-definition-of-watertight-meshes/ (visited on 12/11/2021).

[90] Grimm, Todd. *User’s guide to rapid prototyping*. Dearborn, Mich: Society of Manufacturing Engineeers, 2004.

[91] Kumar, Vinod and Dutta, Debasish. “An assessment of data formats for layered manufacturing”. *Advances in Engineering Software* 28.3 (1997), pp. 151–164.

[92] Kai, Chua Chee; Jacob, Gan G. K., and Mei, Tong. “Interface between CAD and Rapid Prototyping systems. Part 1: A study of existing interfaces”. *The International Journal of Advanced Manufacturing Technology* 13.8 (1997), pp. 566–570.

[93] Kai, Chua Chee; Jacob, Gan G. K., and Mei, Tong. “Interface between CAD and Rapid Prototyping systems. Part 2: LMI - An improved interface”. *The International Journal of Advanced Manufacturing Technology* 13.8 (1997), pp. 571–576.

[94] Gebhardt, Andreas. *Additive Fertigungsverfahren: Additive Manufacturing und 3D-Drucken für Prototyping - Tooling - Produktion*. 5., neu bearbeitete und erweiterte Auflage. München: Hanser, 2016. http://www.hanser-fachbuch.de/9783446444010.

[95] Ennex Research Corporation. *The StL Format: Standard Data Format for Fabbers*. 1999. http://www.fabbers.com/tech/STL_Format (visited on 11/20/2021).

[96] All3DP GmbH. *STL File Format: Everything You Need to Know*. 2021. https://all3dp.com/1/stl-file-format-3d-printing/ (visited on 11/20/2021).

[97] *IEEE Std 1541-2002 (R2008): IEEE Standard for Prefixes for Binary Multiplies*. https://isotc.iso.org/livelink/livelink/Open/8389141.

[98] *IEC 80000-13:2008: Quantities and units - Part 13: Information science and technology*. https://www.iso.org/standard/31898.html.

[99] Moler, Cleve. “Floating points: IEEE Standard unifies arithmetic model”. MATLAB News and Notes, 1996. https://www.mathworks.com/content/dam/mathworks/mathworks-dot-com/company/newsletters/news_notes/pdf/Fall96Cleve.pdf.

[100] The MathWorks, Inc. *Floating-point relative accuracy - MATLAB eps*. 2021. https://de.mathworks.com/help/matlab/ref/eps.html (visited on 11/21/2021).

[101] Toth, Csaba D.; O’Rourke, Joseph, and Goodman, Jacob E., eds. *Handbook of Discrete and Computational Geometry*. Third edition. Discrete Mathematics and Its Applications. Boca Raton, FL: CRC Press, 2017. https://www.taylorfrancis.com/books/e/9781498711425.

[102] Rajan, V. T. “Optimality of the Delaunay triangulation in ⍰ d”. *Discrete & Computational Geometry* 12.2 (1994), pp. 189–202.

[103] Edelsbrunner, Herbert. *Algorithms in Combinatorial Geometry*. Berlin, Heidelberg: Springer Berlin Heidelberg, 1987.

[104] Bowyer, A. "Computing Dirichlet tessellations". *The Computer Journal* 24.2 (1981), pp. 162–166.

[105] Watson, D. F. "Computing the n-dimensional Delaunay tessellation with application to Voronoi polytopes". *The Computer Journal* 24.2 (1981), pp. 167–172.

[106] Edelsbrunner, H. and Shah, N. R. "Incremental topological flipping works for regular triangulations". *Algorithmica* 15.3 (1996), pp. 223–241.

[107] Lee, D. T. and Lin, A. K. "Generalized delaunay triangulation for planar graphs". *Discrete & Computational Geometry* 1.3 (1986), pp. 201–217.

[108] Shewchuk, Jonathan Richard. "A condition guaranteeing the existence of higher-dimensional constrained Delaunay triangulations". *Proceedings of the fourteenth annual symposium on Computational geometry - SCG '98*. Ed. by Janardan, Ravi. New York, New York, USA: ACM Press, 1998, pp. 76–85.

[109] Shewchuk, Jonathan Richard. "General-Dimensional Constrained Delaunay and Constrained Regular Triangulations, I: Combinatorial Properties". *Discrete & Computational Geometry* 39.1-3 (2008), pp. 580–637.

[110] BIPM. *Le Système international d'unités / The International System of Units ('The SI Brochure')*. Ninth. Bureau international des poids et mesures, 2019. http://www.bipm.org/en/si/si_brochure/.

[111] Physikalisch-technische Bundesanstalt. *Neue Definitionen im Internationalen Einheitensystem (SI)*. Braunschweig, 2019. http://www.ptb.de/cms/fileadmin/internet/forschung_entwicklung/countdown_new_si/Lesezeichen_zum_neuen_SI.pdf (visited on 05/27/2022).

[112] *RICHTLINIE (EU) 2019/1258 DER KOMMISSION zur Änderung des Anhangs der Richtlinie 80/181/EWG des Rates hinsichtlich der Definitionen der SI-Basiseinheiten zwecks ihrer Anpassung an den technischen Fortschritt*. 2019.

[113] *DIN EN ISO 9001:2015-11, Quality management systems - Requirements (ISO 9001:2015); German and English version EN ISO 9001:2015*.

[114] *DIN EN ISO/IEC 17025:2018-03, General requirements for the competence of testing and calibration laboratories (ISO/IEC 17025:2017); German and English version EN ISO/IEC 17025:2017*.

[115] Phillips, Steven D. and Krystek, Michael. "Assessment of conformity, decision rules and risk analysis". *teme* 81.5 (2014), pp. 237–245.

[116] Knapp, W. "Tolerance and uncertainty". *Laser metrology and machine performance V.* /WIT transactions on engineering sciences]. Southampton: WIT Press, 2001. https://www.witpress.com/elibrary/wit-transactions-on-engineering-sciences/34/3553.

[117] Berndt, Georg; Hultzsch, Erasmus, and Weinhold, Herbert. "Funktionstoleranz und Meßunsicherheit". *Wissenschaftliche Zeitschrift der Technischen Universität Dresden* 17.2 (1968), p. 465.

[118] *ISO/IEC GUIDE 98-1:2009 (E): Uncertainty of measurement - Part 1: Introduction to the expression of uncertainty in measurement*. https://isotc.iso.org/livelink/livelink/Open/8389141.

[119] *ISO/IEC GUIDE 98-3:2008/Suppl.2:2011 (E): Uncertainty of measurement - Part 3: Guide to the expression of uncertainty in measurement (GUM:1995) - Supplement 2: Extension to any number of output quantities*. https://isotc.iso.org/livelink/livelink/Open/8389141.

[120] *ISO/IEC GUIDE 98-4:2012 (E): Uncertainty of measurement - Part 4: Role of measurement uncertainty in conformity assessment*. https://isotc.iso.org/livelink/livelink/Open/8389141.

[121] *ISO/IEC GUIDE 98-6:2021 (E): Uncertainty of measurement - Part 6: Developing and using measurement models*. https://isotc.iso.org/livelink/livelink/Open/8389141.

[122] BIPM - Bureau International des Poids et Mesures. *JCGM Publications: Guides in Metrology: GUM: Guide to the Expression of Uncertainty in Measurement*. https://www.bipm.org/en/committees/jc/jcgm/publications (visited on 03/14/2023).

[123] Streinz, Wolfgang; Hausberger, Hermann, and Anghel, Constantin. "Unsymmetriegrößen erster und zweiter Art richtig auswerten: Teil 1: Unsymmetriegrößen erster Art". *QZ* 37.12 (1992).

[124] Anghel, Constantin; Hausberger, Hermann, and Streinz, Wolfgang. "Unsymmetriegrößen erster und zweiter Art richtig auswerten: Teil 2: Unsymmetriegrößen zweiter Art". *QZ* 38.1 (1993).

[125] Physikalisch-technische Bundesanstalt. *PTB statement regarding systematic errors to be taken into account in the calculation of the uncertainty in measurement - Revised version*. 2019. https://www.ptb.de/cms/fileadmin/internet/fachabteilungen/abteilung_8/8.4_mathematische_modellierung/8.42/PraktMU/GUM_-_systematische_Abweichungen_en.pdf (visited on 12/03/2021).

[126] Lira, Ignacio H. and Wöger, Wolfgang. “Evaluation of the uncertainty associated with a measurement result not corrected for systematic effects”. *Measurement Science and Technology* 9.6 (1998), pp. 1010–1011.

[127] Härtig, Frank; Hirsch, Jürgen; Jusko, Otto; Kniel, Karin; Neuschaefer-Rube, Ulrich, and Wendt, Klaus. “Koordinatenmesstechnik als Schlüsseltechnologie der FertigungsmesstechnikCoordinate Metrology as a Key Technology in Production Measurement”. *teme* 76.2 (2009), pp. 73–82.

[128] Klauenberg, Katy; Wübbeler, Gerd, and Elster, Clemens. “About not Correcting for Systematic Effects”. *Measurement Science Review* 19.5 (2019), pp. 204–208.

[129] Bernardo, José M. and Smith, Adrian F. M. *Bayesian theory*. Reprint. Wiley series in probability and mathematical statistics. Chichester: Wiley, 1994.

[130] Robert, Christian P. *The Bayesian Choice: From Decision-Theoretic Foundations to Computational Implementation*. New York, NY: Springer New York, 2007.

[131] Willink, Robin. *Measurement Uncertainty and Probability*. Cambridge: Cambridge University Press, 2012. https://ebookcentral.proquest.com/lib/kxp/detail.action?docID=1099890.

[132] Gleser, Leon Jay. “Assessing uncertainty in measurement”. *Statistical Science* 13.3 (1998).

[133] *VDI/VDE 2630 Part 1.1:2016-11, Computed tomography in dimensional measurement - Fundamentals and definitions*. https://www.vdi.de/richtlinien/details/vdivde-2630-blatt-11-computertomografie-in-der-dimensionellen-messtechnik-grundlagen-und-definitionen (visited on 12/06/2021).

[134] *DIN EN ISO 14406:2011-04, Geometrische Produktspezifikation (GPS) - Erfassung (ISO 14406:2010); Deutsche Fassung EN ISO 14406:2010*. Berlin.

[135] *DIN EN ISO 1101:2017-09,Geometrical product specifications (GPS) - Geometrical tolerancing - Tolerances of form, orientation, location and run-out (ISO 1101:2017); German version EN ISO 1101:2017*.

[136] Petitcuenot, Mathieu; Pierre, Laurent, and Anselmetti, Bernard. “ISO Specifications of Complex Surfaces: Application on Aerodynamic Profiles”. *Procedia CIRP* 27 (2015), pp. 16–22.

[137] *DIN EN ISO 9000:2015-11, Quality management systems - Fundamentals and vocabulary (ISO 9000:2015); German and English version EN ISO 9000:2015.*

[138] *VDI/VDE 2630 Part 1.2:2018-06, Computed tomography in dimensional measurement - Influencing variables on measurement results and recommendations for computed tomography dimensional measurements*. https://www.vdi.de/richtlinien/details/vdivde-2630-blatt-12-computed-tomography-in-dimensional-measurement-influencing-variables-on-measurement-results-and-recommendations-for-computed-tomography-dimensional-measurements (visited on 12/06/2021).

[139] *VDI/VDE 2630 Part 2.1:2015-06, Computed tomography in dimensional measurement - Determination of the uncertainty of measurement and the test process suitability of coordinate measurement systems with CT sensors*. https://www.vdi.de/richtlinien/details/vdivde-2630-blatt-21-computertomografie-in-der-dimensionellen-messtechnik-bestimmung-der-messunsicherheit-und-der-pruefprozesseignung-von-koordinatenmessgeraeten-mit-ct-sensoren (visited on 12/06/2021).

[140] Anwer, Nabil; Ballu, Alex, and Mathieu, Luc. “The skin model, a comprehensive geometric model for engineering design”. *CIRP Annals* 62.1 (2013), pp. 143–146.

[141] Srinivasan, Vijay. “Computational Metrology for the Design and Manufacture of Product Geometry: A Classification and Synthesis”. *Journal of Computing and Information Science in Engineering* 7.1 (2007), pp. 3–9.

[142] Zhang, Min; Anwer, Nabil; Stockinger, Andreas; Mathieu, Luc, and Wartzack, Sandro. “Discrete shape modeling for skin model representation”. *Proceedings of the Institution of Mechanical Engineers, Part B: Journal of Engineering Manufacture* 227.5 (2013), pp. 672–680.

[143] Zhang, Min; Anwer, Nabil; Mathieu, Luc, and Zhao, Haibin. “A discrete geometry framework for geometrical product specifications”. *Proceedings of the 21st CIRP Design Conference, Kaist, MK Thompson, ed., Paper*. 2011.

[144] Kaufmann, Manuel; Effenberger, Ira, and Huber, Marco F. “Measurement uncertainty assessment for virtual assembly”. *Journal of Sensors and Sensor Systems* 10.1 (2021), pp. 101–108.

[145] Potter, Kristin. "The Visualization of Uncertainty". Dissertation. University of Utah, 2010. https://collections.lib.utah.edu/ark:/87278/s6d79rwt (visited on 12/08/2021).

[146] Görtler, Jochen. "Quantitative Methods for Uncertainty Visualization". Dissertation. University of Konstanz, 2021. http://nbn-resolving.de/urn:nbn:de:bsz:352-2-ahgl69t7y2u03 (visited on 12/08/2021).

[147] Hansen, Charles D.; Chen, Min; Johnson, Christopher R.; Kaufman, Arie E., and Hagen, Hans. *Scientific Visualization*. London: Springer London, 2014.

[148] Zehner, Björn. *3D geomodelling for Europe (3DGEO-EU): Deliverable 4.1 - State of the art in uncertainty visualization*. 2019. https://geoera.eu/projects/3dgeo-eu/ (visited on 12/08/2021).

[149] Grigoryan, G. and Rheingans, P. "Probabilistic surfaces: point based primitives to show surface uncertainty". *IEEE Visualization, 2002. VIS 2002*. IEEE, 2002, pp. 147–153.

[150] Grigoryan, Gevorg and Rheingans, Penny. "Point-based probabilistic surfaces to show surface uncertainty". *IEEE transactions on visualization and computer graphics* 10.5 (2004), pp. 564–573.

[151] Brunet, Pere and Andújar, Carlos. "Immersive Data Comprehension: Visualizing Uncertainty in Measurable Models". *Frontiers in Robotics and AI* 2 (2015).

[152] Ehlschlaeger, Charles R.; Shortridge, Ashton M., and Goodchild, Michael F. "Visualizing spatial data uncertainty using animation". *Computers & Geosciences* 23.4 (1997), pp. 387–395.

[153] Gillmann, Christina; Saur, Dorothee; Wischgoll, Thomas, and Scheuermann, Gerik. "Uncertainty–aware Visualization in Medical Imaging – A Survey". *Computer Graphics Forum* 40.3 (2021), pp. 665–689.

[154] Pauly, Mark; Mitra, Niloy J., and Guibas, Leonidas J. *Uncertainty and Variability in Point Cloud Surface Data: Eurographics Symposium on Point-Based Graphics*. Ed. by Alexa, M and Rusinkiewicz, S. 2004.

[155] Rhodes, Philip J.; Laramee, Robert S.; Bergeron, R. Daniel, and Sparr, Ted M. *Uncertainty Visualization Methods in Isosurface Rendering: EUROGRAPHICS*. Ed. by Chover, M; Hagen, H, and Tost, D. 2003.

[156] Soodmand, Ehsan; Kluess, Daniel; Varady, Patrick A.; Cichon, Robert; Schwarze, Michael; Gehweiler, Dominic; Niemeyer, Frank; Pahr, Dieter, and Woiczinski, Matthias. "Interlaboratory comparison of femur surface reconstruction from CT data compared to reference optical 3D scan". *Biomedical engineering online* 17.1 (2018), p. 29.

[157] Huotilainen, Eero; Jaanimets, Risto; Valášek, Jiří; Marcián, Petr; Salmi, Mika; Tuomi, Jukka; Mäkitie, Antti, and Wolff, Jan. “Inaccuracies in additive manufactured medical skull models caused by the DICOM to STL conversion process”. *Journal of cranio-maxillo-facial surgery : official publication of the European Association for Cranio-Maxillo-Facial Surgery* 42.5 (2014), e259–e265.

[158] Senin, N.; Catalucci, S.; Moretti, M., and Leach, R. K. “Statistical point cloud model to investigate measurement uncertainty in coordinate metrology”. *Precision Engineering* 70 (2021), pp. 44–62.

[159] Catalucci, Sofia. “Automated assessment of measurement performance in optical coordinate metrology”. Dissertation. University of Nottingham, 2021. https://eprints.nottingham.ac.uk/65560/ (visited on 12/08/2021).

[160] Catalucci, Sofia; Senin, Nicola; Piano, Samanta, and Leach, Richard. “Intelligent systems for optical form measurement: automated assessment of pose and coverage”. *34th ASPE annual meeting*. 2019. https://nottingham-repository.worktribe.com/output/3059678.

[161] Catalucci, Sofia; Senin, Nicola; Sims-Waterhouse, Danny; Ziegelmeier, Stefan; Piano, Samanta, and Leach, Richard. “Measurement of complex freeform additively manufactured parts by structured light and photogrammetry”. *Measurement* 164 (2020), p. 108081.

[162] Catalucci, Sofia; Senin, Nicola; Piano, Samanta, and Leach, Richard. “Automated assessment of measurement quality in optical coordinate metrology of complex freeform parts”. 2021. https://nottingham-repository.worktribe.com/output/6137308.

[163] Malengo, Andrea and Pennecchi, Francesca. “A weighted total least-squares algorithm for any fitting model with correlated variables”. *Metrologia* 50.6 (2013), pp. 654–662.

[164] Krystek, Michael and Anton, Mathias. “A weighted total least-squares algorithm for fitting a straight line”. *Measurement Science and Technology* 18.11 (2007), pp. 3438–3442.

[165] Forbes, Alistair B. “Uncertainty evaluation associated with fitting geometric surfaces to coordinate data”. *Metrologia* 43.4 (2006), S282–S290.

[166] Forbes, Alistair. “Surface fitting taking into account uncertainty structure in coordinate data”. *Measurement Science and Technology* 17.3 (2006), pp. 553–558.

[167] Shakarji, Craig and Raffaldi, J., eds. *Should You Be Concerned with Software Measurement Uncertainty?* Proceedings of the International Dimensional Workshop, USA, 2003. https://tsapps.nist.gov/publication/get_pdf.cfm?pub_id=822070.

[168] The MathWorks, Inc. *Array Indexing*. 2021. https://de.mathworks.com/help/matlab/math/array-indexing.html (visited on 12/09/2021).

[169] The MathWorks, Inc. *Unique values in array - MATLAB unique*. 2021. https://de.mathworks.com/help/matlab/ref/double.unique.html (visited on 11/21/2021).

[170] The MathWorks, Inc. *Reshape array - MATLAB reshape*. 2021. https://de.mathworks.com/help/matlab/ref/reshape.html (visited on 11/21/2021).

[171] The MathWorks, Inc. *MATLAB Documentation: The Language of Technical Computing*. 2021. https://de.mathworks.com/help/matlab/ (visited on 12/09/2021).

[172] Zill, Dennis G. and Cullen, Michael R. *Advanced engineering mathematics*. 3. ed. Boston: Jones and Bartlett, 2006.

[173] The MathWorks, Inc. *Create array of all NaN values - MATLAB NaN*. 2021. https://de.mathworks.com/help/matlab/ref/nan.html (visited on 12/09/2021).

[174] The MathWorks, Inc. *Missing Data in MATLAB*. 2021. https://de.mathworks.com/help/matlab/data_analysis/missing-data-in-matlab.html (visited on 12/09/2021).

[175] Thürrner, Grit and Wüthrich, Charles A. “Computing Vertex Normals from Polygonal Facets”. *Journal of Graphics Tools* 3.1 (1998), pp. 43–46.

[176] Max, Nelson. “Weights for Computing Vertex Normals from Facet Normals”. *Journal of Graphics Tools* 4.2 (1999), pp. 1–6.

[177] Glassner, Andrew S. “Computing Surface Normals For 3D Models”. *Graphics Gems*. Elsevier, 1990, pp. 562–566.

[178] Glassner, Andrew. “Building Vertex Normals from an Unstructured Polygon List”. *Graphics Gems*. Elsevier, 1994, pp. 60–73.

[179] Bærentzen, Jakob Andreas; Gravesen, Jens; Anton, François, and Aanæs, Henrik. “Curvature in Triangle Meshes”. *Guide to Computational Geometry Processing*. Ed. by Bærentzen, Jakob Andreas; Gravesen, Jens; Anton, François, and Aanæs, Henrik. London: Springer London, 2012, pp. 143–158.

[180] Wikipedia, ed. *Centroid*. 2023. https://en.wikipedia.org/w/index.php?title=Centroid&oldid=1146773736 (visited on 03/29/2023).

[181] Wikipedia, ed. *Circumscribed circle*. 2022. https://en.wikipedia.org/w/index.php?title=Circumscribed_circle&oldid=1074823775 (visited on 05/14/2022).

[182] Boyd, Stephen P. and Vandenberghe, Lieven. *Convex optimization*. 18. print. Cambridge: Cambridge Univ. Press, 2015.

[183] Herlihy, Maurice and Shavit, Nir. *The art of multiprocessor programming*. Amsterdam, Heidelberg, and Burlington, MA: Elsevier and Morgan Kaufmann, 2008.

[184] Ju, Tao. "Fixing Geometric Errors on Polygonal Models: A Survey". *Journal of Computer Science and Technology* 24.1 (2009), pp. 19–29.

[185] Campen, Marcel; Attene, Marco, and Kobbelt, Leif. *A Practical Guide to Polygon Mesh Repairing*. 2012.

[186] Jacobson, Alec; Kavan, Ladislav, and Sorkine, Olga. "Robust Inside-Outside Segmentation using Generalized Winding Numbers". *ACM Trans. Graph.* 32.4 (2013). https://igl.ethz.ch/projects/winding-number/ (visited on 01/11/2022).

[187] Barill, Gavin; Dickson, Neil G.; Schmidt, Ryan; Levin, David I. W., and Jacobson, Alec. "Fast winding numbers for soups and clouds". *ACM Trans. Graph.* 37.4 (2018), pp. 1–12.

[188] Si, Hang. *TetGen: A Quality Tetrahedral Mesh Generator and a 3D Delaunay Triangulator*. 2022. https://wias-berlin.de/software/index.jsp?id=TetGen&lang=1 (visited on 01/04/2022).

[189] Si, Hang. "TetGen, a Delaunay-Based Quality Tetrahedral Mesh Generator". *ACM Transactions on Mathematical Software* 41.2 (2015), pp. 1–36.

[190] Boykov, Yuri and Funka-Lea, Gareth. "Graph Cuts and Efficient N-D Image Segmentation". *International Journal of Computer Vision* 70.2 (2006), pp. 109–131.

[191] Kleinberg, Jon and Tardos, Éva. *Algorithm design*. Boston: Pearson/Addison-Wesley, 2006.

[192] Friedman, Jerome H.; Bentley, Jon Louis, and Finkel, Raphael Ari. "An Algorithm for Finding Best Matches in Logarithmic Expected Time". *ACM Transactions on Mathematical Software* 3.3 (1977), pp. 209–226.

[193] Klein, Rolf. *Algorithmische Geometrie: Grundlagen, Methoden, Anwendungen*. 2., vollst. überarb. Aufl. eXamen.press. Berlin and Heidelberg: Springer, 2005. http://bvbr.bib-bvb.de:8991/F?func=service&doc_library=BVB01&doc_number=013103718&line_number=0002&func_code=DB_RECORDS&service_type=MEDIA.

[194] Aurenhammer, Franz. "Voronoi diagrams—a survey of a fundamental geometric data structure". *ACM Computing Surveys* 23.3 (1991), pp. 345–405.

[195] Möller, Tomas and Trumbore, Ben. "Fast, Minimum Storage Ray-Triangle Intersection". *Journal of Graphics Tools* 2.1 (1997), pp. 21–28.

[196] Havel, Jirí and Herout, Adam. "Yet faster ray-triangle intersection (using SSE4)". *IEEE transactions on visualization and computer graphics* 16.3 (2010), pp. 434–438.

[197] Wald, Ingo. "Realtime ray tracing and interactive global illumination". Dissertation. Saarbrücken: Universität des Saarlandes, 2004. (Visited on 08/17/2021).

[198] Badouel, Didier. "An efficient ray-polygon intersection". *Graphics Gems*. Elsevier, 1990.

[199] Kensler, Andrew and Shirley, Peter. "Optimizing Ray-Triangle Intersection via Automated Search". *2006 IEEE Symposium on Interactive Ray Tracing*. IEEE, 2006, pp. 33–38.

[200] Glassner, Andrew S, ed. *An introduction to ray tracing*. London: Acad. Press, 1989.

[201] Koecher, Max and Krieg, Aloys. *Ebene Geometrie*. Dritte, neu bearbeitete und erweiterte Auflage. Springer-Lehrbuch. Berlin, Heidelberg: Springer-Verlag Berlin Heidelberg, 2007. http://site.ebrary.com/lib/alltitles/docDetail.action?docID=10167630.

[202] Freedman, David and Diaconis, Persi. "On the histogram as a density estimator:L 2 theory". *Z. Wahrscheinlichkeitstheorie verw Gebiete (Zeitschrift für Wahrscheinlichkeitstheorie und Verwandte Gebiete)* 57.4 (1981), pp. 453–476.

[203] Scott, David W. *Multivariate Density Estimation*. Wiley, 1992.

[204] *VDI/VDE 2630 Part 1.3:2011-12, Computed tomography in dimensional measurement - Guideline for the application of DIN EN ISO 10360 for coordinate measuring machines with CT-sensors*. https://www.beuth.de/de/technische-regel/vdi-vde-2617-blatt-13-vdi-vde-2630-blatt-1-3/143044428 (visited on 04/19/2022).

[205] *DIN EN ISO 10360-11:2021-04, Geometrical product specifications (GPS) - Acceptance and reverification tests for coordinate measuring machines (CMM) - Part 11: CMMs using the principle of X-ray computed tomography (CT) (ISO/DIS 10360-11:2021); German and English version prEN ISO 10360-11:2021.*

[206] Fleßner, Matthias; Vujaklija, Nemanja; Helmecke, Eric, and Hausotte, Tino. *Determination of metrological structural resolution of a CT system using the frequency response on surface structures*. 2015.

[207] Fleßner, M.; Blauhöfer, M.; Helmecke, E.; Hausotte, T., and Staude, A. "C8.2 - CT measurements of microparts: Numerical uncertainty determination and structural resolution". *Proceedings SENSOR 2015*. AMA Service GmbH, Von-Münchhausen-Str. 49, 31515 Wunstorf, Germany, 2015, pp. 483–488.

[208] Staude, Andreas and Bam, Jürgen Goebbels. "Determining the Spatial Resolution in Computed Tomography – Comparison of MTF and Line-Pair Structures". *The e-Journal of Nondestructive Testing* 16.11 (2011). https://www.ndt.net/article/dir2011/papers/tu41.pdf (visited on 04/19/2022).

[209] Wohlgemuth, Florian; Fleßner, Matthias, and Hausotte, Tino. "Determination of Metrological Structural Resolution using an Aperiodic Spatial Frequency Standard". *The e-Journal of Nondestructive Testing* 24.11 (2019). https://www.ndt.net/article/dir2019/papers/We.4.A.1.pdf (visited on 04/19/2022).

[210] Illemann, Jens. "Traceable measurement of the instrument transfer function in dXCT". *The e-Journal of Nondestructive Testing* 25.2 (2020). https://www.ndt.net/article/ctc2020/papers/ICT2020_paper_id134.pdf (visited on 04/19/2022).

[211] Busch, Matthias and Hausotte, Tino. "Determination of the Interface Structural Resolution of an Industrial X-Ray Computed Tomograph Using a Spherical Specimen and a Gap Specimen Consisting of Gauge Blocks". *Key Engineering Materials* 883 (2021), pp. 41–48.

[212] Stopp, Joachim; Sprankel, Henrik; Seewig, Jörg; Nikolaus, Kai; Antonyuk, Sergiy; Christoph, Raoul, and Weise, Hartmut. "Optimization and determination of the volume structural resolution of a coordinate measuring system with sub-micrometer X-ray tube". *The e-Journal of Nondestructive Testing* 27.03 (2022).

[213] Stedman, M. "Basis for comparing the performance of surface-measuring machines". *Precision Engineering* 9.3 (1987), pp. 149–152.

[214] Stedman, Margaret. "Mapping The Performance Of Surface-Measuring Instruments". *Micromachining of Elements with Optical and Other Submicrometer Dimensional and Surface Specifications*. Ed. by Weck, Manfred. SPIE Proceedings. SPIE, 1987, p. 138.

[215] Franks, A. "Nanometric Surface Metrology at the National Physical Laboratory". *Metrologia* 28.6 (1991), pp. 471–482.

[216] Villarraga-Gómez, Herminso; Körner, Lars; Leach, Richard, and Smith, Stuart T. “Amplitude-wavelength maps for X-ray computed tomography systems”. *Precision Engineering* 64 (2020), pp. 228–242.

[217] Villarraga-Gómez, Herminso; Körner, Lars; Leach, Richard, and Smith, Stuart T. “Corrigendum to “Amplitude-wavelength maps for X-ray computed tomography systems” [Precis Eng 64 (2020) 228–242]”. *Precision Engineering* 71 (2021), pp. 324–325.

[218] Nyquist, H. “Certain Topics in Telegraph Transmission Theory”. *Transactions of the American Institute of Electrical Engineers* 47.2 (1928), pp. 617–644.

[219] Shannon, C. E. “Communication in the Presence of Noise”. *Proceedings of the IRE* 37.1 (1949), pp. 10–21.

[220] *Multi-Feature-Check [Internet]. Aalen (DE): eumetron GmbH*. 2022. https://www.eumetron.de/en-gb/artefacts-and-standards#Multi-Feature-Check (visited on 12/16/2022).

[221] Amidror, Isaac. “Scattered data interpolation methods for electronic imaging systems: a survey”. *Journal of Electronic Imaging* 11.2 (2002), p. 157.

[222] Goshtasby, A. Ardeshir. *Image Registration*. London: Springer London, 2012.

[223] Jian, Bing and Vemuri, Baba C. “Robust Point Set Registration Using Gaussian Mixture Models”. *IEEE transactions on pattern analysis and machine intelligence* 33.8 (2011), pp. 1633–1645.

[224] Bellekens, Ben; Spruyt, Vincent; Berkvens, Raf; Penne, Rudi, and Weyn, Maarten. “A Benchmark Survey of Rigid 3D Point Cloud Registration Algorithms”. *International Journal On Advances in Intelligent Systems* 1 (2015).

[225] Eberly, David. *Converting between Coordinate Systems*. 2020. https://www.geometrictools.com/Documentation/ConvertingBetweenCoordinateSystems.pdf (visited on 02/27/2022).

[226] *DIN EN ISO 5459:2013-05, Geometrical product specifications (GPS) - Geometrical tolerancing - Datums and datum systems (ISO 5459:2011); German version EN ISO 5459:2011.*

[227] Ahn, Sung Joon. *Least Squares Orthogonal Distance Fitting of Curves and Surfaces in Space*. Vol. 3151. Springer eBook Collection. Berlin and Heidelberg: Springer, 2004.

[228] Pomerleau, François; Colas, Francis, and Siegwart, Roland. “A Review of Point Cloud Registration Algorithms for Mobile Robotics”. *Foundations and Trends in Robotics* 4.1 (2015), pp. 1–104.

[229] Gottschalk, Stefan Aric; Manocha, Dinesh, and Lin, Ming C. “Collision Queries Using Oriented Bounding Boxes”. PhD thesis. The University of North Carolina at Chapel, 2000.

[230] O’Rourke, Joseph. “Finding minimal enclosing boxes”. *International Journal of Computer & Information Sciences* 14.3 (1985), pp. 183–199.

[231] Díez, Yago; Roure, Ferran; Lladó, Xavier, and Salvi, Joaquim. “A Qualitative Review on 3D Coarse Registration Methods”. *ACM Computing Surveys* 47.3 (2015), pp. 1–36.

[232] Besl, P. J. and McKay, Neil D. “A method for registration of 3-D shapes”. *IEEE transactions on pattern analysis and machine intelligence* 14.2 (1992), pp. 239–256.

[233] Chen, Y. and Medioni, G. “Object modeling by registration of multiple range images”. *Proceedings. 1991 IEEE International Conference on Robotics and Automation*. IEEE Comput. Soc. Press, 1991, pp. 2724–2729.

[234] Rusinkiewicz, S. and Levoy, M. “Efficient variants of the ICP algorithm”. *Proceedings Third International Conference on 3-D Digital Imaging and Modeling*. IEEE Comput. Soc, 2001, pp. 145–152.

[235] Arun, K. S.; Huang, T. S., and Blostein, S. D. “Least-squares fitting of two 3-d point sets”. *IEEE transactions on pattern analysis and machine intelligence* 9.5 (1987), pp. 698–700.

[236] Low, Kok-Lim. *Linear Least-Squares Optimization for Point-to-Plane ICP Surface Registration*. 2004.

[237] The MathWorks, Inc. *Solve nonlinear least-squares (nonlinear data-fitting) problems - MATLAB lsqnonlin*. 2022. https://www.mathworks.com/help/optim/ug/lsqnonlin.html (visited on 05/15/2022).

[238] Yanghai Tsin. “Kernel Correlation as an Affinity Measure in Point-Sampled Vision Problems”. PhD thesis. Pittsburgh, PA: Carnegie Mellon University, 2003.

[239] Tsin, Yanghai and Kanade, Takeo. “A Correlation-Based Approach to Robust Point Set Registration”. *Computer Vision - ECCV 2004*. Ed. by Kanade, Takeo; Kittler, Josef; Kleinberg, Jon M.; Mattern, Friedemann; Mitchell, John C.; Nierstrasz, Oscar; Pandu Rangan, C.; Steffen, Bernhard; Sudan, Madhu; Terzopoulos, Demetri; Tygar, Dough; Vardi, Moshe Y.; Weikum, Gerhard; Pajdla, Tomáš, and Matas, Jiří. Vol. 3023.

Lecture Notes in Computer Science. Berlin, Heidelberg: Springer Berlin Heidelberg, 2004, pp. 558–569.

[240] The MathWorks, Inc. *Find minimum of unconstrained multivariable function - MATLAB fminunc*. 2022. https://www.mathworks.com/help/optim/ug/fminunc.html (visited on 03/11/2022).

[241] The MathWorks, Inc. *Register two point clouds using ICP algorithm - MATLAB pcregistericp*. 2022. https://www.mathworks.com/help/vision/ref/pcregistericp.html (visited on 03/14/2022).

[242] The MathWorks, Inc. *Object for storing 3-D point cloud - MATLAB*. 2022. https://www.mathworks.com/help/vision/ref/pointcloud.html (visited on 03/14/2022).

[243] Fischler, Martin A. and Bolles, Robert C. “Random sample consensus”. *Communications of the ACM* 24.6 (1981), pp. 381–395.

[244] Rodehorst, Volker. *Photogrammetrische 3D-Rekonstruktion im Nahbereich durch Auto-Kalibrierung mit projektiver Geometrie: Zugl.: Berlin, Techn. Univ., Diss., 2004*. Berlin: wvb Wiss. Verl. Berlin, 2004.

[245] Li, Jiayuan; Hu, Qingwu, and Ai, Mingyao. “Point Cloud Registration Based on One-Point RANSAC and Scale-Annealing Biweight Estimation”. *IEEE Transactions on Geoscience and Remote Sensing* 59.11 (2021), pp. 9716–9729.

[246] Härtig, Frank and Krystek, Michael. “Berücksichtigung systematischer Fehler im Messunsicherheitsbudget”. *4. Fachtagung Messunsicherheit*. Erfurt, 2008.

[247] Doane, David P. and Seward, Lori E. “Measuring Skewness: A Forgotten Statistic?” *Journal of Statistics Education* 19.2 (2011).

[248] Fischer, Hans. *A History of the Central Limit Theorem*. New York, NY: Springer New York, 2011.

[249] Flessner, Matthias and Hausotte, Tino. “Verfahren und System zur Bestimmung der lokalen Qualität von aus Volumendaten extrahierten Oberflächendaten”. DE102015201271 (A1). 2016.

[250] Flessner, Matthias and Hausotte, Tino. “METHOD AND SYSTEM FOR DETERMINING THE LOCAL QUALITY OF SURFACE DATA EXTRACTED FROM VOLUME DATA”. EP3195258 (A1). 2017.

[251] Flessner, Matthias and Hausotte, Tino. “METHOD AND SYSTEM FOR DETERMINING THE LOCAL QUALITY OF SURFACE DATA EXTRACTED FROM VOLUME DATE”. US2017256048 (A1). 2017.

[252] Flessner, Matthias and Hausotte, Tino. “METHOD AND SYSTEM FOR DETERMINING THE LOCAL QUALITY OF SURFACE DATA EXTRACTED FROM VOLUME DATA”. CA2961701 (A1). 2016.

[253] Flessner, Matthias and Hausotte, Tino. “Method and system for determining the local quality of surface data extracted from volume data”. CN106716487 (A). 2017.

[254] Flessner, Matthias and Hausotte, Tino. “Method and system for determining the local quality of surface data extracted from volume data”. KR20170056602 (A). 2017.

[255] Schönfeld, Torsten; Bartscher, Markus; Günther, Thomas, and Dierig, Tobias. “Softwarebasierte Bestimmung von Qualitätskenngrößen in der dimensionellen Computertomograhie”. *The e-Journal of Nondestructive Testing* 21.04 (2016). https://www.ndt.net/article/dgzfp2015/papers/m02a3.pdf (visited on 03/25/2022).

[256] Schönfeld, Torsten and Bartscher, Markus. “Verification and Application of Quality Measures in Dimensional Computed Tomography”. *The e-Journal of Nondestructive Testing* 20.08 (2015). https://www.ndt.net/events/DIR2015/app/content/Paper/47_Schonfeld.pdf (visited on 03/25/2022).

[257] Fleßner, Matthias; Schönfeld, Torsten; Bartscher, Markus, and Gondrom-Linke, Sven. “Condition Monitoring of a Comuted Tomography System without Dedicated Master Workpiece”. *The e-Journal of Nondestructive Testing* 23.03 (2018). https://www.ndt.net/events/APCNDT2017/app/content/Paper/81_Flesner.pdf (visited on 04/19/2022).

[258] Lifton, J. J.; Malcolm, A. A., and McBride, J. W. “On the uncertainty of surface determination in x-ray computed tomography for dimensional metrology”. *Measurement Science and Technology* 26.3 (2015), p. 035003.

[259] Christoph, Raoul; Weise, Hartmut; Leinweber, Carsten, and Kachelrieß, Marc. “Examination of a Method for the Optimization of Scan Parameters for Measuring with Computed Tomography”. *The e-Journal of Nondestructive Testing* 23.2 (2018). https://www.ndt.net/article/ctc2018/papers/ICT2018_paper_id137.pdf (visited on 04/19/2022).

[260] Shefer, Efrat; Altman, Ami; Behling, Rolf; Goshen, Raffy; Gregorian, Lev; Roterman, Yalon; Uman, Igor; Wainer, Naor; Yagil, Yoad, and Zarchin, Oren. “State of the Art of CT Detectors and Sources: A Literature Review”. *Current Radiology Reports* 1.1 (2013), pp. 76–91.

[261] Barnea, Zwi; Chantler, Christopher T.; Glover, Jack L.; Grigg, Mark W.; Islam, M. Tauhidul; Jonge, Martin D. de; Rae, Nicholas A., and Tran, Chanh Q. “Measuring the linearity of X-ray detectors: consequences for absolute attenuation, scattering and absolute Bragg intensities”. *Journal of Applied Crystallography* 44.2 (2011), pp. 281–286.

[262] Buzug, Thorsten M. *Einführung in die Computertomographie*. Berlin, Heidelberg: Springer Berlin Heidelberg, 2004.

[263] Physikalisch-technische Bundesanstalt. *17IND08 AdvanCT: Advanced Computed Tomography for dimensional and surface measurements in industry*. 2018. https://www.ptb.de/empir2018/advanct/home/ (visited on 04/24/2022).

[264] Binder, Felix; Bircher, Benjamin A.; Laquai, René; Küng, Alain; Bellon, Carsten; Meli, Felix; Deresch, Andreas; Neuschaefer-Rube, Ulrich, and Hausotte, Tino. “Methodologies for model parameterization of virtual CTs for measurement uncertainty estimation”. *Measurement Science and Technology* 33.10 (2022), p. 104002.

[265] Pastre, Marc-Antoine de; Thompson, Adam; Quinsat, Yann; Albajez García, José A.; Senin, Nicola, and Leach, Richard. “Polymer powder bed fusion surface texture measurement”. *Measurement Science and Technology* 31.5 (2020), p. 055002.

[266] *DIN EN ISO 14405-1:2017-07, Geometrical product specifications (GPS) - Dimensional tolerancing - Part 1: Linear sizes (ISO 14405-1:2016); German version EN ISO 14405-1:2016*.

[267] Heling, Bjoern; Oberleiter, Thomas; Rohrmoser, Andreas; Kiener, Christoph; Schleich, Benjamin; Hagenah, Hinnerk; Merklein, Marion; Willner, Kai, and Wartzack, Sandro. “A Concept for Process-Oriented Interdisciplinary Tolerance Management Considering Production-Specific Deviations”. *Proceedings of the Design Society: International Conference on Engineering Design* 1.1 (2019), pp. 3441–3450.

[268] *DFG - GEPRIS - FOR 2271: Prozessorientiertes Toleranzmanagement mit virtuellen Absicherungsmethoden*. 2022. https://gepris.dfg.de/gepris/projekt/260682773 (visited on 03/27/2022).

[269] Tsutsui, Shigeyoshi and Collet, Pierre. *Massively Parallel Evolutionary Computation on GPGPUs*. Berlin, Heidelberg: Springer Berlin Heidelberg, 2013.

[270] Skiena, Steven S. *The Algorithm Design Manual*. Cham: Springer International Publishing, 2020.

[271] Bentley, Jon Louis. “Multidimensional binary search trees used for associative searching”. *Communications of the ACM* 18.9 (1975), pp. 509–517.

[272] Knuth, Donald E. “Big Omicron and big Omega and big Theta”. *ACM SIGACT News* 8.2 (1976), pp. 18–24.

[273] Kirk, David and Hwu, Wen-mei. *Programming massively parallel processors: A hands-on approach*. Third edition. Amsterdam: Morgan Kaufmann, 2016. http://www.sciencedirect.com/science/book/9780128119860.

[274] Sanders, Jason and Kandrot, Edward. *CUDA by example: An introduction to general-purpose GPU programming*. Upper Saddle River, NJ: Addison-Wesley, 2011.

[275] Owens, John D.; Luebke, David; Govindaraju, Naga; Harris, Mark; Krüger, Jens; Lefohn, Aaron E., and Purcell, Timothy J. *A Survey of General-Purpose Computation on Graphics Hardware*. 2005.

[276] Malik, Maria; Li, Teng; Sharif, Umar; Shahid, Rabia; El-Ghazawi, Tarek, and Newby, Greg. “Productivity of GPUs under different programming paradigms”. *Concurrency and Computation: Practice and Experience* 24.2 (2012), pp. 179–191.

[277] Owens, J. D.; Houston, M.; Luebke, D.; Green, S.; Stone, J. E., and Phillips, J. C. “GPU Computing”. *Proceedings of the IEEE* 96.5 (2008), pp. 879–899.

[278] Keckler, Stephen W.; Dally, William J.; Khailany, Brucek; Garland, Michael, and Glasco, David. “GPUs and the Future of Parallel Computing”. *IEEE Micro* 31.5 (2011), pp. 7–17.

[279] Navarro, Cristóbal A.; Hitschfeld-Kahler, Nancy, and Mateu, Luis. “A Survey on Parallel Computing and its Applications in Data-Parallel Problems Using GPU Architectures”. *Communications in Computational Physics* 15.2 (2014), pp. 285–329.

[280] Nvidia Corporation. *Nvidia Turing GPU Architecture: Graphics Revinvented: WP-09183-001_v01*. 2018. https://www.nvidia.com/content/dam/en-zz/Solutions/design-visualization/technologies/turing-architecture/NVIDIA-Turing-Architecture-Whitepaper.pdf (visited on 04/08/2022).

[281] NVIDIA Technical Blog. *NVIDIA Turing Architecture In-Depth | NVIDIA Technical Blog*. 2018. https://developer.nvidia.com/blog/nvidia-turing-architecture-in-depth/ (visited on 04/08/2022).

[282] NVIDIA Developer. *NVIDIA OptiX™ Ray Tracing Engine*. 2012. https://developer.nvidia.com/rtx/ray-tracing/optix (visited on 04/08/2022).

[283] The MathWorks, Inc. *Find k-nearest neighbors using input data - MATLAB knnsearch*. 2022. https://www.mathworks.com/help/stats/knnsearch.html (visited on 05/10/2022).

[284] Moore, Gordon E. "Cramming more components onto integrated circuits, Reprinted from Electronics, volume 38, number 8, April 19, 1965, pp.114 ff". *IEEE Solid-State Circuits Society Newsletter* 11.3 (2006), pp. 33–35.

[285] McCool, Michael. *Structured parallel programming: Patterns for efficient computation*. Online-Ausg. Amsterdam and Boston, Mass: Elsevier/Morgan Kaufmann, 2012. http://site.ebrary.com/lib/alltitles/Doc?id=10574665.

[286] Asanović, Krste; Bodik, Ras; Catanzaro, Bryan Christopher; Gebis, Joseph James; Husbands, Parry; Keutzer, Kurt; Patterson, David A.; Plishker, William Lester; Shalf, John; Williams, Samuel Webb, and Yelick, Katherine A. *The Landscape of Parallel Computing Research: A View from Berkeley*. 2006. http://www2.eecs.berkeley.edu/Pubs/TechRpts/2006/EECS-2006-183.html.

[287] Hennessy, John L. and Patterson, David A. *Computer architecture: A quantitative approach*. 3. ed., [Nachdr.] Morgan Kaufmann series in computer architecture and design. Amsterdam: Morgan Kaufmann, 2004.

[288] Wulf, Wm. A. and McKee, Sally A. "Hitting the memory wall". *ACM SIGARCH Computer Architecture News* 23.1 (1995), pp. 20–24.

[289] Nvidia Corporation. *CUDA Toolkit Documentation - CUDA C++ Programming Guide*. 2022. https://docs.nvidia.com/cuda/cuda-c-programming-guide/index.html (visited on 05/07/2022).

[290] Brodtkorb, Andre R.; Dyken, Christopher; Hagen, Trond R.; Hjelmervik, Jon M., and Storaasli, Olaf O. "State-of-the-art in Heterogeneous Computing". *Scientific Programming* 18.1 (2010), pp. 1–33.

[291] Bryant, Randal E. and O'Hallaron, David R. *Computer systems: A programmer's perspective*. Third edition. Boston: Pearson, 2016.

[292] Gustafson, John L. "Reevaluating Amdahl's law". *Communications of the ACM* 31.5 (1988), pp. 532–533.

[293] Hillis, W. Daniel and Steele, Guy L. "Data parallel algorithms". *Communications of the ACM* 29.12 (1986), pp. 1170–1183.

[294] The MathWorks, Inc. *C Matrix API - MATLAB & Simulink*. 2022. https://www.mathworks.com/help/matlab/cc-mx-matrix-library.html (visited on 05/07/2022).

[295] The MathWorks, Inc. *MATLAB Data API for C++ - MATLAB & Simulink*. 2022. https://www.mathworks.com/help/matlab/matlab-data-array.html (visited on 05/07/2022).

[296] The MathWorks, Inc. *GPU CUDA and MEX Programming - MATLAB & Simulink*. 2022. https://www.mathworks.com/help/parallel-computing/gpu-cuda-and-mex-programming.html? (visited on 05/07/2022).

[297] The MathWorks, Inc. *Execute for-loop iterations in parallel on workers - MATLAB parfor*. 2022. https://www.mathworks.com/help/parallel-computing/parfor.html (visited on 05/10/2022).

[298] Hillmann, W. and Kunzmann, H. “Surface Profiles Obtained by Means of Optical Methods — Are They True Representations of the Real Surface?” *CIRP Annals* 39.1 (1990), pp. 581–583.

[299] Haitjema, H. “International comparison of depth-setting standards”. *Metrologia* 34.2 (1997), pp. 161–167.

[300] Rhee, Hyug-Gyo; Vorburger, Theodore V.; Lee, Jonathan W., and Fu, Joseph. “Discrepancies between roughness measurements obtained with phase-shifting and white-light interferometry”. *Applied optics* 44.28 (2005), pp. 5919–5927.

[301] Ottevaere, H.; Schwider, J.; Kacperski, J.; Steinbock, L.; Weible, K.; Kujawinska, M., and Thienpont, H. “Benchmarking instrumentation tools for the characterization of microlenses within the EC Network of Excellence on Micro-Optics (NEMO)”. *Optical Micro- and Nanometrology in Microsystems Technology II*. Ed. by Gorecki, Christophe; Asundi, Anand K., and Osten, Wolfgang. SPIE Proceedings. SPIE, 2008, 69950J.

[302] McCarthy, Michael B.; Brown, Stephen B.; Evenden, Anthony, and Robinson, Andy D. “NPL freeform artefact for verification of non-contact measuring systems”. *Three-Dimensional Imaging, Interaction, and Measurement*. Ed. by Beraldin, J. Angelo; Cheok, Geraldine S.; McCarthy, Michael B.; Neuschaefer-Rube, Ulrich; Baskurt, Atilla M.; McDowall, Ian E., and Dolinsky, Margaret. SPIE Proceedings. SPIE, 2011, 78640K.

[303] Tosello, G.; Haitjema, H.; Leach, R. K.; Quagliotti, D.; Gasparin, S., and Hansen, H. N. “An international comparison of surface texture parameters quantification on polymer artefacts using optical instruments”. *CIRP Annals* 65.1 (2016), pp. 529–532.

[304] Launhardt, M.; Wörz, A.; Loderer, A.; Laumer, T.; Drummer, D.; Hausotte, T., and Schmidt, M. "Detecting surface roughness on SLS parts with various measuring techniques". *Polymer Testing* 53 (2016), pp. 217–226.

[305] Heinl, M.; Greiner, S.; Wudy, K.; Pobel, C.; Rasch, M.; Huber, F.; Papke, T.; Merklein, M.; Schmidt, M.; Körner, C.; Drummer, D., and Hausotte, T. "Measuring procedures for surface evaluation of additively manufactured powder bed-based polymer and metal parts". *Measurement Science and Technology* 31.9 (2020), p. 095202.

[306] Schleich, Benjamin. "Skin model shapes". Dissertation. Friedrich-Alexander-Universität Erlangen-Nürnberg, 2017.

[307] *DIN EN ISO 10360-5:2020-11, Geometrical product specifications (GPS) - Acceptance and reverification tests for coordinate measuring systems (CMS) - Part 5: Coordinate measuring machines (CMMs) using single and multiple stylus contacting probing systems using discrete point and/or scanning measuring mode (ISO 10360-5:2020); German version EN ISO 10360-5:2020.*

[308] *DIN EN ISO 21204:2022-01, Geometrical product specifications (GPS) - Transition specification (ISO 21204:2020); German version EN ISO 21204:2020.*

[309] *DIN EN ISO 13715:2020-01, Technical product documentation - Edges of undefined shape - Indication and dimensioning (ISO 13715:2017); German version EN ISO 13715:2019.*

[310] *DIN ISO 2768-1:1991-06, General tolerances; tolerances for linear and angular dimensions without individual tolerance indications; identical with ISO 2768-1:1989.*

Own publications referring to this work

[P1] Müller, Andreas Michael. “Bestimmung der Güte von Oberflächenpunkten in der industriellen Computertomografie: BA198-14”. Bachelor thesis. Friedrich-Alexander-Universität Erlangen-Nürnberg, 2014.

[P2] Müller, Andreas Michael. “Datenfusion von Oberflächendatensätzen aus CT-Messungen unter Einbezug lokaler Oberflächenqualitätskennwerte: MA0626-16”. Master thesis. Friedrich-Alexander-Universität Erlangen-Nürnberg, 2016.

[P3] Müller, Andreas Michael and Hausotte, Tino. “Data fusion of surface data sets of X-ray computed tomography measurements using locally determined surface quality values”. *Journal of Sensors and Sensor Systems* 7 (2018), pp. 551–557. https://doi.org/10.5194/jsss-7-551-2018.

[P4] Müller, Andreas Michael and Hausotte, Tino. “Comparison of different measures for the single point uncertainty in industrial X-ray computed tomography”. *The e-Journal of Nondestructive Testing* 24.03 (2019). https://www.ndt.net/?id=23666 (visited on 03/29/2023).

[P5] Müller, Andreas Michael and Hausotte, Tino. “Utilization of single point uncertainties for geometry element regression analysis in dimensional X-ray computed tomography”. *The e-Journal of Nondestructive Testing* 24.03 (2019). https://www.ndt.net/?id=23665 (visited on 03/29/2023).

[P6] Orgeldinger, Christian; Wohlgemuth, Florian; Müller, Andreas Michael, and Hausotte, Tino. “Spot size and detector unsharpness determination for numerical measurement uncertainty determination”. *The e-Journal of Nondestructive Testing* 24.03 (2019). https://www.ndt.net/?id=23649 (visited on 03/29/2023).

[P7] Müller, Andreas Michael; Butzhammer, Lorenz; Wohlgemuth, Florian, and Hausotte, Tino. “Automated evaluation of the surface point quality in dimensional X-ray computed tomography”. *tm - Technisches Messen* 87.2 (2020), pp. 111–121. https://doi.org/10.1515/teme-2019-0116.

[P8] Butzhammer, Lorenz; Müller, Andreas Michael, and Hausotte, Tino. “Comparison of Geometrically Derived Quality Criteria regarding Optimal Workpiece Orientation for Computed Tomography Measurements”. *The e-Journal of Nondestructive Testing* 25.02 (2020). https://www.ndt.net/?id=25083 (visited on 03/29/2023).

[P9] Müller, Andreas Michael; Schubert, Dominik; Drummer, Dietmar, and Hausotte, Tino. "Determination of the single point uncertainty of customized polymer gear wheels using structured-light scanning with various polygonization settings". *Journal of Sensors and Sensor Systems* 9.1 (2020), pp. 51–60. https://doi.org/10.5194/jsss-9-51-2020.

[P10] Müller, Andreas Michael and Hausotte, Tino. "Determination of the single point precision associated with tactile gear measurements in scanning mode". *Journal of Sensors and Sensor Systems* 9.1 (2020), pp. 61–70. https://doi.org/10.5194/jsss-9-61-2020.

[P11] Müller, Andreas Michael and Hausotte, Tino. "Analysis of the random measurement error of areal 3D coordinate measurements exclusively based on measurement repetitions". *tm - Technisches Messen* 88.2 (2021), pp. 71–77. https://doi.org/10.1515/teme-2020-0087.

[P12] Müller, Andreas Michael and Hausotte, Tino. "Improving template-based CT data evaluation by integrating CMM reference data into a CAD model-based high fidelity triangle mesh". *Nondestructive Testing and Evaluation* (2022). https://doi.org/10.1080/10589759.2022.2091135.

[P13] Reuter, Tamara; Müller, Andreas Michael, and Hausotte, Tino. "Propagation of image noise through the measurement chain in industrial X-ray computed tomography: Einfluss des Bildrauschens innerhalb der Messkette eines industriellen Computertomografen". *DGZfP Jahrestagung 2022* (2022). https://www.ndt.net/?id=27037 (visited on 03/29/2023).

[P14] Orgeldinger, Christian; Wohlgemuth, Florian; Müller, Andreas Michael, and Hausotte, Tino. "Towards efficient application-dependent dimensional measurements with computed tomography: optimized reduction of measurement duration using continuous scan mode: experimental investigations". *Journal of Sensors and Sensor Systems* 11.2 (2022), pp. 219–223. https://doi.org/10.5194/jsss-11-219-2022.

[P15] Butzhammer, Lorenz; Müller, Andreas Michael, and Hausotte, Tino. "Calibration of 3D scan trajectories for an industrial computed tomography setup with 6-DOF object manipulator system using a single sphere". *Measurement Science and Technology* 34.1 (2023), p. 015403. https://doi.org/10.1088/1361-6501/ac9856.

[P16] Reuter, Tamara; Dittrich, Verena; Müller, Andreas Michael, and Hausotte, Tino. "Transferring measured X-ray focal spots to virtual CT systems for more realistic simulations of dimensional measurements". *The e-Journal of Nondestructive Testing* 29.3 (2024).

[P17] Fleßner, Matthias; Müller, Andreas; Helmecke, Eric, and Hausotte, Tino. "Evaluating and visualizing the quality of surface points determined from computed tomography volume data". *Physikalisch-Technische Bundesanstalt (PTB)* (2015). https://doi.org/10.7795/810.20150223A.

[P18] Fleßner, Matthias; Müller, Andreas Michael; Helmecke, Eric, and Hausotte, Tino. "Automated detection of artefacts for computed tomography in dimensional metrology". *The e-Journal of Nondestructive Testing* 20.08 (2015). https://www.ndt.net/?id=18042 (visited on 03/29/2023).

[P19] Fleßner, Matthias; Müller, Andreas Michael; Götz, Daniela; Helmecke, Eric, and Hausotte, Tino. "Assessment of the single point uncertainty of dimensional CT measurements". *The e-Journal of Nondestructive Testing* 21.02 (2016). https://www.ndt.net/?id=18766 (visited on 03/29/2023).

[P20] Metzner, Sebastian; Ramesh, Rahul; Müller, Andreas Michael, and Hausotte, Tino. "Evaluation of reflection properties of sheet bulk metal formed parts by pixel wise analysis of camera images provided for triangulation measurement". *ITG-Fachbericht 281 Sensoren und Messsysteme*. Berlin: VDE Verlag GmbH, 2018, pp. 203–206. https://ieeexplore.ieee.org/document/8436166 (visited on 03/29/2023).

[P21] Wohlgemuth, Florian; Müller, Andreas Michael, and Hausotte, Tino. "Development of a virtual metrological CT for numerical measurement uncertainty determination using aRTist 2". *tm - Technisches Messen* 85.12 (2018), pp. 728–737. https://doi.org/10.1515/teme-2018-0044.

[P22] Heling, Björn; Müller, Andreas Michael; Schleich, Benjamin; Hausotte, Tino, and Wartzack, Sandro. "Consideration and Impact Assessment of Measurement Uncertainty in the Context of Tolerance Analysis". *Volume 2B: Advanced Manufacturing*. American Society of Mechanical Engineers, 2019. https://doi.org/10.1115/IMECE2019-11328.

[P23] Heling, Björn; Müller, Andreas Michael; Schleich, Benjamin; Hausotte, Tino, and Wartzack, Sandro. "Bestimmung und Berücksichtigung der Einzelpunktmessunsicherheit in virtuellen Toleranzanalysen". *4. Summer School Toleranzmanagement* (2020).

[P24] Oberleiter, Thomas; Müller, Andreas Michael; Hausotte, Tino, and Willner, Kai. "Surrogate modeling considering measuring data and their measurement uncertainty". *Proceedings of the 3rd International Conference on Uncertainty Quantification in Computational Sciences* *and Engineering (UNCECOMP 2019)*. Ed. by Papadrakakis, Manolis; Papadopoulos, V., and Stefanou, G. Athens: Institute of Structural Analysis and Antiseismic Research School of Civil Engineering National Technical University of Athens (NTUA) Greece, 2019, pp. 367–378. https://doi.org/10.7712/120219.6347.18786.

[P25] Müller, Andreas Michael; Wohlgemuth, Florian, and Hausotte, Tino. “Simulation-based correction of systematic errors for CT measurements”. *The e-Journal of Nondestructive Testing* 23.02 (2018). https://www.ndt.net/?id=21921 (visited on 03/29/2023).

[P26] Müller, Andreas Michael; Heling, Björn; Schleich, Benjamin; Oberleiter, Thomas; Willner, Kai; Wartzack, Sandro, and Hausotte, Tino. “Methoden zur Reduzierung und Berücksichtigung der Unsicherheiten von dimensionellen Messgrößen in der Toleranzanalyse”. *Industriekolloquium der Forschergruppe FOR 2271*. Ed. by Wartzack. Stamsried: Druck+Verlag Ernst Vögel GmbH, 2019, pp. 64–73. https://www.archiv.mfk.tf.fau.de?file=pubmfk_5c6a7ab3612b6 (visited on 03/29/2023).

[P27] Müller, Andreas; Metzner, Sebastian, and Hausotte, Tino. “Characterization of the single point precision of steel gear wheel measurements using tactile coordinate measurement machines in scanning mode”. *20. GMA/ITG-Fachtagung Sensoren und Messsysteme 2019*. Ed. by AMA Service GmbH. 2019, pp. 756–762. https://doi.org/10.5162/sensoren2019/P2.18.

[P28] Müller, Andreas Michael; Metzner, Sebastian; Hausotte, Tino; Schubert, Dominik, and Drummer, Dietmar. “Separation of locally determined work piece deviations and measurement uncertainties for structured-light scanning of customized polymer gear wheels”. *20. GMA/ITG-Fachtagung Sensoren und Messsysteme 2019*. Ed. by AMA Service GmbH. 2019, pp. 527–534. https://doi.org/10.5162/sensoren2019/6.4.1.

[P29] Müller, Andreas Michael; Butzhammer, Lorenz, and Hausotte, Tino. “Implementation of a beam hardening correction method for mono material parts using a linearization technique”. *The e-Journal of Nondestructive Testing* 24.11 (2019). https://www.ndt.net/?id=24756 (visited on 03/29/2023).

[P30] Müller, Andreas Michael; Oberleiter, Thomas; Willner, Kai, and Hausotte, Tino. “Implementation of Parameterized Work Piece Deviations and Measurement Uncertainties into Performant Meta-models for an Improved Tolerance Specification”. *Proceedings of the Design*

Society: International Conference on Engineering Design 1.1 (2019), pp. 3501–3510. https://doi.org/10.1017/dsi.2019.357.

[P31] Müller, Andreas Michael and Hausotte, Tino. "About the need for optical gear measurements using a beam diversion mechanism in order to obtain truthful surface texture parameters / Beurteilung der Notwendigkeit einer Strahlumlenkung für optische Zahnradmessungen zur Bestimmung korrekter Oberflächentexturkennwerte". *tm - Technisches Messen* 86.s1 (2019), pp. 87–91. https://doi.org/10.1515/teme-2019-0044.

[P32] Müller, Andreas Michael and Hausotte, Tino. "Verbesserung dimensioneller Messungen auf Grundlage der Einzelpunktgüte und -Messunsicherheit". *Messunsicherheit - Prüfprozesse 2019*. VDI-Berichte. 2019, pp. 179–191.

[P33] Müller, Andreas Michael and Hausotte, Tino. "Improving geometry element regression analysis for dimensional X-ray computed tomography measurements using locally determined quality values". *The e-Journal of Nondestructive Testing* 25.02 (2020). https://www.ndt.net/?id=25116 (visited on 03/29/2023).

[P34] Müller, Andreas Michael; Binder, Felix, and Hausotte, Tino. "Teilprojekt 3: Metrologie und Messdatenverarbeitung für die geometrische Produktverifikation im Rahmen eines ganzheitlichen Toleranzmanagements". *Abschlussbericht DFG-Forschungsgruppe FOR 2271, 2. Phase. Prozessorientiertes Toleranzmanagement mit virtuellen Absicherungsmethoden*. Ed. by Wartzack, Sandro. FAU University Press, 2023, pp. 65–84. https://doi.org/10.25593/978-3-96147-660-2.

Students' theses referring to this work

[S1] Schmitt, Fabian Karl. "Kantenerfassung der Sinterkontor beim selektiven Lasersintern: PA0688-17". Project thesis. Friedrich-Alexander-Universität Erlangen-Nürnberg, 2017.

[S2] Krist, Benedikt. "Abschätzung der zufälligen Messunsicherheitsbeiträge bei der Messung von Kunststoffzahnrädern und Stahlritzeln mittels Röntgencomputertomografie: PA0723-17". Project thesis. Friedrich-Alexander-Universität Erlangen-Nürnberg, 2017.

[S3] D'Heureuse, Philipp. "Optimierung der optischen Oberflächeneigenschaften von stritzgegossenen Zahnrädern durch Modifikation von Kunststoff-Compounds: MA0724-17". Master thesis. Friedrich-Alexander-Universität Erlangen-Nürnberg, 2017.

[S4] Harant, Michael. "Optische dreidimensionale Erfassung von Zahnradprototypen aus POM: MA0725-17". Project thesis. Friedrich-Alexander-Universität Erlangen-Nürnberg, 2017.

[S5] Binder, Felix. "Softwaretechnische Realisierung von Rekonstruktionsalgorithmen für die industrielle Computertomografie mit der Entwicklungsumgebung MATLAB: MA0739-18". Master thesis. Friedrich-Alexander-Universität Erlangen-Nürnberg, 2018.

[S6] Pielenhofer, Anja. "Abschätzung des Einflusses des Verhältnisses der effektiven Voxelgröße zur Spotsize auf die lokalen zufälligen Messunsicherheitsbeiträge in der industriellen CT: BA0760-18". Bachelor thesis. Friedrich-Alexander-Universität Erlangen-Nürnberg, 2018.

[S7] Krist, Benedikt. "Realisierung und Untersuchung einer Korrektur von Strahlaufhärtungsartefakten mit Hilfe der Linearisierungstechnik für Stahlbauteile an einem industriellen Computertomografen: MA0796-18". Master thesis. Friedrich-Alexander-Universität Erlangen-Nürnberg, 2018.

[S8] Chenskaia, Olesia. "Mathematische Korrekturmethoden zur Reduzierung von geometrischen Messabweichungen in der industriellen Röntgencomputertomografie: MA0845-20". Master thesis. Friedrich-Alexander-Universität Erlangen-Nürnberg, 2020.

[S9] Pielenhofer, Anja. "Experimentelle Bestimmung des Einflusses der Messdauer auf die Messunsicherheit in der industriellen Röntgencomputertomografie: MA0852-20". Master thesis. Friedrich-Alexander-Universität Erlangen-Nürnberg, 2020.

[S10] Rumpler, Katharina. “Stochastische Modellierung der Wechselwirkung von Röntgenstrahlung mit Materie in der industriellen Computertomografie: MA0869-21”. Master thesis. Friedrich-Alexander-Universität Erlangen-Nürnberg, 2021.

Reihenübersicht

Koordination der Reihe (Stand 2024):
Geschäftsstelle Maschinenbau, Dr.-Ing. Oliver Kreis, www.mb.fau.de/diss/

Im Rahmen der Reihe sind bisher die nachfolgenden Bände erschienen.

Band 1 – 52
Fertigungstechnik – Erlangen
ISSN 1431-6226
Carl Hanser Verlag, München

Band 53 – 307
Fertigungstechnik – Erlangen
ISSN 1431-6226
Meisenbach Verlag, Bamberg

ab Band 308
FAU Studien aus dem Maschinenbau
ISSN 2625-9974
FAU University Press, Erlangen

Die Zugehörigkeit zu den jeweiligen Lehrstühlen ist wie folgt gekennzeichnet:

Lehrstühle:

FAPS	Lehrstuhl für Fertigungsautomatisierung und Produktionssystematik
FMT	Lehrstuhl für Fertigungsmesstechnik
KTmfk	Lehrstuhl für Konstruktionstechnik
LFT	Lehrstuhl für Fertigungstechnologie
LGT	Lehrstuhl für Gießereitechnik
LPT	Lehrstuhl für Photonische Technologien
REP	Lehrstuhl für Ressourcen- und Energieeffiziente Produktionsmaschinen

Band 1: Andreas Hemberger
Innovationspotentiale in der rechnerintegrierten Produktion durch wissensbasierte Systeme
FAPS, 208 Seiten, 107 Bilder. 1988.
ISBN 3-446-15234-2.

Band 2: Detlef Classe
Beitrag zur Steigerung der Flexibilität automatisierter Montagesysteme durch Sensorintegration und erweiterte Steuerungskonzepte
FAPS, 194 Seiten, 70 Bilder. 1988.
ISBN 3-446-15529-5.

Band 3: Friedrich-Wilhelm Nolting
Projektierung von Montagesystemen
FAPS, 201 Seiten, 107 Bilder, 1 Tab.
1989.ISBN 3-446-15541-4.

Band 4: Karsten Schlüter
Nutzungsgradsteigerung von Montagesystemen durch den Einsatz der Simulationstechnik
FAPS, 177 Seiten, 97 Bilder. 1989.
ISBN 3-446-15542-2.

Band 5: Shir-Kuan Lin
Aufbau von Modellen zur Lageregelung von Industrierobotern
FAPS, 168 Seiten, 46 Bilder. 1989.
ISBN 3-446-15546-5.

Band 6: Rudolf Nuss
Untersuchungen zur Bearbeitungsqualität im Fertigungssystem Laserstrahlschneiden
LFT, 206 Seiten, 115 Bilder, 6 Tab.
1989. ISBN 3-446-15783-2.

Band 7: Wolfgang Scholz
Modell zur datenbankgestützten Planung automatisierter Montageanlagen
FAPS, 194 Seiten, 89 Bilder. 1989.
ISBN 3-446-15825-1.

Band 8: Hans-Jürgen Wißmeier
Beitrag zur Beurteilung des Bruchverhaltens von Hartmetall-Fließpreßmatrizen
LFT, 179 Seiten, 99 Bilder, 9 Tab.
1989. ISBN 3-446-15921-5.

Band 9: Rainer Eisele
Konzeption und Wirtschaftlichkeit von Planungssystemen in der Produktion
FAPS, 183 Seiten, 86 Bilder. 1990.
ISBN 3-446-16107-4.

Band 10: Rolf Pfeiffer
Technologisch orientierte Montageplanung am Beispiel der Schraubtechnik
FAPS, 216 Seiten, 102 Bilder, 16
Tab. 1990. ISBN 3-446-16161-9.

Band 11: Herbert Fischer
Verteilte Planungssysteme zur Flexibilitätssteigerung der rechnerintegrierten Teilefertigung
FAPS, 201 Seiten, 82 Bilder. 1990.
ISBN 3-446-16105-8.

Band 12: Gerhard Kleineidam
CAD/CAP: Rechnergestützte Montagefeinplanung
FAPS, 203 Seiten, 107 Bilder. 1990.
ISBN 3-446-16112-0.

Band 13: Frank Vollertsen
Pulvermetallurgische Verarbeitung eines übereutektoiden verschleißfesten Stahls
LFT, XIII u. 217 Seiten, 67 Bilder,
34 Tab. 1990.
ISBN 3-446-16133-3.

Band 14: Stephan Biermann
Untersuchungen zur Anlagen- und Prozeßdiagnostik für das Schneiden mit CO2-Hochleistungslasern
LFT, VIII u. 170 Seiten, 93 Bilder, 4
Tab. 1991. ISBN 3-446-16269-0.

Band 15: Uwe Geißler
Material- und Datenfluß in einer flexiblen Blechbearbeitungszelle
LFT, 124 Seiten, 41 Bilder, 7 Tab.
1991. ISBN 3-446-16358-1.

Band 16: Frank Oswald Hake
Entwicklung eines rechnergestützten Diagnosesystems für automatisierte Montagezellen
FAPS, XIV u. 166 Seiten, 77 Bilder.
1991. ISBN 3-446-16428-6.

Band 17: Herbert Reichel
Optimierung der Werkzeugbereitstellung durch rechnergestützte Arbeitsfolgenbestimmung
FAPS, 198 Seiten, 73 Bilder, 2 Tab.
1991. ISBN 3-446-16453-7.

Band 18: Josef Scheller
Modellierung und Einsatz von Softwaresystemen für rechnergeführte Montagezellen
FAPS, 198 Seiten, 65 Bilder. 1991.
ISBN 3-446-16454-5.

Band 19: Arnold vom Ende
Untersuchungen zum Biegeumforme mit elastischer Matrize
LFT, 166 Seiten, 55 Bilder, 13 Tab.
1991. ISBN 3-446-16493-6.

Band 20: Joachim Schmid
Beitrag zum automatisierten Bearbeiten von Keramikguß mit Industrierobotern
FAPS, XIV u. 176 Seiten, 111 Bilder,
6 Tab. 1991.
ISBN 3-446-16560-6.

Band 21: Egon Sommer
Multiprozessorsteuerung für kooperierende Industrieroboter in Montagezellen
FAPS, 188 Seiten, 102 Bilder. 1991.
ISBN 3-446-17062-6.

Band 22: Georg Geyer
Entwicklung problemspezifischer Verfahrensketten in der Montage
FAPS, 192 Seiten, 112 Bilder. 1991.
ISBN 3-446-16552-5.

Band 23: Rainer Flohr
Beitrag zur optimalen Verbindungstechnik in der Oberflächenmontage (SMT)
FAPS, 186 Seiten, 79 Bilder. 1991.
ISBN 3-446-16568-1.

Band 24: Alfons Rief
Untersuchungen zur Verfahrensfolge Laserstrahlschneiden und -schweißen in der Rohkarosseriefertigung
LFT, VI u. 145 Seiten, 58 Bilder, 5
Tab. 1991. ISBN 3-446-16593-2.

Band 25: Christoph Thim
Rechnerunterstützte Optimierung von Materialflußstrukturen in der Elektronikmontage durch Simulation
FAPS, 188 Seiten, 74 Bilder. 1992.
ISBN 3-446-17118-5.

Band 26: Roland Müller
CO2 -Laserstrahlschneiden von kurzglasverstärkten Verbundwerkstoffen
LFT, 141 Seiten, 107 Bilder, 4 Tab.
1992. ISBN 3-446-17104-5.

Band 27: Günther Schäfer
Integrierte Informationsverarbeitung bei der Montageplanung
FAPS, 195 Seiten, 76 Bilder. 1992.
ISBN 3-446-17117-7.

Band 28: Martin Hoffmann
Entwicklung einerCAD/CAM-Prozeßkette für die Herstellung von Blechbiegeteilen
LFT, 149 Seiten, 89 Bilder. 1992.
ISBN 3-446-17154-1.

Band 29: Peter Hoffmann
Verfahrensfolge Laserstrahlschneiden und –schweißen: Prozeßführung und Systemtechnik in der 3D-Laserstrahlbearbeitung von Blechformteilen
LFT, 186 Seiten, 92 Bilder, 10 Tab.
1992. ISBN 3-446-17153-3.

Band 30: Olaf Schrödel
Flexible Werkstattsteuerung mit objektorientierten Softwarestrukturen
FAPS, 180 Seiten, 84 Bilder. 1992.
ISBN 3-446-17242-4.

Band 31: Hubert Reinisch
Planungs- und Steuerungswerkzeuge zur impliziten Geräteprogrammierung in Roboterzellen
FAPS, XI u. 212 Seiten, 112 Bilder.
1992. ISBN 3-446-17380-3.

Band 32: Brigitte Bärnreuther
Ein Beitrag zur Bewertung des Kommunikationsverhaltens von Automatisierungsgeräten in flexiblen Produktionszellen
FAPS, XI u. 179 Seiten, 71 Bilder.
1992. ISBN 3-446-17451-6.

Band 33: Joachim Hutfless
Laserstrahlregelung und Optikdiagnostik in der Strahlführung einer CO2-Hochleistungslaseranlage
LFT, 175 Seiten, 70 Bilder, 17 Tab.
1993. ISBN 3-446-17532-6.

Band 34: Uwe Günzel
Entwicklung und Einsatz eines Simula-tionsverfahrens für operative undstrategische Probleme der Produktionsplanung und -steuerung
FAPS, XIV u. 170 Seiten, 66 Bilder,
5 Tab. 1993. ISBN 3-446-17604-7.

Band 35: Bertram Ehmann
Operatives Fertigungscontrolling durch Optimierung auftragsbezogener Bearbeitungsabläufe in der Elektronikfertigung
FAPS, XV u. 167 Seiten, 114 Bilder.
1993. ISBN 3-446-17658-6.

Band 36: Harald Kolléra
Entwicklung eines benutzerorientierten Werkstattprogrammiersystems für das Laserstrahlschneiden
LFT, 129 Seiten, 66 Bilder, 1 Tab.
1993. ISBN 3-446-17719-1.

Band 37: Stephanie Abels
Modellierung und Optimierung von Montageanlagen in einem integrierten Simulationssystem
FAPS, 188 Seiten, 88 Bilder. 1993.
ISBN 3-446-17731-0.

Band 38: Robert Schmidt-Hebbel
Laserstrahlbohren durchflußbestimmender Durchgangslöcher
LFT, 145 Seiten, 63 Bilder, 11 Tab.
1993. ISBN 3-446-17778-7.

Band 39: Norbert Lutz
Oberflächenfeinbearbeitung keramischer Werkstoffe mit XeCl-Excimerlaserstrahlung
LFT, 187 Seiten, 98 Bilder, 29 Tab.
1994. ISBN 3-446-17970-4.

Band 40: Konrad Grampp
Rechnerunterstützung bei Test und Schulung an Steuerungssoftware von SMD-Bestücklinien
FAPS, 178 Seiten, 88 Bilder. 1995.
ISBN 3-446-18173-3.

Band 41: Martin Koch
Wissensbasierte Unterstützung derAngebotsbearbeitung in der Investitionsgüterindustrie
FAPS, 169 Seiten, 68 Bilder. 1995.
ISBN 3-446-18174-1.

Band 42: Armin Gropp
Anlagen- und Prozeßdiagnostik beim Schneiden mit einem gepulsten Nd:YAG-Laser
LFT, 160 Seiten, 88 Bilder, 7 Tab.
1995. ISBN 3-446-18241-1.

Band 43: Werner Heckel
Optische 3D-Konturerfassung und on-line Biegewinkelmessung mit dem Lichtschnittverfahren
LFT, 149 Seiten, 43 Bilder, 11 Tab.
1995. ISBN 3-446-18243-8.

Band 44: Armin Rothhaupt
Modulares Planungssystem zur Optimierung der Elektronikfertigung
FAPS, 180 Seiten, 101 Bilder. 1995.
ISBN 3-446-18307-8.

Band 45: Bernd Zöllner
Adaptive Diagnose in der Elektronikproduktion
FAPS, 195 Seiten, 74 Bilder, 3 Tab.
1995. ISBN 3-446-18308-6.

Band 46: Bodo Vormann
Beitrag zur automatisierten Handhabungsplanung komplexer Blechbiegeteile
LFT, 126 Seiten, 89 Bilder, 3 Tab.
1995. ISBN 3-446-18345-0.

Band 47: Peter Schnepf
Zielkostenorientierte Montageplanung
FAPS, 144 Seiten, 75 Bilder. 1995.
ISBN 3-446-18397-3.

Band 48: Rainer Klotzbücher
Konzept zur rechnerintegrierten Materialversorgung in flexiblen Fertigungssystemen
FAPS, 156 Seiten, 62 Bilder. 1995.
ISBN 3-446-18412-0.

Band 49: Wolfgang Greska
Wissensbasierte Analyse undKlassifizierung von Blechteilen
LFT, 144 Seiten, 96 Bilder. 1995.
ISBN 3-446-18462-7.

Band 50: Jörg Franke
Integrierte Entwicklung neuer Produkt- und Produktionstechnologien für räumliche spritzgegossene Schaltungsträger (3-D MID)
FAPS, 196 Seiten, 86 Bilder, 4 Tab.
1995. ISBN 3-446-18448-1.

Band 51: Franz-Josef Zeller
Sensorplanung und schnelle Sensorregelung für Industrieroboter
FAPS, 190 Seiten, 102 Bilder, 9 Tab.
1995. ISBN 3-446-18601-8.

Band 52: Michael Solvie
Zeitbehandlung und Multimedia-Unterstützung in Feldkommunikationssystemen
FAPS, 200 Seiten, 87 Bilder, 35
Tab. 1996. ISBN 3-446-18607-7.

Band 53: Robert Hopperdietzel
Reengineering in der Elektro- und Elektronikindustrie
FAPS, 180 Seiten, 109 Bilder, 1 Tab.
1996. ISBN 3-87525-070-2.

Band 54: Thomas Rebhahn
Beitrag zur Mikromaterialbearbeitung mit Excimerlasern - Systemkomponenten und Verfahrensoptimierungen
LFT, 148 Seiten, 61 Bilder, 10 Tab. 1996. ISBN 3-87525-075-3.

Band 55: Henning Hanebuth
Laserstrahlhartlöten mit Zweistrahltechnik
LFT, 157 Seiten, 58 Bilder, 11 Tab. 1996. ISBN 3-87525-074-5.

Band 56: Uwe Schönherr
Steuerung und Sensordatenintegration für flexible Fertigungszellen mitkooperierenden Robotern
FAPS, 188 Seiten, 116 Bilder, 3 Tab. 1996. ISBN 3-87525-076-1.

Band 57: Stefan Holzer
Berührungslose Formgebung mitLaserstrahlung
LFT, 162 Seiten, 69 Bilder, 11 Tab. 1996. ISBN 3-87525-079-6.

Band 58: Markus Schultz
Fertigungsqualität beim 3D-Laserstrahlschweißen vonBlechformteilen
LFT, 165 Seiten, 88 Bilder, 9 Tab. 1997. ISBN 3-87525-080-X.

Band 59: Thomas Krebs
Integration elektromechanischer CA-Anwendungen über einem STEP-Produktmodell
FAPS, 198 Seiten, 58 Bilder, 8 Tab. 1997. ISBN 3-87525-081-8.

Band 60: Jürgen Sturm
Prozeßintegrierte Qualitätssicherung in der Elektronikproduktion
FAPS, 167 Seiten, 112 Bilder, 5 Tab. 1997. ISBN 3-87525-082-6.

Band 61: Andreas Brand
Prozesse und Systeme zur Bestückung räumlicher elektronischer Baugruppen (3D-MID)
FAPS, 182 Seiten, 100 Bilder. 1997. ISBN 3-87525-087-7.

Band 62: Michael Kauf
Regelung der Laserstrahlleistung und der Fokusparameter einer CO2-Hochleistungslaseranlage
LFT, 140 Seiten, 70 Bilder, 5 Tab. 1997. ISBN 3-87525-083-4.

Band 63: Peter Steinwasser
Modulares Informationsmanagement in der integrierten Produkt- und Prozeßplanung
FAPS, 190 Seiten, 87 Bilder. 1997. ISBN 3-87525-084-2.

Band 64: Georg Liedl
Integriertes Automatisierungskonzept für den flexiblen Materialfluß in der Elektronikproduktion
FAPS, 196 Seiten, 96 Bilder, 3 Tab. 1997. ISBN 3-87525-086-9.

Band 65: Andreas Otto
Transiente Prozesse beim Laserstrahlschweißen
LFT, 132 Seiten, 62 Bilder, 1 Tab. 1997. ISBN 3-87525-089-3.

Band 66: Wolfgang Blöchl
Erweiterte Informationsbereitstellung an offenen CNC-Steuerungen zur Prozeß- und Programmoptimierung
FAPS, 168 Seiten, 96 Bilder. 1997. ISBN 3-87525-091-5.

Band 67: Klaus-Uwe Wolf
Verbesserte Prozeßführung und Prozeßplanung zur Leistungs- und Qualitätssteigerung beim Spulenwickeln
FAPS, 186 Seiten, 125 Bilder. 1997. ISBN 3-87525-092-3.

Band 68: Frank Backes
Technologieorientierte Bahnplanung für die 3D-Laserstrahlbearbeitung
LFT, 138 Seiten, 71 Bilder, 2 Tab. 1997. ISBN 3-87525-093-1.

Band 69: Jürgen Kraus
Laserstrahlumformen von Profilen
LFT, 137 Seiten, 72 Bilder, 8 Tab. 1997. ISBN 3-87525-094-X.

Band 70: Norbert Neubauer
Adaptive Strahlführungen für CO2-Laseranlagen
LFT, 120 Seiten, 50 Bilder, 3 Tab. 1997. ISBN 3-87525-095-8.

Band 71: Michael Steber
Prozeßoptimierter Betrieb flexibler Schraubstationen in der automatisierten Montage
FAPS, 168 Seiten, 78 Bilder, 3 Tab. 1997. ISBN 3-87525-096-6.

Band 72: Markus Pfestorf
Funktionale 3D-Oberflächenkenngrößen in der Umformtechnik
LFT, 162 Seiten, 84 Bilder, 15 Tab. 1997. ISBN 3-87525-097-4.

Band 73: Volker Franke
Integrierte Planung und Konstruktion von Werkzeugen für die Biegebearbeitung
LFT, 143 Seiten, 81 Bilder. 1998. ISBN 3-87525-098-2.

Band 74: Herbert Scheller
Automatisierte Demontagesysteme und recyclinggerechte Produktgestaltung elektronischer Baugruppen
FAPS, 184 Seiten, 104 Bilder, 17 Tab. 1998. ISBN 3-87525-099-0.

Band 75: Arthur Meßner
Kaltmassivumformung metallischer Kleinstteile – Werkstoffverhalten, Wirkflächenreibung, Prozeßauslegung
LFT, 164 Seiten, 92 Bilder, 14 Tab. 1998. ISBN 3-87525-100-8.

Band 76: Mathias Glasmacher
Prozeß- und Systemtechnik zum Laserstrahl-Mikroschweißen
LFT, 184 Seiten, 104 Bilder, 12 Tab. 1998. ISBN 3-87525-101-6.

Band 77: Michael Schwind
Zerstörungsfreie Ermittlung mechanischer Eigenschaften von Feinblechen mit dem Wirbelstromverfahren
LFT, 124 Seiten, 68 Bilder, 8 Tab. 1998. ISBN 3-87525-102-4.

Band 78: Manfred Gerhard
Qualitätssteigerung in der Elektronikproduktion durch Optimierung der Prozeßführung beim Löten komplexer Baugruppen
FAPS, 179 Seiten, 113 Bilder, 7 Tab. 1998. ISBN 3-87525-103-2.

Band 79: Elke Rauh
Methodische Einbindung der Simulation in die betrieblichen Planungs- und Entscheidungsabläufe
FAPS, 192 Seiten, 114 Bilder, 4 Tab. 1998. ISBN 3-87525-104-0.

Band 80: Sorin Niederkorn
Meßeinrichtung zur Untersuchung der Wirkflächenreibung bei umformtechnischen Prozessen
LFT, 99 Seiten, 46 Bilder, 6 Tab. 1998. ISBN 3-87525-105-9.

Band 81: Stefan Schuberth
Regelung der Fokuslage beim Schweißen mit CO2-Hochleistungslasern unter Einsatz von adaptiven Optiken
LFT, 140 Seiten, 64 Bilder, 3 Tab. 1998. ISBN 3-87525-106-7.

Band 82: Armando Walter Colombo
Development and Implementation of Hierarchical Control Structures of Flexible Production Systems Using High Level Petri Nets
FAPS, 216 Seiten, 86 Bilder. 1998. ISBN 3-87525-109-1.

Band 83: Otto Meedt
Effizienzsteigerung bei Demontage und Recycling durch flexible Demontagetechnologien und optimierte Produktgestaltung
FAPS, 186 Seiten, 103 Bilder. 1998. ISBN 3-87525-108-3.

Band 84: Knuth Götz
Modelle und effiziente Modellbildung zur Qualitätssicherung in der Elektronikproduktion
FAPS, 212 Seiten, 129 Bilder, 24 Tab. 1998. ISBN 3-87525-112-1.

Band 85: Ralf Luchs
Einsatzmöglichkeiten leitender Klebstoffe zur zuverlässigen Kontaktierung elektronischer Bauelemente in der SMT
FAPS, 176 Seiten, 126 Bilder, 30 Tab. 1998. ISBN 3-87525-113-7.

Band 86: Frank Pöhlau
Entscheidungsgrundlagen zur Einführung räumlicher spritzgegossener Schaltungsträger (3-D MID)
FAPS, 144 Seiten, 99 Bilder. 1999. ISBN 3-87525-114-8.

Band 87: Roland T. A. Kals
Fundamentals on the miniaturization of sheet metal working processes
LFT, 128 Seiten, 58 Bilder, 11 Tab. 1999. ISBN 3-87525-115-6.

Band 88: Gerhard Luhn
Implizites Wissen und technisches Handeln am Beispiel der Elektronikproduktion
FAPS, 252 Seiten, 61 Bilder, 1 Tab. 1999. ISBN 3-87525-116-4.

Band 89: Axel Sprenger
Adaptives Streckbiegen von Aluminium-Strangpreßprofilen
LFT, 114 Seiten, 63 Bilder, 4 Tab. 1999. ISBN 3-87525-117-2.

Band 90: Hans-Jörg Pucher
Untersuchungen zur Prozeßfolge Umformen, Bestücken und Laserstrahllöten von Mikrokontakten
LFT, 158 Seiten, 69 Bilder, 9 Tab. 1999. ISBN 3-87525-119-9.

Band 91: Horst Arnet
Profilbiegen mit kinematischer Gestalterzeugung
LFT, 128 Seiten, 67 Bilder, 7 Tab. 1999. ISBN 3-87525-120-2.

Band 92: Doris Schubart
Prozeßmodellierung und Technologieentwicklung beim Abtragen mit CO2-Laserstrahlung
LFT, 133 Seiten, 57 Bilder, 13 Tab. 1999. ISBN 3-87525-122-9.

Band 93: Adrianus L. P. Coremans
Laserstrahlsintern von Metallpulver - Prozeßmodellierung, Systemtechnik, Eigenschaften laserstrahlgesinterter Metallkörper
LFT, 184 Seiten, 108 Bilder, 12 Tab. 1999. ISBN 3-87525-124-5.

Band 94: Hans-Martin Biehler
Optimierungskonzepte für Qualitätsdatenverarbeitung und Informationsbereitstellung in der Elektronikfertigung
FAPS, 194 Seiten, 105 Bilder. 1999. ISBN 3-87525-126-1.

Band 95: Wolfgang Becker
Oberflächenausbildung und tribologische Eigenschaften excimerlaserstrahlbearbeiteter Hochleistungskeramiken
LFT, 175 Seiten, 71 Bilder, 3 Tab. 1999. ISBN 3-87525-127-X.

Band 96: Philipp Hein
Innenhochdruck-Umformen von Blechpaaren: Modellierung, Prozeßauslegung und Prozeßführung
LFT, 129 Seiten, 57 Bilder, 7 Tab. 1999. ISBN 3-87525-128-8.

Band 97: Gunter Beitinger
Herstellungs- und Prüfverfahren für thermoplastische Schaltungsträger
FAPS, 169 Seiten, 92 Bilder, 20 Tab. 1999. ISBN 3-87525-129-6.

Band 98: Jürgen Knoblach
Beitrag zur rechnerunterstützten verursachungsgerechten Angebotskalkulation von Blechteilen mit Hilfe wissensbasierter Methoden
LFT, 155 Seiten, 53 Bilder, 26 Tab. 1999. ISBN 3-87525-130-X.

Band 99: Frank Breitenbach
Bildverarbeitungssystem zur Erfassung der Anschlußgeometrie elektronischer SMT-Bauelemente
LFT, 147 Seiten, 92 Bilder, 12 Tab. 2000. ISBN 3-87525-131-8.

Band 100: Bernd Falk
Simulationsbasierte Lebensdauervorhersage für Werkzeuge der Kaltmassivumformung
LFT, 134 Seiten, 44 Bilder, 15 Tab. 2000. ISBN 3-87525-136-9.

Band 101: Wolfgang Schlögl
Integriertes Simulationsdaten-Management für Maschinenentwicklung und Anlagenplanung
FAPS, 169 Seiten, 101 Bilder, 20 Tab. 2000. ISBN 3-87525-137-7.

Band 102: Christian Hinsel
Ermüdungsbruchversagen hartstoffbeschichteter Werkzeugstähle in der Kaltmassivumformung
LFT, 130 Seiten, 80 Bilder, 14 Tab. 2000. ISBN 3-87525-138-5.

Band 103: Stefan Bobbert
Simulationsgestützte Prozessauslegung für das Innenhochdruck-Umformen von Blechpaaren
LFT, 123 Seiten, 77 Bilder. 2000. ISBN 3-87525-145-8.

Band 104: Harald Rottbauer
Modulares Planungswerkzeug zum Produktionsmanagement in der Elektronikproduktion
FAPS, 166 Seiten, 106 Bilder. 2001.
ISBN 3-87525-139-3.

Band 105: Thomas Hennige
Flexible Formgebung von Blechen durch Laserstrahlumformen
LFT, 119 Seiten, 50 Bilder. 2001.
ISBN 3-87525-140-7.

Band 106: Thomas Menzel
Wissensbasierte Methoden für die rechnergestützte Charakterisierung und Bewertung innovativer Fertigungsprozesse
LFT, 152 Seiten, 71 Bilder. 2001.
ISBN 3-87525-142-3.

Band 107: Thomas Stöckel
Kommunikationstechnische Integration der Prozeßebene in Produktionssysteme durch Middleware-Frameworks
FAPS, 147 Seiten, 65 Bilder, 5 Tab. 2001. ISBN 3-87525-143-1.

Band 108: Frank Pitter
Verfügbarkeitssteigerung von Werkzeugmaschinen durch Einsatz mechatronischer Sensorlösungen
FAPS, 158 Seiten, 131 Bilder, 8 Tab. 2001. ISBN 3-87525-144-X.

Band 109: Markus Korneli
Integration lokaler CAP-Systeme in einen globalen Fertigungsdatenverbund
FAPS, 121 Seiten, 53 Bilder, 11 Tab. 2001. ISBN 3-87525-146-6.

Band 110: Burkhard Müller
Laserstrahljustieren mit Excimer-Lasern - Prozeßparameter und Modelle zur Aktorkonstruktion
LFT, 128 Seiten, 36 Bilder, 9 Tab. 2001. ISBN 3-87525-159-8.

Band 111: Jürgen Göhringer
Integrierte Telediagnose via Internet zum effizienten Service von Produktionssystemen
FAPS, 178 Seiten, 98 Bilder, 5 Tab. 2001. ISBN 3-87525-147-4.

Band 112: Robert Feuerstein
Qualitäts- und kosteneffiziente Integration neuer Bauelementetechnologien in die Flachbaugruppenfertigung
FAPS, 161 Seiten, 99 Bilder, 10 Tab. 2001. ISBN 3-87525-151-2.

Band 113: Marcus Reichenberger
Eigenschaften und Einsatzmöglichkeiten alternativer Elektroniklote in der Oberflächenmontage (SMT)
FAPS, 165 Seiten, 97 Bilder, 18 Tab. 2001. ISBN 3-87525-152-0.

Band 114: Alexander Huber
Justieren vormontierter Systeme mit dem Nd:YAG-Laser unter Einsatz von Aktoren
LFT, 122 Seiten, 58 Bilder, 5 Tab. 2001. ISBN 3-87525-153-9.

Band 115: Sami Krimi
Analyse und Optimierung von Montagesystemen in der Elektronikproduktion
FAPS, 155 Seiten, 88 Bilder, 3 Tab. 2001. ISBN 3-87525-157-1.

Band 116: Marion Merklein
Laserstrahlumformen von Aluminiumwerkstoffen - Beeinflussung der Mikrostruktur und der mechanischen Eigenschaften
LFT, 122 Seiten, 65 Bilder, 15 Tab. 2001. ISBN 3-87525-156-3.

Band 117: Thomas Collisi
Ein informationslogistisches Architekturkonzept zur Akquisition simulationsrelevanter Daten
FAPS, 181 Seiten, 105 Bilder, 7 Tab. 2002. ISBN 3-87525-164-4.

Band 118: Markus Koch
Rationalisierung und ergonomische Optimierung im Innenausbau durch den Einsatz moderner Automatisierungstechnik
FAPS, 176 Seiten, 98 Bilder, 9 Tab. 2002. ISBN 3-87525-165-2.

Band 119: Michael Schmidt
Prozeßregelung für das Laserstrahl-Punktschweißen in der Elektronikproduktion
LFT, 152 Seiten, 71 Bilder, 3 Tab. 2002. ISBN 3-87525-166-0.

Band 120: Nicolas Tiesler
Grundlegende Untersuchungen zum Fließpressen metallischer Kleinstteile
LFT, 126 Seiten, 78 Bilder, 12 Tab. 2002. ISBN 3-87525-175-X.

Band 121: Lars Pursche
Methoden zur technologieorientierten Programmierung für die 3D-Lasermikrobearbeitung
LFT, 111 Seiten, 39 Bilder, 0 Tab. 2002. ISBN 3-87525-183-0.

Band 122: Jan-Oliver Brassel
Prozeßkontrolle beim Laserstrahl-Mikroschweißen
LFT, 148 Seiten, 72 Bilder, 12 Tab. 2002. ISBN 3-87525-181-4.

Band 123: Mark Geisel
Prozeßkontrolle und -steuerung beim Laserstrahlschweißen mit den Methoden der nichtlinearen Dynamik
LFT, 135 Seiten, 46 Bilder, 2 Tab. 2002. ISBN 3-87525-180-6.

Band 124: Gerd Eßer
Laserstrahlunterstützte Erzeugung metallischer Leiterstrukturen auf Thermoplastsubstraten für die MID-Technik
LFT, 148 Seiten, 60 Bilder, 6 Tab. 2002. ISBN 3-87525-171-7.

Band 125: Marc Fleckenstein
Qualität laserstrahl-gefügter Mikroverbindungen elektronischer Kontakte
LFT, 159 Seiten, 77 Bilder, 7 Tab. 2002. ISBN 3-87525-170-9.

Band 126: Stefan Kaufmann
Grundlegende Untersuchungen zum Nd:YAG- Laserstrahlfügen von Silizium für Komponenten der Optoelektronik
LFT, 159 Seiten, 100 Bilder, 6 Tab. 2002. ISBN 3-87525-172-5.

Band 127: Thomas Fröhlich
Simultanes Löten von Anschlußkontakten elektronischer Bauelemente mit Diodenlaserstrahlung
LFT, 143 Seiten, 75 Bilder, 6 Tab. 2002. ISBN 3-87525-186-5.

Band 128: Achim Hofmann
Erweiterung der Formgebungsgrenzen beim Umformen von Aluminiumwerkstoffen durch den Einsatz prozessangepasster Platinen
LFT, 113 Seiten, 58 Bilder, 4 Tab.
2002. ISBN 3-87525-182-2.

Band 129: Ingo Kriebitzsch
3 - D MID Technologie in der Automobilelektronik
FAPS, 129 Seiten, 102 Bilder, 10 Tab. 2002. ISBN 3-87525-169-5.

Band 130: Thomas Pohl
Fertigungsqualität und Umformbarkeit laserstrahlgeschweißter Formplatinen aus Aluminiumlegierungen
LFT, 133 Seiten, 93 Bilder, 12 Tab.
2002. ISBN 3-87525-173-3.

Band 131: Matthias Wenk
Entwicklung eines konfigurierbaren Steuerungssystems für die flexible Sensorführung von Industrierobotern
FAPS, 167 Seiten, 85 Bilder, 1 Tab.
2002. ISBN 3-87525-174-1.

Band 132: Matthias Negendanck
Neue Sensorik und Aktorik für Bearbeitungsköpfe zum Laserstrahlschweißen
LFT, 116 Seiten, 60 Bilder, 14 Tab.
2002. ISBN 3-87525-184-9.

Band 133: Oliver Kreis
Integrierte Fertigung - Verfahrensintegration durch Innenhochdruck-Umformen, Trennen und Laserstrahlschweißen in einem Werkzeug sowie ihre tele- und multimediale Präsentation
LFT, 167 Seiten, 90 Bilder, 43 Tab.
2002. ISBN 3-87525-176-8.

Band 134: Stefan Trautner
Technische Umsetzung produktbezogener Instrumente der Umweltpolitik bei Elektro- und Elektronikgeräten
FAPS, 179 Seiten, 92 Bilder, 11 Tab.
2002. ISBN 3-87525-177-6.

Band 135: Roland Meier
Strategien für einen produktorientierten Einsatz räumlicher spritzgegossener Schaltungsträger (3-D MID)
FAPS, 155 Seiten, 88 Bilder, 14 Tab.
2002. ISBN 3-87525-178-4.

Band 136: Jürgen Wunderlich
Kostensimulation - Simulationsbasierte Wirtschaftlichkeitsregelung komplexer Produktionssysteme
FAPS, 202 Seiten, 119 Bilder, 17 Tab.
2002. ISBN 3-87525-179-2.

Band 137: Stefan Novotny
Innenhochdruck-Umformen von Blechen aus Aluminium- und Magnesiumlegierungen bei erhöhter Temperatur
LFT, 132 Seiten, 82 Bilder, 6 Tab.
2002. ISBN 3-87525-185-7.

Band 138: Andreas Licha
Flexible Montageautomatisierung zur Komplettmontage flächenhafter Produktstrukturen durch kooperierende Industrieroboter
FAPS, 158 Seiten, 87 Bilder, 8 Tab.
2003. ISBN 3-87525-189-X.

Band 139: Michael Eisenbarth
Beitrag zur Optimierung der Aufbau- und Verbindungstechnik für mechatronische Baugruppen
FAPS, 207 Seiten, 141 Bilder, 9 Tab.
2003. ISBN 3-87525-190-3.

Band 140: Frank Christoph
Durchgängige simulationsgestützte Planung von Fertigungseinrichtungen der Elektronikproduktion
FAPS, 187 Seiten, 107 Bilder, 9 Tab.
2003. ISBN 3-87525-191-1.

Band 141: Hinnerk Hagenah
Simulationsbasierte Bestimmung der zu erwartenden Maßhaltigkeit für das Blechbiegen
LFT, 131 Seiten, 36 Bilder, 26 Tab.
2003. ISBN 3-87525-192-X.

Band 142: Ralf Eckstein
Scherschneiden und Biegen metallischer Kleinstteile - Materialeinfluss und Materialverhalten
LFT, 148 Seiten, 71 Bilder, 19 Tab.
2003. ISBN 3-87525-193-8.

Band 143: Frank H. Meyer-Pittroff
Excimerlaserstrahlbiegen dünner metallischer Folien mit homogener Lichtlinie
LFT, 138 Seiten, 60 Bilder, 16 Tab.
2003. ISBN 3-87525-196-2.

Band 144: Andreas Kach
Rechnergestützte Anpassung von Laserstrahlschneidbahnen
an Bauteilabweichungen
LFT, 139 Seiten, 69 Bilder, 11 Tab.
2004. ISBN 3-87525-197-0.

Band 145: Stefan Hierl
System- und Prozeßtechnik für das simultane Löten mit Diodenlaserstrahlung von elektronischen Bauelementen
LFT, 124 Seiten, 66 Bilder, 4 Tab.
2004. ISBN 3-87525-198-9.

Band 146: Thomas Neudecker
Tribologische Eigenschaften keramischer Blechumformwerkzeuge-Einfluss einer Oberflächenendbearbeitung mittels Excimerlaserstrahlung
LFT, 166 Seiten, 75 Bilder, 26 Tab.
2004. ISBN 3-87525-200-4.

Band 147: Ulrich Wenger
Prozessoptimierung in der Wickeltechnik durch innovative maschinenbauliche und regelungstechnische Ansätze
FAPS, 132 Seiten, 88 Bilder, 0 Tab.
2004. ISBN 3-87525-203-9.

Band 148: Stefan Slama
Effizienzsteigerung in der Montage durch marktorientierte Montagestrukturen und erweiterte Mitarbeiterkompetenz
FAPS, 188 Seiten, 125 Bilder, 0 Tab.
2004. ISBN 3-87525-204-7.

Band 149: Thomas Wurm
Laserstrahljustieren mittels Aktoren-Entwicklung von Konzepten und Methoden für die rechnerunterstützte Modellierung und Optimierung von komplexen Aktorsystemen in der Mikrotechnik
LFT, 122 Seiten, 51 Bilder, 9 Tab.
2004. ISBN 3-87525-206-3.

Band 150: Martino Celeghini
Wirkmedienbasierte Blechumformung: Grundlagenuntersuchungen zum Einfluss von Werkstoff und Bauteilgeometrie
LFT, 146 Seiten, 77 Bilder, 6 Tab.
2004. ISBN 3-87525-207-1.

Band 151: Ralph Hohenstein
Entwurf hochdynamischer Sensor- und Regelsysteme für die adaptiveLaserbearbeitung
LFT, 282 Seiten, 63 Bilder, 16 Tab.
2004. ISBN 3-87525-210-1.

Band 152: Angelika Hutterer
Entwicklung prozessüberwachender Regelkreise für flexible Formgebungsprozesse
LFT, 149 Seiten, 57 Bilder, 2 Tab.
2005. ISBN 3-87525-212-8.

Band 153: Emil Egerer
Massivumformen metallischer Kleinstteile bei erhöhter Prozesstemperatur
LFT, 158 Seiten, 87 Bilder, 10 Tab.
2005. ISBN 3-87525-213-6.

Band 154: Rüdiger Holzmann
Strategien zur nachhaltigen Optimierung von Qualität und Zuverlässigkeit in der Fertigung hochintegrierter Flachbaugruppen
FAPS, 186 Seiten, 99 Bilder, 19 Tab.
2005. ISBN 3-87525-217-9.

Band 155: Marco Nock
Biegeumformen mit Elastomerwerkzeugen Modellierung, Prozessauslegung und Abgrenzung des Verfahrens am Beispiel des Rohrbiegens
LFT, 164 Seiten, 85 Bilder, 13 Tab.
2005. ISBN 3-87525-218-7.

Band 156: Frank Niebling
Qualifizierung einer Prozesskette zum Laserstrahlsintern metallischer Bauteile
LFT, 148 Seiten, 89 Bilder, 3 Tab.
2005. ISBN 3-87525-219-5.

Band 157: Markus Meiler
Großserientauglichkeit trockenschmierstoffbeschichteter Aluminiumbleche im Presswerk Grundlegende Untersuchungen zur Tribologie, zum Umformverhalten und Bauteilversuche
LFT, 104 Seiten, 57 Bilder, 21 Tab.
2005. ISBN 3-87525-221-7.

Band 158: Agus Sutanto
Solution Approaches for Planning of Assembly Systems in Three-Dimensional Virtual Environments
FAPS, 169 Seiten, 98 Bilder, 3 Tab.
2005. ISBN 3-87525-220-9.

Band 159: Matthias Boiger
Hochleistungssysteme für die Fertigung elektronischer Baugruppen auf der Basis flexibler Schaltungsträger
FAPS, 175 Seiten, 111 Bilder, 8 Tab.
2005. ISBN 3-87525-222-5.

Band 160: Matthias Pitz
Laserunterstütztes Biegen höchstfester Mehrphasenstähle
LFT, 120 Seiten, 73 Bilder, 11 Tab.
2005. ISBN 3-87525-223-3.

Band 161: Meik Vahl
Beitrag zur gezielten Beeinflussung des Werkstoffflusses beim Innenhochdruck-Umformen von Blechen
LFT, 165 Seiten, 94 Bilder, 15 Tab.
2005. ISBN 3-87525-224-1.

Band 162: Peter K. Kraus
Plattformstrategien - Realisierung einer varianz- und kostenoptimierten Wertschöpfung
FAPS, 181 Seiten, 95 Bilder, 0 Tab.
2005. ISBN 3-87525-226-8.

Band 163: Adrienn Cser
Laserstrahlschmelzabtrag - Prozessanalyse und -modellierung
LFT, 146 Seiten, 79 Bilder, 3 Tab.
2005. ISBN 3-87525-227-6.

Band 164: Markus C. Hahn
Grundlegende Untersuchungen zur Herstellung von Leichtbauverbundstrukturen mit Aluminiumschaumkern
LFT, 143 Seiten, 60 Bilder, 16 Tab.
2005. ISBN 3-87525-228-4.

Band 165: Gordana Michos
Mechatronische Ansätze zur Optimierung von Vorschubachsen
FAPS, 146 Seiten, 87 Bilder, 17 Tab.
2005. ISBN 3-87525-230-6.

Band 166: Markus Stark
Auslegung und Fertigung hochpräziser Faser-Kollimator-Arrays
LFT, 158 Seiten, 115 Bilder, 11 Tab.
2005. ISBN 3-87525-231-4.

Band 167: Yurong Zhou
Kollaboratives Engineering Management in der integrierten virtuellen Entwicklung der Anlagen für die Elektronikproduktion
FAPS, 156 Seiten, 84 Bilder, 6 Tab.
2005. ISBN 3-87525-232-2.

Band 168: Werner Enser
Neue Formen permanenter und lösbarer elektrischer Kontaktierungen für mechatronische Baugruppen
FAPS, 190 Seiten, 112 Bilder, 5 Tab.
2005. ISBN 3-87525-233-0.

Band 169: Katrin Melzer
Integrierte Produktpolitik bei elektrischen und elektronischen Geräten zur Optimierung des Product-Life-Cycle
FAPS, 155 Seiten, 91 Bilder, 17 Tab.
2005. ISBN 3-87525-234-9.

Band 170: Alexander Putz
Grundlegende Untersuchungen zur Erfassung der realen Vorspannung von armierten Kaltfließpresswerkzeugen mittels Ultraschall
LFT, 137 Seiten, 71 Bilder, 15 Tab.
2006. ISBN 3-87525-237-3.

Band 171: Martin Prechtl
Automatisiertes Schichtverfahren für metallische Folien - System- und Prozesstechnik
LFT, 154 Seiten, 45 Bilder, 7 Tab.
2006. ISBN 3-87525-238-1.

Band 172: Markus Meidert
Beitrag zur deterministischen Lebensdauerabschätzung von Werkzeugen der Kaltmassivumformung
LFT, 131 Seiten, 78 Bilder, 9 Tab.
2006. ISBN 3-87525-239-X.

Band 173: Bernd Müller
Robuste, automatisierte Montagesysteme durch adaptive Prozessführung und montageübergreifende Fehlerprävention am Beispiel flächiger Leichtbauteile
FAPS, 147 Seiten, 77 Bilder, 0 Tab.
2006. ISBN 3-87525-240-3.

Band 174: Alexander Hofmann
Hybrides Laserdurchstrahlschweißen von Kunststoffen
LFT, 136 Seiten, 72 Bilder, 4 Tab.
2006. ISBN 978-3-87525-243-9.

Band 175: Peter Wölflick
Innovative Substrate und Prozesse mit feinsten Strukturen für bleifreie Mechatronik-Anwendungen
FAPS, 177 Seiten, 148 Bilder, 24 Tab. 2006.
ISBN 978-3-87525-246-0.

Band 176: Attila Komlodi
Detection and Prevention of Hot Cracks during Laser Welding of Aluminium Alloys Using Advanced Simulation Methods
LFT, 155 Seiten, 89 Bilder, 14 Tab. 2006. ISBN 978-3-87525-248-4.

Band 177: Uwe Popp
Grundlegende Untersuchungen zum Laserstrahlstrukturieren von Kaltmassivumformwerkzeugen
LFT, 140 Seiten, 67 Bilder, 16 Tab. 2006. ISBN 978-3-87525-249-1.

Band 178: Veit Rückel
Rechnergestützte Ablaufplanung und Bahngenerierung Für kooperierende Industrieroboter
FAPS, 148 Seiten, 75 Bilder, 7 Tab. 2006. ISBN 978-3-87525-250-7.

Band 179: Manfred Dirscherl
Nicht-thermische Mikrojustiertechnik mittels ultrakurzer Laserpulse
LFT, 154 Seiten, 69 Bilder, 10 Tab. 2007. ISBN 978-3-87525-251-4.

Band 180: Yong Zhuo
Entwurf eines rechnergestützten integrierten Systems für Konstruktion und Fertigungsplanung räumlicher spritzgegossener Schaltungsträger (3D-MID)
FAPS, 181 Seiten, 95 Bilder, 5 Tab. 2007. ISBN 978-3-87525-253-8.

Band 181: Stefan Lang
Durchgängige Mitarbeiterinformation zur Steigerung von Effizienz und Prozesssicherheit in der Produktion
FAPS, 172 Seiten, 93 Bilder. 2007.
ISBN 978-3-87525-257-6.

Band 182: Hans-Joachim Krauß
Laserstrahlinduzierte Pyrolyse präkeramischer Polymere
LFT, 171 Seiten, 100 Bilder. 2007.
ISBN 978-3-87525-258-3.

Band 183: Stefan Junker
Technologien und Systemlösungen für die flexibel automatisierte Bestückung permanent erregter Läufer mit oberflächenmontierten Dauermagneten
FAPS, 173 Seiten, 75 Bilder. 2007.
ISBN 978-3-87525-259-0.

Band 184: Rainer Kohlbauer
Wissensbasierte Methoden für die simulationsgestützte Auslegung wirkmedienbasierter Blechumformprozesse
LFT, 135 Seiten, 50 Bilder. 2007.
ISBN 978-3-87525-260-6.

Band 185: Klaus Lamprecht
Wirkmedienbasierte Umformung tiefgezogener Vorformen unter besonderer Berücksichtigung maßgeschneiderter Halbzeuge
LFT, 137 Seiten, 81 Bilder. 2007.
ISBN 978-3-87525-265-1.

Band 186: Bernd Zolleiß
Optimierte Prozesse und Systeme für die Bestückung mechatronischerBaugruppen
FAPS, 180 Seiten, 117 Bilder. 2007.
ISBN 978-3-87525-266-8.

Band 187: Michael Kerausch
Simulationsgestützte Prozessauslegung für das Umformen lokal wärmebehandelter Aluminiumplatinen
LFT, 146 Seiten, 76 Bilder, 7 Tab. 2007. ISBN 978-3-87525-267-5.

Band 188: Matthias Weber
Unterstützung der Wandlungsfähigkeit von Produktionsanlagen durch innovative Softwaresysteme
FAPS, 183 Seiten, 122 Bilder, 3 Tab. 2007. ISBN 978-3-87525-269-9.

Band 189: Thomas Frick
Untersuchung der prozessbestimmenden Strahl-Stoff-Wechselwirkungen beim Laserstrahlschweißen von Kunststoffen
LFT, 104 Seiten, 62 Bilder, 8 Tab. 2007. ISBN 978-3-87525-268-2.

Band 190: Joachim Hecht
Werkstoffcharakterisierung und Prozessauslegung für die wirkmedienbasierte Doppelblech-Umformung von Magnesiumlegierungen
LFT, 107 Seiten, 91 Bilder, 2 Tab. 2007. ISBN 978-3-87525-270-5.

Band 191: Ralf Völkl
Stochastische Simulation zur Werkzeuglebensdaueroptimierung und Präzisionsfertigung in der Kaltmassivumformung
LFT, 178 Seiten, 75 Bilder, 12 Tab. 2008. ISBN 978-3-87525-272-9.

Band 192: Massimo Tolazzi
Innenhochdruck-Umformen verstärkter Blech-Rahmenstrukturen
LFT, 164 Seiten, 85 Bilder, 7 Tab. 2008. ISBN 978-3-87525-273-6.

Band 193: Cornelia Hoff
Untersuchung der Prozesseinflussgrößen beim Presshärten des höchstfesten Vergütungsstahls 22MnB5
LFT, 133 Seiten, 92 Bilder, 5 Tab. 2008. ISBN 978-3-87525-275-0.

Band 194: Christian Alvarez
Simulationsgestützte Methoden zur effizienten Gestaltung von Lötprozessen in der Elektronikproduktion
FAPS, 149 Seiten, 86 Bilder, 8 Tab. 2008. ISBN 978-3-87525-277-4.

Band 195: Andreas Kunze
Automatisierte Montage von makromechatronischen Modulen zur flexiblen Integration in hybride Pkw-Bordnetzsysteme
FAPS, 160 Seiten, 90 Bilder, 14 Tab. 2008.
ISBN 978-3-87525-278-1.

Band 196: Wolfgang Hußnätter
Grundlegende Untersuchungen zur experimentellen Ermittlung und zur Modellierung von Fließortkurven bei erhöhten Temperaturen
LFT, 152 Seiten, 73 Bilder, 21 Tab. 2008. ISBN 978-3-87525-279-8.

Band 197: Thomas Bigl
Entwicklung, angepasste Herstellungsverfahren und erweiterte Qualitätssicherung von einsatzgerechten elektronischen Baugruppen
FAPS, 175 Seiten, 107 Bilder, 14 Tab. 2008.
ISBN 978-3-87525-280-4.

Band 198: Stephan Roth
Grundlegende Untersuchungen zum Excimerlaserstrahl-Abtragen unter Flüssigkeitsfilmen
LFT, 113 Seiten, 47 Bilder, 14 Tab. 2008. ISBN 978-3-87525-281-1.

Band 199: Artur Giera
Prozesstechnische Untersuchungen zum Rührreibschweißen metallischer Werkstoffe
LFT, 179 Seiten, 104 Bilder, 36 Tab. 2008. ISBN 978-3-87525-282-8.

Band 200: Jürgen Lechler
Beschreibung und Modellierung des Werkstoffverhaltens von presshärtbaren Bor-Manganstählen
LFT, 154 Seiten, 75 Bilder, 12 Tab. 2009. ISBN 978-3-87525-286-6.

Band 201: Andreas Blankl
Untersuchungen zur Erhöhung der Prozessrobustheit bei der Innenhochdruck-Umformung von flächigen Halbzeugen mit vor- bzw. nachgeschalteten Laserstrahlfügeoperationen
LFT, 120 Seiten, 68 Bilder, 9 Tab. 2009. ISBN 978-3-87525-287-3.

Band 202: Andreas Schaller
Modellierung eines nachfrageorientierten Produktionskonzeptes für mobile Telekommunikationsgeräte
FAPS, 120 Seiten, 79 Bilder, 0 Tab. 2009. ISBN 978-3-87525-289-7.

Band 203: Claudius Schimpf
Optimierung von Zuverlässigkeitsuntersuchungen, Prüfabläufen und Nacharbeitsprozessen in der Elektronikproduktion
FAPS, 162 Seiten, 90 Bilder, 14 Tab. 2009.
ISBN 978-3-87525-290-3.

Band 204: Simon Dietrich
Sensoriken zur Schwerpunktslagebestimmung der optischen Prozessemissionen beim Laserstrahltiefschweißen
LFT, 138 Seiten, 70 Bilder, 5 Tab. 2009. ISBN 978-3-87525-292-7.

Band 205: Wolfgang Wolf
Entwicklung eines agentenbasierten Steuerungssystems zur Materialflussorganisation im wandelbaren Produktionsumfeld
FAPS, 167 Seiten, 98 Bilder. 2009. ISBN 978-3-87525-293-4.

Band 206: Steffen Polster
Laserdurchstrahlschweißen transparenter Polymerbauteile
LFT, 160 Seiten, 92 Bilder, 13 Tab. 2009. ISBN 978-3-87525-294-1.

Band 207: Stephan Manuel Dörfler
Rührreibschweißen von walzplattiertem Halbzeug und Aluminiumblech zur Herstellung flächiger Aluminiumschaum-Sandwich-Verbundstrukturen
LFT, 190 Seiten, 98 Bilder, 5 Tab. 2009. ISBN 978-3-87525-295-8.

Band 208: Uwe Vogt
Seriennahe Auslegung von Aluminium Tailored Heat Treated Blanks
LFT, 151 Seiten, 68 Bilder, 26 Tab. 2009. ISBN 978-3-87525-296-5.

Band 209: Till Laumann
Qualitative und quantitative Bewertung der Crashtauglichkeit von höchstfesten Stählen
LFT, 117 Seiten, 69 Bilder, 7 Tab. 2009. ISBN 978-3-87525-299-6.

Band 210: Alexander Diehl
Größeneffekte bei Biegeprozessen-Entwicklung einer Methodik zur Identifikation und Quantifizierung
LFT, 180 Seiten, 92 Bilder, 12 Tab. 2010. ISBN 978-3-87525-302-3.

Band 211: Detlev Staud
Effiziente Prozesskettenauslegung für das Umformen lokal wärmebehandelter und geschweißter Aluminiumbleche
LFT, 164 Seiten, 72 Bilder, 12 Tab. 2010. ISBN 978-3-87525-303-0.

Band 212: Jens Ackermann
Prozesssicherung beim Laserdurchstrahlschweißen thermoplastischer Kunststoffe
LPT, 129 Seiten, 74 Bilder, 13 Tab. 2010. ISBN 978-3-87525-305-4.

Band 213: Stephan Weidel
Grundlegende Untersuchungen zum Kontaktzustand zwischen Werkstück und Werkzeug bei umformtechnischen Prozessen unter tribologischen Gesichtspunkten
LFT, 144 Seiten, 67 Bilder, 11 Tab. 2010. ISBN 978-3-87525-307-8.

Band 214: Stefan Geißdörfer
Entwicklung eines mesoskopischen Modells zur Abbildung von Größeneffekten in der Kaltmassivumformung mit Methoden der FE-Simulation
LFT, 133 Seiten, 83 Bilder, 11 Tab. 2010. ISBN 978-3-87525-308-5.

Band 215: Christian Matzner
Konzeption produktspezifischer Lösungen zur Robustheitssteigerung elektronischer Systeme gegen die Einwirkung von Betauung im Automobil
FAPS, 165 Seiten, 93 Bilder, 14 Tab. 2010. ISBN 978-3-87525-309-2.

Band 216: Florian Schüßler
Verbindungs- und Systemtechnik für thermisch hochbeanspruchte und miniaturisierte elektronische Baugruppen
FAPS, 184 Seiten, 93 Bilder, 18 Tab. 2010.
ISBN 978-3-87525-310-8.

Band 217: Massimo Cojutti
Strategien zur Erweiterung der Prozessgrenzen bei der Innhochdruck-Umformung von Rohren und Blechpaaren
LFT, 125 Seiten, 56 Bilder, 9 Tab. 2010. ISBN 978-3-87525-312-2.

Band 218: Raoul Plettke
Mehrkriterielle Optimierung komplexer Aktorsysteme für das Laserstrahljustieren
LFT, 152 Seiten, 25 Bilder, 3 Tab. 2010. ISBN 978-3-87525-315-3.

Band 219: Andreas Dobroschke
Flexible Automatisierungslösungen für die Fertigung wickeltechnischer Produkte
FAPS, 184 Seiten, 109 Bilder, 18 Tab. 2011.
ISBN 978-3-87525-317-7.

Band 220: Azhar Zam
Optical Tissue Differentiation for Sensor-Controlled Tissue-Specific Laser Surgery
LPT, 99 Seiten, 45 Bilder, 8 Tab. 2011. ISBN 978-3-87525-318-4.

Band 221: Michael Rösch
Potenziale und Strategien zur Optimierung des Schablonendruckprozesses in der Elektronikproduktion
FAPS, 192 Seiten, 127 Bilder, 19 Tab. 2011.
ISBN 978-3-87525-319-1.

Band 222: Thomas Rechtenwald
Quasi-isothermes Laserstrahlsintern von Hochtemperatur-Thermoplasten - Eine Betrachtung werkstoff-prozessspezifischer Aspekte am Beispiel PEEK
LPT, 150 Seiten, 62 Bilder, 8 Tab. 2011. ISBN 978-3-87525-320-7.

Band 223: Daniel Craiovan
Prozesse und Systemlösungen für die SMT-Montage optischer Bauelemente auf Substrate mit integrierten Lichtwellenleitern
FAPS, 165 Seiten, 85 Bilder, 8 Tab. 2011. ISBN 978-3-87525-324-5.

Band 224: Kay Wagner
Beanspruchungsangepasste Kaltmassivumformwerkzeuge durch lokal optimierte Werkzeugoberflächen
LFT, 147 Seiten, 103 Bilder, 17 Tab. 2011. ISBN 978-3-87525-325-2.

Band 225: Martin Brandhuber
Verbesserung der Prognosegüte des Versagens von Punktschweißverbindungen bei höchstfesten Stahlgüten
LFT, 155 Seiten, 91 Bilder, 19 Tab. 2011. ISBN 978-3-87525-327-6.

Band 226: Peter Sebastian Feuser
Ein Ansatz zur Herstellung von pressgehärteten Karosseriekomponenten mit maßgeschneiderten mechanischen Eigenschaften: Temperierte Umformwerkzeuge. Prozessfenster, Prozesssimuation und funktionale Untersuchung
LFT, 195 Seiten, 97 Bilder, 60 Tab. 2012. ISBN 978-3-87525-328-3.

Band 227: Murat Arbak
Material Adapted Design of Cold Forging Tools Exemplified by Powder Metallurgical Tool Steels and Ceramics
LFT, 109 Seiten, 56 Bilder, 8 Tab. 2012. ISBN 978-3-87525-330-6.

Band 228: Indra Pitz
Beschleunigte Simulation des Laserstrahlumformens von Aluminiumblechen
LPT, 137 Seiten, 45 Bilder, 27 Tab. 2012. ISBN 978-3-87525-333-7.

Band 229: Alexander Grimm
Prozessanalyse und -überwachung des Laserstrahlhartlötens mittels optischer Sensorik
LPT, 125 Seiten, 61 Bilder, 5 Tab. 2012. ISBN 978-3-87525-334-4.

Band 230: Markus Kaupper
Biegen von höhenfesten Stahlblechwerkstoffen - Umformverhalten und Grenzen der Biegbarkeit
LFT, 160 Seiten, 57 Bilder, 10 Tab. 2012. ISBN 978-3-87525-339-9.

Band 231: Thomas Kroiß
Modellbasierte Prozessauslegung für die Kaltmassivumformung unter Brücksichtigung der Werkzeug- und Pressenauffederung
LFT, 169 Seiten, 50 Bilder, 19 Tab. 2012. ISBN 978-3-87525-341-2.

Band 232: Christian Goth
Analyse und Optimierung der Entwicklung und Zuverlässigkeit räumlicher Schaltungsträger (3D-MID)
FAPS, 176 Seiten, 102 Bilder, 22 Tab. 2012.
ISBN 978-3-87525-340-5.

Band 233: Christian Ziegler
Ganzheitliche Automatisierung mechatronischer Systeme in der Medizin am Beispiel Strahlentherapie
FAPS, 170 Seiten, 71 Bilder, 19 Tab. 2012. ISBN 978-3-87525-342-9.

Band 234: Florian Albert
Automatisiertes Laserstrahllöten und -reparaturlöten elektronischer Baugruppen
LPT, 127 Seiten, 78 Bilder, 11 Tab. 2012. ISBN 978-3-87525-344-3.

Band 235: Thomas Stöhr
Analyse und Beschreibung des mechanischen Werkstoffverhaltens von presshärtbaren Bor-Manganstählen
LFT, 118 Seiten, 74 Bilder, 18 Tab. 2013. ISBN 978-3-87525-346-7.

Band 236: Christian Kägeler
Prozessdynamik beim Laserstrahlschweißen verzinkter Stahlbleche im Überlappstoß
LPT, 145 Seiten, 80 Bilder, 3 Tab. 2013. ISBN 978-3-87525-347-4.

Band 237: Andreas Sulzberger
Seriennahe Auslegung der Prozesskette zur wärmeunterstützten Umformung von Aluminiumblechwerkstoffen
LFT, 153 Seiten, 87 Bilder, 17 Tab. 2013. ISBN 978-3-87525-349-8.

Band 238: Simon Opel
Herstellung prozessangepasster Halbzeuge mit variabler Blechdicke durch die Anwendung von Verfahren der Blechmassivumformung
LFT, 165 Seiten, 108 Bilder, 27 Tab. 2013. ISBN 978-3-87525-350-4.

Band 239: Rajesh Kanawade
In-vivo Monitoring of Epithelium Vessel and Capillary Density for the Application of Detection of Clinical Shock and Early Signs of Cancer Development
LPT, 124 Seiten, 58 Bilder, 15 Tab. 2013. ISBN 978-3-87525-351-1.

Band 240: Stephan Busse
Entwicklung und Qualifizierung eines Schneidclinchverfahrens
LFT, 119 Seiten, 86 Bilder, 20 Tab. 2013. ISBN 978-3-87525-352-8.

Band 241: Karl-Heinz Leitz
Mikro- und Nanostrukturierung mit kurz und ultrakurz gepulster Laserstrahlung
LPT, 154 Seiten, 71 Bilder, 9 Tab. 2013. ISBN 978-3-87525-355-9.

Band 242: Markus Michl
Webbasierte Ansätze zur ganzheitlichen technischen Diagnose
FAPS, 182 Seiten, 62 Bilder, 20 Tab. 2013.
ISBN 978-3-87525-356-6.

Band 243: Vera Sturm
Einfluss von Chargenschwankungen auf die Verarbeitungsgrenzen von Stahlwerkstoffen
LFT, 113 Seiten, 58 Bilder, 9 Tab. 2013. ISBN 978-3-87525-357-3.

Band 244: Christian Neudel
Mikrostrukturelle und mechanisch-technologische Eigenschaften widerstandspunktgeschweißter Aluminium-Stahl-Verbindungen für den Fahrzeugbau
LFT, 178 Seiten, 171 Bilder, 31 Tab. 2014. ISBN 978-3-87525-358-0.

Band 245: Anja Neumann
Konzept zur Beherrschung der Prozessschwankungen im Presswerk
LFT, 162 Seiten, 68 Bilder, 15 Tab. 2014. ISBN 978-3-87525-360-3.

Band 246: Ulf-Hermann Quentin
Laserbasierte Nanostrukturierung mit optisch positionierten Mikrolinsen
LPT, 137 Seiten, 89 Bilder, 6 Tab. 2014. ISBN 978-3-87525-361-0.

Band 247: Erik Lamprecht
Der Einfluss der Fertigungsverfahren auf die Wirbelstromverluste von Stator-Einzelzahnblechpaketen für den Einsatz in Hybrid- und Elektrofahrzeugen
FAPS, 148 Seiten, 138 Bilder, 4 Tab. 2014. ISBN 978-3-87525-362-7.

Band 248: Sebastian Rösel
Wirkmedienbasierte Umformung von Blechhalbzeugen unter Anwendung magnetorheologischer Flüssigkeiten als kombiniertes Wirk- und Dichtmedium
LFT, 148 Seiten, 61 Bilder, 12 Tab. 2014. ISBN 978-3-87525-363-4.

Band 249: Paul Hippchen
Simulative Prognose der Geometrie indirekt pressgehärteter Karosseriebauteile für die industrielle Anwendung
LFT, 163 Seiten, 89 Bilder, 12 Tab. 2014. ISBN 978-3-87525-364-1.

Band 250: Martin Zubeil
Versagensprognose bei der Prozesssimulation von Biegeumform- und Falzverfahren
LFT, 171 Seiten, 90 Bilder, 5 Tab. 2014. ISBN 978-3-87525-365-8.

Band 251: Alexander Kühl
Flexible Automatisierung der Statorenmontage mit Hilfe einer universellen ambidexteren Kinematik
FAPS, 142 Seiten, 60 Bilder, 26 Tab. 2014.
ISBN 978-3-87525-367-2.

Band 252: Thomas Albrecht
Optimierte Fertigungstechnologien für Rotoren getriebeintegrierter PM-Synchronmotoren von Hybridfahrzeugen
FAPS, 198 Seiten, 130 Bilder, 38 Tab. 2014.
ISBN 978-3-87525-368-9.

Band 253: Florian Risch
Planning and Production Concepts for Contactless Power Transfer Systems for Electric Vehicles
FAPS, 185 Seiten, 125 Bilder, 13 Tab. 2014.
ISBN 978-3-87525-369-6.

Band 254: Markus Weigl
Laserstrahlschweißen von Mischverbindungen aus austenitischen und ferritischen korrosionsbeständigen Stahlwerkstoffen
LPT, 184 Seiten, 110 Bilder, 6 Tab. 2014. ISBN 978-3-87525-370-2.

Band 255: Johannes Noneder
Beanspruchungserfassung für die Validierung von FE-Modellen zur Auslegung von Massivumformwerkzeugen
LFT, 161 Seiten, 65 Bilder, 14 Tab. 2014. ISBN 978-3-87525-371-9.

Band 256: Andreas Reinhardt
Ressourceneffiziente Prozess- und Produktionstechnologie für flexible Schaltungsträger
FAPS, 123 Seiten, 69 Bilder, 19 Tab. 2014. ISBN 978-3-87525-373-3.

Band 257: Tobias Schmuck
Ein Beitrag zur effizienten Gestaltung globaler Produktions- und Logistiknetzwerke mittels Simulation
FAPS, 151 Seiten, 74 Bilder. 2014.
ISBN 978-3-87525-374-0.

Band 258: Bernd Eichenhüller
Untersuchungen der Effekte und Wechselwirkungen charakteristischer Einflussgrößen auf das Umformverhalten bei Mikroumformprozessen
LFT, 127 Seiten, 29 Bilder, 9 Tab. 2014. ISBN 978-3-87525-375-7.

Band 259: Felix Lütteke
Vielseitiges autonomes Transportsystem basierend auf Weltmodellerstellung mittels Datenfusion von Deckenkameras und Fahrzeugsensoren
FAPS, 152 Seiten, 54 Bilder, 20 Tab. 2014.
ISBN 978-3-87525-376-4.

Band 260: Martin Grüner
Hochdruck-Blechumformung mit formlos festen Stoffen als Wirkmedium
LFT, 144 Seiten, 66 Bilder, 29 Tab. 2014. ISBN 978-3-87525-379-5.

Band 261: Christian Brock
Analyse und Regelung des Laserstrahltiefschweißprozesses durch Detektion der Metalldampffackelposition
LPT, 126 Seiten, 65 Bilder, 3 Tab. 2015. ISBN 978-3-87525-380-1.

Band 262: Peter Vatter
Sensitivitätsanalyse des 3-Rollen-Schubbiegens auf Basis der Finite Elemente Methode
LFT, 145 Seiten, 57 Bilder, 26 Tab. 2015. ISBN 978-3-87525-381-8.

Band 263: Florian Klämpfl
Planung von Laserbestrahlungen durch simulationsbasierte Optimierung
LPT, 169 Seiten, 78 Bilder, 32 Tab. 2015. ISBN 978-3-87525-384-9.

Band 264: Matthias Domke
Transiente physikalische Mechanismen bei der Laserablation von dünnen Metallschichten
LPT, 133 Seiten, 43 Bilder, 3 Tab.
2015. ISBN 978-3-87525-385-6.

Band 265: Johannes Götz
Community-basierte Optimierung des Anlagenengineerings
FAPS, 177 Seiten, 80 Bilder, 30 Tab.
2015.
ISBN 978-3-87525-386-3.

Band 266: Hung Nguyen
Qualifizierung des Potentials von Verfestigungseffekten zur Erweiterung des Umformvermögens aushärtbarer Aluminiumlegierungen
LFT, 137 Seiten, 57 Bilder, 16 Tab.
2015. ISBN 978-3-87525-387-0.

Band 267: Andreas Kuppert
Erweiterung und Verbesserung von Versuchs- und Auswertetechniken für die Bestimmung von Grenzformänderungskurven
LFT, 138 Seiten, 82 Bilder, 2 Tab.
2015. ISBN 978-3-87525-388-7.

Band 268: Kathleen Klaus
Erstellung eines Werkstofforientierten Fertigungsprozessfensters zur Steigerung des Formgebungsvermögens von Alumi-niumlegierungen unter Anwendung einer zwischengeschalteten Wärmebehandlung
LFT, 154 Seiten, 70 Bilder, 8 Tab.
2015. ISBN 978-3-87525-391-7.

Band 269: Thomas Svec
Untersuchungen zur Herstellung von funktionsoptimierten Bauteilen im partiellen Presshärtprozess mittels lokal unterschiedlich temperierter Werkzeuge
LFT, 166 Seiten, 87 Bilder, 15 Tab.
2015. ISBN 978-3-87525-392-4.

Band 270: Tobias Schrader
Grundlegende Untersuchungen zur Verschleißcharakterisierung beschichteter Kaltmassivumformwerkzeuge
LFT, 164 Seiten, 55 Bilder, 11 Tab.
2015. ISBN 978-3-87525-393-1.

Band 271: Matthäus Brela
Untersuchung von Magnetfeld-Messmethoden zur ganzheitlichen Wertschöpfungsoptimierung und Fehlerdetektion an magnetischen Aktoren
FAPS, 170 Seiten, 97 Bilder, 4 Tab.
2015. ISBN 978-3-87525-394-8.

Band 272: Michael Wieland
Entwicklung einer Methode zur Prognose adhäsiven Verschleißes an Werkzeugen für das direkte Presshärten
LFT, 156 Seiten, 84 Bilder, 9 Tab.
2015. ISBN 978-3-87525-395-5.

Band 273: René Schramm
Strukturierte additive Metallisierung durch kaltaktives Atmosphärendruckplasma
FAPS, 136 Seiten, 62 Bilder, 15 Tab.
2015. ISBN 978-3-87525-396-2.

Band 274: Michael Lechner
Herstellung beanspruchungsangepasster Aluminiumblechhalbzeuge durch eine maßgeschneiderte Variation der Abkühlgeschwindigkeit nach Lösungsglühen
LFT, 136 Seiten, 62 Bilder, 15 Tab.
2015. ISBN 978-3-87525-397-9.

Band 275: Kolja Andreas
Einfluss der Oberflächenbeschaffenheit auf das Werkzeugeinsatzverhalten beim Kaltfließpressen
LFT, 169 Seiten, 76 Bilder, 4 Tab.
2015. ISBN 978-3-87525-398-6.

Band 276: Marcus Baum
Laser Consolidation of ITO Nanoparticles for the Generation of Thin Conductive Layers on Transparent Substrates
LPT, 158 Seiten, 75 Bilder, 3 Tab.
2015. ISBN 978-3-87525-399-3.

Band 277: Thomas Schneider
Umformtechnische Herstellung dünnwandiger Funktionsbauteile aus Feinblech durch Verfahren der Blechmassivumformung
LFT, 188 Seiten, 95 Bilder, 7 Tab.
2015. ISBN 978-3-87525-401-3.

Band 278: Jochen Merhof
Sematische Modellierung automatisierter Produktionssysteme zur Verbesserung der IT-Integration zwischen Anlagen-Engineering und Steuerungsebene
FAPS, 157 Seiten, 88 Bilder, 8 Tab.
2015. ISBN 978-3-87525-402-0.

Band 279: Fabian Zöller
Erarbeitung von Grundlagen zur Abbildung des tribologischen Systems in der Umformsimulation
LFT, 126 Seiten, 51 Bilder, 3 Tab.
2016. ISBN 978-3-87525-403-7.

Band 280: Christian Hezler
Einsatz technologischer Versuche zur Erweiterung der Versagensvorhersage bei Karosseriebauteilen aus höchstfesten Stählen
LFT, 147 Seiten, 63 Bilder, 44 Tab.
2016. ISBN 978-3-87525-404-4.

Band 281: Jochen Bönig
Integration des Systemverhaltens von Automobil-Hochvoltleitungen in die virtuelle Absicherung durch strukturmechanische Simulation
FAPS, 177 Seiten, 107 Bilder, 17 Tab.
2016.
ISBN 978-3-87525-405-1.

Band 282: Johannes Kohl
Automatisierte Datenerfassung für diskret ereignisorientierte Simulationen in der energieflexibelen Fabrik
FAPS, 160 Seiten, 80 Bilder, 27 Tab.
2016.
ISBN 978-3-87525-406-8.

Band 283: Peter Bechtold
Mikroschockwellenumformung mittels ultrakurzer Laserpulse
LPT, 155 Seiten, 59 Bilder, 10 Tab.
2016. ISBN 978-3-87525-407-5.

Band 284: Stefan Berger
Laserstrahlschweißen thermoplastischer Kohlenstofffaserverbundwerkstoffe mit spezifischem Zusatzdraht
LPT, 118 Seiten, 68 Bilder, 9 Tab.
2016. ISBN 978-3-87525-408-2.

Band 285: Martin Bornschlegl
Methods-Energy Measurement - Eine Methode zur Energieplanung für Fügeverfahren im Karosseriebau
FAPS, 136 Seiten, 72 Bilder, 46 Tab. 2016.
ISBN 978-3-87525-409-9.

Band 286: Tobias Rackow
Erweiterung des Unternehmenscontrollings um die Dimension Energie
FAPS, 164 Seiten, 82 Bilder, 29 Tab. 2016.
ISBN 978-3-87525-410-5.

Band 287: Johannes Koch
Grundlegende Untersuchungen zur Herstellung zyklisch-symmetrischer Bauteile mit Nebenformelementen durch Blechmassivumformung
LFT, 125 Seiten, 49 Bilder, 17 Tab. 2016. ISBN 978-3-87525-411-2.

Band 288: Hans Ulrich Vierzigmann
Beitrag zur Untersuchung der tribologischen Bedingungen in der Blechmassivumformung - Bereitstellung von tribologischen Modellversuchen und Realisierung von Tailored Surfaces
LFT, 174 Seiten, 102 Bilder, 34 Tab. 2016. ISBN 978-3-87525-412-9.

Band 289: Thomas Senner
Methodik zur virtuellen Absicherung der formgebenden Operation des Nasspressprozesses von Gelege-Mehrschichtverbunden
LFT, 156 Seiten, 96 Bilder, 21 Tab. 2016. ISBN 978-3-87525-414-3.

Band 290: Sven Kreitlein
Der grundoperationsspezifische Mindestenergiebedarf als Referenzwert zur Bewertung der Energieeffizienz in der Produktion
FAPS, 185 Seiten, 64 Bilder, 30 Tab. 2016.
ISBN 978-3-87525-415-0.

Band 291: Christian Roos
Remote-Laserstrahlschweißen verzinkter Stahlbleche in Kehlnahtgeometrie
LPT, 123 Seiten, 52 Bilder, 0 Tab. 2016. ISBN 978-3-87525-416-7.

Band 292: Alexander Kahrimanidis
Thermisch unterstützte Umformung von Aluminiumblechen
LFT, 165 Seiten, 103 Bilder, 18 Tab. 2016. ISBN 978-3-87525-417-4.

Band 293: Jan Tremel
Flexible Systems for Permanent Magnet Assembly and Magnetic Rotor Measurement / Flexible Systeme zur Montage von Permanentmagneten und zur Messung magnetischer Rotoren
FAPS, 152 Seiten, 91 Bilder, 12 Tab. 2016. ISBN 978-3-87525-419-8.

Band 294: Ioannis Tsoupis
Schädigungs- und Versagensverhalten hochfester Leichtbauwerkstoffe unter Biegebeanspruchung
LFT, 176 Seiten, 51 Bilder, 6 Tab. 2017. ISBN 978-3-87525-420-4.

Band 295: Sven Hildering
Grundlegende Untersuchungen zum Prozessverhalten von Silizium als Werkzeugwerkstoff für das Mikroscherschneiden metallischer Folien
LFT, 177 Seiten, 74 Bilder, 17 Tab. 2017. ISBN 978-3-87525-422-8.

Band 296: Sasia Mareike Hertweck
Zeitliche Pulsformung in der Lasermikromaterialbearbeitung – Grundlegende Untersuchungen und Anwendungen
LPT, 146 Seiten, 67 Bilder, 5 Tab. 2017. ISBN 978-3-87525-423-5.

Band 297: Paryanto
Mechatronic Simulation Approach for the Process Planning of Energy-Efficient Handling Systems
FAPS, 162 Seiten, 86 Bilder, 13 Tab. 2017. ISBN 978-3-87525-424-2.

Band 298: Peer Stenzel
Großserientaugliche Nadelwickeltechnik für verteilte Wicklungen im Anwendungsfall der E-Traktionsantriebe
FAPS, 239 Seiten, 147 Bilder, 20 Tab. 2017.
ISBN 978-3-87525-425-9.

Band 299: Mario Lušić
Ein Vorgehensmodell zur Erstellung montageführender Werkerinformationssysteme simultan zum Produktentstehungsprozess
FAPS, 174 Seiten, 79 Bilder, 22 Tab. 2017.
ISBN 978-3-87525-426-6.

Band 300: Arnd Buschhaus
Hochpräzise adaptive Steuerung und Regelung robotergeführter Prozesse
FAPS, 202 Seiten, 96 Bilder, 4 Tab. 2017. ISBN 978-3-87525-427-3.

Band 301: Tobias Laumer
Erzeugung von thermoplastischen Werkstoffverbunden mittels simultanem, intensitätsselektivem Laserstrahlschmelzen
LPT, 140 Seiten, 82 Bilder, 0 Tab. 2017. ISBN 978-3-87525-428-0.

Band 302: Nora Unger
Untersuchung einer thermisch unterstützten Fertigungskette zur Herstellung umgeformter Bauteile aus der höherfesten Aluminiumlegierung EN AW-7020
LFT, 142 Seiten, 53 Bilder, 8 Tab. 2017. ISBN 978-3-87525-429-7.

Band 303: Tommaso Stellin
Design of Manufacturing Processes for the Cold Bulk Forming of Small Metal Components from Metal Strip
LFT, 146 Seiten, 67 Bilder, 7 Tab. 2017. ISBN 978-3-87525-430-3.

Band 304: Bassim Bachy
Experimental Investigation, Modeling, Simulation and Optimization of Molded Interconnect Devices (MID) Based on Laser Direct Structuring (LDS) / Experimentelle Untersuchung, Modellierung, Simulation und Optimierung von Molded Interconnect Devices (MID) basierend auf Laser Direktstrukturierung (LDS)
FAPS, 168 Seiten, 120 Bilder, 26 Tab. 2017.
ISBN 978-3-87525-431-0.

Band 305: Michael Spahr
Automatisierte Kontaktierungsverfahren für flachleiterbasierte Pkw-Bordnetzsysteme
FAPS, 197 Seiten, 98 Bilder, 17 Tab. 2017. ISBN 978-3-87525-432-7.

Band 306: Sebastian Suttner
Charakterisierung und Modellierung des spannungszustandsabhängigen Werkstoffverhaltens der Magnesiumlegierung AZ31B für die numerische Prozessauslegung
LFT, 150 Seiten, 84 Bilder, 19 Tab. 2017. ISBN 978-3-87525-433-4.

Band 307: Bhargav Potdar
A reliable methodology to deduce thermo-mechanical flow behaviour of hot stamping steels
LFT, 203 Seiten, 98 Bilder, 27 Tab. 2017. ISBN 978-3-87525-436-5.

Band 308: Maria Löffler
Steuerung von Blechmassivumformprozessen durch maßgeschneiderte tribologische Systeme
LFT, viii u. 166 Seiten, 90 Bilder, 5 Tab. 2018. ISBN 978-3-96147-133-1.

Band 309: Martin Müller
Untersuchung des kombinierten Trenn- und Umformprozesses beim Fügen artungleicher Werkstoffe mittels Schneidclinchverfahren
LFT, xi u. 149 Seiten, 89 Bilder, 6 Tab. 2018.
ISBN: 978-3-96147-135-5.

Band 310: Christopher Kästle
Qualifizierung der Kupfer-Drahtbondtechnologie für integrierte Leistungsmodule in harschen Umgebungsbedingungen
FAPS, xii u. 167 Seiten, 70 Bilder, 18 Tab. 2018.
ISBN 978-3-96147-145-4.

Band 311: Daniel Vipavc
Eine Simulationsmethode für das 3-Rollen-Schubbiegen
LFT, xiii u. 121 Seiten, 56 Bilder, 17 Tab. 2018. ISBN 978-3-96147-147-8.

Band 312: Christina Ramer
Arbeitsraumüberwachung und autonome Bahnplanung für ein sicheres und flexibles Roboter-Assistenzsystem in der Fertigung
FAPS, xiv u. 188 Seiten, 57 Bilder, 9 Tab. 2018.
ISBN 978-3-96147-153-9.

Band 313: Miriam Rauer
Der Einfluss von Poren auf die Zuverlässigkeit der Lötverbindungen von Hochleistungs-Leuchtdioden
FAPS, xii u. 209 Seiten, 108 Bilder, 21 Tab. 2018.
ISBN 978-3-96147-157-7.

Band 314: Felix Tenner
Kamerabasierte Untersuchungen der Schmelze und Gasströmungen beim Laserstrahlschweißen verzinkter Stahlbleche
LPT, xxiii u. 184 Seiten, 94 Bilder, 7 Tab. 2018.
ISBN 978-3-96147-160-7.

Band 315: Aarief Syed-Khaja
Diffusion Soldering for High-temperature Packaging of Power Electronics
FAPS, x u. 202 Seiten, 144 Bilder, 32 Tab. 2018.
ISBN 978-3-87525-162-1.

Band 316: Adam Schaub
Grundlagenwissenschaftliche Untersuchung der kombinierten Prozesskette aus Umformen und Additive Fertigung
LFT, xi u. 192 Seiten, 72 Bilder, 27 Tab. 2019.
ISBN 978-3-96147-166-9.

Band 317: Daniel Gröbel
Herstellung von Nebenformelementen unterschiedlicher Geometrie an Blechen mittels Fließpressverfahren der Blechmassivumformung
LFT, x u. 165 Seiten, 96 Bilder, 13 Tab. 2019. ISBN 978-3-96147-168-3.

Band 318: Philipp Hildenbrand
Entwicklung einer Methodik zur Herstellung von Tailored Blanks mit definierten Halbzeugeigenschaften durch einen Taumelprozess
LFT, ix u. 153 Seiten, 77 Bilder, 4 Tab. 2019. ISBN 978-3-96147-174-4.

Band 319: Tobias Konrad
Simulative Auslegung der Spann- und Fixierkonzepte im Karosserierohbau: Bewertung der Baugruppenmaßhaltigkeit unter Berücksichtigung schwankender Einflussgrößen
LFT, x u. 203 Seiten, 134 Bilder, 32 Tab. 2019.
ISBN 978-3-96147-176-8.

Band 320: David Meinel
Architektur applikationsspezifischer Multi-Physics-Simulationskonfiguratoren am Beispiel modularer Triebzüge
FAPS, xii u. 166 Seiten, 82 Bilder, 25 Tab. 2019.
ISBN 978-3-96147-184-3.

Band 321: Andrea Zimmermann
Grundlegende Untersuchungen zum Einfluss fertigungsbedingter Eigenschaften auf die Ermüdungsfestigkeit kaltmassivumgeformter Bauteile
LFT, ix u. 160 Seiten, 66 Bilder, 5 Tab. 2019.
ISBN 978-3-96147-190-4.

Band 322: Christoph Amann
Simulative Prognose der Geometrie nassgepresster Karosseriebauteile aus Gelege-Mehrschichtverbunden
LFT, xvi u. 169 Seiten, 80 Bilder, 13 Tab. 2019.
ISBN 978-3-96147-194-2.

Band 323: Jennifer Tenner
Realisierung schmierstofffreier Tiefziehprozesse durch maßgeschneiderte Werkzeugoberflächen
LFT, x u. 187 Seiten, 68 Bilder, 13 Tab. 2019.
ISBN 978-3-96147-196-6.

Band 324: Susan Zöller
Mapping Individual Subjective Values to Product Design
KTmfk, xi u. 223 Seiten, 81 Bilder, 25 Tab. 2019.
ISBN 978-3-96147-202-4.

Band 325: Stefan Lutz
Erarbeitung einer Methodik zur semiempirischen Ermittlung der Umwandlungskinetik durchhärtender Wälzlagerstähle für die Wärmebehandlungssimulation
LFT, xiv u. 189 Seiten, 75 Bilder, 32 Tab. 2019.
ISBN 978-3-96147-209-3.

Band 326: Tobias Gnibl
Modellbasierte Prozesskettenabbildung rührreibgeschweißter Aluminiumhalbzeuge zur umformtechnischen Herstellung höchstfester Leichtbau-strukturteile
LFT, xii u. 167 Seiten, 68 Bilder, 17 Tab. 2019.
ISBN 978-3-96147-217-8.

Band 327: Johannes Bürner
Technisch-wirtschaftliche Optionen zur Lastflexibilisierung durch intelligente elektrische Wärmespeicher
FAPS, xiv u. 233 Seiten, 89 Bilder, 27 Tab. 2019.
ISBN 978-3-96147-219-2.

Band 328: Wolfgang Böhm
Verbesserung des Umformverhaltens von mehrlagigen Aluminiumblechwerkstoffen mit ultrafeinkörnigem Gefüge
LFT, ix u. 160 Seiten, 88 Bilder, 14 Tab. 2019.
ISBN 978-3-96147-227-7.

Band 329: Stefan Landkammer
Grundsatzuntersuchungen, mathematische Modellierung und Ableitung einer Auslegungsmethodik für Gelenkantriebe nach dem Spinnenbeinprinzip
LFT, xii u. 200 Seiten, 83 Bilder, 13 Tab. 2019.
ISBN 978-3-96147-229-1.

Band 330: Stephan Rapp
Pump-Probe-Ellipsometrie zur Messung transienter optischer Materialeigen-schaften bei der Ultrakurzpuls-Lasermaterialbearbeitung
LPT, xi u. 143 Seiten, 49 Bilder, 2 Tab. 2019.
ISBN 978-3-96147-235-2.

Band 331: Michael Scholz
Intralogistics Execution System mit integrierten autonomen, servicebasierten Transportentitäten
FAPS, xi u. 195 Seiten, 55 Bilder, 11 Tab. 2019.
ISBN 978-3-96147-237-6.

Band 332: Eva Bogner
Strategien der Produktindividualisierung in der produzierenden Industrie im Kontext der Digitalisierung
FAPS, ix u. 201 Seiten, 55 Bilder, 28 Tab. 2019.
ISBN 978-3-96147-246-8.

Band 333: Daniel Benjamin Krüger
Ein Ansatz zur CAD-integrierten muskuloskelettalen Analyse der Mensch-Maschine-Interaktion
KTmfk, x u. 217 Seiten, 102 Bilder, 7 Tab. 2019.
ISBN 978-3-96147-250-5.

Band 334: Thomas Kuhn
Qualität und Zuverlässigkeit laserdirektstrukturierter mechatronisch integrierter Baugruppen (LDS-MID)
FAPS, ix u. 152 Seiten, 69 Bilder, 12 Tab. 2019.
ISBN: 978-3-96147-252-9.

Band 335: Hans Fleischmann
Modellbasierte Zustands- und Prozessüberwachung auf Basis sozio-cyber-physischer Systeme
FAPS, xi u. 214 Seiten, 111 Bilder, 18 Tab. 2019.
ISBN: 978-3-96147-256-7.

Band 336: Markus Michalski
Grundlegende Untersuchungen zum Prozess- und Werkstoffverhalten bei schwingungsüberlagerter Umformung
LFT, xii u. 197 Seiten, 93 Bilder, 11 Tab. 2019.
ISBN: 978-3-96147-270-3.

Band 337: Markus Brandmeier
Ganzheitliches ontologiebasiertes Wissensmanagement im Umfeld der industriellen Produktion
FAPS, xi u. 255 Seiten, 77 Bilder, 33 Tab. 2020.
ISBN: 978-3-96147-275-8.

Band 338: Stephan Purr
Datenerfassung für die Anwendung lernender Algorithmen bei der Herstellung von Blechformteilen
LFT, ix u. 165 Seiten, 48 Bilder, 4 Tab. 2020.
ISBN: 978-3-96147-281-9.

Band 339: Christoph Kiener
Kaltfließpressen von gerad- und schrägverzahnten Zahnrädern
LFT, viii u. 151 Seiten, 81 Bilder, 3 Tab. 2020.
ISBN 978-3-96147-287-1.

Band 340: Simon Spreng
Numerische, analytische und empirische Modellierung des Heißcrimpprozesses
FAPS, xix u. 204 Seiten, 91 Bilder, 27 Tab. 2020.
ISBN 978-3-96147-293-2.

Band 341: Patrik Schwingenschlögl
Erarbeitung eines Prozessverständnisses zur Verbesserung der tribologischen Bedingungen beim Presshärten
LFT, x u. 177 Seiten, 81 Bilder, 8 Tab. 2020.
ISBN 978-3-96147-297-0.

Band 342: Emanuela Affronti
Evaluation of failure behaviour of sheet metals
LFT, ix u. 136 Seiten, 57 Bilder, 20 Tab. 2020.
ISBN 978-3-96147-303-8.

Band 343: Julia Degner
Grundlegende Untersuchungen zur Herstellung hochfester Aluminiumblechbauteile in einem kombinierten Umform- und Abschreckprozess
LFT, x u. 172 Seiten, 61 Bilder, 9 Tab. 2020.
ISBN 978-3-96147-307-6.

Band 344: Maximilian Wagner
Automatische Bahnplanung für die Aufteilung von Prozessbewegungen in synchrone Werkstück- und Werkzeugbewegungen mittels Multi-Roboter-Systemen
FAPS, xxi u. 181 Seiten, 111 Bilder, 15 Tab. 2020.
ISBN 978-3-96147-309-0.

Band 345: Stefan Härter
Qualifizierung des Montageprozesses hochminiaturisierter elektronischer Bauelemente
FAPS, ix u. 194 Seiten, 97 Bilder, 28 Tab. 2020.
ISBN 978-3-96147-314-4.

Band 346: Toni Donhauser
Ressourcenorientierte Auftragsregelung in einer hybriden Produktion mittels betriebsbegleitender Simulation
FAPS, xix u. 242 Seiten, 97 Bilder, 17 Tab. 2020.
ISBN 978-3-96147-316-8.

Band 347: Philipp Amend
Laserbasiertes Schmelzkleben von Thermoplasten mit Metallen
LPT, xv u. 154 Seiten, 67 Bilder. 2020. ISBN 978-3-96147-326-7.

Band 348: Matthias Ehlert
Simulationsunterstützte funktionale Grenzlagenabsicherung
KTmfk, xvi u. 300 Seiten, 101 Bilder, 73 Tab. 2020.
ISBN 978-3-96147-328-1.

Band 349: Thomas Sander
Ein Beitrag zur Charakterisierung und Auslegung des Verbundes von Kunststoffsubstraten mit harten Dünnschichten
KTmfk, xiv u. 178 Seiten, 88 Bilder, 21 Tab. 2020.
ISBN 978-3-96147-330-4.

Band 350: Florian Pilz
Fließpressen von Verzahnungselementen an Blechen
LFT, x u. 170 Seiten, 103Bilder, 4 Tab. 2020.
ISBN 978-3-96147-332-8.

Band 351: Sebastian Josef Katona
Evaluation und Aufbereitung von Produktsimulationen mittels abweichungsbehafteter Geometriemodelle
KTmfk, ix u. 147 Seiten, 73 Bilder, 11 Tab. 2020.
ISBN 978-3-96147-336-6.

Band 352: Jürgen Herrmann
Kumulatives Walzplattieren. Bewertung der Umformeigenschaften mehrlagiger Blechwerkstoffe der ausscheidungshärtbaren Legierung AA6014
LFT, x u. 157 Seiten, 64 Bilder, 5 Tab. 2020.
ISBN 978-3-96147-344-1.

Band 353: Christof Küstner
Assistenzsystem zur Unterstützung der datengetriebenen Produktentwicklung
KTmfk, xii u. 219 Seiten, 63 Bilder, 14 Tab. 2020.
ISBN 978-3-96147-348-9.

Band 354: Tobias Gläßel
Prozessketten zum Laserstrahlschweißen von flachleiterbasierten Formspulenwicklungen für automobile Traktionsantriebe
FAPS, xiv u. 206 Seiten, 89 Bilder, 11 Tab. 2020.
ISBN 978-3-96147-356-4.

Band 355: Andreas Meinel
Experimentelle Untersuchung der Auswirkungen von Axialschwingungen auf Reibung und Verschleiß in Zylinderrol-lenlagern
KTmfk, xii u. 162 Seiten, 56 Bilder, 7 Tab. 2020.
ISBN 978-3-96147-358-8.

Band 356: Hannah Riedle
Haptische, generische Modelle weicher anatomischer Strukturen für die chirurgische Simulation
FAPS, xxx u. 179 Seiten, 82 Bilder, 35 Tab. 2020.
ISBN 978-3-96147-367-0.

Band 357: Maximilian Landgraf
Leistungselektronik für den Einsatz dielektrischer Elastomere in aktorischen, sensorischen und integrierten sensomotorischen Systemen
FAPS, xxiii u. 166 Seiten, 71 Bilder, 10 Tab. 2020.
ISBN 978-3-96147-380-9.

Band 358: Alireza Esfandyari
Multi-Objective Process Optimization for Overpressure Reflow Soldering in Electronics Production
FAPS, xviii u. 175 Seiten, 57 Bilder, 23 Tab. 2020.
ISBN 978-3-96147-382-3.

Band 359: Christian Sand
Prozessübergreifende Analyse komplexer Montageprozessketten mittels Data Mining
FAPS, XV u. 168 Seiten, 61 Bilder, 12 Tab. 2021.
ISBN 978-3-96147-398-4.

Band 360: Ralf Merkl
Closed-Loop Control of a Storage-Supported Hybrid Compensation System for Improving the Power Quality in Medium Voltage Networks
FAPS, xxvii u. 200 Seiten, 102 Bilder, 2 Tab. 2021.
ISBN 978-3-96147-402-8.

Band 361: Thomas Reitberger
Additive Fertigung polymerer optischer Wellenleiter im Aerosol-Jet-Verfahren
FAPS, xix u. 141 Seiten, 65 Bilder, 11 Tab. 2021.
ISBN 978-3-96147-400-4.

Band 362: Marius Christian Fechter
Modellierung von Vorentwürfen in der virtuellen Realität mit natürlicher Fingerinteraktion
KTmfk, x u. 188 Seiten, 67 Bilder, 19 Tab. 2021.
ISBN 978-3-96147-404-2.

Band 363: Franziska Neubauer
Oberflächenmodifizierung und Entwicklung einer Auswertemethodik zur Verschleißcharakterisierung im Presshärteprozess
LFT, ix u. 177 Seiten, 42 Bilder, 6 Tab. 2021.
ISBN 978-3-96147-406-6.

Band 364: Eike Wolfram Schäffer
Web- und wissensbasierter Engineering-Konfigurator für roboterzentrierte Automatisierungslösungen
FAPS, xxiv u. 195 Seiten, 108 Bilder, 25 Tab. 2021.
ISBN 978-3-96147-410-3.

Band 365: Daniel Gross
Untersuchungen zur kohlenstoffdioxidbasierten kryogenen Minimalmengenschmierung
REP, xii u. 184 Seiten, 56 Bilder, 18 Tab. 2021.
ISBN 978-3-96147-412-7.

Band 366: Daniel Junker
Qualifizierung laser-additiv gefertigter Komponenten für den Einsatz im Werkzeugbau der Massivumformung
LFT, vii u. 142 Seiten, 62 Bilder, 5 Tab. 2021.
ISBN 978-3-96147-416-5.

Band 367: Tallal Javied
Totally Integrated Ecology Management for Resource Efficient and Eco-Friendly Production
FAPS, xv u. 160 Seiten, 60 Bilder, 13 Tab. 2021.
ISBN 978-3-96147-418-9.

Band 368: David Marco Hochrein
Wälzlager im Beschleunigungsfeld – Eine Analysestrategie zur Bestimmung des Reibungs-, Axialschub- und Temperaturverhaltens von Nadelkränzen –
KTmfk, xiii u. 279 Seiten, 108 Bilder, 39 Tab. 2021.
ISBN 978-3-96147-420-2.

Band 369: Daniel Gräf
Funktionalisierung technischer Oberflächen mittels prozessüberwachter aerosolbasierter Drucktechnologie
FAPS, xxii u. 175 Seiten, 97 Bilder, 6 Tab. 2021.
ISBN 978-3-96147-433-2.

Band 370: Andreas Gröschl
Hochfrequent fokusabstandsmodulierte Konfokalsensoren für die Nanokoordinatenmesstechnik
FMT, x u. 144 Seiten, 98 Bilder, 6 Tab. 2021.
ISBN 978-3-96147-435-6.

Band 371: Johann Tüchsen
Konzeption, Entwicklung und Einführung des Assistenzsystems D-DAS für die Produktentwicklung elektrischer Motoren
KTmfk, xii u. 178 Seiten, 92 Bilder, 12 Tab. 2021.
ISBN 978-3-96147-437-0.

Band 372: Max Marian
Numerische Auslegung von Oberflächenmikrotexturen für geschmierte tribologische Kontakte
KTmfk, xviii u. 276 Seiten, 85 Bilder, 45 Tab. 2021.
ISBN 978-3-96147-439-4.

Band 373: Johannes Strauß
Die akustooptische Strahlformung in der Lasermaterialbearbeitung
LPT, xvi u. 113 Seiten, 48 Bilder. 2021. ISBN 978-3-96147-441-7.

Band 374: Martin Hohmann
Machine learning and hyper spectral imaging: Multi Spectral Endoscopy in the Gastro Intestinal Tract towards Hyper Spectral Endoscopy
LPT, x u. 137 Seiten, 62 Bilder, 29 Tab. 2021.
ISBN 978-3-96147-445-5.

Band 375: Timo Kordaß
Lasergestütztes Verfahren zur selektiven Metallisierung von epoxidharzbasierten Duromeren zur Steigerung der Integrationsdichte für dreidimensionale mechatronische Package-Baugruppen
FAPS, xviii u. 198 Seiten, 92 Bilder, 24 Tab. 2021.
ISBN 978-3-96147-443-1.

Band 376: Philipp Kestel
Assistenzsystem für den wissensbasierten Aufbau konstruktionsbegleitender Finite-Elemente-Analysen
KTmfk, xviii u. 209 Seiten, 57 Bilder, 17 Tab. 2021.
ISBN 978-3-96147-457-8.

Band 377: Martin Lerchen
Messverfahren für die pulverbettbasierte additive Fertigung zur Sicherstellung der Konformität mit geometrischen Produktspezifikationen
FMT, x u. 150 Seiten, 60 Bilder, 9 Tab. 2021.
ISBN 978-3- 96147-463-9.

Band 378: Michael Schneider
Inline-Prüfung der Permeabilität in weichmagnetischen Komponenten
FAPS, xxii u. 189 Seiten, 79 Bilder, 14 Tab. 2021.
ISBN 978-3-96147-465-3.

Band 379: Tobias Sprügel
Sphärische Detektorflächen als Unterstützung der Produktentwicklung zur Datenanalyse im Rahmen des Digital Engineering
KTmfk, xiii u. 213 Seiten, 84 Bilder, 33 Tab. 2021.
ISBN 978-3-96147-475-2.

Band 380: Tom Häfner
Multipulseffekte beim Mikro-Materialabtrag von Stahllegierungen mit Pikosekunden-Laserpulsen
LPT, xxviii u. 159 Seiten, 57 Bilder, 13 Tab. 2021.
ISBN 978-3-96147-479-0.

Band 381: Björn Heling
Einsatz und Validierung virtueller Absicherungsmethoden für abweichungs-behaftete Mechanismen im Kontext des Robust Design
KTmfk, xi u. 169 Seiten, 63 Bilder, 27 Tab. 2021.
ISBN 978-3-96147-487-5.

Band 382: Tobias Kolb
Laserstrahl-Schmelzen von Metallen mit einer Serienanlage – Prozesscharakterisierung und Erweiterung eines Überwachungssystems
LPT, xv u. 170 Seiten, 128 Bilder, 16 Tab. 2021.
ISBN 978-3-96147-491-2.

Band 383: Mario Meinhardt
Widerstandselementschweißen mit gestauchten Hilfsfügeelementen - Umformtechnische Wirkzusammenhänge zur Beeinflussung der Verbindungsfestigkeit
LFT, xii u. 189 Seiten, 87 Bilder, 4 Tab. 2022.
ISBN 978-3-96147-473-8.

Band 384: Felix Bauer
Ein Beitrag zur digitalen Auslegung von Fügeprozessen im Karosseriebau mit Fokus auf das Remote-Laserstrahlschweißen unter Einsatz flexibler Spanntechnik
LFT, xi u. 185 Seiten, 74 Bilder, 12 Tab. 2022.
ISBN 978-3-96147-498-1.

Band 385: Jochen Zeitler
Konzeption eines rechnergestützten Konstruktionssystems für optomechatronische Baugruppen
FAPS, xix u. 172 Seiten, 88 Bilder, 11 Tab. 2022.
ISBN 978-3-96147-499-8.

Band 386: Vincent Mann
Einfluss von Strahloszillation auf das Laserstrahlschweißen hochfester Stähle
LPT, xiii u. 172 Seiten, 103 Bilder, 18 Tab. 2022.
ISBN 978-3-96147-503-2.

Band 387: Chen Chen
Skin-equivalent opto-/elastofluidic in-vitro microphysiological vascular models for translational studies of optical biopsies
LPT, xx u. 126 Seiten, 60 Bilder, 10 Tab. 2022.
ISBN 978-3-96147-505-6.

Band 388: Stefan Stein
Laser drop on demand joining as bonding method for electronics assembly and packaging with high thermal requirements
LPT, x u. 112 Seiten, 54 Bilder, 10 Tab. 2022.
ISBN 978-3-96147-507-0

Band 389: Nikolaus Urban
Untersuchung des Laserstrahlschmelzens von Neodym-Eisen-Bor zur additiven Herstellung von Permanentmagneten
FAPS, x u. 174 Seiten, 88 Bilder, 18 Tab. 2022.
ISBN 978-3-96147-501-8.

Band 390: Yiting Wu
Großflächige Topographiemessungen mit einem Weißlichtinterferenzmikroskop und einem metrologischen Rasterkraftmikroskop
FMT, xii u. 142 Seiten, 68 Bilder, 11 Tab. 2022.
ISBN: 978-3-96147-513-1.

Band 391: Thomas Papke
Untersuchungen zur Umformbarkeit hybrider Bauteile aus Blechgrundkörper und additiv gefertigter Struktur
LFT, xii u. 194 Seiten, 71 Bilder, 16 Tab. 2022.
ISBN 978-3-96147-515-5.

Band 392: Bastian Zimmermann
Einfluss des Vormaterials auf die mehrstufige Kaltumformung vom Draht
LFT, xi u. 182 Seiten, 36 Bilder, 6 Tab. 2022.
ISBN 978-3-96147-519-3.

Band 393: Harald Völkl
Ein simulationsbasierter Ansatz zur Auslegung additiv gefertigter FLM-Faserverbundstrukturen
KTmfk, xx u. 204 Seiten, 95 Bilder, 22 Tab. 2022.
ISBN 978-3-96147-523-0.

Band 394: Robert Schulte
Auslegung und Anwendung prozessangepasster Halbzeuge für Verfahren der Blechmassivumformung
LFT, x u. 163 Seiten, 93 Bilder, 5 Tab. 2022.
ISBN 978-3-96147-525-4.

Band 395: Philipp Frey
Umformtechnische Strukturierung metallischer Einleger im Folgeverbund für mediendichte Kunststoff-Metall-Hybridbauteile
LFT, ix u. 180 Seiten, 83 Bilder, 7 Tab. 2022.
ISBN 978-3-96147-534-6.

Band 396: Thomas Johann Luft
Komplexitätsmanagement in der Produktentwicklung - Holistische Modellierung, Analyse, Visualisierung und Bewertung komplexer Systeme
KTmfk, xiii u. 510 Seiten, 166 Bilder, 16 Tab. 2022.
ISBN 978-3-96147-540-7.

Band 397: Li Wang
Evaluierung der Einsetzbarkeit des lasergestützten Verfahrens zur selektiven Metallisierung für die Verbesserung passiver Intermodulation in Hochfrequenzanwendungen
FAPS, xxii u.151 Seiten, 72 Bilder, 22 Tab. 2022.
ISBN 978-3-96147-542-1.

Band 398: Sebastian Reitelshöfer
Der Aerosol-Jet-Druck Dielektrischer Elastomere als additives Fertigungsverfahren für elastische mechatronische Komponenten
FAPS, xxv u. 206 Seiten, 87 Bilder, 13 Tab. 2022.
ISBN 978-3-96147-547-6.

Band 399: Alexander Meyer
Selektive Magnetmontage zur Verringerung des Rastmomentes permanenterregter Synchronmotoren
FAPS, xv u. 164 Seiten, 90 Bilder, 18 Tab. 2022.
ISBN 978-3-96147-555-1.

Band 400: Rong Zhao
Design verschleißreduzierender amorpher Kohlenstoffschichtsysteme für trockene tribologische Gleitkontakte
KTmfk, x u. 148 Seiten, 69 Bilder, 14 Tab. 2022.
ISBN 978-3-96147-557-5.

Band 401: Christian P. J. Schwarzer
Kupfersintern als Fügetechnologie für Leistungselektronik
FAPS, xxvii u. 234 Seiten, 125 Bilder, 24 Tab. 2022.
ISBN 978-3-96147-566-7.

Band 402: Alexander Horn
Grundlegende Untersuchungen zur Gradierung der mechanischen Eigenschaften pressgehärteter Bauteile durch eine örtlich begrenzte Aufkohlung
LFT, xii u. 204 Seiten, 58 Bilder, 6 Tab. 2022.
ISBN 978-3-96147-568-1.

Band 403: Artur Klos
Werkstoff- und umformtechnische Bewertung von hochfesten Aluminiumblechwerkstoffen für den Karosseriebau
LFT, x u. 192 Seiten, 73 Bilder, 12 Tab. 2022.
ISBN 978-3-96147-572-8.

Band 404: Harald Schmid
Ganzheitliche Erarbeitung eines Prozessverständnisses von Tiefziehprozessen mit Ziehsicken auf Basis mechanischer und tribologischer Analysen
LFT, xiii u. 211 Seiten, 78 Bilder, 5 Tab. 2022.
ISBN 978-3-96147-577-3.

Band 405: Johannes Henneberg
Blechmassivumformung von Funktionsbauteilen aus Bandmaterial
LFT, viii u. 176 Seiten, 101 Bilder, 2 Tab. 2022.
ISBN 978-3-96147-579-7.

Band 406: Anton Schmailzl
Festigkeits- und zeitoptimierte Prozessführung beim quasi-simultanen Laser-Durchstrahlschweißen
LPT, xiii u. 157 Seiten, 84 Bilder, 7 Tab. 2022.
ISBN 978-3-96147-583-4.

Band 407: Alexander Wolf
Modellierung und Vorhersage menschlichen Interaktionsverhaltens zur Analyse der Mensch-Produkt Interaktion
KTmfk, x u. 207 Seiten, 69 Bilder, 10 Tab. 2022.
ISBN 978-3-96147-585-8.

Band 408: Tim Weikert
Modifikationen amorpher Kohlenstoffschichten zur Anpassung der Reibungsbedingungen und zur Erhöhung des Verschleißschutzes
KTmfk, xvii u. 258 Seiten, 91 Bilder, 9 Tab. 2022.
ISBN 978-3-96147-589-6.

Band 409: Stefan Götz
Frühzeitiges konstruktionsbegleitendes Toleranzmanagement
KTmfk, ix u. 276 Seiten, 127 Bilder, 13 Tab. 2022.
ISBN 978-3-96147-593-3.

Band 410: Markus Hubert
Einsatzpotenziale der Rotationsschneidtechnologie in der Verarbeitung von metallischen Funktionsfolien für mechatronische Produkte
FAPS, xviii u. 139 Seiten, 86 Bilder, 7 Tab. 2022.
ISBN 978-3-96147-603-9.

Band 411: Manfred Vogel
Grundlagenuntersuchungen und Erarbeitung einer Methodik zur Herstellung maßgeschneiderter Halbzeuge auf Basis eines neuartigen flexiblen Walzprozesses
LFT, ix u. 176 Seiten, 61 Bilder, 11 Tab. 2022.
ISBN 978-3-96147-605-3.

Band 412: Michael Weigelt
Multidimensionale Optionenanalyse alternativer Antriebskonzepte für die individuelle Langstreckenmobilität
FAPS, xv u. 222 Seiten, 89 Bilder, 38 Tab. 2022.
ISBN 978-3-96147-607-7.

Band 413: Frank Bodendorf
Machine Learning im Cost Engineering des Supply Managements
FAPS, xiii u. 165 Seiten, 75 Bilder, 13 Tab. 2023.
ISBN 978-3-96147-609-1.

Band 414: Maximilian Metzner
Planung und Simulation taktiler, intelligenter und kollaborativer Roboterfähigkeiten in der Montage
FAPS, xix u. 174 Seiten, 72 Bilder, 3 Tab. 2023.
ISBN 978-3-96147-611-4.

Band 415: Tina Buker
Ein Ansatz zur Reduktion produktinduzierter Nutzerstigmatisierung durch Förderung einer gleichermaßen gebrauchstauglichen wie emotionalen Produktgestalt
KTmfk, x u. 236 Seiten, 54 Bilder, 44 Tab. 2022.
ISBN 978-3-96147-613-8.

Band 416: Marlene Kuhn
Model-based Traceability System Development for Complex Manufacturing Applying Blockchain and Graphs
FAPS, xv u. 167 Seiten, 63 Bilder, 10 Tab. 2022.
ISBN 978-3-96147-615-2.

Band 417: Benjamin Lengenfelder
Remote photoacoustic sensing using speckle-analysis for biomedical imaging
LPT, xv u. 124 Seiten, 86 Bilder, 10 Tab. 2023.
ISBN 978-3-96147-617-6.

Band 418: Benjamin Pohrer
Analyse des Zusammenhangs zwischen dem tribochemischen Aufbau von Grenzschichten und der Ausbildung von White Etching Crack-Schäden
KTmfk, xv u. 258 Seiten, 103 Bilder, 10 Tab. 2023.
ISBN 978-3-96147- 621-3.

Band 419: Matthias Friedlein
Zuverlässigkeitsmethoden zur Beschleunigung von Qualifizierungsuntersuchungen für Steckkontakte
FAPS, xxv u. 162 Seiten, 98 Bilder, 7 Tab. 2023.
ISBN 978-3-96147-625-1.

Band 420: Thomas Stoll
Laser Powder Bed Fusion von Kupfer auf Aluminiumoxid-Keramiken
FAPS, xxvii u. 236 Seiten, 103 Bilder, 11 Tab. 2023.
ISBN 978-3-96147-631-2.

Band 421: Eric Eschner
Relation of Particle Motion and Process Zone Formation as a Basis for Sensing Approaches within PBF-LB/M
LPT, xiv u. 143 Seiten, 87 Bilder, 0 Tab. 2023.
ISBN 978-3-96147-633-6.

Band 422: Fanuel Mehari
Laser-induced Breakdown Spectroscopy (LIBS) as a diagnostics tool for biological tissue analysis.
LPT, xv u. 145 Seiten, 68 Bilder, 12 Tab. 2023.
ISBN 978-3-96147-641-1.

Band 423: Uwe Leicht
Ultraschallüberlagertes Umformen und Verstemmen von Stahlwerkstoffen
LFT, xi u. 165 Seiten, 65 Bilder, 6 Tab. 2023.
ISBN 978-3-96147-643-5.

Band 424: Thomas Braun
Potenzialanalyse der plasmabasierten, strukturierten Metallisierung thermoaktiver Oberflächen im industriellen Hausbau
FAPS, xvii u. 152 Seiten, 72 Bilder, 11 Tab. 2023.
ISBN 978-3-96147-653-4.

Band 425: Reinhardt Seidel
Modellbasierte Optimierung des Selektivwellenlötprozesses
FAPS, xxii u. 167 Seiten, 73 Bilder, 23 Tab. 2023.
ISBN: 978-3-96147-651-0.

Band 426: Matthias Lenzen
Maßgeschneiderte Werkstoffcharakterisierung für die numerische Auslegung von Blechumformprozessen
LFT, xi u. 187 Seiten, 77 Bilder, 13 Tab. 2023.
ISBN: 978-3-96147-663-3.

Band 427: Matthias Graser
Analyse lokaler Kurzzeitwärmebehandlungsmethoden zur Verbesserung des Umformverhaltens und der Bauteileigenschaften von Aluminiumstrangpresshohlprofilen
LFT, xi u. 169 Seiten, 81 Bilder, 1 Tab. 2023.
ISBN: 978-3-96147-666-4.

Band 428: Markus Lieret
Sicheres autonomes Flugrobotersystem für den Einsatz im Produktions- und Logistikumfeld
FAPS, xix u. 198 Seiten, 54 Bilder, 7 Tab. 2023.
ISBN 978-3-96147-668-8.

Band 429: Petar Vukovic
Simulation komplexer Kommunikationssysteme in der Fertigungsautomatisierung
FAPS, xiv u. 163 Seiten, 57 Bilder, 21 Tab. 2023.
ISBN 978-3-96147-673-2.

Band 430: Fabian Knieps
Finite Elemente Simulation dünnster Verpackungsstähle: Entwicklung einer geeigneten Charakterisierungs- und Validierungsstrategie
LFT, xix, 189 Seiten, 122 Bilder, 17 Tab. 2023.
ISBN 978-3-96147-689-3

Band 431: Julian Seßner
Multimodale Bildsegmentierung gering strukturierter Umgebungen für die Navigation am Beispiel eines Assistenzsystems für sehbeeinträchtigte Personen
FAPS, xxv, 203 Seiten, 57 Bilder, 25 Tab. 2023.
ISBN 978-3-96147-697-8

Band 432: Benjamin Samuel Lutz
Smart Manufacturing System for Process Optimization Regarding Deviations among Material Batches
FAPS, xix, 208 Seiten, 77 Bilder, 14 Tab. 2023.
ISBN 978-3-96147-703-6

Band 433: Michael Jüttner
Bewertung von Kantenpressungen auf Basis von Simulationen mehrfach überrollter elasto-plastischer Kontakte
KTmfk, xii, 162 Seiten, 59 Bilder, 7 Tab. 2024.
ISBN 978-3-96147-713-5.

Band 434: Sebastian Wiesenmayer
Untersuchungen zur Stoffflusssteuerung beim Fügen durch Umformen von hochfesten Aluminiumlegierungen mittels lokaler Kurzzeitwärmebehandlung
LFT, xii u. 197 Seiten, 81 Bilder, 19 Tab. 2024.
ISBN 978-3-96147-715-9.

Band 435: Clara-Maria Kuball
Grundlegende Untersuchungen zur umformtechnischen Herstellung von Halbhohlstanznieten aus hochverfestigenden Werkstoffen
LFT, viii u. 180 Seiten, 64 Bilder, 13 Tab. 2024.
ISBN 978-3-96147-717-3.

Band 436: Martin Roth
Sampling-based Tolerance-Cost Optimization: The Key to Optimal Tolerance Allocation
KTmfk, xxxvii u. 337 Seiten, 97 Bilder, 56 Tab. 2024.
ISBN 978-3-96147-719-7.

Band 437: Stephan Schirdewahn
Verbesserung des tribologischen Einsatzverhaltens im Presshärteprozess durch Verwendung maßgeschneiderter laserimplantierter Werkzeuge
LFT, viii u. 177 Seiten, 63 Bilder, 7 Tab. 2024.
ISBN 978-3-96147-721-0.

Band 438: Andreas Rohrmoser
Erarbeitung eines grundlegenden Verständnisses zum Fließpressen betriebsangepasster Verzahnungen für den Einsatz in der Materialpaarung Metall-Kunststoff
LFT, x u. 166 Seiten, 94 Bilder, 6 Tab. 2024.
ISBN: 978-3-96147-723-4.

Band 439: Andreas Selmaier
DMAICS-Zyklus zur Digitalisierung in produzierenden Unternehmen
FAPS, xv u. 185 Seiten, 73 Bilder, 19 Tab. 2024.
ISBN: 978-3-96147-733-3.

Band 440: Thomas Kistner
Entwicklung von Modellen der Oberflächenform für die Messunsicherheitsbestimmung von taktilen Koordinatenmessungen durch Simulation
FMT, xiii u. 134 Seiten, 64 Bilder, 9 Tab. 2024.
ISBN 978-3-96147-735-7.

Band 441: Fabian Dworschak
Selbstverstärkendes Lernen als Beitrag zur Automatisierung der Anpassungskonstruktion
KTmfk, x, 205 Seiten, 87 Bilder, 16 Tab. 2024.
ISBN 978-3-96147-739-5.

Band 442: Martin Killmann
Vorspannung und Ermüdung von Kaltmassivumformwerkzeugen für unrunde Bauteilgeometrien
LFT, ix u. 160 Seiten, 85 Bilder, 6 Tab. 2024.
ISBN 978-3-96147-741-8.

Band 443: Ann-Kathrin Wiemann
Beitrag zur Messunsicherheitsermittlung für die Messung großer Zahnräder zur Erweiterung des virtuellen Koordinatenmessgerätes der Physikalisch-Technischen Bundesanstalt
FMT, xxiv u. 133 Seiten, 41 Bilder, 22 Tab. 2024.
ISBN 978-3-96147-747-0.

Band 444: Andreas Jobst
Eigenspannungen beim Voll-Vorwärts-Fließpressen – Entstehung, Einstellung und Stabilität
LFT, ix u. 162 Seiten, 89 Bilder, 5 Tab. 2024.
ISBN: 978-3-96147-749-4.

Band 445: Martin Anton Kraus
Grundlagenwissenschaftliche Untersuchungen zum Kaltfließpressen kleinster metallischer Pin-Strukturen aus der Blechebene
LFT, x u. 191 Seiten, 64 Bilder, 10 Tab. 2024.
ISBN: 978-3-96147-757-9.

Band 446: Moritz Späth
Assessment of microcirculation by shifted position-diffuse reflectance imaging (SP-DRI)
LPT, xi u. 109 Seiten, 37 Bilder, 8 Tab. 2024.
ISBN 978-3-96147-759-3.

Band 447: Benedikt Göddeke
Methode zur Auswahl eines alternativen Blechwerkstoffes für flexibel gewalzte und direkt warmumgeformte Karosseriestrukturbauteile
LFT, xvi u. 222 Seiten, 66 Bilder, 27 Tab. 2024.
ISBN 978-3-96147-762-3.

Band 448: Jan Hafenecker
Systematische Untersuchung zur Blechumformung von Hybridbauteilen
LFT, xxi u. 173 Seiten, 78 Bilder, 6 Tab. 2024.
ISBN 978-3-96147-764-7.

Band 449: Sven Wirsching
Numerische Optimierung von sekundären, geschmierten Punkt- und Ellipsenkontakten zur gezielten Auslegung von Rollenlagern
KTmfk, xxv u. 206 Seiten, 70 Bilder, 16 Tab. 2024.
ISBN: 978-3-96147-766-1.

Band 450: Tobias Lechler
Der Digitale Zwilling im Rampdown automatisierter Produktionssysteme
FAPS, xvii u. 152 Seiten, 83 Bilder, 4 Tab. 2024
ISBN: 978-3-96147-691-6.

Band 451: Eva Russwurm
Kombinierte Material- und Energieflusssimulation gleichstrombasierter, automatisierter Produktionsanlagen
FAPS, xvi u. 165 Seiten, 67 Bilder, 13 Tab. 2024
ISBN: 978-3-96147-770-8.

Band 452: Janik Schaude
Untersuchungen zur rasterkraft- und konfokalmikroskopischen Charakterisierung nanometrologischer Referenzkörper
FMT, x u. 167 Seiten, 74 Bilder, 4 Tab. 2024

ISBN: 978-3-96147-776-0.

Band 453: Philipp Bräuer
Nahinfrarot-Laser-Strukturierung und nasschemische Metallisierung von Aluminiumoxid mittels Laser-Absorptionsschicht
FAPS, xx u. 152 Seiten, 55 Bilder, 19 Tab. 2024.
ISBN 978-3-96147-780-7.

Band 454: Andreas Michael Müller
Definition and applications of the spatially discrete metrological descriptor framework for triangle mesh geometry data in 3D coordinate metrology
FMT, x u. 220 Seiten, 75 Bilder, 16 Tab. 2024.
ISBN 978-3-96147-782-1.

Kurzfassung

In der 3D-Koordinatenmesstechnik wird die Oberfläche des zu untersuchenden Messobjekts angetastet und auf Basis der ermittelten Messpunkte eine Entscheidung bzgl. der Konformität des Objekts im Vergleich mit der Spezifikation getroffen. Jeder Messpunkt kann grundsätzlich nur mit endlicher Genauigkeit aufgenommen werden. Somit wirkt sich die aus den Messabweichungen abgeleitete Messunsicherheit direkt auf die Konformitätsbewertung aus. Aufgrund der technischen Eigenschaften des Messsystems ist die Messunsicherheit verschiedener Messpunkte in der Regel nicht identisch. Diese Arbeit beschreibt die Entwicklung und Anwendung eines Rahmens mit dem die Messunsicherheit an beliebigen Punkten auf der Geometrie des Bauteils bestimmt werden kann und basiert dabei ausschließlich auf der statistischen Verarbeitung von Referenzmessdaten, Messdaten des Zielsystems und der Nominalgeometrie des Objekts. Dabei wird auf die Bestimmung von Ersatzgeometrieelementen verzichtet und lediglich die lokale Beziehung der Geometriedaten ausgewertet. Verschiedene metrologische Deskriptoren (u. a. die Messunsicherheit) bieten die Möglichkeit einer detaillierten Analyse des Zielmesssystems hinsichtlich seiner messtechnischen Eigenschaften. Somit können durch die Verfügbarkeit von punktweisen Informationen umfassende Messsystemanalysen mit einer hohen Sensitivität durchgeführt werden, mit der die lokalen Auswirkungen verschiedener Einflüsse auf die Messkette zuverlässig identifiziert und quantisiert werden.

In 3D coordinate metrology, the surface of a measurement object is probed and a decision is made regarding the conformity of the object with respect to the specification on the basis of the measuring points determined. In principle, each measuring point can only be captured with finite accuracy. Thus, the measurement uncertainty derived from the measurement deviations has a direct effect on the conformity assessment. Due to the technical limitations of the measurement system, the uncertainty of different data points is usually not identical. This work describes the development and application of a framework with which the measurement uncertainty can be determined at arbitrary points on the geometry of the component. It is based exclusively on the statistical processing of reference measurement data, measurement data of the target system and the nominal geometry of the object. The determination of substitute geometry elements is avoided and in return only the local relationship of the different geometry data is evaluated. Various metrological descriptors (e.g. the measurement uncertainty) offer the possibility of a detailed analysis of the target measurement system with regard to its metrological properties. Thus, due to the availability of point-by-point information, comprehensive measurement system analyses with a high sensitivity can be carried out, with which the local effects of various influences on the measurement chain can be reliably identified and quantified.

ISBN 978-3-96147-782-1
9 783961 477821

FAU UNIVERSITY PRESS 2024